DISSECTING THE FLOW PHYSICS OF AEROELASTIC OSCILLATIONS AND VORTEX-DOMINATED FLOWS: COMPUTATIONAL AND DATA-DRIVEN METHODS

by

Karthik Menon

A dissertation submitted to The Johns Hopkins University in conformity with the requirements for the degree of Doctor of Philosophy.

Baltimore, Maryland

June, 2021

Abstract

Fluid flows interact with flexible and moving bodies in a wide range of natural and engineering applications. These problems are often characterized by highly non-linear flow physics due to the generation and shedding of several vortices, their interactions, and the forces they induce on surfaces within the flow. However, our current understanding of the force producing mechanisms in these flows and our ability to accurately quantify their influence remains limited. As a result, the dynamics of many such vortex-dominated problems involving fluid-structure interactions and unsteady aerodynamics are notoriously hard to predict.

In this work, we use computational modeling in conjunction with data-driven techniques to analyze the flow physics of these problems. We particularly focus on the flow-induced oscillation of wings and cylindrical bluff-bodies at low Reynolds numbers. Using simulations based on a sharp-interface immersed boundary method, we demonstrate the large range of oscillation responses and parametric dependencies that these systems exhibit. We propose

an energy-based tool to analyze, predict and control the non-linear, and often non-intuitive, oscillation responses observed. We show that "energy maps" identify all possible flow-induced oscillation response branches and bifurcations in a system, thus allowing their use in the prediction and control of pitching oscillations for wings interacting with incoming gusts. Furthermore, we also formulate and demonstrate a novel extension to Dynamic Mode Decomposition for the analysis of such flows involving moving boundaries.

A second focus of this work is on disentangling the various mechanisms at play in the generation of loads on surfaces within vortex-dominated flows. To this end, we develop a force and moment partitioning method which allows us to rigorously quantify the influence of distinct physical mechanisms as well as individual flow features in force/moment production. This method is combined with data-driven techniques to estimate the influence of each individual vortex in a flow-field, while also tracking and categorizing these vortices as they evolve with the flow. We utilize these tools to reveal new insights into fundamental phenomena in aerodynamics and flow-induced oscillations – such as the mechanisms that drive the flow-induced oscillation of cylinders and the production of lift during dynamic stall and on three-dimensional wings.

Primary Reader and Advisor: Rajat Mittal

Secondary Readers: Charles Meneveau and Joseph Katz

Acknowledgments

I would first and foremost like to thank my advisor, Professor Rajat Mittal, for his support and encouragement throughout my doctoral studies. His keen physical insight and knack for turning simple ideas into intriguing scientific questions have served as a constant source of learning and motivation. I have truly enjoyed and benefited from his ability to balance the right amount of guidance with the freedom to explore my interests.

I am very grateful for all the wonderful faculty and staff I have had the opportunity to meet at the Department of Mechanical Engineering and elsewhere at Hopkins. In particular, I am thankful to Professors Charles Meneveau and Joe Katz for serving on my dissertation committee, and Professors Harihar Rajaram, Jamie Guest and Takeru Igusa for serving on my GBO committee. Many thanks to Professors Tamer Zaki and Dennice Gayme for several enlightening discussions inside and outside the classroom. I am especially grateful to Professor Jung-Hee Seo for all his invaluable help with *ViCar3D*.

I was first ushered into the world of academic research by Professors Rama

ACKNOWLEDGMENTS

Govindarajan and Shubha Tewari to whom I am deeply indebted. The environment of curiosity, passion and care that they fostered made a great impression on me as a naïve undergraduate student. It made me appreciate viewing all aspects of our world through the lens of an inquisitive academic – from questions of physics and nature to less familiar questions of culture and society.

Many thanks to my friends and colleagues at Hopkins for making my time in Baltimore enjoyable and barely keeping me from devolving into complete workaholism. I will fondly remember the endless coffee breaks, lunch conversations and the pandemic-induced cooking sessions and board games. I am also very grateful to my friends away from Hopkins. I will continue to look forward to the video calls and virtual game sessions we have had since the COVID-19 pandemic began.

Lastly, my family has been the pillar on which much of this rests. Their unyielding love, care and drama have kept me going through this journey. Their pride in my work (and marginally successful attempts at explaining it to anyone who will listen) has made me constantly strive to do better.

This work has been funded by the Air Force Office of Scientific Research Grant Number FA 9550-16-1-0404. Computational resources at Extreme Science and Engineering Discovery Environment (XSEDE) and at the Maryland Advanced Research Computing Center (MARCC) are also acknowledged.

Contents

List of Tables

List of Figures

Chapter 1

Introduction

The interaction of fluid flows with flexible and moving bodies is an everyday occurrence that has profound implications. From the opening and closing of heart valves, to the flapping flight of birds and the swimming of fish – the natural world is rife with examples. In a wide range of such situations, the fluid flow has the ability to induce oscillations of the flexible bodies it interacts with. Depending on the scenario, these *flow-induced oscillations* can be innocuous, desirable, or highly destructive. On one hand, this phenomenon is the basis for the vibrations of reeds in a saxophone, as well as the flapping of flags and the rustling of leaves in breeze. On the other hand, flow-induced oscillations have the potential to distort aircraft wings and bring down bridges (famously, the Tacoma Narrows Bridge), if not adequately accounted for.

Flow-induced oscillations are a result of a complex interplay amongst many

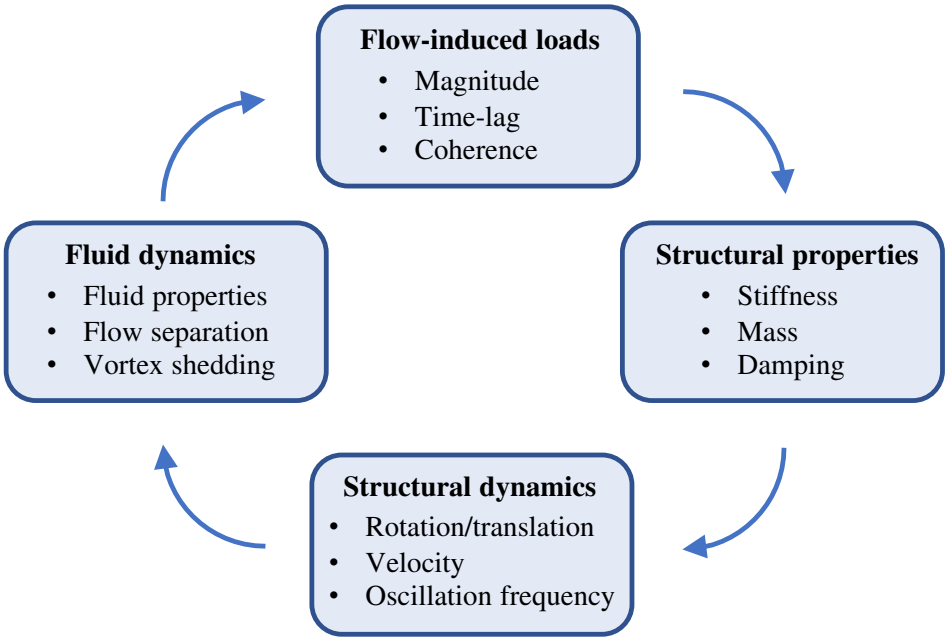

Figure 1.1: A schematic showing the various fluid-structure interaction factors involved in the dynamics of flow-induced oscillations. Adapted from Blevins [1].

factors involving the fluid flow, the forces induced by the fluid on structures within it, and properties of the elastic structures themselves. Fluid flows have the capacity for inducing large forces on bodies immersed within them – as we are reminded to be grateful for every time we sit in an airplane. These forces tend to deform flexible bodies within them, which alters the flow around these bodies. The modified flow results in modified forces on the body, which in turn leads to further deformations. This two-way *fluid-structure interaction* plays out in many different ways, one of which is the occurrence of self-excited oscillations of the body. A schematic of the many factors involved in this interdependence is shown in figure 1.1.

Two model problems involving flow-induced oscillations that are of academic as well as practical interest are the oscillation of wings and the vibration of cylindrical bluff bodies. The former is generally termed *aeroelastic flutter*, and has attracted scientific attention for many decades on account of its importance in air-vehicle design and performance. Recently, it has garnered renewed interest due to the drive towards higher efficiency aircraft that use lighter (and therefore more flexible) materials. Furthermore, the advent of micro- and unmanned air-vehicles has also spurred research in aeroelastic phenomena, particularly at lower Reynolds numbers [2]. Interest in the flow-induced vibration of cylindrical bluff bodies has similarly been motivated by applications such as the design safety of riser tubes, heat exchangers, as well as civil structures such as bridges and buildings – all of which are susceptible to unwanted vibrations. While most of these applications have historically aimed at suppressing flow-induced oscillations, there has also been recent research in enhancing such oscillations as a way to harness energy. These energy harvesting systems generally aim to exploit the propensity of naturally occurring fluid flows, such as rivers and tides, for generating flow-induced oscillations [3–5].

This dissertation explores some of the fundamental flow physics that governs the forces induced on surfaces within fluid flows and gives rise to flow-induced oscillations. The primary focus will be on pitching (or angular) oscillations of wings, with some discussion of heave (or transverse) oscillations of

bluff cylindrical bodies. Using computational simulations, we will investigate the mechanisms that initiate and drive these oscillations, make connections to simpler systems that enable the prediction of these oscillations, and demonstrate methods to analyze the physics of such problems.

1.1 Aeroelastic wing flutter and cylinder vibrations

1.1.1 Background

The classical work of Theodorsen [6] was amongst the earliest attempts at modelling oscillating wings (as airfoils) within fluid flows, and the associated unsteady loading induced on the wing. This historical model, due to the fact that it is based on simple assumptions, continues to be used as the basis for newer modeling efforts in this area [7]. However, the Theodorsen model is based on simplified assumptions of inviscid and attached flow over the airfoil. In reality, the unsteady aerodynamics of pitching airfoils is characterized by the generation and shedding of strong leading-edge vortices, accompanied by large regions of separating and reattaching flow on the suction surface of the airfoil [8, 9]. This leads to non-linear aerodynamic loads which play a central role in flow-induced pitch oscillations (as will be shown in subsequent chapters)

as well as phenomena such as insect flight. The need to better understand this non-linear phenomenon has therefore motivated significant research in the characterization of aerodynamic loads on unsteady airfoils that go beyond classical theories [10–15].

However, these prior studies of the aerodynamic loads on unsteady/oscillating airfoils have predominantly focused on prescribed kinematics, i.e. the motion of the airfoil is not flow-induced but is specified so as to investigate the effect of specific prescribed motion patterns on the aerodynamic loads. There have been comparatively fewer analyses where the oscillations are induced by the flow while fully accounting for the non-linearities inherent in the flow physics. Historical efforts to model such flow-induced oscillations have mainly relied on simplified or inviscid flow models [16–19]. As with the Theodorsen theory [6], these models are often inadequate to capture the entire range of dynamics and are usually limited to small-amplitude oscillations of the wing where assumptions of linearity are valid. The use of reduced-order models have also allowed for accurate, computationally economical modelling of aeroelastic flutter [20–22]. However, the accuracy of reduced-order models is predicated on detailed knowledge of the flow physics and dynamics of flutter, which is often available only through high-fidelity analyses of the problem.

These limitations of simplified and reduced-order models have therefore prompted some recent efforts in higher fidelity investigations of aeroelastic

flutter. In one such set of high-fidelity analyses, Poirel *et al.* used a combination of experimental [23] and computational [24] studies to investigate the effect of flow speed and free-stream turbulence, among other factors, on small amplitude flow-induced pitching oscillations of an airfoil at transitional Reynolds numbers ($Re_c \sim 10^4 - 10^5$). A key finding from their work was that laminar separation is a driving factor for triggering the oscillations in this range of Reynolds number. In another study using numerical simulations, Ducoin & Young [25] studied the stability of a flexible hydrofoil section to bend and twist deformations. Specifically, they investigated the influence of laminar to turbulent transition and viscous effects on the location of the center-of-pressure with respect to the elastic-axis as well as the static divergence velocity.

There have also been some recent experimental works investigating the flow-induced oscillation of wings. Dimitriadis & Li [26] performed a study of a two-degree-of freedom airfoil that was allowed to perform flow-induced pitch and heave oscillations at a higher Reynolds number. They showed the occurrence of various bifurcations as a function of freestream velocity, which produce symmetric, antisymmetric, as well as hysteretic pitching oscillations. Furthermore, the recent development of so-called cyber-physical experimental facilities by various research groups [27,28] has spurred on experimental studies on flow-induced oscillations. Onoue & Breuer [28] were able to use this experimental system to map out the bifurcation diagram for an oscillating air-

foil system over a large range of oscillation amplitudes. Zhu *et al.* [29] used the same setup to show that the flow-induced pitch oscillations show different response branches and bifurcations depending on the inertia of the wing. There has also been work on flow-induced oscillations in energy harvesting applications, using both experimental [28] as well as modeling techniques [30].

Another important aspect of aeroelastic wing flutter that is of relevance is the response of elastic wings to gusts and other perturbations. As with the case of pitching airfoils discussed above, much of the research in this context too has focused on determining the aerodynamic loads induced on wings during transient gust encounters. Of particular interest has been the efficacy of analytical inviscid flow models, such as that of von Kármán & Sears [31], Küssner [32] and their extensions, in predicting the transient gust-induced loads on wings. This has been investigated through experimental [33–37] as well as computational [38–42] techniques and has produced mixed results, especially in the presence of viscous effects and flow separation. There has also been some work on modeling the aeroelastic response of wings during gust encounters, although these have generally been limited to small-amplitude oscillations of the wing [41, 43]. A popular approach to study the aeroelastic gust response has been to use reduced-order models for the forces induced on the wing during gust encounters. These models have generally been built either on linear theory or by using a few high-fidelity simulations to approximate the forces during

a broad range of gust conditions [44–49].

These studies of the aeroelastic oscillation of wings as well as their response to gusts have highlighted the rich physics in the oscillation response, bifurcations and forces induced on oscillating wings. This vast parameter space and wide range of resulting dynamics has also been shown to occur in another canonical fluid-structure interaction problem – the flow-induced vibration of cylinders. An over-arching theme in studies of vibrating cylinders has been the characterization of the amplitude response and the occurrence frequency lock-in. The phenomenon of lock-in, which was first observed by Bishop & Hassan [50] and Feng [51], refers to the dramatic increase in oscillation amplitude and the synchronization of oscillation and fluid forcing frequencies that is observed within a certain range of incoming flow velocities. The lock-in regime has been shown to include multiple distinct response branches, the dependence of which on Reynolds number [52–54], as well as structural parameters, such as mass-damping [55], has been of particular interest. Furthermore, the amplitude response on these various branches has been shown to exhibit hysteretic behaviour at the either end of the lock-in regime, as well as intermittent switching between response branches [54–56].

Ever since the first observations of these complex oscillation responses and non-linear flow-induced loads in wing flutter as well as cylinder oscillations, there has been interest in identifying their underlying fluid dynamic mecha-

nisms. These efforts have generally centered around the analysis of specific flow features and their correspondence with observed loads on the body. In the context of pitching airfoils, the leading-edge vortex that is generated and shed over the suction surface of the airfoil is generally implicated in the development of non-linear loads as well as phenomena such as dynamic stall [9, 57]. Similarly, there has been intense study of vortex patterns in the wake of oscillating airfoils [58–61] as well as cylinders [54, 56, 62–68] with the aim to relate the changes in vortex-shedding modes to the occurrence of different response branches in free-vibration.

1.1.2 Motivation

These studies of oscillating airfoils and cylinders have been able to provide a wealth of insight into the phenomenon of flow-induced oscillations. They have shown its dependence on a wide range of parameters, and highlighted the rich physics involved in the oscillation response, bifurcations and forces induced on oscillating wings. However, it is evident from the above discussion that the bulk of research on the aeroelastic oscillation of wings and their response to gusts has been performed at high Reynolds numbers and by using simplified and/or inviscid flow models. There is very little analysis of these dynamics at low Reynolds numbers where viscous effects become dominant. This is due to the inaccessibility of this regime to experiments and the challenge associated

with modeling such systems computationally.

However, it is well-known that the low Reynolds number behaviour of airfoils is markedly different from that at high Reynolds number. Mueller & DeLaurier [69] attributed this to the laminar state of the boundary layer, due to which separated flow fails to reattach, causing very different lift and drag behaviour in this regime. In addition, the vortex shedding behaviour and associated timescales, both of which are important factors in driving flow-induced oscillations, are known to vary with Reynolds number. This is especially true at the low range of Reynolds numbers. Moreover, the low Reynolds number physics of this problem is very pertinent to modern developments in micro-air vehicles and biomimetic propulsion. These factors therefore motivate the need for high-fidelity, fully viscous and non-linear computational modeling of flow-induced oscillations – to enable the exploration of its vast parameter space as well as to probe the flow physics in ways that are beyond the reach of laboratory experiments.

A common theme that emerges from the literature discussed above (in section 1.1.1) is the existence of multiple response branches, accompanied by the emergence of dynamically significant flow features, such as vortices, and/or changes in vortex shedding patterns. However, these observed changes in the flow-field have only been qualitatively related to the underlying aerodynamic loads that drive flow-induced oscillations. The issue of *quantitatively* correlat-

ing specific flow features, such as individual vortices, vortex-shedding patterns and shear layer formation, to the growth/decay of flow-induced oscillations has not been rigorously addressed.

Hence the task of precisely dissecting the physical mechanisms that govern the observed complexity in flow-induced oscillations evidently requires a two-pronged approach. This can be posed as the following two questions:

1. Can we *quantify* the contribution of specific force-producing mechanisms and flow features in the loads induced on bodies interacting with a fluid flow?

2. What is the *direct effect* of these observed forces on the growth/decay of flow-induced oscillations, while accounting for the interplay between the motion of the body and the fluid dynamic forces?

1.2 Energy extraction: Connecting flow-induced and prescribed oscillations

Of the two questions posed at the end of section 1.1.2 for uncovering the driving mechanisms behind flow-induced oscillations, the second, i.e. the task of evaluating the direct effect of force measurements on the observed oscillation response, has been more extensively addressed in existing literature. It should

be noted here that the amplitude of flow-induced oscillations is not dictated purely by the magnitude of forces induced on the body by the fluid flow; it also depends on factors such as the timing (or phase) between oscillating forces and the oscillations of the body, variations in this phase difference as the oscillation grows/decays, etc.

Investigations into this have been primarily motivated by a slightly different but equally relevant question – can we use measurements of the forces/moments on a body performing oscillations with prescribed kinematics to predict the corresponding flow-induced oscillation response of the same body? This relationship between forced (or prescribed) and flow-induced vibrations is a theme that has been raised multiple times in the literature on flow-induced oscillation of cylinders [70–74]. Recently, the use of energy extraction in this context by Morse & Williamson [27] and Kumar *et al.* [75] has made the correspondence between flow-induced and forced vibration more explicit. They showed that the amplitude response of a cylinder performing flow-induced oscillations is closely related to the energy extracted by a cylinder undergoing forced oscillations with carefully matching kinematics. This therefore makes a direct connection between the forces on an oscillating cylinder and the corresponding flow-induced oscillation response.

Using this idea of energy extraction, Morse & Williamson [27] showed the ability to explain various features of the response branches seen in the case of

flow-induced heaving cylinders, based on force measurements from prescribed oscillations and the energy transfer. In the context of pitching airfoils, Bhat & Govardhan [76] used forced oscillations in their experiments to calculate the energy transfer between the fluid and the airfoil, and demarcate flutter boundaries based on this information. The use of energy extraction has recently been extended by Menon & Mittal [77–79] and Zhu *et al.* [29] to analyze of the amplitude response branches corresponding to flow-induced pitch oscillation of airfoils.

In this dissertation, we explore this idea to analyze bifurcations in flow-induced oscillation response branches and predict the complex response of aeroelastically fluttering airfoils as well as oscillating cylinders. As will be seen in subsequent chapters, this is a particularly valuable tool in the context of pitching airfoils because the flow as well as the dynamical response is significantly more complicated than that observed in the case of transverse oscillations of bluff bodies. This added complexity is in part due to the presence of multiple interacting shear layers and vortices, as well as the introduction of additional free parameters such as the location of the elastic axis and the equilibrium angle of attack. Furthermore, we also demonstrate the use of energy extraction in precisely quantifying the influence of distinct force-producing mechanisms in driving flow-induced vibrations.

1.3 Mechanisms for force generation: Vortices *et al.*

As highlighted in section 1.1.2, an integral aspect in the analysis of flow-induced oscillations is the task of disentangling the various mechanisms responsible for the production of fluid dynamic loads on bodies within a fluid flow. It is well-known that vortices and vortex-induced loads on immersed surfaces play a central role in our understanding of a wide variety of phenomena in fluid mechanics – from fundamental problems such as dynamic stall to applied areas like flow-induced oscillation, biological propulsion and physiological flows [9, 57, 80–86]. This is particularly true of the fluid-structure interaction and unsteady aerodynamics problems of interest in this dissertation. In these *vortex-dominated flows*, coherent vortex structures and their interactions exert a dominant influence on the force/moment production on immersed surfaces. These flows are often characterized by several interacting vortex structures. The dynamical influence of these vortices on surfaces within the flow is governed by their inception, phase, location, as well as their interactions with each other and the immersed surface.

While prior studies have highlighted the dynamical importance of specific vortex structures, such as the leading-edge vortex [9] and distinct vortex-wake patterns [82], they have largely been limited to qualitatively correlating the

occurrence and evolution of these structures to the observed dynamics of the problem. The question of precisely *quantifying* the dynamical influence of specific flow features in terms of force and moment production on an immersed body has not been adequately addressed. This is a challenging task due to the ellipticity of pressure in incompressible flows. The pressure field at every point in the flow is simultaneously influenced by the entire flow-field – including all the vortices, shear-layers and other force producing mechanisms in the vicinity. This makes disentangling the contributions of specific flow features on pressure-induced loads on immersed surfaces a non-trivial task.

Although there have been previous efforts to quantify the effects of different hydrodynamic mechanisms on the total flow-induced force on oscillating bodies, these have mostly been based on simplified physics. In the context of oscillating cylinders, these force decomposition methods have predominantly focused on the inertial (or added-mass effects) and viscous (or vortex) effects, and have been accompanied by vigorous debate. One such method separates potential flow (added mass) force contributions from viscous effects, or the "vortex-flow force" [87]. This was used by Govardhan & Williamson [67] and Carberry *et al.* [68] to show that different amplitude response branches are associated with changes in the vortex-shedding mode as well as the phase difference between the vortex force and the cylinder motion. However, this definition of vortex force does not explicitly separate the vorticity from other viscous contributions,

and leads to the notion of "additional vorticity" to distinguish the inviscid vortex sheet on the cylinder from the vorticity in the rest of the flow. Furthermore, there is disagreement about the validity of isolating added-mass contributions in a general viscous flow, which assumes that this inviscid contribution operates independently from viscous effects [88].

Similarly, there have been efforts to quantify the force production from vortex-induced mechanisms on unsteady airfoils. These have generally used inviscid vortex models and vortex impulse formulations, such as the work of Wang & Eldredge [89] and Graham *et al.* [90]. Moreover, these prior studies have mostly focused on analyzing the *global* effect of vorticity in the flow on force production. Estimations of force/moment production due to *local* vortical regions have thus far been limited. Two studies that are particularly relevant here are those of Pitt Ford & Babinsky [91] and Onoue & Breuer [92] who analyzed the loading induced by the leading and trailing-edge vortices using experimental measurements in unsteady airfoil flows. Both these analyses were based on inviscid flow assumptions, and utilized point vortices combined with conformal mapping to model the flow. Furthermore, the vortices of interest were parameterized by their circulation based on experimental flow field data. While the force predictions from such models can be quite good and have led to excellent insights into vortex-induced aerodynamic loads, the extension of these methods to general viscous flows is unclear. Furthermore, these invis-

cid point vortex models generally require the assumption of two-dimensional flow, and are predicated on accurate flow regularization around sharp edges (by enforcing the Kutta condition) and conformal mapping treatments. These introduce additional contraints on their use in general vortex-dominated flow problems.

In this work, we use a mathematical formulation that allows us to rigorously (from first principles) partition the fluid dynamic forces and moments on an immersed body into contributions from distinct physically meaningful mechanisms, such as vorticity, added-mass, and viscous effects. In addition, this method also allows us to quantify the contributions of particular spatial regions of the flow, such as individual vortices and shear layers, on the total flow-induced loads. The force partitioning method used here is based on the work of Quartappelle and Napolitano [93]. They showed that the forces and moments on an immersed boundary can be written as integrals of the velocity-field and its derivatives by projecting the Navier-Stokes equations onto the gradient of an auxiliary harmonic potential. This was extended by Chang [94] and Zhang et al. [95] where the partitioning of flow-induced forces into physically relevant mechanisms were recognized. Simplifications of this method, particularly for the computation of the auxiliary potential [96, 97], and generalization for arbitrary immersed bodies and flow inhomogeneities have also been developed [98, 99].

This force partitioning method has been used to investigate the aerodynamics of insect flight [95], as well as the force generation mechanisms of pitching airfoils [100, 101] and oscillating cylinders [79, 102]. As shown in these studies, there are multiple advantages of such a force partitioning over those described earlier. This method allows us to separate added-mass, vorticity-induced, and shear contributions to the force on the body rigorously. Further, we will show that the ability to dissect the contribution of individual flow structures, or regions of the flow-field, is particularly valuable in the analysis of flow-induced vibrations. Furthermore, the specific formulation developed in this work results in force/moment components that have clear physical interpretations, thereby allowing us to relate, using first principles, the mechanisms behind force/moment generation in incompressible flows to the local kinematics of the flow.

1.4 Data-driven analysis techniques

In recent years, there has been tremendous growth in the popularity and effectiveness of data-driven methods to analyze, predict and model the physics of various problems in fluid dynamics. This is in large part due to the availability of increasingly high quality flow-field data from improved computational capabilities as well as laboratory experiments. Many contemporary methods that

have used such data to build predictive models of fluid flows have been based on recent advances made in the data science and machine learning communities [103–105].

1.4.1 Modal decomposition in fluid-structure interactions

One class of data-driven methods that has become especially popular in the fluid dynamics community is modal decomposition techniques [106]. These techniques aim to identify dominant spatial and/or temporal patterns (or *modes*) in complicated flows using flow-field data. This is particularly useful in the context of the problems of interest here due to the dominant influence of specific flow or vortical features on the dynamics. In the context of flow-induced oscillations, the interplay between flow and structural timescales can determine whether they interact constructively or destructively to cause growth or decay of oscillations. Hence the ability to extract dominant spatial as well as temporal scales is valuable in the analysis of these problems.

A technique that does just this is Dynamic Mode Decomposition (DMD). This method uses snapshots of the flow-field and allows the identification of spatial structures with characteristic frequencies and growth/decay rates associated with these structures [107, 108]. For nonlinear dynamical systems, such

as most fluid dynamics problems, the spatial modes extracted by DMD are the eigenvectors of the best-fit linear operator that approximates the dynamics of the field. Details of this analytical tool, its mathematical properties, as well as some simple applications of this method are presented in papers by Rowley *et al.* [107, 109] and Schmid *et al.* [108, 110, 111].

DMD has been used in the analysis of a wide variety of relevant applications including the wake of a circular cylinder [112], separated flow [113], stall control [114] and the wake of a flapped airfoil [115]. However, these studies as well as the majority of others in the literature involve the use of DMD in problems with stationary boundaries. There have been far fewer applications of DMD in fluid-structure interaction problems due to the fact that this method, without modification, cannot account for a body of nonzero thickness moving through the field of interest. It must be noted that this is not an issue in the case of an infinitely thin body, as demonstrated for a flapping membrane by Goza & Colonius [116]. However, the motion of finite-thickness bodies introduces spurious structures in the computed DMD modes due to the time-varying position of the body in the field of interest. On account of this, some studies have limited their analyses to regions of the flow-field that are outside the envelope of the immersed body's motion, such as the wake behind the body [108, 117]. However, by employing such constraints, relevant flow features close to the immersed body as well as within the shear layer are ignored.

This deficiency of DMD was recognized by Mohan *et al.* [118], who performed a decomposition of the flow near the suction-side of a plunging airfoil by analyzing a region of the flow-field moving with the airfoil. They therefore did not have a body moving through the field of interest. While the simulations in their case were performed using a grid moving with the airfoil, it is non-trivial to use such an approach in experimental datasets and other methods where the locations of data-acquisition are fixed in the lab frame. In particular, one computational method where this difficulty is apparent is in immersed boundary methods, which have become increasingly popular in flow simulations of fluid-structure interactions due to their ability to handle complex geometries and arbitrary motions in a robust manner [119]. Furthermore, as was discussed in section 1.2, the energy transfer between a fluid flow and body moving within it has been shown to be a useful tool in understanding and predicting flow-induced oscillations [27, 75–77]. However, the energy transfer is a frame-dependent quantity, which is in fact zero in the frame of the moving body. For these reasons, the development of a robust method to decompose the flow near a moving boundary of non-zero thickness without resorting to the use of a non-inertial reference frame could prove to have wide-ranging applications.

Although there have been several improvements and modifications to DMD since its introduction, they have not addressed the difficulty involved in accounting for moving boundaries in the flow-field. Therefore in this disserta-

tion, we propose a method to decompose the flow around a moving boundary by transforming the analysis to a body-fitted frame as discussed above. However, by exploiting the linearity of the formulation, we show rigorously how the modes computed in a moving coordinate system are related to those of the underlying flow dynamics in the lab-frame. We use this to apply a correction to the modes and recover the DMD modes of the lab-frame flow-field, thus alleviating some of the issues outlined above.

1.4.2 Analysis of vortex-dominated flows using clustering

Another class of data-driven methods that we make use of in this dissertation for the analysis of vortex dominated flows is clustering techniques. These are unsupervised statistical inference methods [120,121] which attempt to find clusters of data that share similar characteristics within a large set of data. Here we leverage these techniques for the analysis of vortex-dominated flows at the level of individual vortices as well as in identifying large-scale vortex patterns in flow-field data.

As mentioned in section 1.3, there have been very few prior studies demonstrating the estimation of fluid dynamic loads due to *individual* vortices in flow-fields. This is primarily due to the computational complexity associated

with accurately isolating and tracking several interacting vortical regions that are evolving in highly complicated, time-varying flow fields. Therefore, a critical aspect in deploying methods, such as that mentioned in section 1.3, for the estimation of force/moment due to individual flow features in highly dynamic vortex-dominated flow-fields is a systematic way to individually isolate and track these vortical regions.

Here we leverage data-driven clustering techniques to perform this task of isolating and tracking several vortices in high-dimensional, unsteady flow-fields. In previous studies, this has been used in identifying coherent structures in a flow-field, by clustering regions that share similar dynamic or Lagrangian behaviour [122–127]. In the context of this work, clustering provides an automated way to isolate an arbitrary number of spatial regions corresponding to individual vortex structures from high-dimensional flow-fields. Furthermore, this data-driven approach also facilitates the spatio-temporal tracking of these vortex structures, as well as the grouping of vortices in distinct categories (such as LEVs or TEVs) based on various attributes. The automated isolation of these distinct vortical regions therefore provides an efficient way to employ the aforementioned force and moment partitioning methods in precisely quantifying their contributions to force/moment production.

A second application of clustering that we will demonstrate is its use in the identification of distinct flow regimes based on classes of vortex shedding pat-

terns. In the context of fluid-structure interaction problems, interest in identifying distinct vortex patterns stems from the seminal works of Zdravkovich [128], Ongoren & Rockwell [63] and Williamson & Roshko [64]. These studies were amongst the first to demonstrate that the correlation between vortex wake patterns behind oscillating cylinders and changes in the forces on the cylinder. As mentioned in section 1.1.1, this has led to a vast body of literature concerning vortex shedding patterns and their connection to flow-induced oscillations [82, 129] and biomimetic propulsion [58–60]. However, these studies have mostly focused on relatively simple wakes, and the visual identification of wakes they employed is impractical for more complex flows. This has motivated data-driven approaches to this task, such as the works of Hemati *et al.* [130, 131] and Colvert *et al.* [132]. However, while these prior works have demonstrated considerable success, they have all focused on idealized models of vortex-dynamics, such as point vortices, and have mostly assumed apriori knowledge of the possible wake patterns to perform the classification. In this dissertation, we demonstrate a more robust method to identify distinct flow regimes from high-dimensional, time-resolved flow-fields by using dimensionality reduction and clustering techniques to identify patterns in large ensembles of these flow-fields. The approach presented here also obviates the need for a-priori definitions of the possible wake patterns in a given problem.

1.5 Outline of this dissertation

This dissertation works towards developing an improved understanding of flow-induced oscillations, and the mechanisms underlying the force production on unsteady bodies in vortex-dominated flows. In particular, much of the focus is on the flow physics and dynamics of pitching wings. We use a combination of computational modeling and data-driven methods to dissect the underlying physics of the fluid-structure interaction phenomenon and the role of vortices in the dynamics.

We begin by describing the computational methods employed for the simulation of fluid flows over moving bodies as well as the models used to study the flow-induced oscillation of wings and cylinders in chapter 2.

In chapter 3, these computational methods are used to study the flow-induced oscillation response of pitching airfoils. We show in this chapter that the system is capable of highly complex responses, which justify the development of many of the analysis tools discussed in subsequent chapters.

One of these tools is an energy-based method for the analysis, prediction and control of flow-induced oscillations which is introduced in chapter 4. This tool allows us to map out all the response branches of a flow-induced oscillator within a parameter range of interest. A practical application of this energy-based analysis to the predict and control the response of an aeroelastic wing to

gust perturbations is then presented in chapter 5.

Subsequently, chapter 6 introduces a novel formulation of the popular Dynamic Mode Decomposition method to provide insight into some of the findings of the energy-based analysis in previous chapters. This proposed formulation extends the applicability of Dynamic Mode Decomposition to flows interacting with moving boundaries and allows us to probe the phase relationship between the pitching airfoil and the flow around it.

In chapter 7, a mathematical force and moment partitioning method which is extensively used in the subsequent chapters is introduced. This is a mathematical formulation that allows us to rigorously estimate the role of different physical mechanisms as well as distinct flow features on the loads induced on immersed bodies within a flow. As will be shown, this method allows us to disentangle fundamental aspects of the physics underlying force production in fluid-structure interactions as well as unsteady aerodynamics.

An application of this method is presented in chapter 8, where we combine force partitioning with the energy-based analysis mentioned above to uncover the mechanisms that initiate and sustain the flow-induced vibration of cylinders.

In chapter 9 we develop an automated physics-based and data-driven framework which enables the use of the force/moment partitioning method in estimating loads induced by individual vortices in complex vortex-dominated flows.

This framework takes in time-resolved flow-field data and automatically isolates, tracks and categorizes each vortex in the flow while also analyzing their kinematics and dynamical influence.

An application of this analysis framework to the problem of dynamic stall is presented in chapter 10. Using this analysis, we show that the force production on an unstedy wing during dynamic stall is not just dictated by vortices; it is strongly influenced by vortex-induced strain, which is often ignored in such analyses.

Lastly, chapter 11 discusses some preliminary first steps in extending the analysis of vortex-induced forces due to distinct vortex structures to three-dimensional problems where isolating and tracking individual vortex structures is considerably more complicated. We present a simple analysis of the separate roles that spanwise and non-spanwise vorticity play in lift production on low aspect-ratio wings.

We then conclude by summarizing the work presented in this dissertation in chapter 12, and discuss potential future extensions and open questions.

Chapter 2

Computational methodology

In this thesis, a variety of problems in the domain of unsteady aerodynamics and aeroelastic oscillations are studied using computational modelling and simulation techniques. A common theme in the majority of problems discussed in subsequent chapters is the presence of immersed bodies that interact with fluid flows around them while executing unsteady motions within fluid flow. A challenge in simulating the flow physics of such problems is the accurate treatment of the boundary conditions that arise as a result of interactions between a flow-field and the arbitrary motion of a body within it. Furthermore, as discussed in section 1.2, the motion of immersed bodies within fluid flows can generally be categorized in two ways: (1) the motion is prescribed (or forced) so as to analyze the effect of this unsteadiness on the flow physics; (2) the motion is excited by the flow around the body and is in turn two-way coupled with

the flow. This latter scenario is of primary interest in the domain of aeroelastic oscillations, and the study of these problems requires a prescription of the two-way coupling between the motion of the immersed body and the fluid flow around it. The focus of this chapter is therefore on discussing the computational models and methods used in this thesis for the study of such problems.

2.1 *ViCar3D*: Immersed boundary flow solver

The flow simulations in this thesis have been performed using the sharp-interface immersed boundary method based solver *ViCar3D* described in Mittal *et al.* [133, 134]. This allows us to preserve sharp interfaces along the surface of immersed bodies within a flow using a body-non-conformal Cartesian grid. This is particularly useful in fluid-structure interaction studies as it allows us to simulate a variety of shapes as well large-amplitude motions on simple, non-adaptive Cartesian grids. In particular, this approach has the advantage of not being constrained by highly deformed grid cells or the need to periodically recompute the grid during high-amplitude motions [119]. Furthermore, the ability to preserve the sharp-interface around an immersed boundary ensures very accurate computations of surface quantities. This code has been extensively validated in previous studies [133–135], where its ability to main-

tain local (near the immersed body) as well as global second-order accuracy has been demonstrated. Further, the accuracy of surface measurements has been established for a wide variety of stationary as well as moving boundary problems in these studies. For the purpose of this work, we have performed additional comparisons of results from this code with existing literature. Details of this are in section 2.3.

The fluid equations are solved using a second-order fractional-step method. The time-integration is performed using a second order Adams-Bashforth method and spatial derivatives are discretized using second-order central differences in space. The pressure Poisson equation is solved using the geometric multigrid method. In order to perform accurate computations of surface quantities such as pressure and shear, *ViCar3D* employs a multi-dimensional ghost-cell method for the imposition of boundary conditions on immersed boundaries that can be either stationary or moving. These immersed boundaries are discretized using triangular surface elements where the nodes of these elements represent Lagrangian marker points which move with the body while immersed within the stationary Cartesian fluid grid. The local normal vector to the surface of the immersed body is computed on these triangular elements and boundary conditions are thereby imposed using second order central differences. This immersed boundary treatment is used for boundaries undergoing prescribed motion as well as flow-induced motion.

For the two-way fluid-structure interaction coupling in simulations involving flow-induced motion, a loosely-coupled approach is employed wherein the equations for the flow-field and motion of the immersed body are solved sequentially. At every time step, the pressure and shear on the nodes of the triangular elements on the surface of the immersed body are calculated after solving the pressure Poisson equation. The total force/moment on the immersed body is calculated and passed on to the dynamical equation for the immersed body (discussed in section 2.2). The linear/angular velocity predicted from the dynamical equation is subsequently imposed on to the Lagrangian marker points on the surface of the body, and the motion of the body is advanced in time using a second-order trapezoidal method.

2.2 Aeroelastic modelling

In this research we use a canonical model for two-way coupled aeroelastic systems which consist of a finite-mass body immersed in a fluid flow, with the elasticity of the body modeled as a linear spring with damping. The motion of this spring-mass-damper oscillator is driven by the aerodynamic loads induced by the fluid flow on the immersed body. This simple and widely used elastic model allows us to analyze a variety of complex aeroelastic responses while primarily focusing on the fluid dynamics that drives these responses.

The flow-fields in the simulations performed as part of this thesis are governed by the incompressible Navier-Stokes equations expressed in the dimensionless form as follows:

$$\frac{\partial \vec{u}}{\partial t} + \vec{u} \cdot \nabla \vec{u} = -\nabla p + \frac{1}{Re} \nabla^2 \vec{u} \tag{2.1}$$

where t, $\vec{u}$ and p represent the dimensionless time, fluid velocity vector and pressure respectively. The Reynolds number is given by $Re = \rho U_\infty L/\mu$, where ρ is the fluid density, U_∞ is the incoming freestream velocity, L is the length scale determined by the immersed body, and μ is the viscosity of the fluid. The velocity is scaled as $\vec{u} = \vec{\hat{u}}/U_\infty$, dimensionless time is given by $t = \hat{t}U_\infty/L$, and the coordinate system is scaled as $(x, y) = (\hat{x}/L, \hat{y}/L)$. Here we particularly focus on the flow around unsteady airfoils and cylinders, and in these cases L is specified as the chord-length (C) of the airfoil or the cylinder diameter (D) respectively.

When an immersed body is placed in such a flow-field, the flow induces loads on the body due to the fluid pressure and surface shear. The flow-induced force can be expressed as a dimensionless force coefficient as follows: $C_{F_i} = F_i/(\frac{1}{2}\rho U_\infty^2 L)$, where F_i is the dimensional form of the force in the i-direction. Similarly, the flow-induced coefficient of moment in the k-direction can be written as $C_{M_k} = M_k/(\frac{1}{2}\rho U_\infty^2 L^2)$, where M_k is the dimensional form of the moment.

For the aeroelastic models studied here, these forces and moments drive the dynamics of the immersed body.

2.2.1 Pitching airfoils

For the study of pitching oscillations of airfoils, the current study employs a rigid NACA0015 airfoil with a slightly rounded trailing-edge, immersed in an incompressible flow governed by equation (2.1) with freestream velocity U_∞. The chord-length of the airfoil is given by C. The slight rounding of the trailing-edge ensures that the flow is well-resolved around it, and we have verified that this has no significant effect on the aerodynamic characteristics and forces on the airfoil.

The torsional (pitch degree-of-freedom) elasticity of the airfoil is modelled using a linear torsional spring with spring constant k and damping coefficient b, attached to the rigid airfoil at a prescribed chordwise location (X_e), which we refer to as the elastic axis (normalized location denoted as $X_e^* = X_e/C$). The airfoil is free to pitch about this elastic axis and the equilibrium angular position of the spring is denoted by angle θ_0. Further, the airfoil has a moment of inertia denoted by I and its instantaneous angle is denoted by θ. A schematic of this setup is shown in figure 2.1.

The pitch/torsional motion of this spring-mass-damper system is driven by the pitching moment induced on the airfoil by the surrounding flow. The dy-

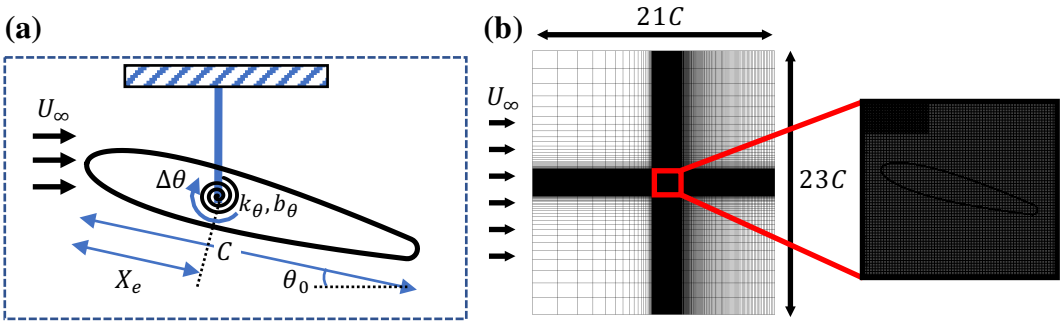

Figure 2.1: (a) Schematic of the aeroelastic system used for pitching airfoils; (b) Computational domain and close-up of the Cartesian computational grid.

namical equation of this motion is scaled by the characteristic variables used for the flow (with length-scale C), and the resulting non-dimensional equation governing the dynamics in pitch of the airfoil is given by

$$I^*\ddot{\theta} + b^*\dot{\theta} + k^*(\theta - \theta_0) = C_M \tag{2.2}$$

where C_M is the coefficient of aerodynamic pitching moment. The quantities $I^* = 2I/(\rho C^4)$, $b^* = 2b/(\rho U_\infty C^3)$, $k^* = 2k/(\rho U_\infty^2 C^2)$ are the dimensionless moment-of-inertia, damping, and spring stiffness respectively. Here, C_M and I^* are calculated with respect to X_e^*. The spring stiffness is commonly expressed in terms of a reduced velocity, $U^* = U_\infty/f_s C$ where $f_s = \frac{1}{2\pi}\sqrt{\frac{k}{I}}$ is the natural frequency of the spring. In essence, U^* is a ratio of the natural time-scale of the elastic system to the convective time-scale of the flow. However, as we will show, the choice of fluid time-scale has significant implications for the dynam-

ics of the system. When presenting our results, we denote the pitch oscillation amplitude by A_θ^* and dimensionless pitch frequency as $f_p^* = f_p C/U_\infty$ where f_p is the pitching frequency.

Thus, even this highly simplified configuration has six governing parameters (Re, X_e^*, I^*, b^*, U^*, θ_0) and this is indicative of the inherent complexity of this configuration. In the current study, we fix the values of Re and I^* to 1000 and 4.1 respectively and explore the effect of the other four parameters. The Reynolds number chosen is high enough so as to generate robust vortex shedding phenomenon, which drives flutter, but is also low enough so as to allow resolved simulations at a reasonable computational expense. The choice of the moment-of-inertia about the elastic axis corresponds to a solid-to-fluid density ratio of ≈ 120. While the effect of varying I^* in this system could be of significant engineering interest, we choose to use a fixed value throughout this study to reduce the number of independent parameters. However, it must be noted that varying I^* is equivalent to changing the natural frequency as $f_s \sim 1/\sqrt{I^*}$, which is an important parameter in this study.

The current study addresses structurally damped as well as undamped systems with damping being defined by $\zeta^* = b/b_{cr}$ where $b_{cr} = 2\sqrt{kI}$, is the critical damping for the harmonic oscillator. For the undamped system $\zeta^* = 0$ and for the damped system we prescribe $\zeta^* = 0.15$ where this lightly damped structure enables us to understand the effect of damping without overly damping

the pitch oscillations. The remaining two parameters, the elastic axis (X_e^*) and the spring stiffness (U^*), are a particular focus of the current study. For X_e^*, we use three values – $X_e^* = 0.50$, 0.33 and 0.25 – and we will show that these generate very significant variations in the pitch response. The final parameter U^* represents the spring stiffness (a larger U^* corresponds to a softer spring) and this parameter is varied from about 2 to 13.

Simulations of the flow around this aeroelastic system are performed in a large $21C \times 23C$ computational domain, where the airfoil is placed 10 chord-lengths from the downstream boundary. The flow is solved on a Cartesian computational grid and the isotropic grid resolution around the solid body corresponds to about 125 points along the chord. The grid is stretched in all directions away from the rectangular region that surrounds the foil and the near-wake resulting in a baseline grid of 384×320 points. A schematic of this setup is shown in figure 2.1(b). A Dirichlet velocity boundary condition is used at the inlet boundary of the domain, and zero-gradient Neumann conditions are specified at all other boundaries.

2.2.2 Heaving cylinders

The aeroelastic system used to model flow-induced heave oscillations of cylinders is setup in a similar manner as the pitching airfoil system described above. The model consists of a finite-mass cylinder attached to a linear spring

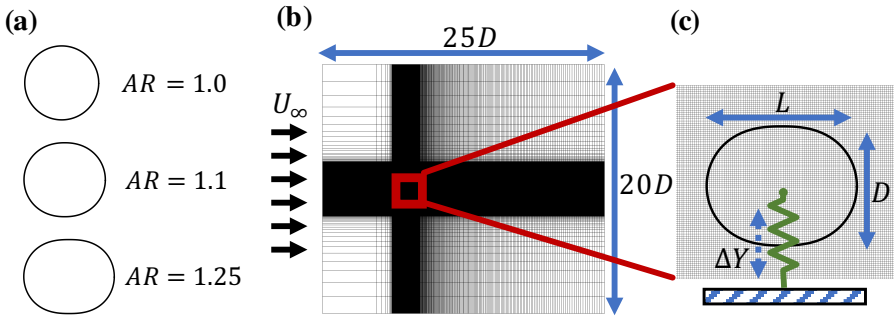

Figure 2.2: Schematic of the aeroelastic system used for heaving cylinders. (a) Cylinder shapes for three aspect-ratios; (b) Computational domain and grid; (c) Zoom-in of the cylinder in a Cartesian grid, along with dimensions and elastic model.

that allows vibrations in a direction transverse to the incoming freestream flow. This aeroelastic system is immersed in an incompressible fluid which drives the transverse motion of the cylinder. Although practical vortex-induced vibration problems can exhibit both transverse and in-line oscillations, the latter has been shown to be small in comparison to transverse oscillations [54, 56, 136, 137], and has a negligible effect on the transverse response [129].

A schematic of this aeroelastic model is shown in figure 2.2(c). The dynamics of the elastic model is governed by the forced spring-mass system consisting of the linear spring attached to the cylinder at its center-of-mass, and a forcing given by the fluid dynamic transverse force on the cylinder, i.e., the lift force. It must be noted that there is zero structural damping in the model used here. The stiffness of the spring is given by spring constant k_y and the mass of the cylinder is m. The equation for the forced spring-mass damper is non-dimensionalized using the same physical scales as for the fluid equations,

with the diameter D of the cylinder as the characteristic length scale. Further, the dimensionless instantaneous transverse position of the cylinder's center-of-mass is denoted by y^*. The dimensionless equation governing the elastic system is given by:

$$m^*\ddot{y}^* + k_y^*(y^* - y_0^*) = C_L \tag{2.3}$$

where $m^* = 2m/(\rho D^2)$ and $k_y^* = 2k_y/(\rho U_\infty^2)$ are the dimensionless forms of the mass of the cylinder and spring stiffness. C_L is the coefficient of lift on the cylinder and y_0^* is the equilibrium position of the cylinder. We denote deflections from this equilibrium position by $\Delta y^* = (y^* - y_0^*)$.

In order to study the effect of aspect-ratio, the cylinder used in this study is a generalized superellipse with its major axis aligned with the incoming flow. We use a superellipse rather than the more conventionally used ellipse in order to avoid the additional effect of increased curvature at the ends of the ellipse while varying the aspect ratio. The length and diameter of the cylinder are specified as L and D respectively, and the equation that governs the surface of this generalized superellipse is given by:

$$\left[\frac{x_s}{L/2}\right]^m + \left[\frac{y_s}{D/2}\right]^n = 1 \tag{2.4}$$

where x_s and y_s are the X and Y coordinates of points along the surface of the cylinder. We define the aspect-ratio of the cylinder as $AR = L/D$. Further, the

exponents are chosen such that $m = 2L$ and $n = 2$, so that this dependence of m on the semi-major axes ensures that the curvature at the ends of the ellipse does not significantly increase with increasing AR. This is meant to approximate a "stretched circular cylinder" when $AR > 1$. Throughout this work we keep D fixed and vary L to achieve cylinders of different aspect-ratios. The range of aspect-ratios analyzed is $1.0 < AR < 1.25$. Some representative cylinders, along with their corresponding aspect ratios, are shown in figure 2.2(a).

As for the pitching airfoil system, an important parameter is the reduced velocity which is defined in this case as $U^* = U_\infty/f_s D = 1/f_s^*$, where f_s is the natural frequency of the spring in vacuum, and $f_s^* = (1/2\pi)\sqrt{k_y^*/m^*}$ is its dimensionless form. In this work, we study the amplitude response of the system as a function of U^* by varying the spring stiffness k_y^*, while keeping m^* constant at $m^* = 10$. It must be noted that m^* is kept constant even while the aspect-ratio of the cylinder is varied, which has the effect of isolating the effect of shape on the fluid mechanics of the problem. In other words, only the RHS of equation (2.3) depends on the aspect ratio, while the LHS is fixed for a given U^*. Further, Re is also kept constant throughout this work, at $Re = 100$. In presenting our results, dimensionless oscillation amplitude is denoted by A_y^* and frequencies are reported in dimensionless form as $f^* = fD/U_\infty$.

The flow around the heaving cylinder is computed in a domain of size $25D \times$

$20D$, and the cylinder is placed at a distance $15D$ from the downstream boundary. The computational grid around the cylinder is Cartesian and isotropic, and the grid is stretched away from the cylinder in all directions. The total grid size is 320×288 cells, and the resolution around the cylinder is 60 cells across the diameter. The boundary conditions used are Dirichlet for the freestream velocity at the upstream boundary, and Neumann zero-gradient conditions at all other external boundaries.

2.3 Validation and grid convergence

The flow solver used in this work has been validated against numerous previous studies in refs. [133–135]. In addition, we have performed comparisons with published literature for some specific aspects of the setup studied in this thesis.

In figure 2.3, the mean and Strouhal number of C_L fluctuations for flow over a static NACA0012 airfoil computed using the present flow solver are compared with the published results of Kurtulus [138], Liu *et al.* [139] and Mittal & Tezduyar [140]. The chord-based Reynolds number for this flow is $Re = 1000$ and the airfoil (chord length C) is immersed in a non-uniform Cartesian grid with 480×448 points within a domain of size $18C \times 20C$. Grid convergence is assessed by simulating the airfoil flow at $Re = 2000$ with grid sizes of 384×320,

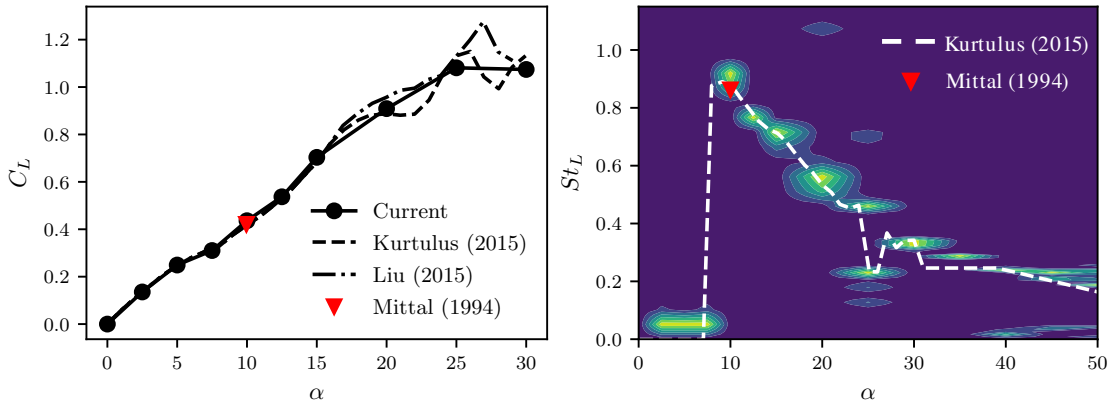

Figure 2.3: Mean and Strouhal number of C_L fluctuations for a static NACA0012 airfoil at $Re = 1000$. Left plot shows a comparison of mean C_L using present flow solver with refs. [138–140]. Right plot compares St of C_L fluctuations from present solver with refs. [138, 140].

480×448 (baseline used in this study), and 544×544. The mean and RMS C_L differ by 4.1% and 1.2% respectively between the coarse and baseline grids, and 4.8% and 0.3% respectively between the fine and baseline grids. The difference in mean and RMS C_M is 2.7% and 1.2% between the coarse and baseline grids, and 1.8% and 0.9% between the fine and baseline grids. Thus, the computed quantities are considered grid independent. Figure 2.3(a) shows a comparison of C_L versus angle of attack (α), and we see that the comparison is good. Figure 2.3(b) shows a comparison of the Strouhal number of C_L fluctuations, defined as $St_L = f_L C/U_\infty$ where f_L is the frequency of C_L fluctuations. The heat-map shows the full frequency spectrum (expressed as St_L) at each angle of attack α from computations using the present flow solver. Overlaid on this is the St_L versus α data from the work of Kurtulus [138] and Mittal & Tezduyar [140]. The comparison is again good.

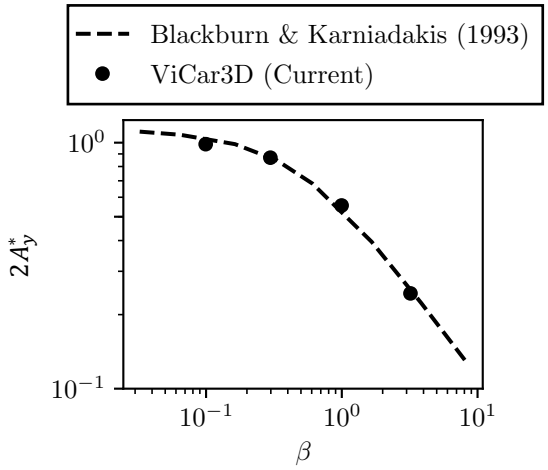

Figure 2.4: Flow-induced oscillation amplitude of a circular cylinder versus mass-damping parameter $\beta = 8\pi^2 St^2 m\zeta/\rho D^2$. Results from the present code are shown using symbols and are compared with results from [141] shown as a dashed line.

In order to validate our fluid-structure interaction solver, we have performed simulations of flow-induced vibration of circular cylinders and compared our amplitude response with the results of Blackburn & Karniadakis [141]. In figure 2.4 we show the amplitude response of a freely vibrating cylinder at $Re_D = 200$ with $m^* = m/\rho D^2 = 10$, against the mass-damping parameter $\beta = 8\pi^2 St^2 m\zeta/\rho D^2$. Here, St, m, ζ, ρ, and D are the vortex shedding Strouhal number, mass, damping ratio, fluid density, and cylinder diameter respectively. The symbols show results from our simulations and the dashed line is from the work of Blackburn & Karniadakis [141]. The agreement is quite good.

A grid convergence study was performed for the setup used to study pitching airfoils by performing forced oscillations of the truncated NACA0015 airfoil used in this study. The oscillations were performed about $\theta_0 = 20^\circ$, with am-

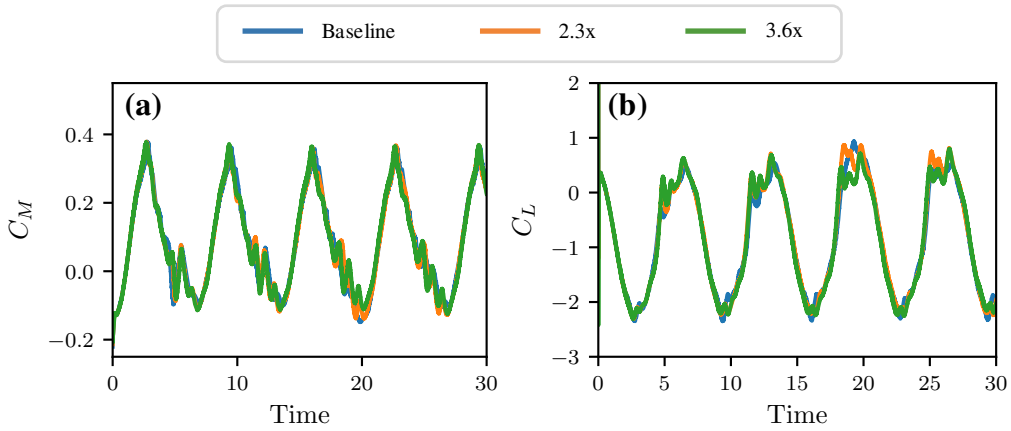

Figure 2.5: Time series of (a) moment, and (b) lift coefficients, for the three grids tested.

plitude $A_\theta = 20^\circ$ and frequency $f_p^* = 0.15$. The baseline grid tested consisted of 384×320 grid cells. This corresponds to a resolution of approx. 125 cells along the chord of the airfoil. This grid was compared to those with 480×448 and 544×544 grid cells, which correspond to 192 and 237 cells along the chord, respectively. These refined grids are $2.3\times$, and $3.6\times$ the size of the baseline grid, in terms of total grid cells. In figure 2.5 we show comparisons of the time-series of lift coefficient and moment coefficient for these three grids. The mean and RMS lift coefficient differ by 3.92% and 1.2% respectively between the baseline and $2.3\times$ grid, and 0.96% and 1.51% respectively between the baseline and $3.6\times$ grid. The corresponding difference in mean and RMS moment coefficient is 1.78% and 1.07% between the baseline and $2.3\times$ grid, and 0.84% and 2.05% between the baseline and $3.6\times$ grid.

The grid convergence demonstrated above, while performed for forced oscil-

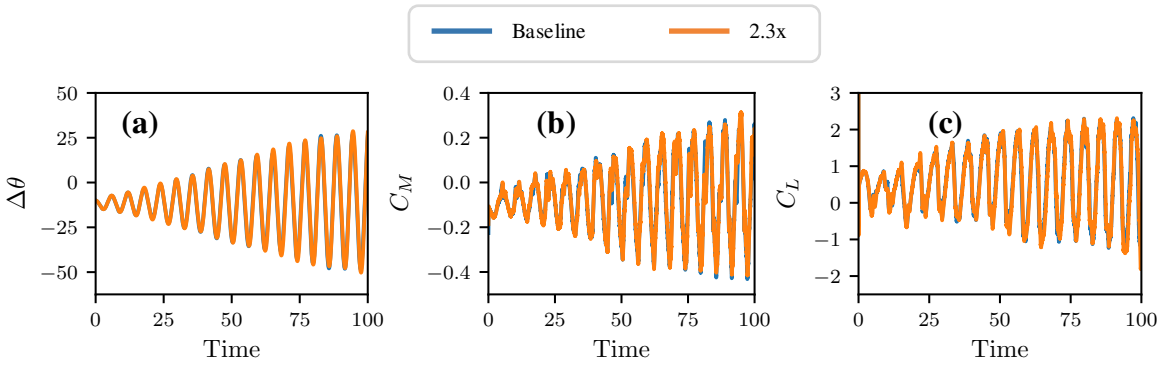

Figure 2.6: Time series of (a) pitch angle; (b) moment coefficient; and (c) lift coefficients, for flow-induced oscillations at $U^* = 6.8$ using the Baseline and $2.3\times$ grids.

lations, is expected to be a reasonably good demonstration of grid convergence for the flow-induced system as well. This is due to the fact that the only term in the dynamical equation for the solid (equation 2.2) that depends on the grid is C_M, which we have shown, is well converged. Further, in order to obtain statistics at a stationary state for the flow-induced system, CFL criterion-related constraints would require simulations with as many as 2,000,000 time-steps on the finer grids. This makes such an exercise computationally cost-prohibitive. However, in order to strengthen this demonstration of our grid convergence, we have performed a comparison of the baseline and $2.3\times$ grid for a flow-induced oscillation simulation during the transient, amplitude-growth phase at $U^* = 6.8$ and $\theta_0 = 15°$. Plots for the pitch angle, and coefficients of moment and lift versus time are shown in figure 2.6. We see that the mean and RMS lift coefficient differ by 0.57% and 1.56% respectively. The mean and RMS moment coeff. differ by 3.78% and 1.22% respectively. The maximum pitching amplitude

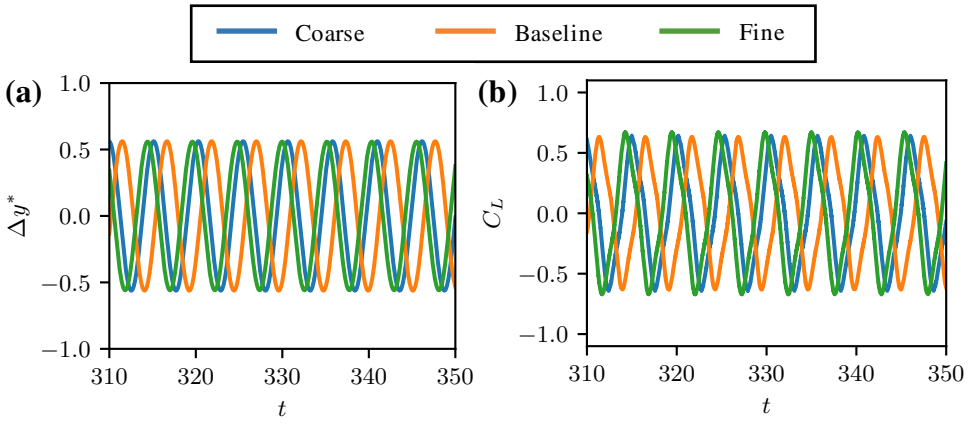

Figure 2.7: Comparison of flow-induced oscillation results using three grids to establish grid convergence. Coarse, baseline, and fine grids correspond to 45, 60 and 90 points across the diameter of the cylinder respectively. Here, $Re = 100$, $AR = 1.0$ and $U^* = 5.0$; (a) Timeseries of heave oscillation amplitude; (b) Timeseries of C_L oscillations.

differs by 6.44%.

Grid convergence is also assessed for the heaving cylinder setup by performing flow-induced oscillation simulations at $Re = 100$, using a circular cylinder ($AR = 1.0$) and fixing $U^* = 5.0$. The size of the grid used for the results reported in this study is 320×288 cells, which corresponds to 60 cells across the diameter of the cylinder. This baseline grid is compared with coarse and fine grids of sizes 288×224 cells, and 384×384 cells respectively. These correspond to 45 and 90 points across the diameter of the cylinder. In figure 2.7(a) we show the timeseries of heave oscillations computed using the three grids, where the maximum heave amplitude differs by 0.9% between the coarse and baseline grid, and 0.7% between the coarse and fine grid. The timeseries of C_L oscillations are shown in figure 2.7(b), and we see that the r.m.s. differs by 0.6%

between the coarse and baseline grids, and 5.3% between the coarse and fine grids. The corresponding differences in the maximum C_L values are 3.8% and 3.0%. Hence, we consider the computations grid independent.

Chapter 3

Flow-induced pitch oscillations of an airfoil

The aeroelastic oscillation response of an elastic airfoil is a problem that has both academic as well as practical applications. As a canonical model for aeroelastic wing flutter, it is pertinent to a wide range of aerospace design and performance applications as well as energy harvesting applications. Some of these applications were outlined in section 1.1. This is also a problem of academic interest due to our limited understanding of the highly nonlinear mechanisms and numerous parameters that dictate the flow-induced oscillation response. Particularly at low Reynolds numbers that are relevant to recent developments in micro-air vehicles and energy harvesting, there is a lack of data concerning this problem in the existing literature, especially from computational models.

Therefore the aim of this chapter is to perform broad parameter sweeps to describe the flow physics governing the onset of flutter, as well as the amplitude and frequency response. We show that this provides fundamental insight into the onset of large amplitude flutter, along with a physically relevant flow timescale. We also discuss the mechanism that determines the frequency of flutter, and demonstrate the (apparent) difficulty in understanding the amplitude response in some cases.

We report on simulations of the two-dimensional incompressible Navier-Stokes equations, which are coupled with an elastically supported NACA0015 airfoil that is allowed to oscillate in pitch. This aeroelastic model is discussed in section 2.2.1. The simulations are performed using the sharp-interface immersed boundary method described in section 2.1 that allows us to model very large amplitude oscillations in a robust manner. For all the flow-induced oscillation cases simulated here, we initialize the airfoil at its equilibrium angle of attack θ_0, with zero initial angular velocity. The constant freestream flow U_∞ is then imposed and the dynamics allowed to evolve until the system reaches a stationary state. For the cases simulated here, it takes between $O(20)$ and $O(200)$ oscillation cycles before this stationary state is achieved. Average quantities are computed after the stationary state is reached.

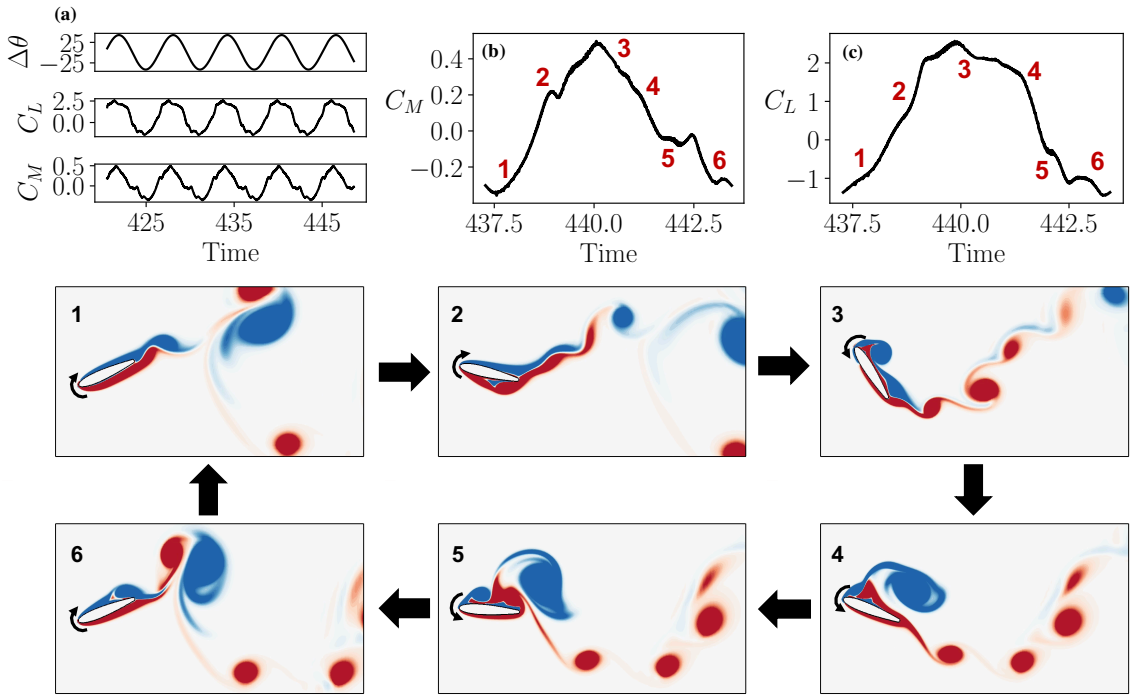

Figure 3.1: A representative case of flow-induced pitching oscillations with $U^* = 6.6$, $X_e^* = 0.50$, $\theta_0 = 15°$ and $\zeta = 0.15$; The top panel shows time series plots of (a) pitch deflection ($\Delta\theta$), coefficient of moment (C_M), and coefficient of lift (C_L); (b) coefficient of moment during one cycle of oscillation (corresponding to the cycle shown in the snapshots); (c) coefficient of lift during the cycle corresponding to the snapshots; (1-6) Snapshots of the flow-field coloured by contours of z-vorticity.

3.1 Qualitative features

We begin our discussion of the aeroelastic response of this system by providing an overview of one representative case for which, $U^* = 6.6$, $X_e^* = 0.5$, $\zeta = 0.15$, and $\theta_0 = 15°$. This case develops fairly large amplitude pitch oscillations ($A_\theta \approx 45°$) and serves to demonstrate the various flow structures and non-linear interactions that drive the pitching of the airfoil. In figure 3.1 are snapshots of the flow over the course of one oscillation cycle. The time series

for the coefficients of moment (C_M) and lift (C_L) corresponding to the same oscillation cycle are shown in figure 3.1(b) and 3.1(c).

As the airfoil pitches up at the start of the cycle, in figure 3.1(1), we see that there is initially a monotonic increase in C_M and C_L. This is related to the fact that the shear layer on the suction side is stabilized by the motion of the airfoil until angles of attack well past the static stall angle (which for this airfoil, at this Reynolds number, is about 20 degrees). This stabilization of the boundary layer over a pitching airfoil was also reported by Lee & Gerontakos [12]. However, this pitch-up motion destabilizes the pressure-side boundary layer. As a result, there is a roll-up of the leading-edge shear layer on the pressure side, and a vortex convects downstream along the pressure side, as seen in figure 3.1(2). As this vortex moves past the trailing edge, there is a sudden drop in C_M and a slight rise in C_L. However, the airfoil continues to rotate on account of inertia, until it reaches its maximum pitch position. Close to the end of this motion, the LEV begins to grow, along with the shedding of a trail of smaller vortices from the trailing edge, seen in figure 3.1(3). A similar observation was made by Onoue & Breuer [92], who attributed the origin of this to a Kelvin-Helmholtz-like instability in the trailing-edge shear layer. This is accompanied by a sharp loss in C_L at the end of the pitch-up motion.

As the airfoil begins pitching down, there is an initial monotonic decrease in C_M and C_L that appears to mirror the initial stage of the pitch-up motion.

We also see that the presence of the LEV over the suction surface in figure 3.1(4) influences the rate of this decrease. This pitch-down motion destabilizes the suction-side shear layer, and leads to the shedding of a second, smaller LEV in figure 3.1(5). At the same time, a trailing-edge vortex is generated and shed, and this vortex seems to be influenced by the strong entrainment due to the LEV convecting past the trailing edge. This effect is seen in the majority of cases simulated. The simultaneous presence of this TEV and LEV near the suction side trailing edge causes a strong uptick in C_M, which causes it go over its pitch-up value. This interesting effect leads to a counter-clockwise loop in the C_M hysteresis curve (not shown here), which has implications for energy harvesting applications. Subsequently, C_M continues to decrease and C_L plateaus as the second LEV convects over the suction side in figure 3.1(6). The movement of this LEV past the trailing edge then produces a drop in C_L and a brief increase in C_M.

This representative case shows that the airfoil experiences strongly non-linear loading over the course of an oscillation cycle. The occurrence of limit-cycle oscillations, which we see in spite of a linear structural model, is only possible in the presence of such non-linearities in the system. Hence, this supports the notion that large scale flow separation is the primary cause of limit cycle oscillations in this system. Further, there is a complex interaction between the leading and trailing edge shear layers, as well as the generation and

shedding of multiple LEVs. The timing and position of these flow structures plays a crucial role in the dynamics of pitch oscillations, and this analysis of some representative flow interactions forms a starting point of our discussion.

3.2 Effect of key parameters on flutter response

The overall effect of spring stiffness (U^*), equilibrium angle-of-attack, and elastic axis location on the flutter amplitude is discussed in this section. In figure 3.2, we show the maximum stationary-state pitch deflection from the equilibrium (denoted as A_θ), as a function of U^* for the case with nonzero structural damping. This is plotted for three different equilibrium pitch angles, $\theta_0 = 5^\circ, 10^\circ, 15^\circ$, and three different locations of the elastic axis, $X_e^* = 0.25, 0.33, 0.50$. It is immediately clear that this system can show very large pitch deflections, going as high as 100°, for the case of $X_e^* = 0.50$. However, the pitch deflections for $X_e^* = 0.25$ and 0.33 are very small for the same range of U^*. Further, while the response for $X_e^* = 0.50$ increases monotonically with U^*, the response for $X_e^* = 0.33$ shows a non-monotonic trend (shown in the inset). These observations suggest that the amplitude response of this system is very sensitive to the location of the elastic axis, and this issue is investigated further in section 3.5 and chapter 4. The lack of response at $X_e^* = 0.25$ is not

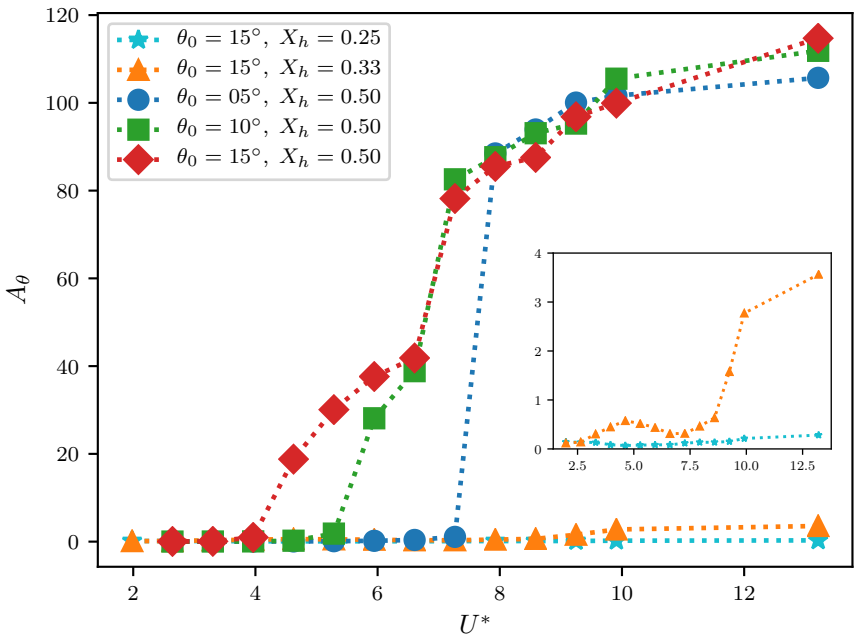

Figure 3.2: Maximum pitch deflection, A_θ, as a function of U^* for different values of θ_0 and X_e^*. For all cases shown here, $\zeta = 0.15$. The inset shows a zoom-in for $X_e^* = 0.25$ and $X_e^* = 0.33$.

surprising since the aerodynamic center of most airfoils is in the vicinity of 25% chord [142] and placing the elastic-axis at or near this location should diminish pitch-instability.

We now focus on the large amplitude flutter observed for the $X_e^* = 0.50$ cases. We see that the onset of these large amplitude oscillations occurs at a different (critical) U^* (referred to as U_c^*) for each value of θ_0. Lower θ_0 require softer springs (or higher U^*) in order to initiate deflections. Interestingly, A_θ for different values of θ_0 approach each other for very large pitch deflections indicating that the system loses memory of the equilibrium condition for very soft springs. As a result of this, and the fact that the bifurcation is delayed for lower

θ_0, the onset of large amplitude oscillations is more abrupt as we go to lower θ_0, i.e., the curve for $\theta_0 = 5^\circ$ has a larger slope than that for $\theta_0 = 10^\circ$. This points to the possibility of a bifurcation that has an increasingly subcritical nature as θ_0 is reduced. This is in agreement with Onoue *et al.* [28] and Dimitriadis & Li [26] who observed a subcritical bifurcation for $\theta_0 = 0^\circ$. It must be noted here that unlike the case of $\theta_0 = 0^\circ$, our system shows small, but nonzero values of A_θ even for very low U^*. These oscillations are associated with the oscillatory pitch-moments induced by Karman vortex shedding. However, we will show the presence of subcritical behaviour even in the case of $\theta_0 = 15^\circ$ later in this paper.

3.3 Frequency response

In the previous section, we showed that the system loses memory of the equilibrium condition (θ_0) for large flutter amplitudes. Considering this, we will conduct a detailed analysis for one case, namely $\theta_0 = 15^\circ$. In figure 3.3 we show the pitch oscillation frequency ($f_p^* = f_p C/U$) compared with the frequency of moment oscillations ($f_m^* = f_m C/U$) for the structurally damped case with $\theta_0 = 15^\circ$ and $\zeta = 0.15$. This is plotted with respect to the dimensionless natural frequency f_s^* as well as $U^* = 1/f_s^*$. The dashed line in figure 3.3 denotes the synchronization condition, i.e., the condition where the pitch frequency equals the

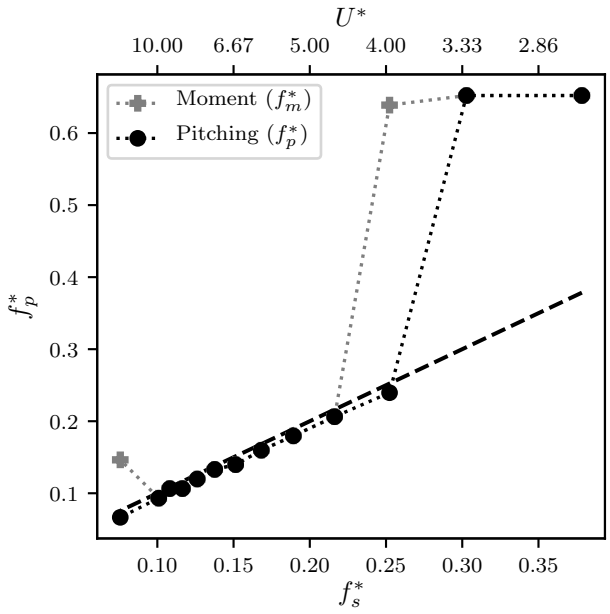

Figure 3.3: Pitch and moment frequency response as a function of U^* for $\theta_0 = 15°$, $X_e^* = 0.50$ and $\zeta = 0.15$. The dashed line shows the natural frequency.

natural frequency of the system. We see that for low (high) values of U^* (f_s^*), the pitch as well as moment oscillations occur at a constant, high frequency. On increasing U^*, there is a sudden drop in frequency – which corresponds to the same U^* value at which the bifurcation to large-amplitude pitch oscillation occurs - following which, the pitch oscillations synchronize with the natural frequency for higher (lower) values of U^* (f_s^*). Hence, there are three distinct frequency response regimes that occur for increasing (decreasing) U^* (f_s^*): constant, high frequency pitch and moment, followed by the moment de-tuning from the pitch at the bifurcation point, and finally the moment and pitch oscillations synchronizing with the natural frequency of the system.

It is instructive to examine the flow quantities during these distinct regimes

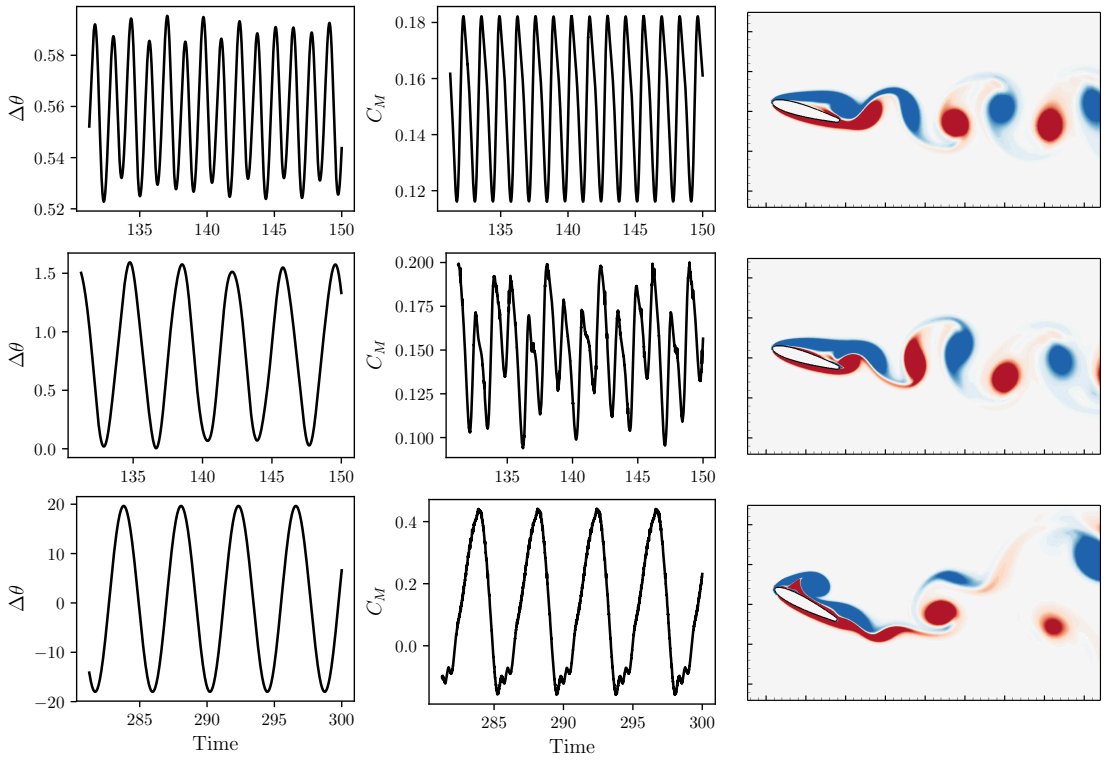

Figure 3.4: Pitch amplitude timeseries, ($\Delta\theta$), coefficient of moment (C_M), and a snapshot of vorticity contours for three regimes of response close to U_c^*; (top panel) $U^* = 3.3$; (middle panel) $U^* = 4.0$; (bottom panel) $U^* = 4.6$

to understand how the flow drives the dynamics of flutter, and vice-versa. In figure 3.4 we show plots of the pitch and moment time series, along with a snapshot of the flow, for three representative cases very close to the bifurcation point. For $U^* = 3.3$, which corresponds to the pre-onset regime, we see that the response amplitude is very small ($A_\theta < 1^\circ$), the frequency is high, and the pitch moment oscillates at a similar high frequency. Due to the small amplitude of oscillation, it makes sense to compare this with the behaviour of a static airfoil and we see that the response frequency is in fact very close to the vortex shedding frequency of a static airfoil at $\theta_0 = 15^\circ$ ($f^* = 0.71$; see timeseries in figure 3.5). From the flow field it is clear that this regime corresponds to a Karman vortex shedding mode, much like the wake due to separated slow around a stationary bluff body. In fact, the dimensionless frequency in this regime, when calculated using the projected frontal length as the length scale, is $f^* \approx 0.17$, which is very close to the frequency of Karman shedding in bluff body wakes. In this regime, the coupling between the flow and airfoil pitching is effectively one-way, with the vortex shedding driving the pitching, but the pitching having virtually no effect on the vortex shedding.

In contrast, the flow field for $U^* = 4.6$, which corresponds to the post-bifurcation regime where the pitch response occurs at the natural frequency of the system, shows a very different character with the presence of a strong dynamic stall vortex generated at the leading edge. This is also apparent in

the time-series of the moment coefficient, where the peak of the oscillation is accompanied by an abrupt drop in forcing. This drop in forcing has been observed by numerous studies as a hallmark of dynamic stall. In this regime, large (20°) amplitude pitch oscillations occur at the natural frequency, which in turn forces the generation and shedding of the stall vortex to occur at this frequency.

For the intermediate case of $U^* = 4.0$, which corresponds to the regime close to the bifurcation, the pitch time series shows low-frequency oscillations at to the natural frequency. The moment time series however seems to have frequency components corresponding to the vortex shedding as well airfoil pitching time-scale. This is qualitatively seen in the flow field too, where the wake has the appearance of a slightly undulating or distorted Karman wake. Hence this is a transitional regime that occurs between the pre- and post-bifurcation regimes.

This regime of oscillation in fact agrees well with the observation of Poirel *et al.* [23] who investigated flutter oscillations in this range of amplitudes. They too observed low-frequency pitch oscillations which showed no signature of the high-frequency Karman shedding occurring in the wake. Further, this low-frequency content is absent in the pre-bifurcation (or static) regime forcing response. The triggering of low-frequency oscillations in the absence of low-frequency forcing suggests that the flutter is not a result of an external periodic

forcing, and is in fact self-sustained.

3.4 Critical reduced velocity

An obvious and important question raised by Figure 3.2 is - why does the critical U^* depend on θ_0? U^* represents a ratio the time-scale of the pitch oscillation to a time-scale for the flow. With regard to the pitch-time-scale, it is clear from the previous subsection that in the post-critical regime, the time-scale for the pitch oscillations does coincide with with the natural time-scale of the elastic system. Turning next to the flow time-scale in U^* we note that in most studies (including the current), the time-scale for the flow is assumed to be the convective time-scale of the flow over the body, i.e. C/U_∞. However, a more appropriate flow time-scale is one that is associated with the mechanism that triggers the flutter instability. In the well-studied case of flow-induced vibrations of circular cylinders, it is known that the trigger for the cylinder vibrations is Karman vortex shedding [129]. The appropriate time-scale for determining the onset of these vibrations is therefore the vortex shedding time-scale (T_v), which is roughly about $5D/U_\infty$. Thus, a reformulation of the reduced velocity as the ratio of the natural time-scale of the elastic structure and the vortex shedding time-scale as $U_v^* = (1/f_s)/(5D/U_\infty)$ leads to the condition that vibrations are initiated when U_v^* approaches and exceeds unity. The identifica-

tion of a similar scaling for the airfoil flutter observed in the current study, is the focus of the rest of this section.

Since we are concerned here with the *onset* of flutter, flow past a static airfoil should provide insights regarding the triggering mechanism. With this in mind we perform a set of simulations of flow over static airfoils at $Re = 1000$ with the angle-of-attack set to θ_0 for each case. The system is held at this angle-of-attack and the flow proceeds through the transient to its final stationary state. In figure 3.5 we show time-series plots of the lift and moment generated by these cases and also the instantaneous contours of spanwise vorticity for each case. The lowest θ_0 exhibits weak vortex shedding beyond the near wake whereas the other two cases exhibit separation of the boundary layer from the suction surface of the airfoil as well as vortex shedding in the wake with a topology that is quite similar to Karman shedding. The frequency corresponding to this vortex shedding is $0.81U_\infty/C$ and $0.71U_\infty/C$ for $\theta_0 = 10^\circ$ and 15°, respectively. However, these are higher than the frequency corresponding to the system at the onset of flutter and can therefore not be the triggering mechanisms for post-onset flutter oscillations. In fact, the static $\theta_0 = 5^\circ$ case does not exhibit vortex shedding but still undergoes a bifurcation to large-scale flutter, further confirming that wake vortex shedding is not the trigger for the bifurcation. This agrees with the observations of Poirel *et al.* [23].

Figure 3.5 however, suggests an alternative time-scale for the onset and

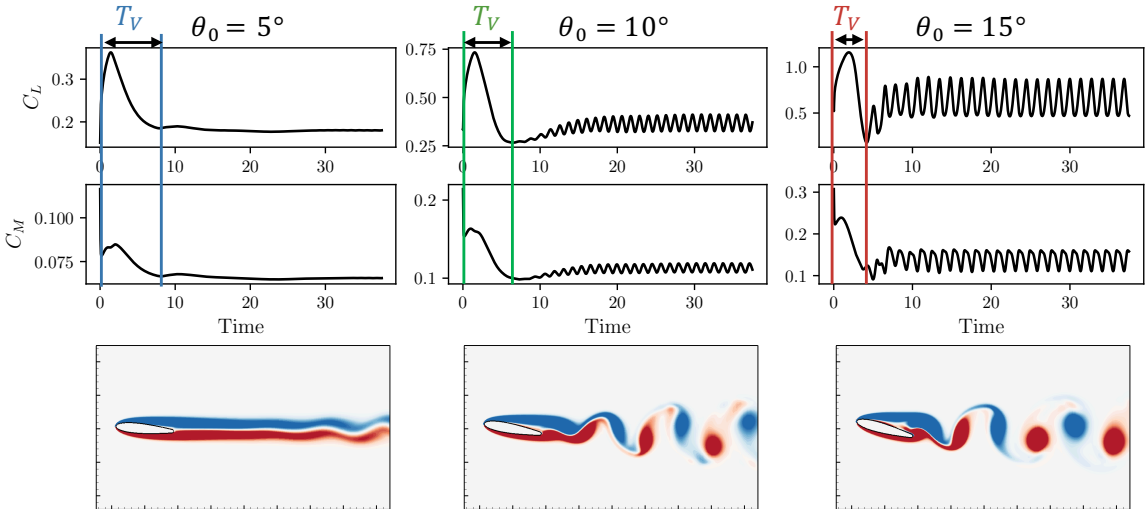

Figure 3.5: Time series of C_L and C_M for static airfoils at $\theta_0 = 5°, 10°, 15°$. The bottom panel shows an instantaneous snapshot of the flow after reaching stationary state for each case, coloured by vorticity contours. Also indicated is T_v, which represents the time-scale of the initial transient. Note: The flow snapshots do not show the entire computational domain, which extends roughly $5C$ beyond the edge of the figure.

sustenance of flutter, which manifests itself during the initial transient over the static airfoil. The initial transient in the current simulations represents the initial growth, development, and saturation of the vorticity layer over the two surfaces of the airfoil and this transient is associated with a distinct, large-magnitude peak in the lift and moment, with a well-defined time-scale. This time-scale is associated with an intrinsic time-scale for the separated shear layer, which is the key driver for flutter. Based on this, we hypothesize that the time-scale that corresponds to the relaxation time of a perturbation in the separated shear layer would be the appropriate time-scale for determining the onset of flutter.

It is possible to estimate this time-scale for the current configuration by using a system-identification approach. This is done by providing a small perturbation to the angle-of-attack of an airfoil which is held stationary before and after the perturbation, and estimating the time it takes for the resulting pitching moment on the airfoil to relax back to the unperturbed state. In this study, the pitch perturbation takes the form $\theta_p(t) = A_p[1-\cos\{2\pi(t-t_0)/\tau_p\}]$, where A_p is the amplitude of the perturbation, t_0 is the time at which the perturbation is applied, and τ_p is the duration of the perturbation. In the current case, τ_p is chosen equal to C/U_∞, which is much smaller than the observed timescales of the initial transient and resembles a "delta" perturbation. A qualitative representation of this perturbation is shown for the case of $\theta_0 = 5^\circ$ in figure 3.6. We then compute the perturbation in the pitching moment by subtracting the unperturbed moment coefficient (which we refer to as C_{M_0}) from the pitching moment measured following the perturbation. For simplicity, these signals are filtered to remove vortex shedding oscillations. The required time-scale (T_v) is then estimated as the time taken by the energy of this perturbation to attain 5% of its peak value. The above procedure is performed for $\theta_0 = 5^\circ, 10^\circ, 15^\circ$ using perturbations at various phases of the natural vortex shedding. Furthermore, the following magnitudes of perturbation, A_p are employed: $0.1^\circ, 0.125^\circ, 0.25^\circ$ for $\theta_0 = 5^\circ$; $0.125^\circ, 0.25^\circ, 0.5^\circ$ for $\theta_0 = 10^\circ$; and $1.5^\circ, 2^\circ, 2.5^\circ$ for $\theta_0 = 15^\circ$.

Figure 3.6 shows the time-variation in the moment coefficient for these var-

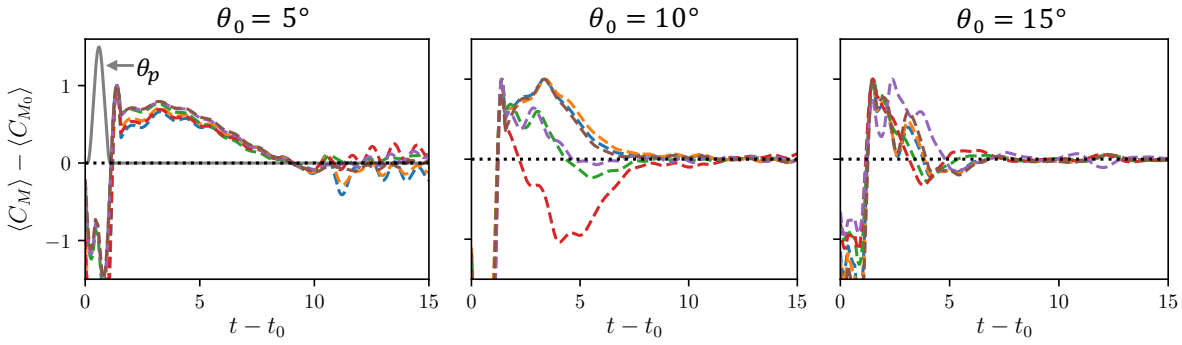

Figure 3.6: Relaxation of perturbed C_M as a result of small perturbations in angle of attack for static airfoils at $\theta_0 = 5°, 10°, 15°$ deg. $\langle C_M \rangle$ and $\langle C_{M_0} \rangle$ are filtered moment coefficients of perturbed and unperturbed cases respectively. The different curves in each plot correspond to different values of A_p and t_0. Also shown qualitatively for the case of $\theta_0 = 5°$ is the pitch angle perturbation, θ_p. Time in these plots is non-dimensionalized by C/U_∞.

ious cases at each θ_0. It is observed that depending on the phase of vortex shedding at which the perturbation is applied, the perturbed moment coefficient can be positive or negative. However, all the perturbation with different phases and magnitudes result in a consistent relaxation time-scale for each θ_0. This time-scale is estimated to be $T_v \approx 7.0$, 5.1 and 4.0 for $\theta_0 = 5°, 10°$ and $15°$, respectively. It is noted that the time-scale reduces with increasing angle-of-attack, a trend that was also observed for the initial transient in figure 3.5.

We now use T_v to define a new reduced velocity $U_v^* = 1/(f_s T_v)$. In figure 3.7 we replot the maximum pitch deflection (which was initially shown in Figure 3.2) v/s U_v^* and we find not only that the bifurcation points for the three cases collapse to nearly the same value, but also that this critical value is slightly above unity. This strongly suggests that T_v is the correct flow time-scale for

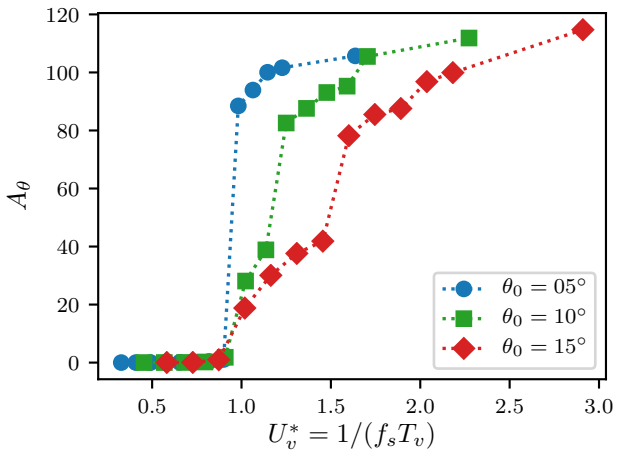

Figure 3.7: Maximum pitch deflection v/s $U_v^* = 1/(f_s T_v)$ for $\theta_0 = 5°, 10°, 15°$. Here $\zeta = 0.15$ and $X_e^* = 0.50$.

this problem and in an analog of the flow-induced vibration of circular cylinder, $U_v^* \gtrapprox 1$ is the simple condition for the generation of large-scale flutter, at least for the low Reynolds numbers investigated here.

The $U_v^* \gtrapprox 1$ condition for flutter also provides a phenomenological basis for the onset of flutter. During the pre-bifurcation regime, where the structural stiffness is higher than the critical value, the natural time-scale is smaller than the flow time-scale. In this condition, the time-variation in pitching moment due to a perturbation in pitch does not have sufficient time to grow before the spring forces the airfoil back towards the equilibrium position. Thus, the interaction between the pitching motion and the pitching moment is not constructive and the system is not able to extract energy from the flow to sustain the oscillation. For $U_v^* > 1$, the natural time-scale exceeds the flow time-scale and the growth in the pitching moment associated with a pitch perturbation can

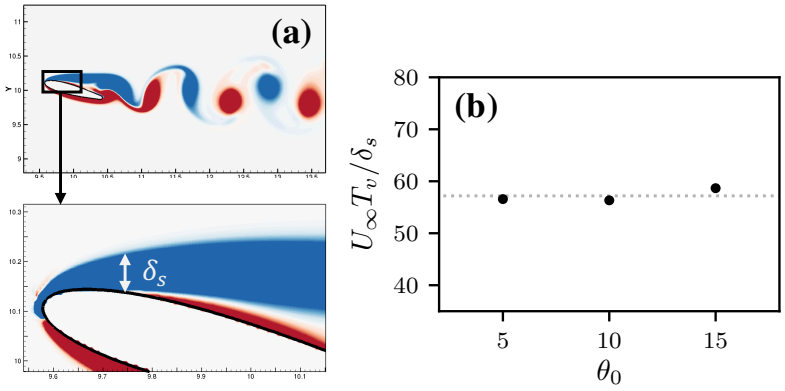

Figure 3.8: (a) Qualitative representation of boundary layer thickness at separation point for $\theta_0 = 15°$; (b) Scaling of the shear-layer timescale (T_v) with estimated boundary layer thickness (δ_s) for $\theta_0 = 5°, 10°, 15°$.

now be accommodated by the spring. This constructive interaction between pitch and pitching moment is able to extract energy from the flow during a pitch perturbation, leading to growth of the pitch instability. In a later section, we will revisit this idea of energy extraction and its influence on driving aeroelastic flutter.

The physical underpinning of the dependence of T_v on the angle-of-attack is the final question regarding the onset of flutter. In particular, why does T_v decrease with increasing angle-of-attack? We base our analysis on the notion that T_v is related to the inherent instability of the shear layer that separates from the suction surface of the airfoil, and the natural time-scale of a shear layer that separates from a surface scales with the thickness of the shear layer at the point of separation. As the angle-of-attack is increased, the separation point moves upstream where the attached boundary layer is thinner, and therefore

the shear layer thickness at the point of separation decreases with increasing angle-of-attack. We have estimated the boundary layer thickness (denoted by δ_s) at the point of separation for the static airfoil at the three angles-of-attack. This is shown qualitatively for $\theta_0 = 15^\circ$ in figure 3.8(a). In figure 3.8(b) we plot the ratio of the shear layer timescale and boundary layer thickness, non-dimensionalized by U_∞ for the three angles-of-attack studied here. This dimensionless number represents a relaxation timescale associated with the shear layer and the plot indicates that δ_s and T_v have an approximately constant scaling with angle-of-attack. This supports our hypothesis that the reduction of T_v with angle-of-attack is related to the shear layer instability, which is in turn governed by its thickness at the point of separation.

3.5 Structural damping and location of elastic axis

In this section, we describe the effects of structural damping as well as the location of the elastic axis on flutter. In previous sections, we have described the response of the system with $b^* = 0.15 b^*_{cr}$ and in this section, we compare these previous cases with the corresponding cases with zero damping. Further, we will make this comparison for two different locations of the elastic axis: $X^*_e = 0.50$ and 0.33. The location of the elastic-axis with respect to the center-

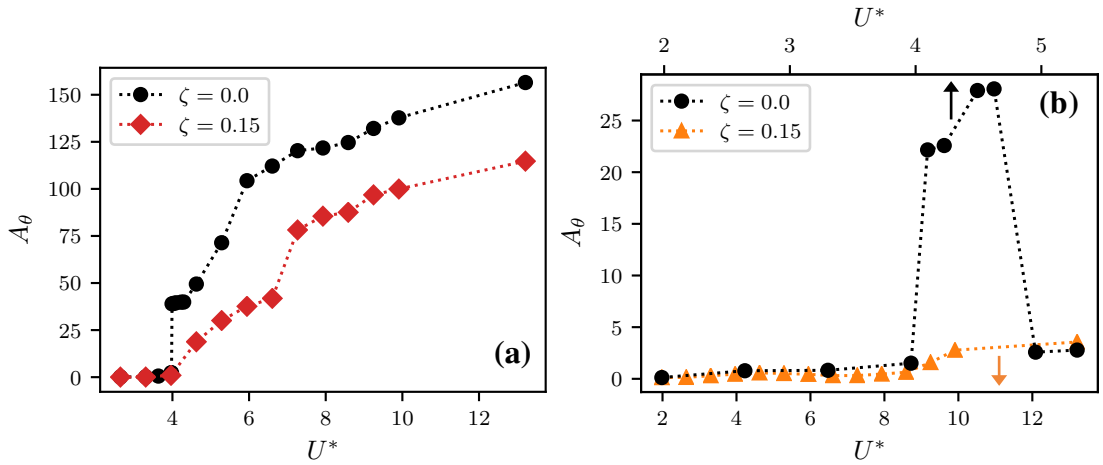

Figure 3.9: Effect of structural damping, ζ, on maximum pitch deflection for $\theta_0 = 15°$. This is shown for two different locations of the elastic axis, (a) $X_e^* = 0.50$; (b) $X_e^* = 0.33$. Note: Range of U^* is different for each value of ζ in the case of $X_e^* = 0.33$.

of-pressure is critical in determining the aeroelastic pitch stability of an airfoil. A center-of-pressure upstream of the elastic-axis leads to an unstable configuration that promotes the pitching instability, and vice-versa. In the context of pitching airfoils, there is the added consideration of the timing of leading-edge vortices convecting past the elastic axis. Each such vortex induces a pitching moment on the airfoil and the direction of this moment changes as the vortex convects past the elastic-axis. This could potentially lead to non-linear and non-monotonic behavior noted in 3.2.

In figures 3.9(a) and (b) we plot the maximum pitch deflection, A_θ, with and without structural damping, as a function of U^*, for two different locations of the elastic-axis and for $\theta_0 = 15°$. For $X_e^* = 0.50$, we see that the overall trend of A_θ does not change significantly with damping. However, as expected, the

undamped case shows a much larger amplitude of oscillations. We also see that the bifurcation to large amplitude oscillations is very abrupt for $\zeta^* = 0.0$, indicating a subcritical bifurcation. This agrees with the classical understanding of dynamical systems where the loss of a low-order damping term leads to a subcritical bifurcation [143]. However, the stabilizing influence of higher order non-linearities (from the flow, in this case) prevents the system from diverging, and hence causes limit-cycle oscillations.

As noted previously, the amplitude response for $X_e^* = 0.33$ exhibits significantly smaller oscillations and a non-monotonic behaviour as the hinge location is moved upstream. Figure 3.9(b) shows that this non-monotonic behaviour of A_θ is much more apparent in the absence of structural damping, where we observe a very large and abrupt jump in flutter amplitude with U^*. However, further increase in U^* results in a large drop in the flutter amplitude. These types of non-monotonic responses have been studied extensively in flow-induced vibration of bluff bodies [144] but are quite unexplored for airfoil flutter.

Figure 3.10 shows the frequency response of the undamped system for $X_e^* = 0.50$ and 0.33 and it is clear that these cases show the same response regimes that were seen before - a high frequency Karman shedding mode, followed by oscillations at the natural frequency for increasing U^*. Further, this synchronization happens close to the critical U^*. Hence the frequency selection in this system follows a mechanism that is similar to that outlined previously, where

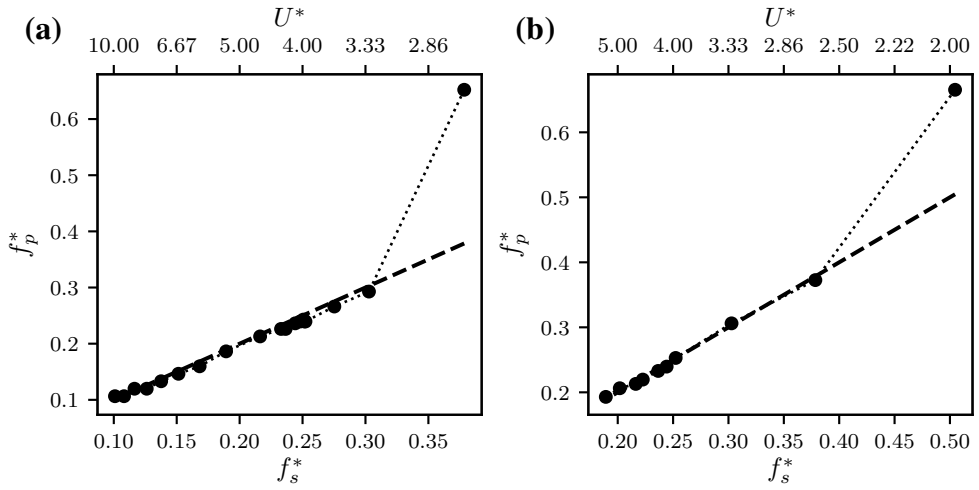

Figure 3.10: Pitching frequency response of undamped oscillations ($\zeta = 0.0$) for $\theta_0 = 15^\circ$ and two different locations of the elastic axis, (a) $X_e^* = 0.50$; (b) $X_e^* = 0.33$. The dashed line shows the natural frequency of the system.

the competition of time-scales determines the response frequency. However, the amplitude response warrants further investigation.

3.6 Conclusions

We have carried out a study of flow-induced airfoil flutter at a chord-based Reynolds number of 1000 using high-fidelity modelling of the fluid dynamics coupled with a linear structural model for deflection in pitch. The objectives of this work were two-fold - to carry out a systematic study of the parameters affecting the dynamics of wing flutter, and to demonstrate the use of the energy exchange between the fluid and the structure as a way to analyze the flutter behavior and its dependence on various parameters such as spring stiffness,

elastic axis location and mean angle-of-attack.

We have shown that the system is capable of producing very large amplitude oscillation responses, and this amplitude response depends on a range of different parameters. In addition, the oscillation amplitude also shows non-monotonic behaviour with respect to U^* in some cases such as when $X_e^* = 0.33$. The flutter response shows three distinct regimes of oscillation on increasing U^* – constant, high frequency pitch and moment oscillations at low values of U^*, followed by the moment de-tuning from the pitch at the bifurcation point, and finally the moment and pitch oscillations synchronizing with the natural frequency of the system. This last regime corresponds to the onset of large-amplitude oscillations.

It is shown that for cases that exhibit significant flutter, the onset of flutter occurs at a reduced velocity ($U^* = U_\infty/Cf_s$) which is dependent on the initial angle-of-attack. Simulations are used to determine a time-scale (T_v) corresponding to the relaxation of a pitch perturbation, which provides a more appropriate flow time-scale for this problem. A reduced velocity defined based on this time-scale, i.e. $U_v^* = f_s^{-1}/T_v$ leads to the simple condition that flutter will occur for $U_v^* > 1$, irrespective of the angle-of-attack. This condition provides a phenomenological basis for the onset of flutter: the natural time-scale of the system (f_s^{-1}) should be larger than the time-scale (T_v) of the flow so as to enable constructive coupling between the flow and the structure and am-

plification of a pitch perturbation. Finally, we provide some evidence that the time-scale T_v is proportional to the thickness of the boundary layer at the point of separation over the suction surface of the static airfoil, thereby connecting this time-scale to the intrinsic instability of the separated shear layer.

The findings discussed here have been published in reference [77].

Chapter 4

Energy maps: Predicting flow-induced oscillation responses

Our analysis in the preceding section indicates a need to better understand the amplitude response of the flow-induced pitching airfoil for a given set of system parameters. We were able to demonstrate the mechanism governing the onset and frequency of oscillation as a competition of time-scales. However, the variations in amplitude with U^* and X_e^* were shown to be complex and non-intuitive. For example, we showed that the flow-induced oscillation amplitude for the case with $X_e^* = 0.33$ exhibits a non-monotonic trend, i.e. the oscillation amplitude initially grows when U^* is increased (or elasticity is increased) but

then abruptly drops to very small amplitudes on further increasing U^*. Such responses are not only counter-intuitive, but also pose a practical challenge in terms of analysis, prediction and control of these systems.

In this chapter, we demonstrate a method to analyze, predict and control the stationary state as well as transient response of pitching airfoils using the energy extracted from the fluid under prescribed conditions. We will show that this method enables us to understand highly complex and non-intuitive amplitude responses and flutter bifurcations, as well as predict such responses in equilibrium and perturbed conditions.

4.1 Energy-based model for amplitude growth

The basis of the methods demonstrated in this section is the simple idea that the growth or decay of flow-induced oscillations of an elastic body immersed in a fluid flow is driven by the energy that the oscillating system extracts or loses to the flow around it. For an airfoil undergoing sinusoidal pitching oscillations in a freestream, we can therefore derive an energy-based model for the growth of its oscillation amplitude as well as its equilibrium oscillation state when undergoing flow-induced oscillations.

This model begins with the spring-mass-damper dynamical equation for the

airfoil's oscillation, which was provided earlier in equation (2.2), and is reiterated below for completeness:

$$I^*\ddot{\theta} + b^*\dot{\theta} + k^*(\theta - \theta_0) = C_M. \tag{4.1}$$

By multiplying equation (4.1) with the angular velocity of oscillation, ($\dot{\theta}$) as follows,

$$I^*\ddot{\theta}\dot{\theta} + k^*(\theta - \theta_0)\dot{\theta} = C_M\dot{\theta} - b^*\dot{\theta}\dot{\theta} \tag{4.2}$$

we obtain a simple energy balance equation describing the rate-of-change of energy in the oscillator, shown below:

$$\implies \frac{d}{dt}\left(\frac{1}{2}I^*\dot{\theta}^2\right) + \frac{d}{dt}\left(\frac{1}{2}k^*\theta^2\right) = \frac{de_f^*}{dt} - \frac{de_d^*}{dt} = \frac{de^*}{dt}. \tag{4.3}$$

Here e_f^* is the energy extracted by the airfoil from the flow and e_d^* is the energy lost to structural damping. Integrating this equation over an oscillation cycle with time period T, where the beginning of the cycle is at time t_n, results in an equation for the change of amplitude over the oscillation cycle. This can be expressed as,

$$I^*[\dot{\theta}^2(t_n+T) - \dot{\theta}^2(t_n)] + k^*[\theta^2(t_n+T) - \theta^2(t_n)] = 2\left[e^*(t_n+T) - e^*(t_n)\right] = 2E^* \tag{4.4}$$

where E^* is the net energy gained by the structure over one cycle.

Assuming the oscillations are purely sinusoidal, the pitch angle (θ) can be written as $\theta = A_\theta \sin(\omega t)$ where $\omega = 2\pi/T$ is the angular frequency and A_θ is the amplitude of oscillation. Substituting this in equation (4.4) for the energy balance yields the following equation for the change in amplitude over an oscillation cycle,

$$A_\theta^2(t_n + T) - A_\theta^2(t_n) = \frac{2E^*}{I^*\omega^2 \cos^2(\omega t_n) + k^* \sin^2(\omega t_n)}. \tag{4.5}$$

Now if the oscillation occurs at the natural structural frequency of the spring, i.e., $\omega = \sqrt{k^*/I^*}$, the above expression for amplitude growth takes the following form in the regime corresponding to locked-in oscillations at the natural frequency:

$$A_\theta^2(t_n + T) - A_\theta^2(t_n) = \frac{2E^*}{k^*} \tag{4.6}$$

$$\implies A_\theta(t_n + T) - A_\theta(t_n) = \frac{E^*}{k^* \bar{A}_\theta} \tag{4.7}$$

where $\bar{A}_\theta = [A_\theta(t_n + T) + A_\theta(t_n)]/2$ is the average amplitude over a cycle.

Equation (4.7) is a model for the amplitude growth of sinusoidal flow-induced oscillations (A_θ) where the energy extraction, $E^* = E_f^* - E_d^*$, directly incorporates the interaction between the oscillation itself (via $\dot{\theta}$) and the flow-induced forcing (C_M). Here E_f^* is the energy extracted by the airfoil from the fluid flow

over one oscillation cycle and is given by,

$$E_f^* = \int_{t_n}^{t_n+T} C_M \dot{\theta} dt \tag{4.8}$$

where $\dot{\theta}$ is the angular velocity and T is the period of oscillation. It is clear from equation (4.7) that for a given flow-induced oscillator, the growth or decay of flow-induced oscillations is primarily dictated by the energy gained by the oscillator. In particular, the sign of E^* determines whether the oscillation amplitude grows or decays during a given oscillation cycle.

Furthermore, equation (4.7) also provides a condition at which the oscillation amplitude ceases to change and reaches a stationary-state. Equilibrium is attained when $A_\theta(t_n + T) = A_\theta(t_n)$, and this corresponds to

$$E^* = 0. \tag{4.9}$$

Therefore the flow-induced oscillator reaches an equilibrium when the flow-induced forcing and kinematics of oscillation interact such that a state of $E^* = 0$ is achieved.

To highlight the physical significance of the energy extraction E_f^*, let's momentarily focus on a simplified case with purely sinusoidal oscillations where $\dot{\theta} = \dot{\Theta}\sin(2\pi t/T)$ as well as sinusoidal forcing where $C_M = K\sin(2\pi t/T + \phi)$. In this case, the energy transfer is given by $E_f^* = (1/2)\,\dot{\Theta} K T \cos\phi$ and this sim-

ple model shows that the sign of energy extraction, which determines whether the airfoil extracts energy from the flow, is governed by the phase difference between the pitch velocity and the pitch moment. The physical interpretation of this phase difference, in the context of flow-induced oscillations, is related to the timing between the pitching and the resulting response of the flow.

This phase difference can depend on a range of factors, and one example highlighted here is the effect of changing the location of the elastic axis. In figure 4.1, we show time series plots of the pitch deflection and moment coefficient for an airfoil forced to oscillate at $A_\theta = 25°$, about two different locations of the elastic axis, $X_e^* = 0.50$ and $X_e^* = 0.33$. The pitching moments plotted for each case in figure 4.1 show that changing the elastic axis, while retaining the kinematics, produces very different moments on the airfoil. This is a result of the timing associated with the shedding as well as convection of vortices past the hinge location. The difference in timing leads to the case with $X_e^* = 0.33$ being damped ($E_f^* < 0$), while the case with $X_e^* = 0.50$ extracts energy ($E_f^* > 0$). These examples suggest that the phase difference, and hence energy extraction, is indeed a function of operation parameters and is an important factor in analyzing the response of flow-induced flutter.

Lastly, while we have thus far discussed the significance of equation (4.7) in the context of amplitude growth and equilibrium oscillations, it is important to note that an equilibrium state may be stable or unstable. Equation (4.7),

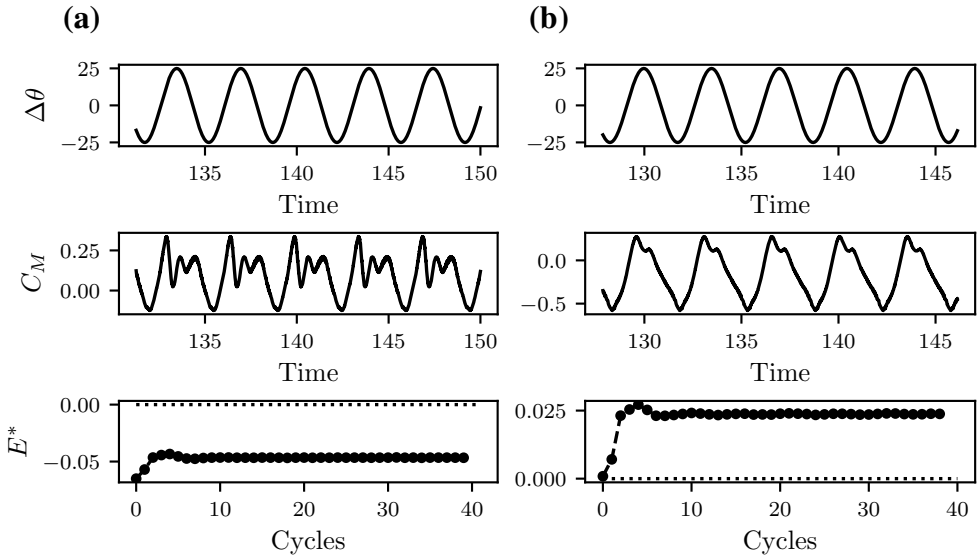

Figure 4.1: Comparison of $\Delta\theta$, C_M and extracted energy E_f^*, for airfoils forced to oscillate with $A_\theta = 25^\circ$ and $f_p^* = 0.25$ about two different hinge locations. (a) $X_e^* = 0.33$; (b) $X_e^* = 0.50$.

which is the Poincaré map of this dynamical system, also allows us to derive a linearized stability condition for this system. For a dynamical system of the form $A_{n+1} = \mathcal{F}(A_n)$, where n is the index of the return map, and $\mathcal{F}$ is some functional form, linear stability requires $d\mathcal{F}/dA < 1$ [143]. For our system, this gives the following condition for stability

$$\frac{d}{dA_\theta}\left(A_\theta + \frac{E^*}{k^*\bar{A}_\theta}\right) < 1 \implies \frac{dE^*}{dA_\theta} < 0 \tag{4.10}$$

Thus, the above indicates that a system allowed to flutter freely will equilibrate only when conditions (4.9) and (4.10) are satisfied simultaneously. We note that this energy-based concept has previously been employed by other groups,

primarily in the context of bluff body vibrations [27, 75]. Furthermore, the equilibrium conditions arrived at here are the same as those employed in these previous studies.

4.2 Introducing energy maps

We now use our knowledge of the energy extraction, as described above, to understand and predict the amplitude response of a flow-induced oscillations. In particular, we propose the use of "energy maps" to identify the energy landscape of a flow-induced oscillator, along with equilibrium states and bifurcations, as a function of the operation parameters of the system. To do this, we first create a "map" of energy transfer as a function of the parameters of interest. In this discussion, we focus on the effect of U^* (or oscillation frequency) on the amplitude response of pitching oscillation.

The energy map is created by performing simulations of airfoils that are forced to undergo sinusoidal pitching oscillations over a range of amplitudes and frequencies, while holding the other parameters such as X_e^* and Re fixed. The angular velocity and pitching moment from each of these simulations is then used to calculate the energy extracted by the airfoil at the prescribed amplitude and frequency of oscillation. The validity of these energy maps, which are obtained from forced oscillations, for the analysis of flow-induced oscilla-

tions hinges on the idea that the energy extracted by an airfoil undergoing forced oscillations at a particular set of operating conditions is equal to the energy extracted by a corresponding flow-induced oscillator when they are oscillating at exactly the same conditions. In the present case, this rests primarily on the assumption that the free oscillations are strictly sinusoidal. We find that this condition is indeed satisfied to a very large degree for all the cases simulated here (see figures 3.1 and 3.4) and a sinusoidal fit to the pitching time-series yields an R-square value of roughly 0.99 for nearly all cases studied.

The first map shown in figure 4.2 is for the case with $X_e^* = 0.50$ and $Re = 1000$. This map is the result of a total of ~ 300 simulations over a range of non-dimensional pitch frequencies $f_p^* = f_p C/U_\infty : [0.10, 0.75]$ and pitch amplitudes $A_\theta : [0, 50^\circ]$. For each case, we simulate over 50 total cycles to ensure that a stationary state is achieved, and obtain E_f^* by integrating over the last 20 cycles. The dashed line in the energy map corresponds to $E_f^* = 0$ and the dotted line corresponds to $E_f^* = E_d^*$, where E_d^* is calculated using the value of structural damping previously specified in section 2.2.1. These represent potential equilibrium conditions in the case of flow-induced flutter.

The primary features in the map are the nearly vertical demarcation between regions of positive and negative energy transfer at about $f_p^* \approx 0.25$ and the small region of positive energy transfer around $f_p^* \approx 0.65$. From this energy

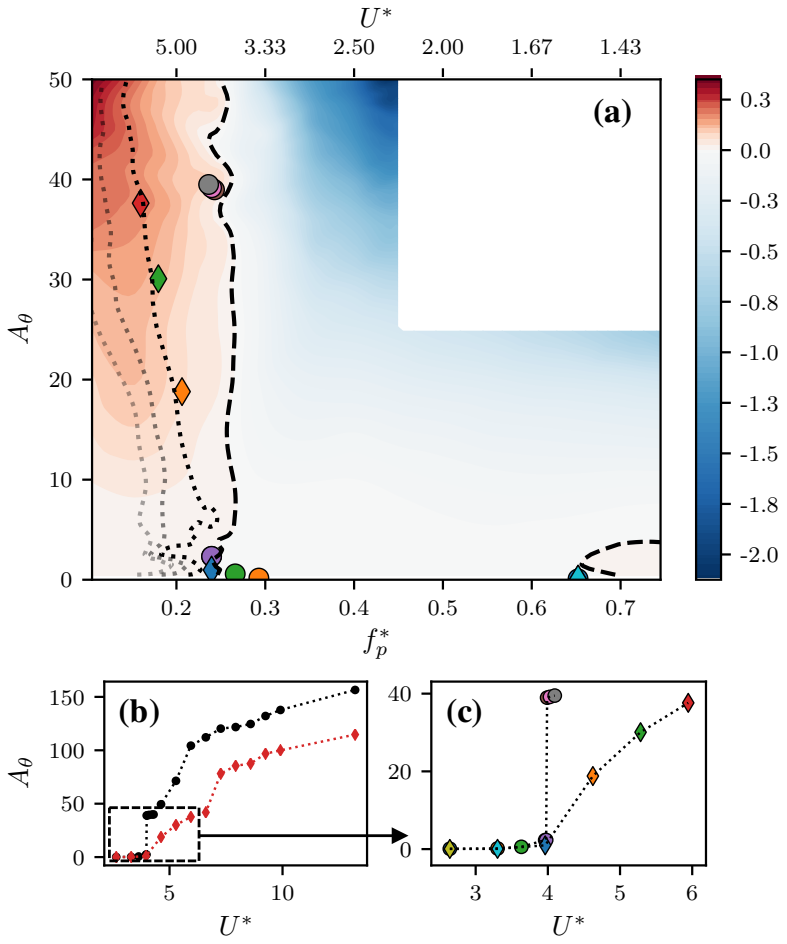

Figure 4.2: (a) Contours of energy extraction, E_f^*, as a function of oscillation amplitude and frequency for $X_e^* = 0.50$, $\theta_0 = 15°$. Symbols represent stationary state f_p^* and A_θ for undamped (○) and damped (◊) flow-induced oscillation cases. Dashed and dotted lines represent undamped ($E_f^* = 0$) and damped ($E_f^* = E_d^*$) equilibrium curves respectively. E_d^* is calculated using $\zeta = 0.15$ for the darkest damped equilibrium curve, and increasing values of ζ for subsequently lighter equilibrium curves ($\zeta = 0.30, 0.45$); (b) Reproduction of figure 3.9(a) with inset box showing range of U^* and A_θ computed in the energy map; (c) Zoom-in of flow-induced oscillation amplitudes for cases compared with the energy map.

map, we expect that sustained flow-induced oscillations for cases with structural damping would occur in the region with $E_f^* > 0$, whereas cases without structural damping should saturate along the $E_f^* = 0$ contour line. To verify this, we superimpose on this map, the stationary-state amplitude and frequencies from the flow-induced flutter simulations for $X_e^* = 0.50$. We find that for all these cases, the system saturates very close to the contour line corresponding to net energy equilibrium, i.e., $E_f^* = 0$ for undamped oscillations and $E_f^* = E_d^*$ for damped oscillations. These observations provide clear confirmation of the validity of these energy maps as a tool for understanding the flow-induced flutter response.

Examining the energy maps further, we note that the nearly vertical $E_f^* = 0$ contour line lies very close to the frequency corresponding to the reciprocal of the critical velocity, which is the frequency at which the bifurcation to large amplitude oscillations occurs for the flow-induced oscillation with $X_e^* = 0.50$. Also, the small region of positive energy transfer on the right side of the map has a frequency that corresponds to the Karman oscillation mode identified earlier (see fig. 3.3). The topology of the energy map and the equilibrium curve provide useful insights regarding the dynamics of this configuration. For instance, the nearly vertical demarcation between the regions of energy growth and decay at $f_p^* \approx 0.25$ suggests that an undamped system would experience rapid growth in flutter amplitude with a relatively small decrease (increase) in pitch

frequency (reduced velocity). Indeed, figure 3.9(a) shows that the undamped system exhibits what seems to be a subcritical bifurcation at $U^* \approx 4.0$ with a jump in amplitude of nearly 40^o. As the structural damping is increased, the equilibrium curve bends to the left (i.e. increasingly negative slope) indicating a smoother onset of flutter. Furthermore, increased damping significantly limits the maximum amplitude attained by the system. Other implications of the topology of the energy map for the system dynamics are explored in the next section.

4.3 Analysis of aeroelastic response using energy maps

As seen in chapter 3, the flow-induced oscillation response for the case with $X_e^* = 0.33$ exhibits a very complex, non-monotonic trend with U^*. We now demonstrate the utility of the energy maps in providing insight into this response. As shown in equation (4.7), oscillations in the absence of structural damping are expected to grow (decay) in regions of positive (negative) E_f^*. The requirements for a stable equilibrium are:

$$E_f^* = 0 \quad ; \quad dE_f^*/dA < 0 \tag{4.11}$$

Figure 4.3 shows the energy map for this case which is generated as before by conducting ~ 200 simulations of prescribed oscillations over a large range of pitch frequencies and amplitudes. On this energy map, we have identified the curves corresponding to the equilibrium condition ($E_f^* = 0$) as well as the regions of stability on these equilibrium curves ($dE_f^*/dA < 0$). A number of qualitative observations can immediately be made regarding this energy map. First, the topology is very different from that for $X_e^* = 0.50$. Since free oscillations can only exist within the region of $E_f^* \geq 0$, the energy map suggests an upper limit of $A_\theta \approx 40^\circ$ on the flow-induced oscillation amplitude in this case. The topology of the map is also extremely complicated: two main regions of energy growth and decay are separated by a complex equilibrium curve that extends over the entire range of frequencies considered here. There also exist multiple "islands" with $E_f^* < 0$ within the large region of energy growth in the low-amplitude ($< 10^\circ$) portion of the map, and this points to the possibility of multiple equilibrium states for a given conditions as well as abrupt changes in oscillation amplitude with changes in the underlying parameters.

4.3.1 Stationary-state response

To compare our prediction for the equilibrium positions on this energy map, we superimpose the stationary state locations of our flow-induced data for $X_e^* = 0.33$ on the energy map using circle ($\circ$) symbols. This data set was de-

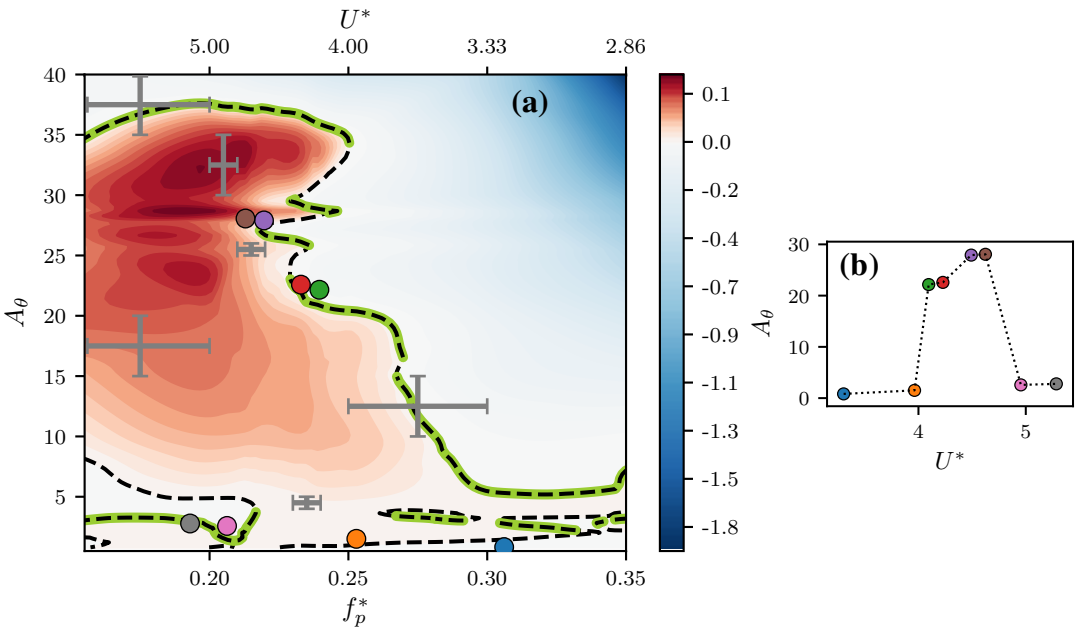

Figure 4.3: (a) Energy map for $X_e^* = 0.33$ and $\theta_0 = 15°$, with the equilibrium curve ($E_f^* = 0$) shown as a dashed line, and stable equilibrium ($E_f^* = 0$, $dE^*/dA < 0$) highlighted along the equilibrium curve (thick line); (b) Maximum pitch deflections versus U^* for cases with $\zeta = 0$ corresponding to figure 3.9(b); The stationary state oscillation amplitude and frequency of all cases shown in (b) are plotted on the energy map using circles (○). Also shown on the energy map are bars indicating the local resolution in f_p^* and A_θ in various regions of the energy map. Local regions of the map that contain complex topological features have been provided higher resolution.

scribed earlier in section 3.5 (see figure 3.9(b)) and is also shown as maximum pitch deflection versus U^* in figure 4.3(b). This data corresponds to zero structural damping, and is hence expected to lie along stable equilibria identified on the $E_f^* = 0$ curve. In figure 4.3 we see that there is again very good agreement between the flow-induced oscillations data and the energy map. The slight discrepancies in this comparison are a result of the finite resolution of the energy map, which is not able to fully resolve the complicated structure of the map. This is especially apparent at very small oscillation amplitudes, where multiple equilibria exist in close proximity to each other. Hence on figure 4.3 we have also plotted error-bars at various locations indicating the local step size in f_p^* and A_θ used in computing generating the energy map.

In spite of the difficulty in fully resolving the topology of the energy map, it allows us to explain the complex, non-monotonic response of the flow-induced flutter for the undamped $X_e^* = 0.33$ case. The map clearly shows that for $f_p^* > 0.25$ $(U^* < 4)$ the system is trapped in a lower branch of the energy map which has very small amplitude. However, as f_p^* reduces below 0.25 $(U^* > 4)$ the lower branch all but disappears. Thus for the case with $f_p^* > 0.237$ $(U^* = 4.22)$ the system finds itself in a region of positive energy growth and the amplitude grows and saturates at the first stable equilibrium along the vertical line representing its natural frequency in the map, which is about $A_\theta = 22^\circ$. Between $f_p^* = 0.22$ and 0.25, the system continues to grow to the large amplitudes as-

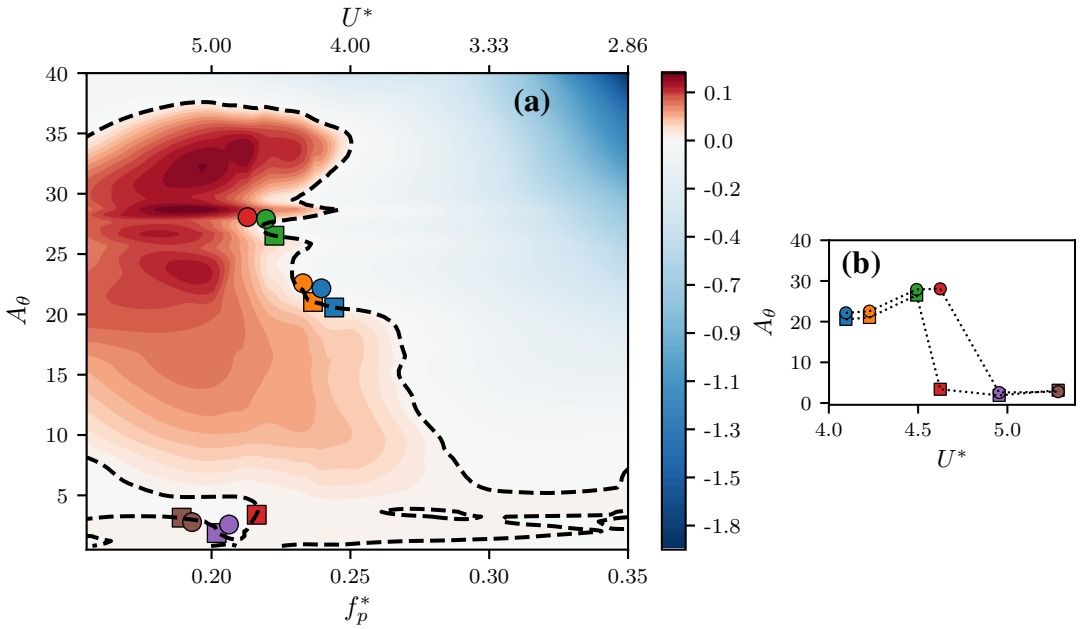

Figure 4.4: Prediction of A_θ using equation (4.6), compared with calculations from flow-induced oscillation simulations. Here, $X_e^* = 0.33$ and $\theta_0 = 15°$; (a) Stationary state amplitudes and frequencies from the model (□), and flow-induced simulations corresponding to figure 4.3 (○) plotted on the energy map; (b) Corresponding amplitudes plotted against U^* using the same symbols as in (a).

sociated with the upper equilibrium curve, however, for $f_p^* < 0.22$ ($U^* > 4.5$), a lower, stable equilibrium branch appears and the system locks on this lower branch. Hence, after the bifurcation to large amplitude oscillations at about $U^* = 4$, the amplitude of the system drops significantly ($\approx 3°$ for $U^* > 4.54$). In contrast, for the case of $X_e^* = 0.50$, there is no such lower branch in the energy map (see figure 4.2). Hence the oscillation amplitude increases monotonically along the $E_f^* = 0$ curve for that case.

Having established that the energy map indeed describes the stationary states of the flow-induced flutter system, we now demonstrate its use in mak-

ing apriori predictions of the stationary state amplitude without the need for flow simulations. This serves as a demonstration of the energy map as a predictive tool as well as a validation of our model for amplitude growth (shown in the appendix). From equation (4.6), we can calculate the amplitude growth of an oscillator at every cycle, with the knowledge of its spring stiffness and cycle-wise energy extraction. As mentioned before, this assumes that the oscillations are purely sinusoidal and occur at the natural frequency of the system. With these assumptions, we can pick the oscillation frequency of the system and predict the growth of amplitude based on the energy map and an initial condition. We iterate equation (4.6) using a semi-implicit Crank-Nicholson scheme, and the iteration is performed until a stationary state is achieved. We demonstrate this for some selected cases in figure 4.4, where we compare the amplitude response observed in flow-induced oscillations (○), with that predicted by our model (□). We see that we are able to predict the amplitude response accurately for most cases by purely using the energy map. One case however, with $U^* = 4.62$, does not agree with the model's predictions. As is apparent in figure 4.4(a), this is because the energy map computed here predicts the existence of a small amplitude stable equilibrium at this oscillation frequency. This is a result of finite resolution in computing the map, as was mentioned earlier. Furthermore, the fact that this region of the map is especially sensitive to small changes in frequency and amplitude amplifies the finite resolution effects. This

sensitivity of the energy prediction to input conditions was also observed by Leontini *et al.* [145].

4.3.2 Transient Response

The energy maps also allow us to understand the transient response of the various flow-induced flutter cases. In figure 4.5 we plot the pitching amplitude timeseries and trajectories of two cases of flow-induced flutter, where the circles represent the location of the oscillator on the frequency-amplitude space during each cycle. This is calculated by dividing the pitch response time series into individual cycles, and calculating the amplitude and timescale associated with each cycle. In the case of $U^* = 4.50$, we observe that the trajectory of the system follows a nearly vertical line on the energy map. This is because this case corresponds to the post-bifurcation regime, and the frequency is selected based on the natural frequency of the system. The system starts at rest, close to $\Delta\theta = 0$, and the amplitude grows due to the positive energy extracted from the flow. We see in figure 4.5(c) that this amplitude growth occurs until it reaches a stable equilibrium position corresponding to its oscillation frequency. However, before reaching this stationary state, the oscillator spends a long time close to a small amplitude equilibrium region, as shown by the density of circles in the zoomed-in trajectory shown in in figure 4.5(d). The effect of this is also seen in the pitch amplitude time series of this case, shown in figure 4.5(a). The system

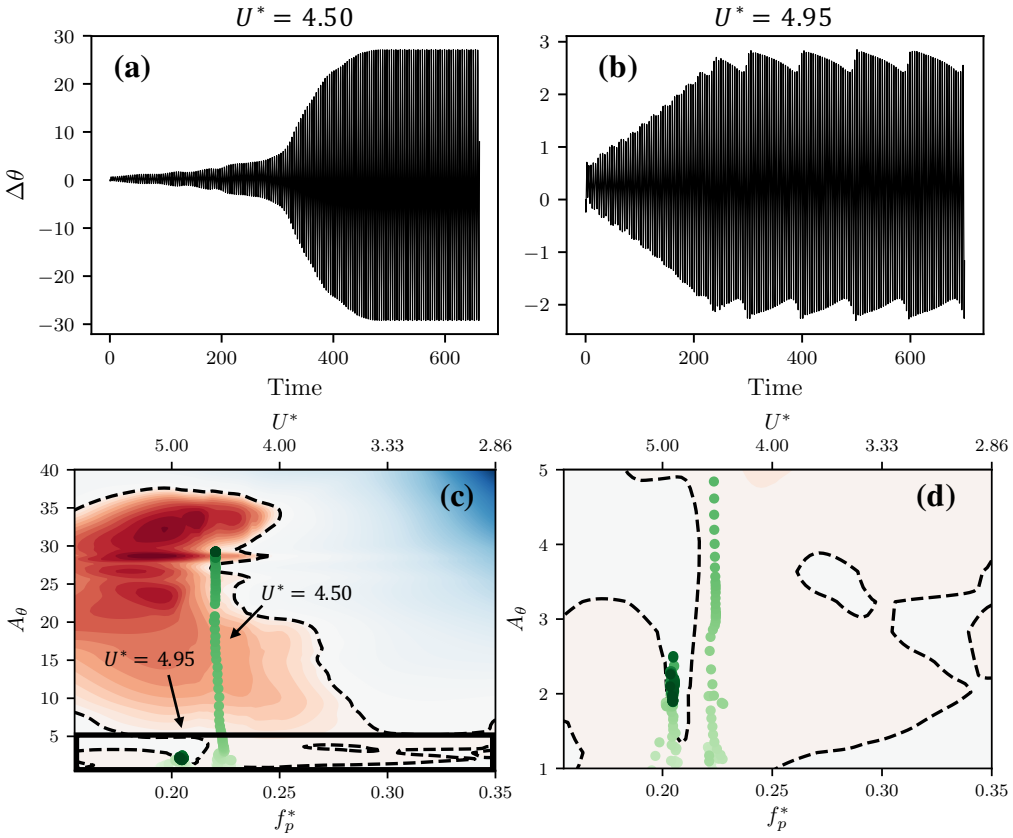

Figure 4.5: Comparison of two flow-induced oscillation cases with $U^* = 4.50$ and $U^* = 4.95$. Top panel shows timeseries of pitch oscillations for (a) $U^* = 4.50$, and (b) $U^* = 4.95$; (c) Amplitude-frequency trajectories of these cases on the energy map. Each circle represents the amplitude and frequency during one oscillation cycle. The colour intensity represents time; (d) Zoom-in of trajectories in the inset box shown in (c).

exhibits small amplitude oscillations for an extended period of time, before a sudden growth in amplitude caused by its escape from the small amplitude stable region.

On slightly increasing U^* to 4.95, the system to get trapped in the low-amplitude stable branch as seen in figure 4.5(c). Further, we see from the pitch response time series in figure 4.5(b) that the oscillation amplitude in this case

shows an interesting beating behaviour. This suggests that the oscillator is trapped in a bi-stable region that allows it to move between two stable equilibrium positions. While the exact structure of this stable region is difficult to resolve, figure 4.5(d) shows that the system gets trapped in a nearly vertical branch of $E_f^* = 0$ that would allow the existence of multiple stable regions. Further, the vertical spread of instantaneous amplitudes after the system has reached a stationary state (shown by the spread of circles) suggests that the system does indeed move between two equilibrium states. The analysis of these cases shows the utility of the energy map in analyzing the stationary state response, as well as the trajectory of the oscillator from the initial condition to the stationary state. We also see that the complicated structure of the energy map leads to interesting behaviour in the pitching response of this system, which would be very difficult to interpret without knowledge of the corresponding energy map.

The energy map also allows us to predict hysteretic behaviour due to the presence of multiple stable equilibria at particular oscillation frequencies. In figure 4.6 we show the energy map, as in figure 4.3, with additional cases that demonstrate hysteresis shown using diamond ($\diamond$) symbols. These simulations were carried out using a previously computed stationary state along the equilibrium curve as an initial condition, changing the value of U^*, and allowing the dynamics to evolve to a new stationary state. We use arrows pointing from

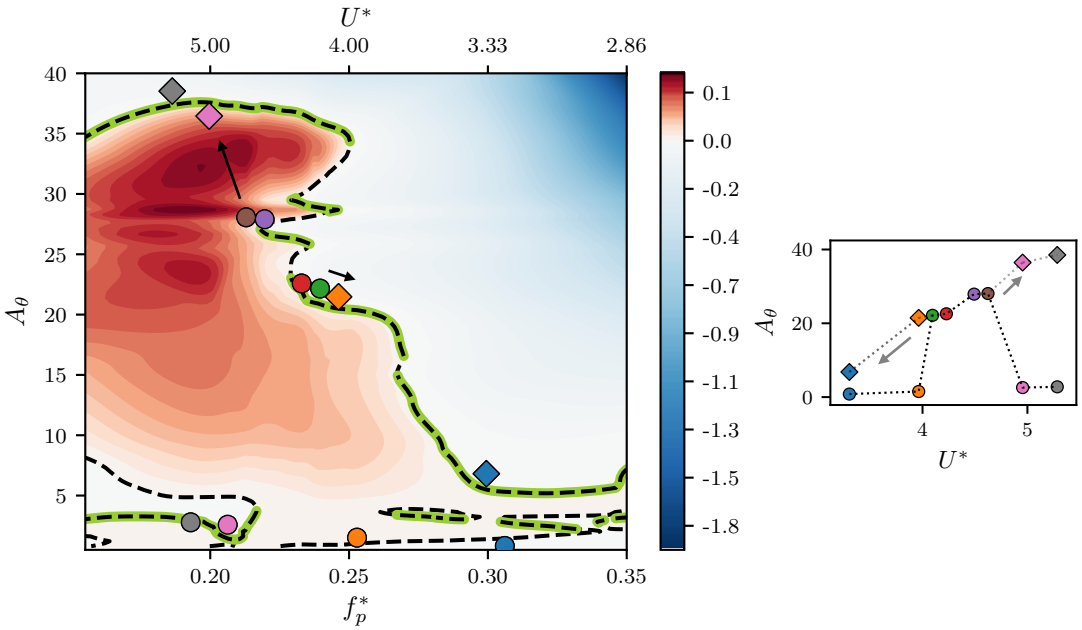

Figure 4.6: (a) Energy map for $X_e^* = 0.33$, with equilibrium curve, stable equilibria, and stationary state frequency and amplitudes as in figure 4.3. Also shown are cases demonstrating hysteresis, represented by diamonds (◇), by continuing along the directions indicated by the arrows; (b) The stationary state oscillation amplitude of all cases shown in the energy map, plotted against U^* using the same symbols.

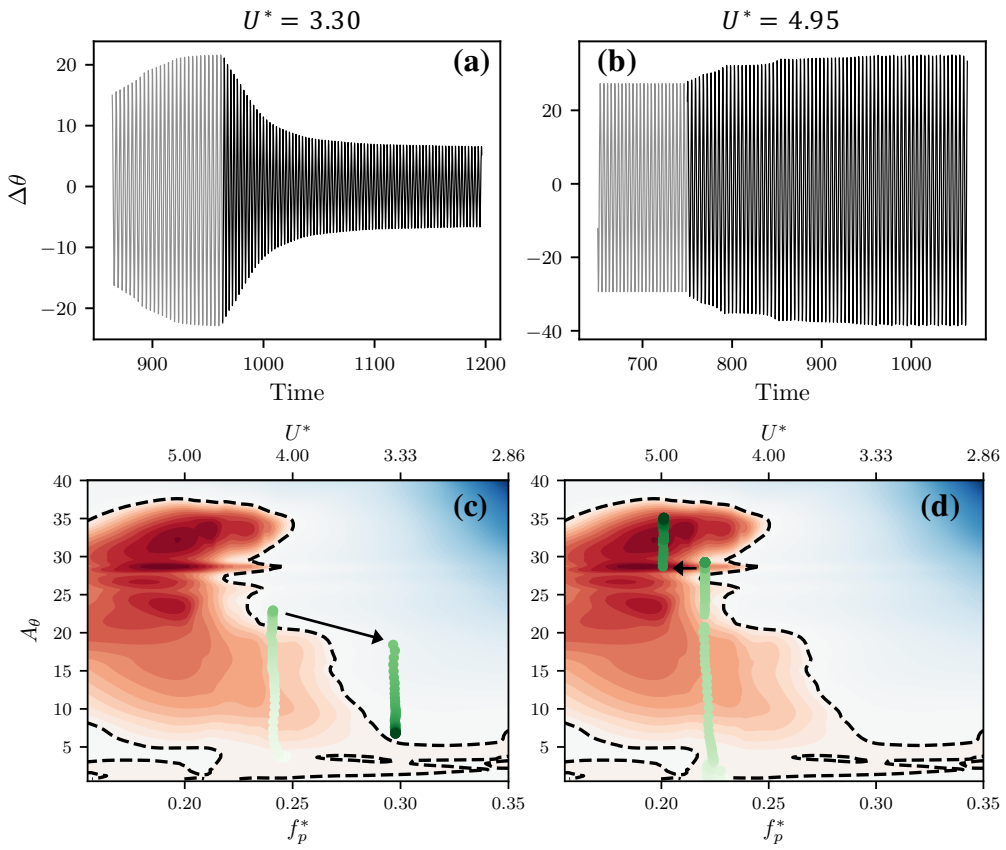

Figure 4.7: Trajectories of flow-induced oscillation cases showing hysteresis. Top panel shows timeseries of pitch oscillations for (a) $U^* = 3.30$, and (b) $U^* = 4.95$, where the lighter timeseries represents the approach to the initial state (before hysteresis) and the darker timeseries shows the evolution after the change of U^*; (c) Amplitude-frequency trajectories of the case with $U^* = 3.30$ on the energy map, where the approach to the initial condition as well as the subsequent evolution at $U^* = 3.30$ is shown; (d) Amplitude-frequency trajectories of the case with $U^* = 4.95$.

the initial to the final stationary state to denote the change in U^* in figure 4.6. We see that these cases agree with the equilibrium and stability conditions predicted by the energy map too.

The transient response of these cases is especially interesting to analyze as they also demonstrate the ability to use these energy maps in flutter amplitude control. In figure 4.7 we plot the pitching time series and trajectories of two such cases showing hysteretic behaviour with $U^* = 3.30$ and $U^* = 4.95$. Figures 4.7(a) and 4.7(b) show timeseries plots of pitching amplitude, where the grey portion represents the last few cycles of the case used as an initial condition, and the black timeseries shows the subsequent amplitude response leading to the new stationary state. In figures 4.7(c) and 4.7(d) we show the trajectories of these cases where the circles show the state of the system on the frequency-amplitude space during each oscillation cycle. Here we show the trajectory leading up to the stationary state that is used as an initial condition, as well as the trajectory from the previous stationary state to the new one. The change in U^* is indicated by the arrow.

For $U^* = 3.30$, the case using the static initial condition shows very small amplitude oscillations ($A_\theta < 1°$) as seen in figure 3.9(b) and is described by the pre-bifurcation regime on section 3.3. However, when initialized with an oscillation amplitude $\sim 25°$, we see that it reaches a stationary state amplitude of roughly $10°$. This new stationary state is achieved through a loss of energy,

which is different from all the cases analyzed in this paper so far. The loss of energy is a consequence of the fact that the initial amplitude of oscillation, which corresponds to a stable equilibrium at a different natural frequency, is in a region of negative energy transfer at the natural frequency corresponding to $U^* = 3.30$. This results in a reduction in amplitude of oscillation as described by equation (4.7), until it reaches a new stable equilibrium. This is an example of the ability to reduce the amplitude of flutter using a knowledge of the energy map.

The case of $U^* = 4.95$ shows a case that is initialized using a stationary state on one portion of the equilibrium curve, and ends up on higher-amplitude portion of the curve on changing its natural frequency. This occurs as the change in natural frequency pushes the system into a region of positive energy transfer, as indicated by the arrow in figure 4.7(d). Due to continuous extraction of energy from the flow, the amplitude grows until it reaches a new stable equilibrium. It must be noted that this is the same U^* value shown in the right-side pane of figure 4.5, where the static initial condition was used.

With these above examples we have been able to demonstrate the use of the idea of an energy map to analyze the dynamics of the flow-induced oscillator apriori, based on our knowledge of the frequency selection mechanism. We have also been able to explain the bizarre non-monotonic amplitude response seen in the case of $X_e^* = 0.33$ using this tool.

4.4 Conclusions

The objectives of this chapter were to demonstrate the use of the energy exchange between the fluid and the structure as a way to analyze the flutter behavior and its dependence on various parameters such as spring stiffness, elastic axis location and mean angle-of-attack. We demonstrated the use of "energy maps", as an analytical tool to analyze the complex flow-induced flutter response of the airfoil. Energy maps are generated by computing the rate of energy exchange between the airfoil and the flow for airfoils undergoing prescribed pitch flutter over a range of amplitude and frequencies. The topology of the energy maps changes significantly with the location of the elastic-axis and we show that the energy maps provide a very effective means for interpreting complex behavior such as non-monotonic saturation amplitudes, hysteresis, subcritical and supercritical bifurcations, and complex limit-cycle behavior. Furthermore, we show that a simple mathematical model based on the energy maps can even predict the saturation amplitude without the need for flow-induced flutter simulation.

The results described in this chapter have been published in reference [77].

Chapter 5

Energy maps in the prediction and control of gust-induced aeroelastic oscillations

Having established the utility of energy maps in analyzing and predicting the stationary-state and transient response of flow-induced oscillations, we now turn our attention to their use in the prediction and control of the response of these systems to gusts and other angle of attack perturbations. The aeroelastic response of wings to incoming gusts has been studied for many years, however most past studies have exclusively focused on the transient force/moment perturbations that are induced on wings during gust encounters [33–42]. There have been far fewer investigations of the aeroelastic oscilla-

tion response of these wings as a result of such perturbations. The studies that have performed such analyses have generally employed various simplifications such as the use of simplified force models and/or the assumption of small amplitude oscillations [41,43–49]. While such assumptions have been shown to be reasonable in aerospace applications, they generally ignore the non-linearities that are inherent in the flow physics of finite amplitude oscillations that are relevant in applications such as energy harvesting.

In this chapter we discuss the gust response of the aeroelastic pitching airfoil system analyzed in previous chapters. The focus is on the use of energy maps in predicting, and possibly enabling control of the response of an aeroelastically pitching airfoil to incoming gusts. This is based on the fact that, as demonstrated in chapter 4, energy map allows us to identify all possible limit cycle response branches (i.e. the "manifold") of an aeroelastic system for a given range of kinematic and structural parameters. This can therefore be used to predict the response of such systems when they are pushed out of equilibrium by perturbations such as gusts. We illustrate this using various examples of airfoil-gust encounters, each highlighting different aspects of the utility of energy maps in such analyses.

5.1 Model for aeroelastic gust interaction

For this analysis, we use the two-dimensional aeroelastic model for flow-induced pitching oscillations of a NACA0015 airfoil that was introduced in section 2.2.1. The elastic model cosists of an airfoil that is free to pitch about its elastic axis location X_e^* (defined in section 2.2.1) and is attached to a torsional spring at X_e^*. This elastic system is governed by equation (2.2) and is immersed in an incompressible fluid flow.

The interaction of this system with an incoming gust is modelled as a time-varying perturbation to the incoming freestream flow using the so-called far-field boundary condition method (FBC). This is implemented as a time-varying vertical velocity of a prescribed strength and duration at the upstream boundary of the computational domain. In spite of limitations of this method [38–40], we use this method here due to its simplicity and ease of implementation. Furthermore, as noted previously, the focus of this work is to demonstrate the use of energy maps in predicting the aeroelastic response to general gusts and gust-like perturbations and the simple gust model is sufficient for this purpose.

The prescribed boundary condition at the upstream boundary takes the shape of a top-hat profile. As expected, diffusive effects upstream of the airfoil smoothen this imposed profile, hence the amplitude and duration of the

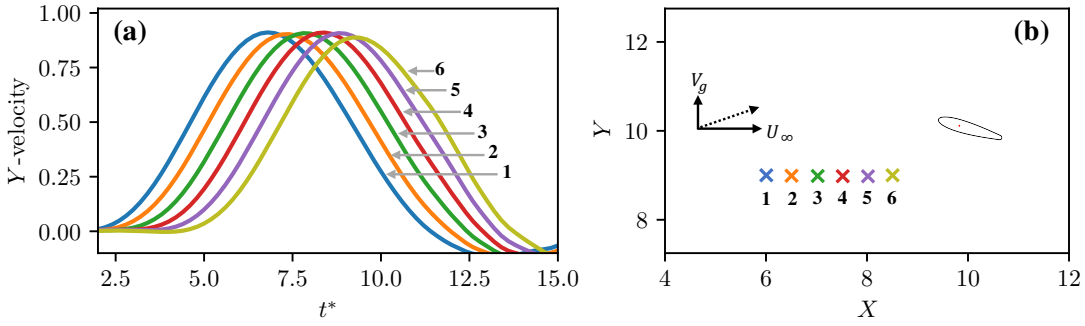

Figure 5.1: (a) The profile of the incoming gust at 6 locations upstream of the airfoil, plotted as a time-series of vertical fluid velocity (Y-velocity) versus time; (b) Schematic showing the locations of the probe points at which Y-velocity is plotted in (a). The points are equally spaced from $X = 6.0$ to $X = 8.5$, with $Y = 9.0$ for all points. The position of the airfoil is $X = 10$, $Y = 10$.

top-hat profile are determined iteratively so as to obtain the required gust profile a short distance downstream of the boundary. The resulting gust profile upstream of the airfoil takes an approximately sine-squared shape, which is quite commonly used in existing literature. The gust can therefore be approximated at a given stream-wise location as a travelling perturbation with a profile $v^* \approx V_g \sin^2(\pi t^*/T_g^*)$, which is defined for the time-interval $0 < (t^* - T_0^*) < T_g^*$. Here T_g^* is the dimensionless timescale of the gust, V_g is the maximum vertical velocity in the gust, and T_0^* is the time-instance at which the gust is incident at the particular stream-wise location. The spatio-temporal evolution this perturbation is shown in figure 5.1(a) for a case with $V_g = 0.9$, where the vertical velocity versus time at 6 upstream locations in the flow domain is plotted. The locations of the velocity probes in relation to the position of the airfoil is shown in figure 5.1(b). Despite the effect of diffusion, we see that the gust profile is

advected accurately for a considerable length in the regions upstream of the airfoil. Figure 5.1 shows this for a length $2.5C$ upstream of the airfoil ($X = 6.0$ to $X = 8.5$), but we have verified that this is true as far as $6C$ upstream of the leading edge of the airfoil. Hence the profile incident on the airfoil is practically unaffected by dissipation in this immediate upstream region, and we can report our results with respect to this profile.

For the cases analyzed in this work, $T_g \approx 10$ (from fitting to a sine-squared profile), and the corresponding length of the gust, $L_g = T_g U_\infty \approx 10$. The scale of the gust is hence much larger than the chord. The strength of the gust is reported in terms of an induced gust angle-of-attack, $\alpha_g = \arctan(V_g/U_\infty)$, where V_g, the peak velocity in the gust profiles shown in figure 5.1(a), is a parameter of interest. This is measured at the location $X = 8$, $Y = 9$ where figure 5.1(a) shows that the profile is well captured and upstream diffusive effects are no longer significant. This location is also chosen to ensure that the measured profile is not affected by the proximity to the airfoil.

For all the cases discussed here, simulations are initialized with the airfoil at its equilibrium angle, $\theta_0 = 15^\circ$, and zero angular velocity. The torsional spring is undamped, i.e $b^* = 0$ in equation (2.2). The Reynolds number is fixed at $Re = 1000$. The freestream velocity, U_∞, is prescribed at the upstream boundary of the domain, and a vertical velocity is added to this upstream boundary condition for a fixed duration. This corresponds to a gust of length $L_g \approx 10$,

as shown in figure 5.1, and angle α_g. For simplicity, this gust perturbation is prescribed early enough in the simulation to ensure that the amplitude of the airfoil's oscillation is small and therefore, its phase at the instant of the gust encounter can be ignored. Subsequently, the dynamics are allowed to evolve until a stationary state is attained.

5.2 Predicting gust-induced aeroelastic flutter

We begin with a discussion of the flutter response of two airfoils with the same structural (elastic) properties, but encountering gusts of different magnitudes. The natural frequency of the elastic systems under consideration is fixed at $f_s^* = 0.19$, which corresponds to a $U* = 5.26$, and the elastic axis is at $X_e^* = 0.33$. The incoming gust angles are $\alpha_g = 24.5^\circ$ and $\alpha_g = 42^\circ$. In figure 5.2 we show snapshots of the flow at a few time instances during and after the wing-gust interaction for one of these cases, with $\alpha_g = 42^\circ$. The flow in these snapshots is represented by contours of Z-vorticity (normal to the plane of the paper). On the right-pane of figure 5.2 we also show the coefficient of pitching moment experienced by the airfoil during the gust encounter for this case. Further, the pitch deflection corresponding to the time instance at each snapshots is shown in figures 5.3(b) and 5.4(b), which are plots of the pitch

deflection time-series for this case. Figure 5.2(i) shows a snapshot of the flow before the gust interaction, where the airfoil is at angle $\theta \approx 15^{\circ}$, and we see the development of a von Karman vortex street in the wake. On initially encountering the gust, the airfoil experiences large-scale flow separation on the suction side, as seen in figure 5.2(ii). This is accompanied by the generation of a large moment transient, seen at time-instance (ii) in the plot of pitching moment, which induces an initial pitch deflection that drives the ensuing dynamics. We show snapshots of this initial deflection at the maximum pitch-down position in figure 5.2(iii) and at the maximum pitch-up position in figure 5.2(iv). The corresponding pitch deflections can be seen in figure 5.4(b), at the time-instances marked as (iii) and (iv), and is measured to be $\Delta\theta \approx 6^{\circ}$. The gust then advects downstream of the airfoil as the pitching dynamics continue to evolve. In the case being discussed here, the initial pitch deflection leads to further growth in the oscillation amplitude, which is shown in figures 5.2(v) and 5.2(vi). We see from figure 5.3(b) that the amplitude of pitch oscillation is $\Delta\theta \approx 15^{\circ}$ during the oscillation cycle shown at time-instance (v). The oscillations are eventually seen to approach a limit-cycle, as shown at time instance (vi) in figure 5.3(b), the amplitude of which is $\Delta\theta \approx 35^{\circ}$. Hence we see that even this simplified aeroelastic model is capable of showing large-amplitude limit-cycle oscillations. Further, the flow physics is influenced by large regions of separated flow, which precludes the use of linear aerodynamic models at these

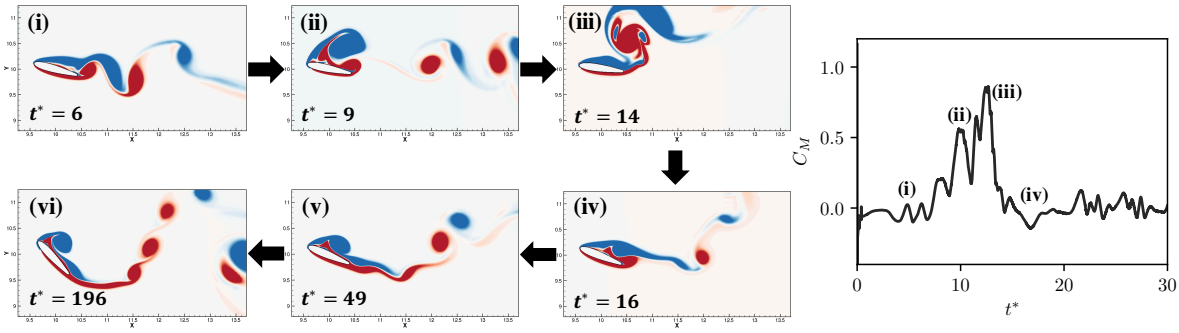

Figure 5.2: For an airfoil encountering a gust of strength $\alpha_g = 42°$, and oscillating about $X_e^* = 0.33$ with frequency $f_n^* = 0.19$, (i)-(vi) show snapshots of the flow-field using contours of vorticity, at various time instances during and after the airfoil-gust encounter. Right pane shows the time-series of moment coefficient, with time-instances corresponding to snapshots marked as (i)-(iv). The corresponding time-series of pitch angle for this case is shown in figures 5.3(b) and 5.4(b), with time-instances corresponding to the snapshots marked as (i)-(vi).

low Reynolds numbers.

Figure 5.3 shows time-series plots of the pitch deflection, $\Delta\theta$, for these cases with $f_n^* = 0.19$ and gust strengths $\alpha_g = 24.5°$ and $\alpha_g = 42°$. We see for the case of $\alpha_g = 24.5°$ that the gust induces an initial pitch-up deflection of $\Delta\theta \approx 4°$, after which the airfoil settles into limit cycle oscillations of amplitude $\Delta\theta \approx 3°$. For the case with $\alpha_g = 42°$, which represents a gust that is almost $2\times$ stronger, we see a very different behaviour. After the initial deflection of $\Delta\theta \approx 7°$, the amplitude of oscillation grows very rapidly to a stationary state of $\Delta\theta \approx 37°$. Hence gusts that differ by a factor of $2\times$ in strength cause stationary state oscillation amplitudes that differ by $> 10\times$. This highlights the inherent non-linearity in the system, despite the linearity of the underlying dynamical

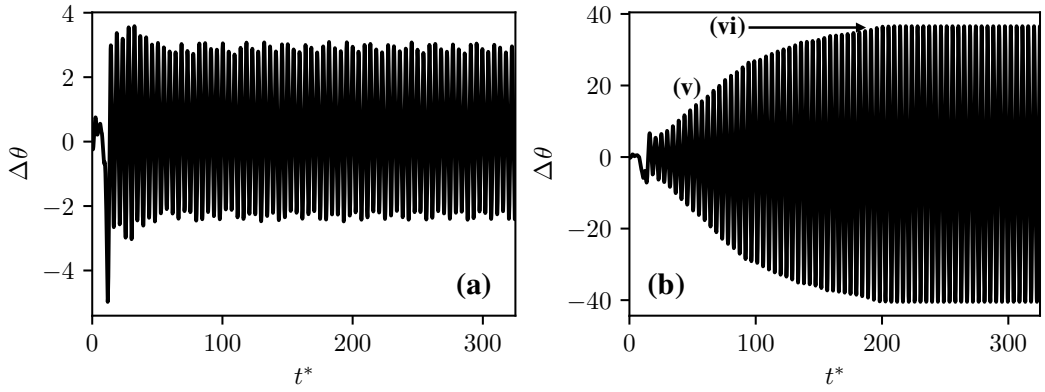

Figure 5.3: Time-series plots of pitch angle for two airfoils with $f_n^* = 0.19$ and $X_e^* = 0.33$, encountering gusts of different strengths. (a) $\alpha_g = 24.5°$; (b) $\alpha_g = 42°$. The time-instances corresponding to snapshots in figures 5.2(v) and 5.2(vi) are shown in (b).

model.

In spite of the order-of-magnitude difference in the stationary state oscillation amplitudes for these cases, the initial pitch deflection induced by the gust shows much less variation. Figure 5.4 shows the time-series of pitch angle plots for the cases with $\alpha_g = 24.5°$ and $\alpha_g = 42°$, focusing on the initial deflection for each case. We measure the peak initial deflection in each of these cases to be $\Delta\theta = 4.98°$ and $\Delta\theta = 5.85°$ for $\alpha_g = 24.5°$ and $\alpha_g = 42°$ respectively. This suggests that a different, and possibly simpler, mechanism governs this initial deflection. Since the length-scale of the gust is much larger than the chord of the airfoil, it is reasonable to assume that the initial force and moment transient due to the gust can be approximated in a quasi-steady manner. Hence we expect that the initial pitch deflection should be governed by the pitching moment generated on an airfoil at a steady apparent angle of at-

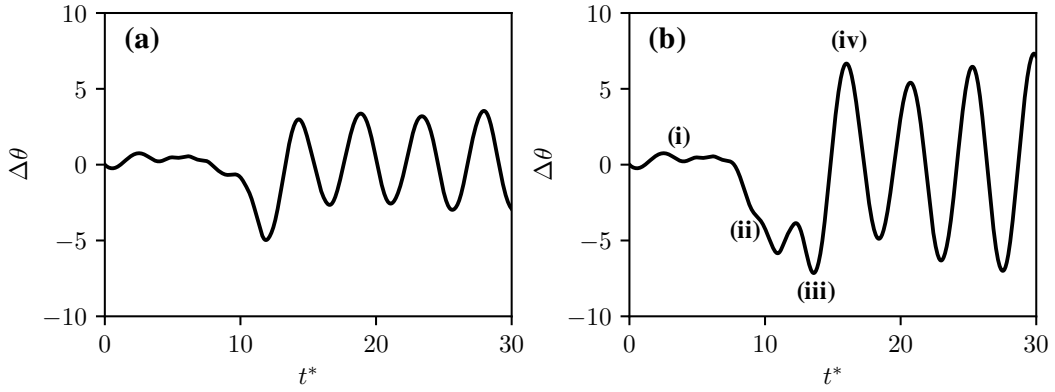

Figure 5.4: (a) Zoom-in of the time-series plots in figure 5.3, focusing on the initial pitch-deflection induced by the gust. The parameters for these cases are the same as in figure 5.3, i.e., $f_n^* = 0.19$, $X_e^* = 0.33$, and gust strengths given by (a) $\alpha_g = 24.5°$; (b) $\alpha_g = 42°$. The time-instances corresponding to snapshots in figures 5.2(i)-(iv) are shown in (b).

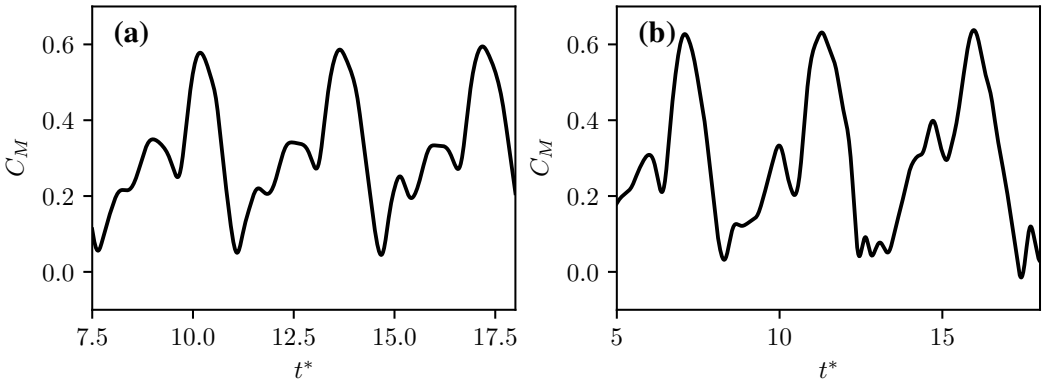

Figure 5.5: Coefficient of moment about $X_e^* = 0.33$, on airfoils at two static angles of attack given by (a) $\theta_s = 39.5°$; (b) $\theta_s = 57°$. Here $\theta_s = \theta_0 + \alpha_g$ is the equivalent quasi-steady angle experienced during the initial gust encounter, for an airfoil at equilibrium angle θ_0 and encountering a gust of strength α_g.

tack given by $\theta_s = \theta_0 + \alpha_g$. For two cases considered here, with $\alpha_g = 24.5^\circ$ and $\alpha_g = 42^\circ$, the resulting steady angles of attack are $\theta_s = 15^\circ + 24.5^\circ = 39.5^\circ$ and $\theta_s = 15^\circ + 42^\circ = 57^\circ$ respectively. In figure 5.5 we show C_M time-series plots at these steady angles θ_s, for the same airfoil used in this study. Here C_M is calculated about a location at 33% of the chord. From this data, we can extract the peak C_M at each θ_s, which we refer to as C'_M. The value of C'_M at $\theta_s = 39.5^\circ$ and $\theta_s = 57^\circ$ are $C'_M = 0.57$ and $C'_M = 0.63$ respectively. For airfoils with elastic stiffness k^*, the initial pitch deflection induced by the gust is expected to be given by $\Delta\theta' = C'_M/k^*$. As mentioned earlier, both these cases have the same elastic properties, with $k^* = 0.1054$. Hence $\Delta\theta'$, based on the quasi-steady assumption, comes out to be $\Delta\theta' = 5.41^\circ$ and $\Delta\theta' = 5.95$ respectively. We note that this is close to the observed values of initial deflection, $\Delta\theta = 4.98^\circ$ and $\Delta\theta = 5.85^\circ$, which confirms the validity of this quasi-steady assumption. As mentioned in the Introduction, a similar finding was made by Perrota & Jones [35] who showed via experiments that the initial lift-force transient was given by the force on a steady wing at an angle of attack given by θ_s.

We now move on to analyzing the final stationary state of the system that results from the interaction with the gust. In this work, as in the work of Menon & Mittal [77], the current state is determined by the amplitude and frequency of the current oscillation cycle and the initial state is determined by the initial deflection induced by the gust. The energy map shows the energy

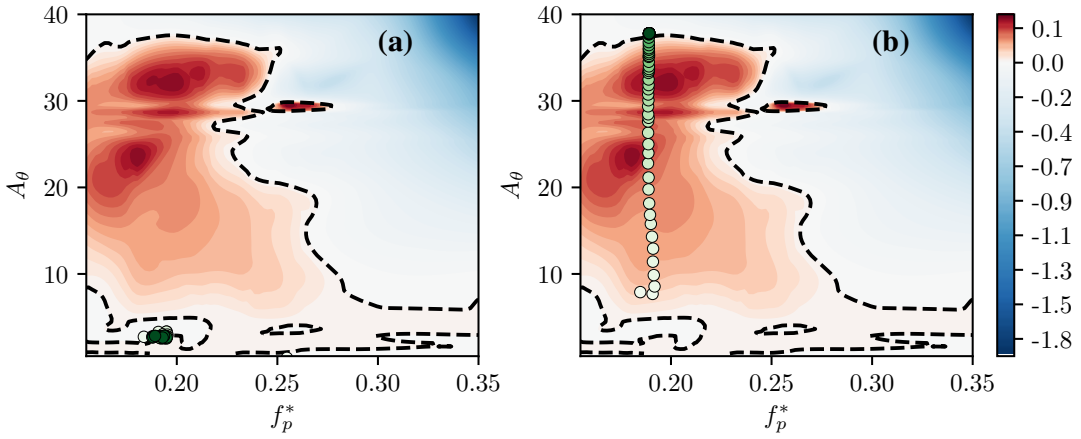

Figure 5.6: (a) Frequency-amplitude trajectories for two cases with different gust strengths, plotted on the energy map for $X_e^* = 0.33$. The trajectories, shown using circles, represent the evolution of the pitching dynamics for each case. The circles represent the cycle-averaged frequency and amplitude at every oscillation cycle. The darkness of the circles represent time, i.e., the darker circles represent the dynamics at later times in the system's evolution. The structural properties of the airfoils in these cases are $f_n^* = 0.19$ and $X_e^* = 0.33$. The gust strengths are (a) $\alpha_g = 24.5°$; (b) $\alpha_g = 42°$.

extraction for the airfoil, E^*, at each state. When the system is at a state with $E^* \neq 0$, the amplitude of oscillation is expected to amplify or decay (as per the sign of E^*) until the system reaches a stable equilibrium. Based on this, and given the initial deflection induced by a gust (or a gust-like perturbation), we expect to be able to use the energy map to predict the final stationary state of the system. We first verify these ideas in the context of the gust response by comparing the observed response with the energy map-based predictions. The energy map used here is essentially the same as that presented by Menon & Mittal [77], except that the resolution of this plot has been improved by adding more simulation data.

In figure 5.6 we plot the energy map for an airfoil pitching about $X_e^* = 0.33$, with equilibrium angle of attack $\theta_0 = 15°$, and at $Re = 1000$. Overlaid on the energy map, is the cycle-averaged oscillation amplitude (maximum pitch angle in every cycle) and frequency for the cases with $\alpha_g = 24.5°$ and $\alpha_g = 42°$ as circles. Time is represented by the darkness of the circle, with darker circles representing the state of the system at later times. We refer to this as the frequency-amplitude trajectory of the system. For the case of $\alpha_g = 24.5°$ in figure 5.6(a), we see that the system settles into a stationary state in the stable region of the lower $E^* = 0$ curve. This is due to the fact that the initial deflection caused by the gust is small enough that the system starts off within the region of negative energy extraction. Therefore the amplitude decays from that initial point to the lower stable equilibrium. On the other hand, the $\alpha_g = 42°$ gust causes an initial deflection that is just large enough to push the system into the $E^* > 0$ region above $A_\theta \approx 5°$. Due to this, the system continues to extract energy and increase in amplitude of oscillation, until it meets the stable equilibrium boundary at $A_\theta \approx 37°$. Thus, the energy map allows us to explain why a $2\times$ difference in α_g leads to a $10\times$ increase in the oscillation amplitude.

5.3 Tailoring the gust response: Structural frequency

The topology of the energy map can also be used to design a system that is robust to specific gust perturbations. As an example, here we demonstrate how a small change in the structural properties of the system described earlier can reduce the stationary state amplitude of the system by a disproportionate amount. By examining the energy map for $X_e^* = 0.33$ (see figure 5.6), we see that for $f_p^* \lessapprox 0.16$ the region of negative energy extraction in the low-amplitude region extends to larger A_θ values than at $f_p^* = 0.19$. Hence the energy map suggests that reducing the natural frequency of the system from $f_n^* = 0.19$ to 0.16 should "trap" the system in this lower "island" of negative energy transfer. In order to verify this, we test a system with natural frequency $f_n^* = 0.16$, oscillating about $X_e^* = 0.33$, encountering the stronger gust case from the preceding discussion (i.e. $\alpha_g = 42°$).

In figure 5.7(a) we plot the time-series of pitch angle for this case and we see that the system settles into stationary state oscillations of $\Delta\theta \approx 6°$. As expected, the stationary state amplitude observed is much smaller than the $\Delta\theta \approx 35°$ seen for the case with $f_n^* = 0.19$. In figure 5.7(b) we focus on the initial deflection of the system after interaction with the gust. As we did for the previous discussion, we can verify the quasi-steady assumption made in

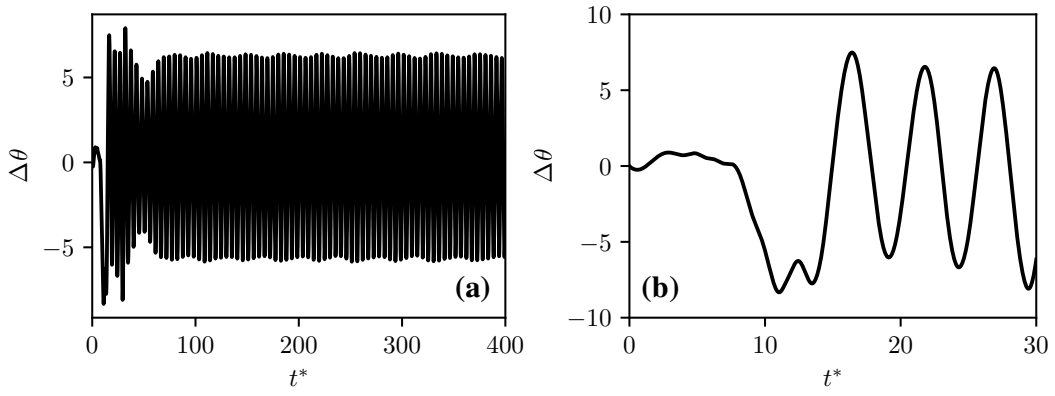

Figure 5.7: (a) Time-series of pitch angle for a system with $f_n^* = 0.16$, $X_e^* = 0.33$, and interacting with a gust of strength $\alpha_g = 42°$; (b) Zoom-in of the time-series in (a), focusing on the initial deflection induced by the gust.

predicting the amplitude of the initial deflection. Since the angle of the gust is $\alpha_g = 42°$, this corresponds to a steady angle of attack of $\theta_s = 57°$. The moment time-series for this steady airfoil was shown previously in figure 5.5(b), and the peak moment for the steady airfoil is $C'_M = 0.63$. Since I^* is kept fixed throughout this study, the change in f_n^* corresponds to changing k^*. For this case, $k^* = 0.0754$ and hence the predicted initial deflection is $\Delta\theta' = 8.32°$. Comparing this to the actual measured deflection of $\Delta\theta = 8.33°$, we see that the quasi-steady assumption can again be verified.

In figure 5.8(a) we plot the frequency-amplitude trajectory for the system on the energy map, and a zoomed-in version of this trajectory is plotted in figure 5.8(b). These figures explain why the system with $f_n^* = 0.16$ does not grow to large amplitude oscillations, and shows that the behaviour agrees with what was expected from the change in f_n^*. Specifically, the fact that the re-

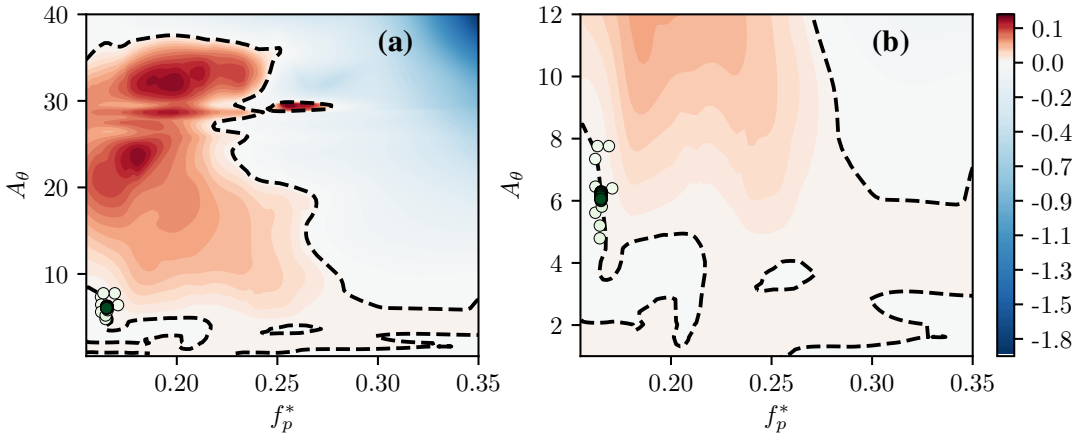

Figure 5.8: (a) Frequency-amplitude trajectory plotted on the energy map (for details, see caption under figure 5.6), for a case with $f_n^* = 0.16$, $X_e^* = 0.33$, and $\alpha_g = 42°$; (b) Zoom-in of the trajectory plotted in (a), showing the system settling on a region of neutral stability (represented by the nearly-vertical equilibrium curve).

gion of $E^* < 0$ extends to larger values of A_θ at this natural frequency causes the amplitude after the initial deflection to stay within this region instead of growing. Interestingly, as seen in figure 5.8(b) the system does not settle into a stable equilibrium in this case but gets trapped on a neutrally stable segment of the $E^* = 0$ curve. As mentioned in section 4.1 chapter 4, the stability of an equilibrium is given by the sign of dE^*/dA_θ [27, 77]. A region of $dE^*/dA_\theta = 0$ corresponds to neutral stability, where small changes in the oscillation amplitude do not change the sign of E^*, and hence do not change the stability of the system. Such a region manifests itself as a vertical contour line of $E^* = 0$ on the energy map. Due to this, as seen in the frequency-amplitude trajectory in figure 5.8(b), the system is able to show small variations in oscillation amplitude while remaining at an equilibrium.

The simulations therefore show that a change of approximately 16% in f_n^* lead to a reduction of about 86% in the flutter amplitude. The simulations also demonstrate how the energy map for a given configuration can inform design changes or control strategies for aeroelastic systems. In this demonstration, we focused on the reduction in flutter amplitude by decreasing the f_n^*, but the same demonstration also works in reverse, i.e. to show how the flutter amplitude could be *increased* (for instance, in energy harvesting applications) by changing the structural attributes of the system. Note that changes in f_n^* can, in principle be achieved by changing I^*, which could be implemented via changes in mass distribution, and/or k^*, which could be implemented with the use of smart materials or other such means.

5.4 Gust-induced flutter below the critical flutter speed

The energy map also allows us to predict when a gust will destabilise an aeroelastic control surface that is operating below the critical flutter speed. The critical flutter speed, is a key feature in the aero-structural design of aerodynamic control surfaces in air-vehicles [146]. The critical flutter speed is however conventionally determined under the assumption of an infinitesimal perturbation and the analysis employs linear methods. The effect of a finite-size

perturbation, which could lead to non-linearity in the response, is therefore not addressed in these analyses. The source of such non-linearity as a result of finite-size perturbations can be either structural or aerodynamic. In the presence of structural non-linearities, such gust-induced subcritical behaviour has been reported by Dessi & Mastroddi [147] and Sarkar & Bijil [148]. In the context of energy maps, the possibility of non-linear subcritical responses due to aerodynamic non-linearities is indicated by the presence of multiple stable equilibrium response branches at a given frequency. For a system operating in a stable state below the flutter boundary, a finite perturbation can push the system towards another response branch at a higher A_θ via a subcritical instability. Here we demonstrate this for a case with $f_n^* = 0.30$.

Menon & Mittal [77] showed a phenomenological condition for the onset of flutter, and showed that the flutter boundary in terms of frequency is at $f_n^* \approx 0.25$ for the system being studied here. The flutter boundary is often expressed in terms of a critical reduced velocity ($U^* = 1/f_n^*$), which for $f_n^* \approx 0.25$, corresponds to $U^* \approx 4$. The energy map for this system, plotted in figures 5.6 and 5.8, also shows a flutter boundary at $U^* \approx 3.8$ which is indicated approximately by the intersection of a negative energy extraction region with the x-axis at $f_p^* \approx 0.25$. Hence an aeroelastic system with $f_n^* = 0.30$ lies on the "linearly stable" side of the flutter boundary. To demonstrate the subcritical response of the "linearly stable" system oscillating with $f_n^* = 0.30$ about $X_e^* = 0.33$,

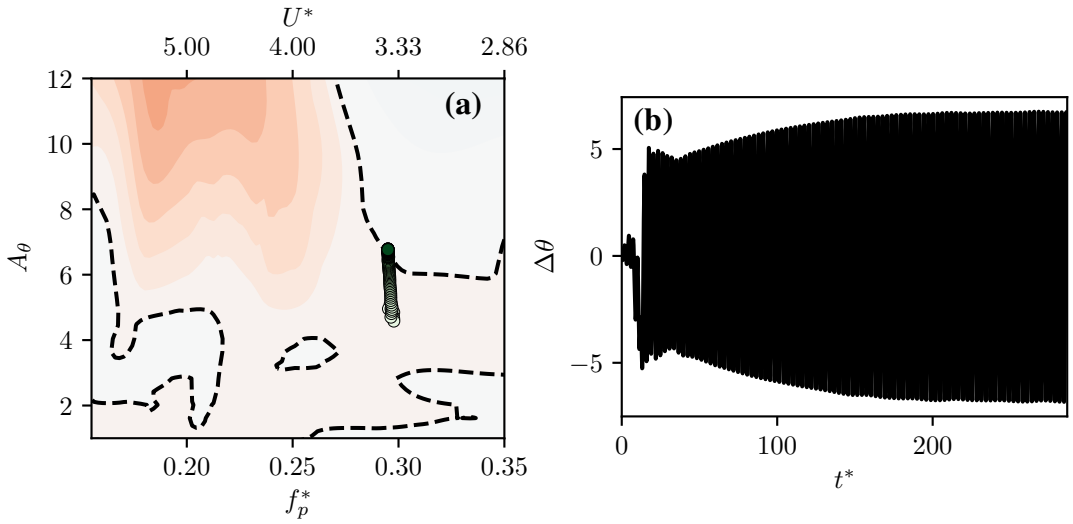

Figure 5.9: (a) Trajectory on the frequency-amplitude space for a system with $f_n^* = 0.30$, oscillating about $X_e^* = 0.33$, and interacting with a gust of strength $\alpha_g = 51°$. The trajectory is plotted on a zoom-in of the energy map as in figure 5.8(b). For details about the trajectory, see caption under figure 5.6; (b) Time-series of pitch angle for the same case as in (a).

the airfoil is subjected to an oncoming gust of strength $\alpha_g = 51°$. Figures 5.9(a) and 5.9(b) show the subsequent response of the system on the energy map as well as the time series of pitch deflection. In order to highlight why a subcritical response is expected in this system, figure 5.9(a) shows the trajectory of the system on the energy map. As we can see, at $f_n^* = 0.30$ there exists a region of negative energy extraction at very small amplitude ($A_\theta \lessapprox 3°$) along with a subcritical stable equilibrium branch at a larger amplitude of $A_\theta \approx 7°$. The gust perturbation of $\alpha_g = 51°$ generates an initial pitch perturbation of about $\Delta\theta = 3°$ degrees (quasi-steady analysis predicts a pitch excursion of $2.4°$) and this relatively small perturbation is sufficient to push the system past the region of stability. The system then finds itself in a state with $E^* > 0$, due to

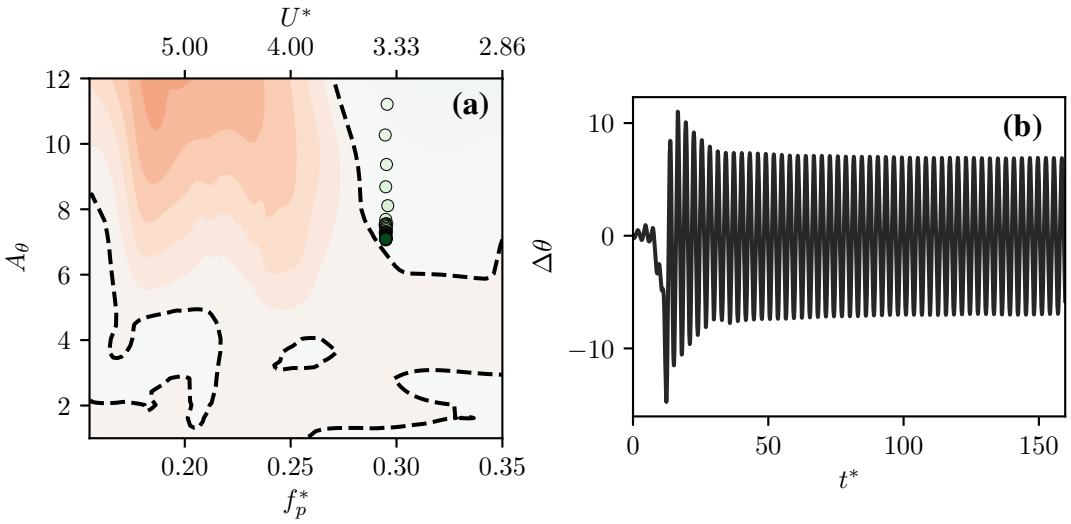

Figure 5.10: (a) Frequency-amplitude trajectory plotted on the energy map, for an airfoil with $f_n^* = 0.30$, oscillating about $X_e^* = 0.33$, and interacting with a gust of strength $\alpha_g = 61°$. For details about the trajectory, see caption under figure 5.6; (b) Time-series of pitch angle for the same case as in (a).

which the amplitude grows until it reaches the stable equilibrium at $A_\theta \approx 7°$. As can be seen in the time series plot in figure 5.9(b), the amplitude growth of $\Delta\theta \approx 7°$ occurs slower in this system than in the others analyzed thus far, due to the fact that there are multiple equilibrium branches in the vicinity of this frequency, and the energy extraction (E^*) is hence small. The fact that long integration times are necessary to compute stationary state responses in flow-induced oscillation systems highlights another advantage of using forced oscillations and energy-based analysis of these systems.

We now demonstrate the robustness of this method in predicting the response to even larger perturbations in this subcritical regime. The system described above, with $f_n^* = 0.30$, oscillating about $X_e^* = 0.33$, is subjected to

a larger gust of strength $\alpha_g = 61°$, and figure 5.10 shows the subsequent response of the system. With this gust, figure 5.10(a) shows that the system is in fact pushed beyond the upper stable branch, and into a region of negative energy extraction. As expected due to the fact that $E^* < 0$, pitch oscillation subsequently decays until the system attains a limit-cycle state with $\Delta\theta \approx 7\circ$. In figure 5.10(b) we show the time-series of pitch angle for this case. It must be noted that an amplitude of $\Delta\theta \approx 7°$ observed in the two cases discussed on this section might be considered excessive for an air-vehicle. In this context, the current analysis shows that a system operating below the flutter boundary could be destabilized by a gust. Further, it is particularly striking that the angular perturbation required for this destabilization could be as small as $\Delta\theta \approx 3°$. On the other hand, for energy harvesting applications, this knowledge could be beneficial in generating large sustained oscillations even in conditions where the system is stationed below the flutter boundary.

5.5 Tailoring the gust response: Elastic axis location

We now demonstrate a different strategy for controlling the subcritical response of the system. All the cases discussed thus far in this work have been airfoils oscillating about $X_e^* = 0.33$. However, Menon & Mittal [77] showed that

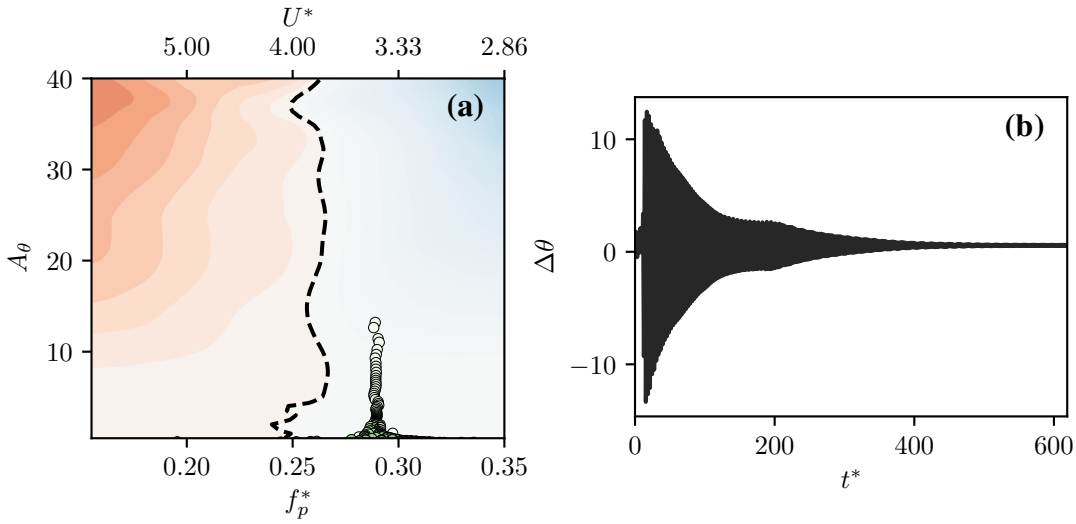

Figure 5.11: (a) Trajectory in frequency-amplitude space for a case with $X_e^* = 0.50$ (all previous cases discussed have $X_e^* = 0.33$), plotted on the energy map corresponding to $X_e^* = 0.50$. The natural frequency and gust strength for this case are the same as that in figure 5.10, i.e., $f_n^* = 0.30$ and $\alpha_g = 61°$. For details about the trajectory, see caption under figure 5.6 (b) Time-series of pitch angle for the same system as in (a).

a relatively small change in X_e^* can have a large effect on the topology of the energy map. In particular, the energy map for an airfoil pitching about $X_e^* = 0.50$ was studied in that work. Here we aim to leverage this change in topology of the energy map to drive the system to a different stationary state. Note that this does not require any simplifying assumptions, as the energy maps include the full nonlinear behaviour of the system. The natural frequency of the system and the strength of the incoming gust that we analyze in this section are maintained at $f_n^* = 0.30$ and $\alpha_g = 61°$ respectively, to enable direct comparison with the previous case in section 5.4.

In figure 5.11(a) we plot the energy map for an airfoil oscillating about

$X_e^* = 0.50$, with mean angle of attack $\theta_0 = 15^\circ$ and at $Re = 1000$. The plot has the same range of f_p^* and A_θ as the rest of the energy maps discussed in this study. We see that the structure of this map is very different from that for $X_e^* = 0.33$. In particular, the flutter boundary is demarcated by a roughly vertical line of $E^* = 0$ at $f_p^* \approx 0.25$, as opposed to the complicated structure with multiple equilibrium branches seen for $X_e^* = 0.33$ in figure 5.10. For the control of subcritical responses this is especially useful, as the simple topology immediately suggests the lack of a subcritical instability at $f_n^* = 0.30$. Further, $f_n^* = 0.30$ lies in the region of $E^* < 0$ for all A_θ, which suggests that any perturbations will decay. To verify this claim, the system with $X_e^* = 0.50$ and $f_n^* = 0.30$ is subjected to a gust of the same strength as the larger of the two cases discussed in the previous section (i.e. section 5.4 and gust strength $\alpha_g = 61^\circ$). The trajectory of the system in figure 5.11(a) shows that the system oscillations decay due to the negative energy extraction. The time-series of pitch angle shown in figure 5.11(b) shows that the initial deflection is of magnitude similar to that of the previous case with $X_e^* = 0.33$. However, the final stationary state shows nearly negligible oscillation amplitude of $\Delta\theta \approx 0.5^\circ$.

In summary, the examples in this section as well as the previous one show that a system designed to operate with $X_e^* = 0.33$ is susceptible to significant flutter amplitude via a subcritical response to perturbations, even when operating at velocities below the flutter boundary. However, the energy maps sug-

gest that a change in X_e^* forces the system into a strongly stable state, thereby eliminating gust-induced aeroelastic oscillations. Note again that this could work the other way in systems where large oscillations are desirable, such as in energy harvesting. In this case, similar ideas can be used to manipulate the system into the state that is optimal for the application.

5.6 Conclusions

We have demonstrated the use of energy maps to accurately predict the response of an aeroelastic control surface to gust-like perturbations. The topology of an energy map enables us to make fast and accurate predictions of the response of the system to gusts of different strengths and for systems with different structural properties. A merit of this method is that it includes the full nonlinear behaviour of the aeroelastic system, thus allowing prediction of the response to large perturbations. This makes the method relevant to a wide range of practical applications ranging from air-vehicles to energy harvesting systems. While energy maps have been utilized where the assumption of equivalent sinusoidal oscillations in both the forced as well as the flow-induced oscillation has been satisfied (as in chapter 4), here we show that this method can be used even in the presence of transient, non-sinusoidal perturbations induced by gusts.

For transverse gusts that are assumed to have length-scales much larger than that of the wing, we showed that the initial pitch deflection induced by the gust is governed by the quasi-steady moment generated on a steady airfoil at an angle of attack that includes the geometric angle of attack and the gust angle. This initial deflection gives us a kinematic initial state of the system, which can then be used to accurately predict the final state on the energy map. We note that for angle-of-attack perturbations generated by other mechanisms, this energy map-based method is equally applicable and only depends on knowledge of the initial deflection. Furthermore, showed that small differences in this initial state can lead to order-of-magnitude differences in the final stationary state oscillation amplitude and explained this behaviour using the structure of the energy map. Further, we illustrated using examples how the topology of the energy map can inform design modifications to control the stationary state flutter amplitude that results from the interaction with the gust. Examples demonstrated for such control strategies include changing the natural frequency of the system as well as changing the location of the elastic axis about which the airfoil is oscillating to push the system into a region where the energy map predicts negative energy extraction. Lastly, we demonstrated the use of the energy map in predicting and controlling the gust response for a system operating below the critical flutter speed. Therefore a-priori knowledge of the topology of the energy landscape can be leveraged in multiple ways to gain

insight into the response of a system, as well as to inform control strategies.

These results have been published in reference [78].

Chapter 6

Analyzing the flow around pitching airfoils using Dynamic Mode Decomposition

Problems in fluid dynamics are often characterized by a range of time and length scales due to the inherent non-linearity of the governing equations. In the particular case of fluid-structure interaction problems, the interplay between natural scales associated with the structure and the flow-field introduces additional complexity into the problem. These flow-field timescales can generally be related to dynamical features in the flow, such as vortices and shear layers, and the identification of these dynamically significant features along with their associated timescales has considerably advanced our

understanding of several problems in the domain of fluid-structure interactions [9, 56, 67, 77, 81, 82, 92]

The importance of this interplay amongst various timescales is evident from the results relating to flow-induced pitch oscillations of an airfoil discussed in previous chapters. For example, competing flow and structural timescales were shown to be responsible for the onset of large amplitude flow-induced oscillations in section 3.4. More generally, the interaction between flow and structural timescales is borne out in the energy extracted by the airfoil, which we showed in chapter 4 is the primary driver of its aeroelastic response as well as the various oscillation response branches. In figure 6.1 we reproduce the energy map from section 4.3 for an airfoil oscillating about a hinge location at 33% of the chord [77]. The curve of zero energy extraction corresponds to equilibrium states for a structurally undamped flow-induced oscillator, and it must be pointed out that the energy map has a very complicated structure. There exist with multiple regions of zero energy transfer for some oscillation frequencies, regions of high gradient in energy, and small ”islands” of negative energy transfer.

A key question that arises immediately is: what determines the topology of this energy map? We showed in section 4.1 that the energy transfer depends on timescales and phase differences between the flow and airfoil’s kinematics. Hence we expect to be able to understand the topology of the energy map

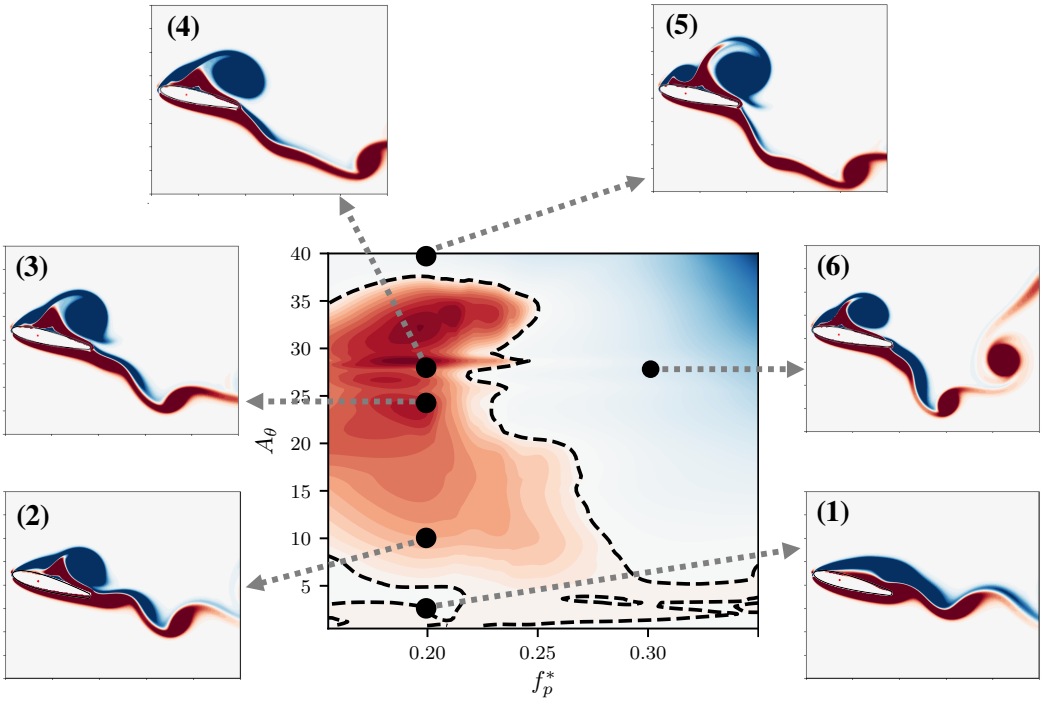

Figure 6.1: (a) Map of energy extraction (E^*) by a pitching airfoil from the surrounding flow, as a function of oscillation amplitude (A_θ) and frequency (f_p^*). Reproduced from [77]. Black circles denote the amplitude and frequency of cases discussed in section 6.4.2 of this work. Vorticity snapshots at the time-instance corresponding to the mean position during pitch-down are shown for each of these cases.

by analyzing the timescales associated with the dominant flow structures and their variation with airfoil kinematics. In figure 6.1 we show snapshots of the instantaneous vorticity field for some cases on the energy map, selected from various regions of interest on the map. Apart from the growth of the leading-edge vortex (LEV) with oscillation amplitude and differences in the wake, it is evident that subtle differences in timing and phase between these cases are difficult to discern from the full flow-field.

Therefore in this chapter, we demonstrate the use of a novel variant of the Dynamic Mode Decomposition technique in analyzing the phase and timing of flow structures in the decomposed flow with respect to the phase of the airfoil motion. Dynamic Mode Decomposition (DMD) is a modal decomposition technique that uses flow-field data to identify spatial modes of the flow-field that each correspond to a specific frequency and growth/decay rate. For nonlinear dynamical systems, such as most problems in fluid dynamics, the spatial modes extracted by DMD are the eigenvectors of the best-fit linear operator that approximates the dynamics [107], [108], [110], [111] [109]. However, the application of DMD has been largely limited to problems with static boundaries within the flow domain. As we will show here, the application of the traditional DMD technique to problems with finite-thickness moving boundaries leads to the presence of spurious structures within the DMD modes identified. A workaround for this problem that has been demonstrated is to perform the decomposition within a frame of reference moving with the body [118]. However this moving-frame analysis has drawbacks too. One particular issue in this context is the fact that energy extraction is a frame-dependent quantity, which is in fact zero in the frame of the moving body (since the immersed body is stationary in that frame). Hence, establishing a connection between the computed modes in the lab-fixed and moving frames is useful.

In this work, we propose a method to decompose the flow around a mov-

ing boundary by transforming the analysis to a body-fitted frame and then applying a correction to yield the lab-frame modes. This exploits the linearity of the formulation to decouple the effect of the moving-frame velocity from the flow dynamics. Further we present a practical implementation of this method, by including the effect of changing coordinate systems, in the context of fluid-structure interactions using simulation data. It must be noted here that while the numerical method used in this work results in lab-frame data, which necessitates this change in coordinate systems on account of the moving body, it is possible for the raw flow-field data to correspond to the non-inertial frame [149]. The method presented here to distill the modes governing the underlying flow from the effects of the non-inertial frame have applications for these problems as well.

6.1 Flow-field data

The flow-fields analyzed here are generated from two-dimensional simulations of the flow around sinusoidally pitching airfoils and cylinders using the computational methods described in sections 2.1 and 2.2. The grid sizes used in the test cases reported, for cylinders and airfoils, are 320×288 and 384×320 cells respectively. The flow within a smaller region of this domain, which includes the immersed body at all times, is the focus of the mode de-

composition described in this work. The size of this interrogation window is $n_x \times n_y = 120 \times 120$ and 250×268 grid points for the cylinder and airfoil cases respectively. This determines the size of the snapshots used in the computation of DMD modes. A schematic of the interrogation window is shown in figure 6.2 using dashed lines. Flow measurements within this window are made on the Cartesian grid, and hence include points that are inside the immersed body (solid points) during some timesteps and outside (fluid points) during others. The DMD modes are computed using 250 snapshots for most of the cases discussed. This corresponds to between 10 and 15 cycles of oscillation, depending on the oscillation frequency. We experimented with using as few as 1-2 cycles for computing the modes, however using too few snapshots was seen to yield modes with non-smooth structures.

For the airfoil as well as cylinder cases demonstrated here, the motion of the moving body is prescribed, although the formulation presented is equally applicable to flow-induced motion. Details about the airfoil simulations can be found in chapter 4 and ref. [77]. The Reynolds number is defined as $Re = \rho U_\infty L/\mu$, where L is the reference length and the prescribed frequency of oscillation is reported in non-dimensional form as $f_p^* = f_p L/U_\infty$, where f_p is the pitching frequency. All other frequencies are denoted by $f^* = fL/U_\infty$. For the cases discussed here, the length-scale used is the chord-length ($L = C$) in the case of airfoils, and the diameter ($L = D$) in the case of cylinders. The amplitude of

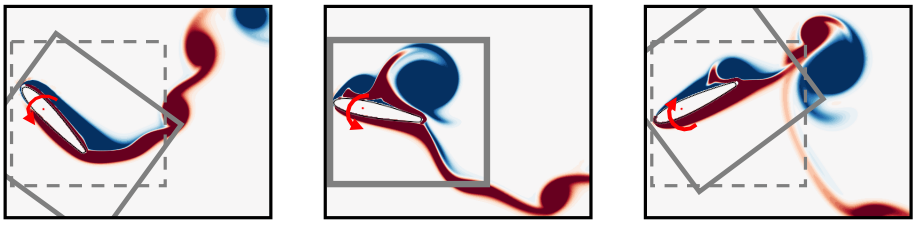

Figure 6.2: Schematic of the interrogation window for a sample case of a pitching airfoil, where the flow is visualized by contours of vorticity. Snapshots are recorded in the moving window (box with solid lines) and the lab-frame is represented using the window with dashed lines.

pitching oscillations is denoted by A_θ.

6.2 Extending DMD to flows around moving bodies

6.2.1 The traditional formulation

The traditional DMD formulation on which this work is based is the so-called "exact DMD" of Tu *et al.* [150]. This is related to the Arnoldi-like formulation of Rowley *et al.* [107] and Schmid [108], but is known to be more numerically stable. This method takes snapshots of observables and computes the modes that govern the dynamics described by the sequence of observables. In this work, the observables correspond to flow-field measurements, separated by a time interval of Δt. They are represented as vectors $\mathbf{q_n} \in \mathbb{R}^{\beta \times N}$, where

$N = n_x \times n_y$ is the number of grid points in each snapshot, β is the number of flow variables included in the snapshot at every grid location, and n is the index of the snapshot. The number of snapshots used in computing the decomposition is N_t, and these snapshots are organized as follows into two data matrices that are staggered in time:

$$\mathrm{Q} = \left[\, \mathbf{q}_0 \mid \mathbf{q}_1 \mid ... \mid \mathbf{q}_{N_t-1} \, \right] \tag{6.1a}$$

$$\mathrm{Q}' = \left[\, \mathbf{q}_1 \mid \mathbf{q}_2 \mid ... \mid \mathbf{q}_{N_t} \, \right]. \tag{6.1b}$$

The idea is to find the best-fit linear operator for the dynamical system described by these observables, such that

$$\mathbf{q}_{n+1} = \mathrm{A}\mathbf{q}_n \tag{6.2}$$

where $\mathrm{A} \in \mathbb{R}^{N \times N}$ is a large matrix that governs this evolution. Note that this best-fit dynamical system that approximates the dynamics is a autonomous. Further, equation (6.2) can also be written in terms of the entire snapshot history as $\mathrm{Q}' = \mathrm{AQ}$, from which A can, in theory, be directly computed as

$$\mathrm{A} = \mathrm{Q}'\mathrm{Q}^{\dagger} \tag{6.3}$$

where $\mathrm{Q}^{\dagger}$ is the Moore-Penrose pseudo-inverse of Q. However, due to the large

size of A, which makes it impractical to compute/store explicitly, a more computationally efficient method to proceed involves projecting the dynamics on the first r principle components of the data matrix, Q. This is done via the Singular Value Decomposition of the data matrix, and by retaining the first r principle components, $\mathrm{Q} \approx \mathrm{U}_r \Sigma_r \mathrm{V}_r^*$, where the subscript r refers to the number of components. We can now compute a more computationally tractable projection of A, given by

$$\tilde{\mathrm{A}} = \mathrm{U}_r^* \mathrm{Q}' \mathrm{V}_r \Sigma_r^{-1}. \tag{6.4}$$

The eigendecomposition of $\tilde{\mathrm{A}}$ then yields eigenvalues λ_k and eigenvectors $\mathbf{w}_k$ that satisfy $\tilde{\mathrm{A}}\mathbf{w}_k = \lambda_k \mathbf{w}_k$. Tu *et al.* [150] showed that the eigenvalues of $\tilde{\mathrm{A}}$ are equal to the eigenvalues of A, and the eigenvectors of A, denoted by $\mathbf{v}_k$, are related to those of $\tilde{\mathrm{A}}$ by

$$\mathbf{v}_k = \frac{1}{\lambda_k} \mathrm{Q}' \mathrm{V}_r \Sigma_r^{-1} \mathbf{w}_k. \tag{6.5}$$

Having computed the eigenvalues and eigenvectors of A, we can express the DMD-approximated dynamics of the system as $\mathbf{q}_n = \mathrm{A}\mathbf{q}_{n-1} = \mathrm{A}^n \mathbf{q}_0$, which follows from equation (6.2). Assuming each snapshot lies in the span of the eigenvectors of A, i.e., $\mathbf{q}_0 = \sum_k b_k \mathbf{v}_k$, we can connect this time-advancement of the system to the DMD modes as follows,

$$\mathbf{q}_n = \mathrm{A}^n \sum_k b_k \mathbf{v}_k = \sum_k \lambda_k^n b_k \mathbf{v}_k. \tag{6.6}$$

Here, b_k are the coefficients corresponding to the Galerkin projection of the DMD modes on the state of the system at the first snapshot, $\mathbf{q}_0$. Equation (6.6) hence describes the dynamics of the discrete map, given by equation (6.2), to the DMD modes and eigenvalues. The time-advancement can also be written in a manner analogous to continuous-time systems as,

$$\mathbf{q}_n = \sum_k b_k \mathbf{v}_k \exp\left(\omega_k t_n\right) \tag{6.7}$$

$$= \sum_k b_k \mathbf{v}_k \exp\left\{\Re(\omega_k) t_n\right\} \exp\left\{i\Im(\omega_k) t_n\right\} \tag{6.8}$$

where $\omega_k = \log(\lambda_k)/\Delta t$, and $\Re(\omega_k)$ and $\Im(\omega_k)$ are its real and imaginary parts. It is evident from equations (6.6) and (6.8) that the time-evolution of each DMD mode, $\mathbf{v}_k$, is determined by its corresponding eigenvalue λ_k, which is related to ω_k for each mode. Further, from equation (6.8) we see that the real and imaginary parts of ω_k determine the amplitude and frequency of each mode. In particular, the frequency of each mode can be written as $f_k = \Im(\omega_k)/2\pi$.

6.2.2 Treatment of a moving body

We now describe a method to compute the DMD modes of the flow around a moving body based on the procedure outlined in section 6.2.1, by using snapshots that include the time-varying position of the immersed body. Further, for the reasons outlined at the start of this chapter, we are specifically interested

in the lab-frame DMD modes. The interrogation window of interest is shown using dashed lines in figure 6.2, and described in section 6.1. For simplicity, we first discuss the specific case of a body performing periodic rotation/pitch oscillations at one frequency. Further, we assume that the observables being used for the decomposition are the X- and Y- components of velocity. Generalizations of this method are discussed subsequently.

We begin with a brief demonstration of the direct application of the procedure described in section 6.2.1 on problems involving moving boundaries. As a sample case, we perform the decomposition on the flow around a sinusoidally pitching airfoil, oscillating about $\theta_0 = 15^\circ$ with amplitude and frequency of oscillation given by $A_\theta = 10^\circ$ and $f_p^* = 0.20$ respectively. Hence the instantaneous geometric angle of attack is given by $\theta = 15^\circ + 10^\circ \sin(2\pi \cdot 0.20 \cdot t)$. Figure 6.3(a) shows a snapshot of the flow for this case, coloured by contours of Z-vorticity, at a time-instance corresponding to the maximum pitch-up angle during the oscillation cycle. As mentioned above, we are interested in decomposing the lab-frame velocity field, given by $\mathbf{u}(\mathbf{x}, t) = (u_x, u_y)$, where position-vectors are denoted by $\mathbf{x}$. The observables are vectors of the form,

$$\mathbf{q}_n \in \mathbb{R}^{2\times N} : \mathbf{q}_n = [u_x(\mathbf{x}_1, t_n), ..., u_x(\mathbf{x}_N, t_n), u_y(\mathbf{x}_1, t_n), ..., u_y(\mathbf{x}_N, t_n)]^T. \tag{6.9}$$

In figure 6.3(b) we plot the Z-vorticity of the computed DMD mode, correspond-

ing to the oscillation frequency $f^* = f_p^* = 0.20$, at the same time-instance as the flow snapshot in figure 6.3(a). We see the presence spurious structures within the region of the window that includes the time-varying position of the body. Specifically, a signature of the airfoil surface in its maximum pitch-up and pitch-down positions appears in the computed mode shape. These structures are highlighted using arrows in figure 6.3(b). Furthermore, the actual instantaneous shape of the airfoil is not retained in the computed mode and therefore the vortex structures that appear inside the actual airfoil shape are also spurious. Further, in figure 6.3(c) we show the reconstruction of the flow using 5 DMD modes, at the same time-instance as that discussed above. We see that the shape of the airfoil is inaccurately reconstructed, which in turn causes inaccuracies in the reconstruction of the shear layer on the surface of the airfoil. This is an effect that is expected, and was alluded to by Goza & Colonius [116]. The inaccurate reconstruction around the moving boundary stems from the fact that the points within the overall envelope of the body's motion switch between being solid points and fluid points as the body moves. Hence the presence of the moving body appears as a diffused structure, as would be expected in the sense of an overall "average" position of the body. In mathematical terms, recall from equation (6.2) that the dynamical system being approximated by this method is necessarily autonomous. However, due to the fact that the fluid domain corresponds to different positions in each snapshot, which

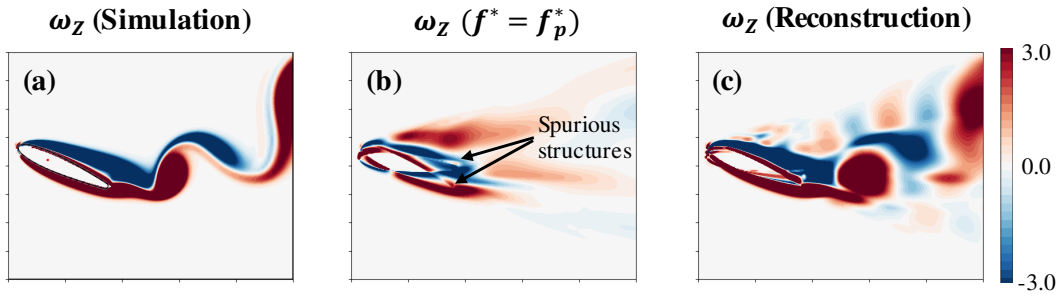

Figure 6.3: Application of DMD without the moving body formulation to the case of a sinusoidally pitching airfoil at $Re = 1000$. The airfoil is oscillating about $\theta = 15°$ with amplitude and frequency of oscillation given by $A_\theta = 10°$ and $f_p^* = 0.20$ respectively. All snapshots are at the time-instance corresponding to the the maximum pitch-up position. (a) Snapshot of Z-vorticity contours; (b) Z-vorticity contours for a computed DMD mode at the oscillation frequency, $f^* = f_p^*$. Spurious structures consisting of signatures of the airfoil surface at different pitch positions are highlighted; (c) Reconstruction of Z-vorticity field using 5 DMD modes.

leads to time-varying discontinuous boundaries in q_n, the snapshots given by equation (6.9) do not satisfy this condition.

In order to circumvent the issue associated with the motion of the body within the lab-frame, we first make a coordinate transformation to a body-fixed reference frame. Snapshots of the flow in this moving-frame are recorded by using an auxiliary interrogation window that moves with the body, where the immersed body appears stationary. A schematic of this moving window is shown in figure 6.2 using solid lines. Additionally, this non-inertial reference frame, in general, includes rotational and/or translational velocities that are related to the motion of the body with respect to the lab frame. Due to the

fact that the body appears stationary in this moving frame, a first step is the straightforward application of the procedure outlined in section 6.2.1 to compute the DMD modes of the flow around the body in the body-fixed frame. We will then show how these modes are related to the decomposition in the lab-frame.

In the present work, this coordinate transformation is done by translating and/or rotating an auxiliary Cartesian grid, of size N' grid points, with the body. For reasons that will become apparent later in this section, this moving window is necessarily larger in size than the lab-frame interrogation window as it is required to include the spatial extent of the lab-frame window at all times. We shall refer to position vectors in this moving-frame by ξ, and the flow-field velocity is denoted by $\mathbf{u}'(\xi, t)$. We calculate the velocity field in the moving frame, at ξ-coordinates, from the simulation data at locations in the lab-frame by using a bilinear interpolation scheme, and taking into consideration the relative velocity between the two frames.

We can now perform the decomposition of the velocity-field in the moving frame. Observables in this frame, $\mathbf{q}'_n \in \mathbb{R}^{2\times N'}$ take the same form as in equation (6.9), but are larger and consist of velocities $\mathbf{u}'(\xi, t_n) = (u'_x, u'_y)$. The decomposition yields moving-frame DMD eigenvalues and modes and we can write the observables in this frame, $\mathbf{q}'_n$, in terms of these eigenvalues and modes as

was done in equation (6.8). This is shown below,

$$\mathbf{q'}_n = \sum_k b_k \mathbf{v'}_k \exp\left(\omega_k t_n\right) \tag{6.10}$$

$$= \sum_k b_k \mathbf{v'}_k \exp\left\{\Re(\omega_k) t_n\right\} \exp\left\{i\Im(\omega_k) t_n\right\} \tag{6.11}$$

where it is implicitly assumed that $\mathbf{q'}_n = \mathbf{q'}(\xi, t_n)$ and $\mathbf{v'}_k = \mathbf{v'}_k(\xi)$, i.e., they refer to quantities in the moving frame. Here, ω_k and $\mathbf{v'}_k$ are the computed DMD eigenvalues and modes in this frame, and b_k is the projection of these modes on the first snapshot, $\mathbf{q'}_0$. The growth and decay of these modes is governed by $\Re(\omega_k)$, and it is seen that for the decomposition of periodic flows in a stationary state, the dynamically relevant modes have non-decaying amplitudes. Hence it is reasonable to assume that $\exp\left[\Re(\omega_k)t\right] \approx 1$, which then yields the following form for the decomposition:

$$\mathbf{q'}_n(\xi) = \sum_k b_k \mathbf{v'}_k \exp\left\{i\Im(\omega_k) t_n\right\} \tag{6.12}$$

We now have the decomposition of the flow-field in the moving-frame, $\mathbf{u'}(\xi, t)$. However, as mentioned previously we are interested in the modes of the lab-frame flow-field, $\mathbf{u}(\mathbf{x}, t)$, i.e., the modes of the observables $\mathbf{q}(\mathbf{x}, t)$. We can write $\mathbf{u}(\mathbf{x}, t)$ in terms of the moving-frame velocity-field using the relative motion between the moving-frame and lab-frame coordinates, which we refer to as $\tilde{\mathbf{r}}$. The

relationship in lab-frame coordinates is as follows:

$$\mathbf{u}(\mathbf{x},t) = \mathbf{u}'(\mathbf{x},t) + \tilde{\mathbf{r}}(\mathbf{x},t). \tag{6.13}$$

For the sake of this formulation, it is clearer to express this relationship in terms of the observables used in the computation of DMD modes. In this form the relative-velocity field, $\tilde{\mathbf{r}}(\mathbf{x},t_n)$, is written as a vector $\mathbf{r}_n(\mathbf{x})$, such that its size and arrangement of grid points is determined by that of $\mathbf{q}_n(\mathbf{x})$.

$$\mathbf{q}_n(\mathbf{x}) = \mathbf{q'}_n(\mathbf{x}) + \mathbf{r}_n(\mathbf{x}). \tag{6.14}$$

As a first step in recovering the decomposition of the lab-frame velocity field, it must be noted that $\mathbf{q'}_n(\mathbf{x})$, i.e., the first term in the right-hand side of equation (6.14), only differs from $\mathbf{q'}_n(\xi)$ in the locations at which measurements are made. Since we have computed the decomposition of $\mathbf{q'}_n(\xi)$, in equation (6.12), we can use a bilinear interpolation from the points in the moving-frame interrogation window to compute the modes of $\mathbf{q}'$ in the lab-frame coordinates. We must point out that this interpolation is the reason for the moving-frame interrogation window to necessarily include the spatial extent of the lab-frame window at all times, as was noted earlier. We refer to these interpolated modes

as $\mathbf{v}_k(\mathbf{x})$. Hence the decomposition of $\mathbf{q}'$ can now be written in the lab-frame as:

$$\mathbf{q'}_n(\mathbf{x}) = \sum_i b_i \mathbf{v}_i \exp\left[i\Im(\omega_i)t_n\right] \tag{6.15}$$

The second term in equation (6.14) is a vector that, in general, includes the rotational and/or translational velocities of the points in the lab-frame interrogation window, as seen from the moving-frame. For the specific case of pure rotation, this velocity is $\tilde{\mathbf{r}}(\mathbf{x}, t) = \mathbf{\Omega}(t) \times \mathbf{x} = (-\Omega y, \Omega x)$. This can be written in the form of the observables (see equation 6.9) as a vector $\mathbf{r}_n = \mathbf{p}\Omega(t_n)$, such that $\mathbf{p}$ is a vector containing the X and Y-coordinates of all points in the interrogation window in the form:

$$\mathbf{p} \in \mathbb{R}^{2\times N} : \mathbf{p} = [-y(\mathbf{x}_1), ..., -y(\mathbf{x}_N), x(\mathbf{x}_1), ..., x(\mathbf{x}_N)]^T. \tag{6.16}$$

Further, assuming a single frequency of oscillation for simplicity, given by ω_0, the angular velocity can be written as $\Omega(t) = A_\omega \cos(\omega_0 t + \phi)$. Using this,we can express $\mathbf{r}_n$ in the following form:

$$\mathbf{r}_n = \mathbf{p}\Omega(t_n) = \mathbf{p}\big[A_\omega \cos\omega_0 t_n + \phi\big] \tag{6.17}$$

$$\mathbf{r}_n = \mathbf{p}A_\omega \left[\frac{\exp\{i(\omega_0 t_n + \phi)\} + \exp\{-i(\omega_0 t_n + \phi)\}}{2}\right] \tag{6.18}$$

From equation (6.18) we see that the relative-velocity vector can be written

in terms of oscillating complex exponentials, much like the form for the the decomposed velocity, in equation (6.15). This suggests we can use the linearity of the decomposition to recover the modes of the lab-frame velocity from the computed modes in the moving-frame. Plugging equations (6.15) and (6.18) into equation (6.14), we get,

$$\mathbf{q}_n(\mathbf{x}) = \sum_k b_k \mathbf{v}_k(\mathbf{x}) \exp\left\{i\Im(\omega_k)t_n\right\} + \mathbf{p}A_\omega \left[\frac{\exp\left\{i(\omega_0 t_n + \phi)\right\} + \exp\left\{-i(\omega_0 t_n + \phi)\right\}}{2}\right] \tag{6.19}$$

The first term in equation (6.19) is a summation over all modes computed in the decomposition, which includes the modes computed at the oscillation frequency and its complex conjugate, which we denote as v_{ω_0} and $v_{-\omega_0}$ respectively. Since this is a linear superposition, we can take these modes out of the summation, and combine them with the second term in equation (6.19) where the complex exponential has the same form as that multiplying the DMD modes. Doing this, we can rewrite equation (6.19) as shown below:

$$\begin{aligned}\mathbf{q}_n(\mathbf{x}) = &\sum_{\omega_k \neq \pm\omega_0} b_k \mathbf{v}_k(\mathbf{x}) \exp\left[i\Im(\omega_k)t_n\right] \\ &+ \left[b_{\omega_0}\mathbf{v}_{\omega_0} + \frac{A_\omega}{2}\mathbf{p}\exp\left(i\phi\right)\right]\exp\left\{i\Im(\omega_0)t_n\right\} \\ &+ \left[b_{-\omega_0}\mathbf{v}_{-\omega_0} + \frac{A_\omega}{2}\mathbf{p}\exp\left(-i\phi\right)\right]\exp\left\{-i\Im(\omega_0)t_n\right\}\end{aligned} \tag{6.20}$$

Equation (6.20) now gives us a form for the decomposition of the lab-frame ve-

locity in terms of the modes computed in the moving frame. We see that the correction to the modes at the oscillation frequency, which come from the rotation term, have a non-trivial form that depends on the magnitude of angular velocity, the vector of y-coordinates, and the phase of this rotation, ϕ. Another interesting observation from equation (6.20) is that this change in reference frame only modifies the modes at the oscillation frequency. We will show in a practical example that this is true.

While we have demonstrated this formulation for a body rotating at one frequency for simplicity, this method can be generalized for bodies performing more complicated combinations of periodic translation and rotation in a straightforward manner. This is done by including the terms for the translational velocity in equation (6.14), and writing those terms as complex exponentials as in equation (6.18). Further, quasi-periodic motions can be treated in a similar manner by including all modes of oscillation in equation (6.17). This will result in corrections to the DMD modes corresponding to all frequencies in the immersed body's oscillation frequency spectrum.

6.3 Rotating cylinder

As a first application of the methods presented above in section 6.2, we analyze the decomposition of the flow around a circular cylinder performing peri-

odic pitch (i.e. rotational) oscillations. This test case is particularly valuable in this study as it is one of few canonical "moving boundary" problems (although it can be implemented using a stationary surface and oscillating boundary conditions) which can be analyzed using the standard DMD formulation of section 6.2.1, as the boundary does not sweep through the fluid domain.

In performing the two variants of DMD on this flow, we use an interrogation window of size $2D \times 2D$, where D is the diameter of the cylinder, and the window is centered on the cylinder. The cylinder is forced to perform pitch oscillations of amplitude $A_\theta = 10^\circ$ and frequency $f_p^* = 0.25$. The Reynolds number used here is $Re = 100$, and the frequency of lift force oscillations on the cylinder is measured to be $f^* \approx 0.17$. This gives rise to two important timescales in the flow, i.e., dynamics governed by the oscillation frequency and that of the forcing frequency. We analyze the computed DMD modes at these frequencies, and compare results from the two methods. Comparisons are made at four phases during one oscillation cycle - the mean position during pitch-up, the peak pitch-up position, the mean position during pitch-down, and the peak pitch-up position.

Figure 6.4 shows snapshots of the DMD mode at $f^* = 0.17$ during these phases of the oscillation cycle. The top panel, figures 6.4(a)-(d), show the modes computed using the standard DMD, and figures 6.4(e)-(h) show modes computed using the moving-body formulation. We see that the modes have the

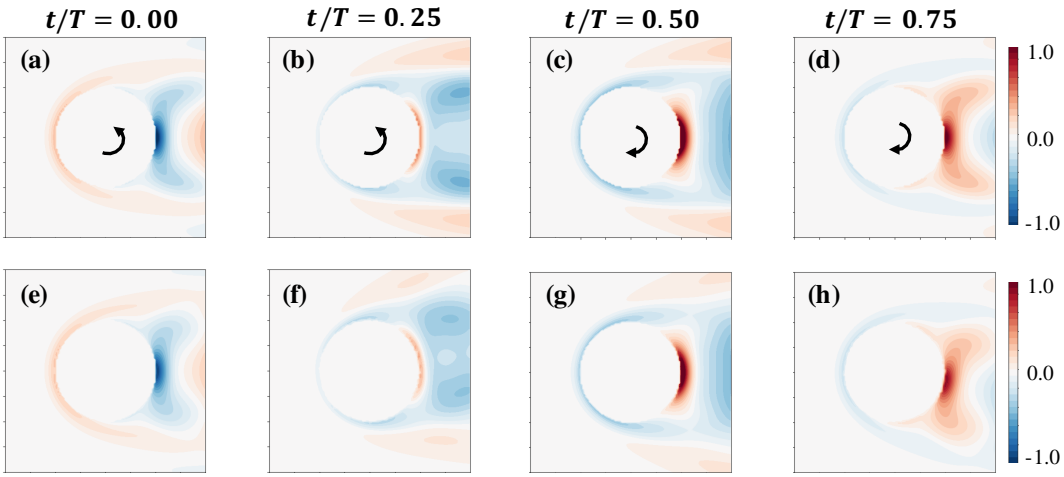

Figure 6.4: Z-vorticity contours of the DMD mode corresponding to $f^* = 0.17$, for the flow around a circular cylinder at $Re = 100$, $f_p^* = 0.25$ and $A_\theta = 10°$. The mode is plotted at four different phases of one oscillation cycle. The text above each panel shows the corresponding time-instance, where $T = 1/f_p^* = 1/0.25$. Arrows show the direction of rotation of the cylinder; (a)-(d) Modes computed using standard DMD; (e)-(h) Modes computed using moving-body formulation.

same topology over time in the two cases. The only difference is the rotation of the mode in the case of the moving body formulation, which is a result of the moving window. This serves as a confirmation of one finding from equation (6.20), that the modes that do not correspond to the oscillation frequency were found to be unmodified. Further, we observe that the vortex structures at this frequency (which is the frequency of lift-forcing) are relatively stronger in the wake than in the shear layer. This suggests that the frequency of vortex shedding in the wake is closely related to the frequency of lift-forcing on the cylinder - a fact that has been widely used in studies of vortex-induced vibration to estimate the shedding frequency and/or identify lock-in [75].

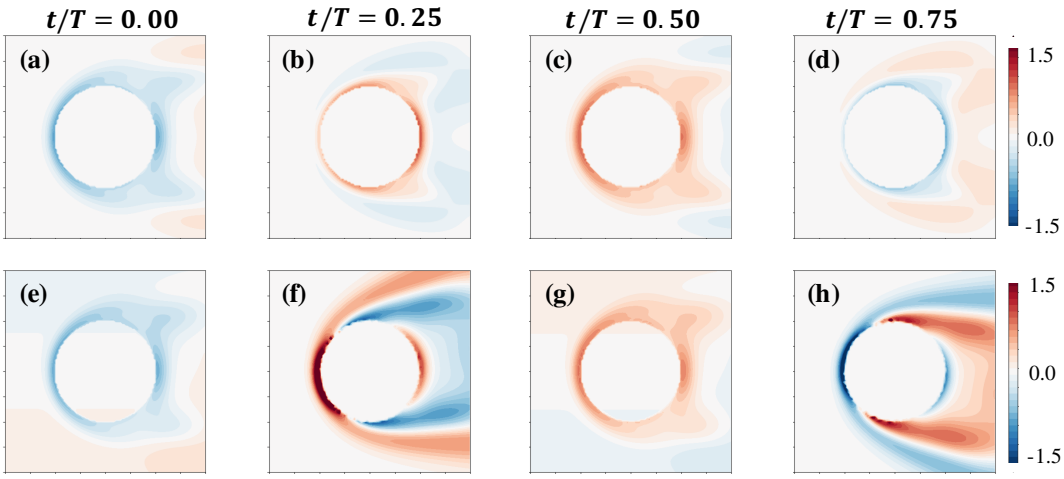

Figure 6.5: Z-vorticity contours of the DMD mode corresponding to $f^* = 0.25$, for flow around a circular cylinder with the same parameters as in figure 6.4. The mode is plotted during different phases of one oscillation cycle. Time-instances and direction of rotation are as in figure 6.4; (a)-(d) Modes computed using standard DMD; (e)-(h) Modes computed using moving-body formulation.

In figure 6.5 we plot the DMD mode at $f^* = 0.25$, at the same instances in time as in the preceding discussion. Figures 6.5(a)-(d) correspond to the standard DMD, and figures 6.5(e)-(h) correspond to the moving body formulation. We see from figures 6.5(a) and 6.5(e), as well as figures 6.5(c) and 6.5(g), that the modes computed by the moving-window and standard formulation share the same structure at the mean position in the oscillation cycle. This is due to the fact that the rotational effects in the flow-field are taken into account in the formulation for the moving window. Additionally, the interrogation windows overlap at this mean position, which removes any spatial differences between the flow seen from the two frames. At the other two time instances shown, which are at the peak pitch-up and pitch-down positions, the

moving and stationary windows are at their maximum rotation angle with respect to each other. Hence spatial differences in the decomposed flow seen from the two frames are most evident at these time instances, which gives rise to qualitatively different structures (the effects of the rotational velocity field are minimum at these time-instances). Both frames show much larger structures around the cylinder surface at this frequency, which are also convected into the wake. The presence of large structures around the shear layer at this frequency is expected, as this corresponds to the frequency of oscillation of the cylinder. Hence we see from this example that even the decomposition of flows in relatively simple fluid-structure interaction problems provides valuable insight into flow modes associated with the different timescales.

6.4 Analysis of the flow around a pitching airfoil

6.4.1 Flow reconstruction

An important application of modal-decomposition techniques is the development of low-order models of the dynamics. This is based on the idea that most of the physically relevant dynamics are governed by a small number of modes. In this section, we demonstrate the reconstruction of the flow-field around a

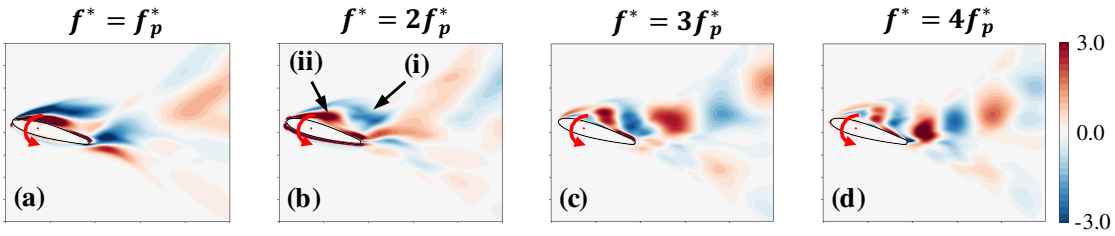

Figure 6.6: DMD modes of the flow around a pitching airfoil at $Re = 1000$, pitching with $f_p^* = 0.20$ and $A_\theta = 10°$. The modes are coloured by contours of Z-vorticity, and the time-instance corresponds to the mean position during the pitch-down phase of oscillation. Modes at the oscillation frequency and its harmonics are shown. (a) $f^* = f_p^*$; (b) $f^* = 2f_p^*$; (c) $f^* = 3f_p^*$; (d) $f^* = 4f_p^*$. Note that this is the same case as that shown in figure 6.3.

pitching airfoil via the DMD modes computed by using the moving-body formulation, which serves as a simple verification of the decomposition method described in this work. The specific case discussed here is that of an airfoil performing periodic pitching oscillations at frequency $f_p^* = 0.20$ and amplitude $A_\theta = 10°$. The Reynolds number is $Re = 1000$, and the interrogation window is of size $2.5C \times 2C$. We focus on the reconstruction of the vorticity field.

We first analyze the flow physics captured by the dynamically important modes that are used in the subsequent reconstruction. Here we assess the relative importance of each mode by the magnitude of its Galerkin projection on the full flow-field. In figure 6.6 we show four leading modes, which are plotted at the time-instance corresponding to the mean position during the pitch-down motion. Note that, the moving boundary DMD formulation does not generate unphysical flow information near the airfoil surface as it did for the original

formulation is figure 6.3. Figure 6.6(a) shows the mode at the oscillation frequency, $f^* = f_p^* = 0.20$, where the dominant structure is the separated shear layer over the suction surface of the airfoil and over the trailing edge. These shear layers are hence the driving mechanism at the fundamental frequency, and give rise to finer-scale vortex-structures at the higher harmonics. The first harmonic of this mode, $f^* = 2f_p^*$ shown in figure 6.6(b), captures the rolled-up vortex structures convecting over the surface of the airfoil (denoted by (i); negative vorticity) as well as the separating shear layer (denoted by (ii); positive vorticity) induced by this vortex. We see evidence of a leading-edge vortex (LEV) that is shed during the pitch-down motion at this frequency. The higher harmonics, $f^* = 3f_p^*$ and $f^* = 4f_p^*$, contain high wavenumber structures and are shown in figures 6.6(c) and 6.6(d). These structures correspond to vortices that form vortex-pairs and subsequently accelerate into the wake as a result of the jet induced between the vortices in each pair. It is interesting to note that these higher-harmonic modes, which are stronger in the wake, are approximately at the vortex shedding frequency of bluff-body wakes when using the projected area as the length scale ($f^* \approx 0.16$).

We can now use just a few of the computed modes, i.e. the leading modes discussed above, to reconstruct the full flow-field. Figures 6.7(a)-(d) show the vorticity field around the airfoil from the flow simulation data, as it goes through four phases during one oscillation cycle - the start of the pitch-down motion,

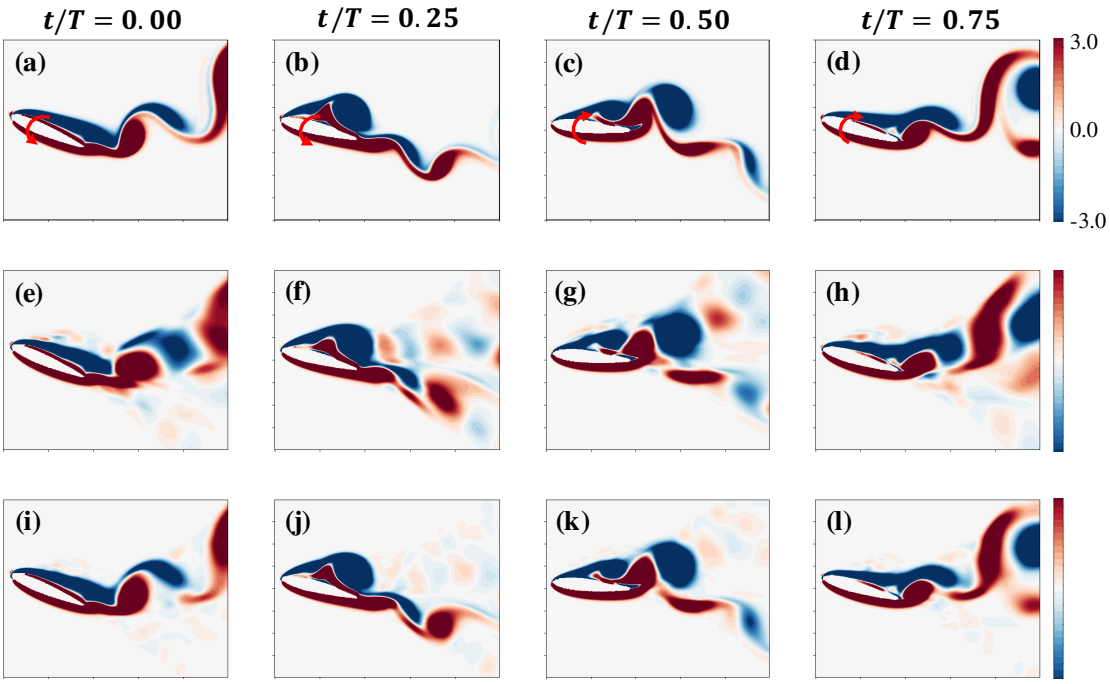

Figure 6.7: Contours of the Z-vorticity field around a pitching airfoil from the flow simulation data and from the reconstruction of the flow using DMD modes. The flow and kinematic parameters are $Re = 1000$, $f_p^* = 0.20$ and $A_\theta = 10°$. Snapshots are shown at four phases over one oscillation cycle (time instance is specified at the top of each column). (a)-(d) Simulation data; (e)-(h) Reconstruction using five modes. This can be compared with the reconstruction in figure 6.3(c); (i)-(l) Reconstruction using ten modes.

the mean position during pitch-down, the start of pitch-up motion, and the mean position during pitch-up, respectively. The primary flow structures we see are the shedding of a leading-edge vortex during pitch-down, followed by the shedding of another smaller vortex later in the pitch-down motion. These vortices entrain the shear layer on the suction side and "jet" into the wake as vortex pairs. In figures 6.7(e)-(h) we show the reconstruction of the flow at the same time-instances as in figures 6.7(a)-(d), using just five DMD modes plus the mean (which corresponds to the $f^* = 0$ mode). We see that these modes are able to capture the significant features of the vortex dynamics, i.e., the shedding and convection of the two vortices during the pitch-down motion. We see that there are also smaller-scale structures that are present in the reconstruction, but absent in the simulation data. These structures are associated with higher harmonic modes that are not included in the reconstruction, and are expected to have minimal dynamical significance in grid-converged simulations. Although not shown here, it must be noted that this reconstruction, when applied to the velocity field, shows smoother fields.

We compare this 5-mode reconstruction with a reconstruction using ten DMD modes, plus the mean, in figures 6.7(i)-(l). It is interesting to note that doubling the number of modes in the reconstruction does not significantly improve the reconstruction, especially very close to the airfoil, which confirms that the 5-mode reconstruction captures the bulk of the dynamics. However,

using more modes does improve the reconstruction in the wake, and also removes the smaller-scale spurious structures to a large degree. This exercise serves as a verification that the method described here is able to accurately reconstruct the flow-field from a small number of DMD modes. It also demonstrates that the dynamics are governed by a few modes even in these complex vortex-dominated flows, which makes them good candidates for the development of lower-order models using such methods.

6.4.2 Flow analysis using DMD

	f_p^*	A_θ	E^*
(1)	0.20	04	2.79×10^{-3}
(2)	0.20	10	3.57×10^{-2}
(3)	0.20	25	6.45×10^{-2}
(4)	0.20	29	8.16×10^{-2}
(5)	0.20	40	-8.94×10^{-2}
(6)	0.30	29	-2.48×10^{-1}

Table 6.1: Table summarizing the oscillation frequency (f_p^*), amplitude (A_θ), and energy transfer (E^*) for the pitching airfoil cases analyzed in this work. For all cases listed in the table $Re = 1000$, the airfoil is pitching about $\theta_0 = 15^\circ$, and the instantaneous geometric angle of attack is given by $\theta = \theta_0 + A_\theta \sin(2\pi f_p^* t)$.

For an airfoil pitching sinusoidally at a single frequency it is easy to show that only the mode of the forcing at the oscillation frequency, and non-harmonics modes, contribute to the structural excitation. For the cases studied here, we have verified that the computed DMD spectrum does not contain non-harmonic

modes of the oscillation frequency. Hence the only mode that contributes to the excitation is the mode at the oscillation frequency. For this reason, the ensuing discussion will focus on the DMD mode at the oscillation frequency, and particularly on the effect of varying the amplitude of oscillation at a fixed frequency. We choose this fixed frequency to be $f_p^* = 0.20$ for most of the discussion, and amplitudes of oscillation from $A_\theta = 4^\circ$ to $A_\theta = 40^\circ$ will be analyzed. We also discuss the effect of changing frequency of oscillation at fixed amplitude, to highlight the different timescales involved. The locations on the energy map of all cases discussed here were shown in figure 6.1. For reference, Table 6.1 shows the kinematic parameters and energy transfer (E^*) calculated for each case.

We begin with a description of the full (undecomposed) vorticity field for the cases with $f_p^* = 0.20$ and amplitude varying from $A_\theta = 4^\circ$ to $A_\theta = 40^\circ$. A snapshot of vorticity at the time-instance corresponding to the mean position during the pitch-down phase of the oscillation cycle for each of these cases is shown in figures 6.8(a)-(e). On increasing A_θ from 4° to 40° we see the growth, separation, and roll-up of the leading-edge shear layer as A_θ is increased. We also see the presence of strong vortex structures in the wake in all these cases. From observing these snapshots of the full flow field it is unclear what dominant flow structures correspond to the oscillation frequency in these cases. Further, we see from figures 6.8(c)-(e) that although the vortex structures in

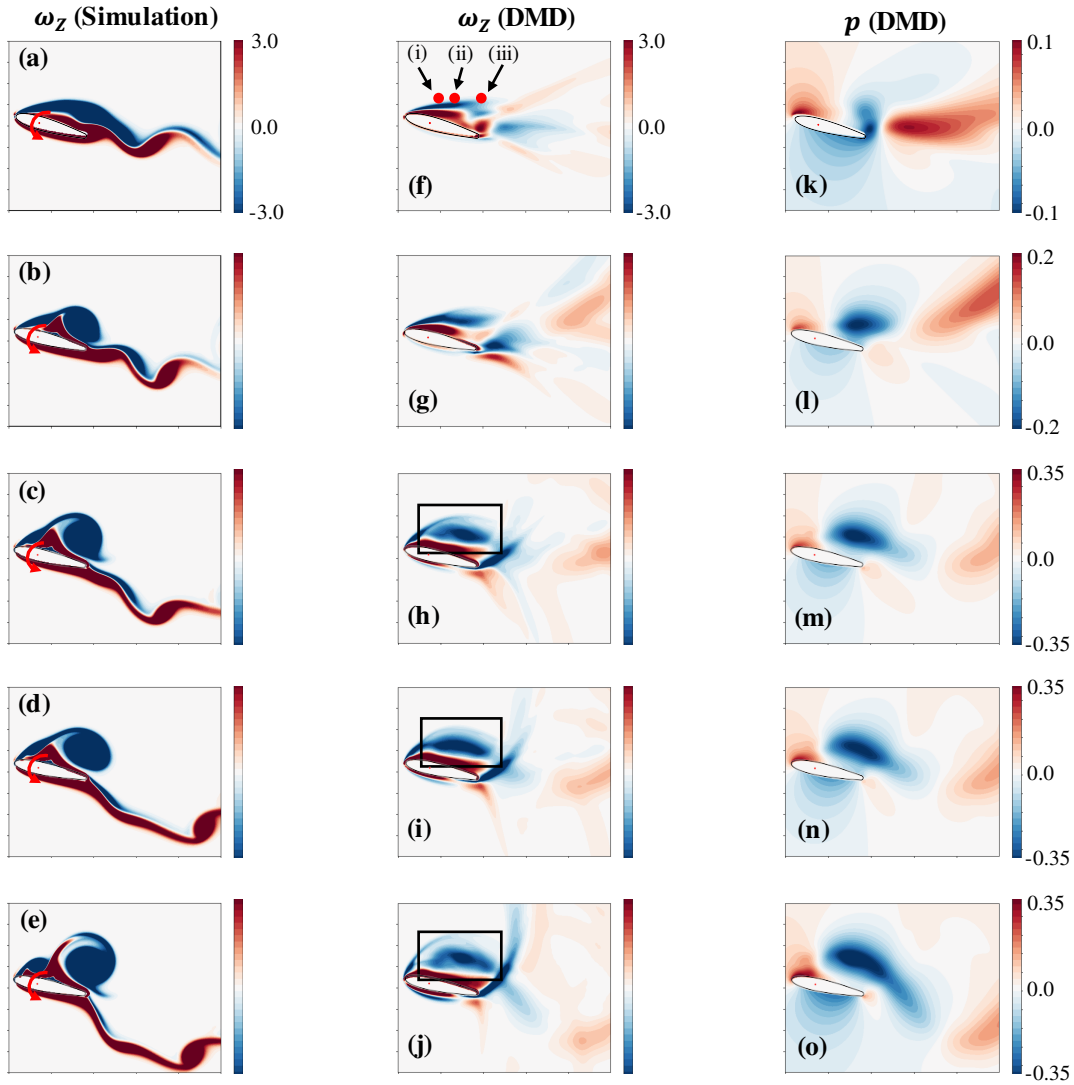

Figure 6.8: Analysis of cases (1)-(5) in table 6.1 using DMD modes of Z-vorticity and pressure. Cases shown correspond to various oscillation amplitudes at frequency of oscillation $f_p^* = 0.20$. All snapshots are plotted at the time instance corresponding to the mean position during pitch-down. (a)-(e) Z-Vorticity contours from the simulation data for amplitudes of $A_\theta = 4°$, $10°$, $25°$, $29°$ and $40°$ respectively; (f)-(j) DMD mode of vorticity at the oscillation frequency $(f^* = f_p^*)$, and amplitudes of oscillation correspond to those in (a)-(e). The rectangles in (h)-(j) highlight the flow structure of interest discussed in the text; (k)-(o) DMD mode of pressure at the oscillation frequency, and amplitudes of oscillation correspond to those in (a)-(e).

these cases have different sizes, they have qualitatively similar features. However these cases show different energy extraction, with the case of $A_\theta = 40°$, shown in figure 6.8(e), showing negative energy extraction, and all other cases showing positive energy extraction. Hence, from observing the full flow field it is not clear what causes the different energy transfer values. This motivates an analysis procedure based on decomposing the flow to extract the important feature that drive the dynamics.

In figures 6.8(f)-(j), we plot the DMD mode of Z-vorticity at the oscillation frequency for an airfoil pitching at $f_p^* = 0.20$ and various amplitudes of oscillation. This is shown at the time-instance corresponding to the airfoil's mean position ($\theta = 15°$) during the pitch-down phase of the oscillation cycle. At small amplitude oscillations of $A_\theta = 4°$, shown in figure 6.8(a), we see that the dominant vortex structures at the oscillation frequency are the separating shear layer near the leading edge, and prominent vortex structures near the trailing edge. This regime of small-amplitude oscillation shows vortex shedding that is very similar to that in bluff-bodies, which is evident from the trailing-edge shedding. On increasing the amplitude of oscillation to $A_\theta = 10°$, in figure 6.8(b), we see the development of a rolled-up shear layer over the suction surface of the airfoil, along with the initial development of an LEV at this amplitude of oscillation. The shear-layer and LEV at the oscillation frequency is presumably responsible for the large increase in energy transfer over the case

with smaller amplitude oscillations, as seen in table 6.1.

As we move to larger amplitude oscillations, from $A_\theta = 25^\circ$ to $A_\theta = 40^\circ$, we see that the dominant vortex structure is again the separating shear layer, which rolls up into an LEV-like structure over the suction surface. This structure is highlighted for $A_\theta = 25^\circ$, $A_\theta = 29^\circ$ and $A_\theta = 40^\circ$ in figures 6.8(h)-(j) respectively, at the mean pitch-down position, which corresponds to the maximum angular velocity of the airfoil. It is particularly interesting to analyze the dominant vortex structure at this time-instance since, in the context of energy transfer, we expect its influence to be maximum (or close to maximum) when the angular velocity of the airfoil goes through a maximum. Hence it is instructive to compare this highlighted structure for the cases discussed here, i.e. $A_\theta = 25^\circ$, $A_\theta = 29^\circ$ and $A_\theta = 40^\circ$, to understand how it affects the energy transfer as we increase the oscillation amplitude.

In the case of $A_\theta = 25^\circ$, shown in figure 6.8(h), we see that the strength of the LEV-like structure does indeed go through a maximum close to the time-instance shown (it must be noted that although we show just one snapshot for brevity, we have confirmed the occurrence of this maximum using time-resolved snapshots). On increasing the amplitude of oscillation to $A_\theta = 29^\circ$, we again see the occurrence of a large LEV-like structure over the airfoil in figure 6.8(i), which goes through its maximum size as the angular velocity of the airfoil peaks. However, it is interesting to note that the extent of this structure is

larger in the case of $A_\theta = 29^\circ$ than for $A_\theta = 25^\circ$, which is evident from comparing the highlighted structures in figures 6.8(h) and 6.8(i). This is in line with the fact that the energy transfer is larger at $A_\theta = 29^\circ$, as seen in table 6.1(b). At $A_\theta = 40^\circ$, which is shown in figure 6.8(j), we see similar structures as in the previous two cases. However, we again see that the spatial extent of the highlighted LEV-like structure is smaller than in the case of $A_\theta = 29^\circ$ as the airfoil goes through its peak pitching velocity. Further, the vorticity over the suction-side of the airfoil extends farther downstream, which suggests that the LEV is shed earlier in the cycle at these larger amplitude oscillations.

Since we are interested in the fluid-structure coupling between the flow and the pitching airfoil, it is instructive to analyze the DMD modes of the pressure field in the flow, since pressure is the dominant forcing mechanism on the airfoil. Here we describe the DMD modes of the fluid pressure at $f^* = f_p^* = 0.20$ for the cases discussed above, which corresponds to the oscillation frequency of the airfoil for these cases. In figure 6.8(k)-(o) we plot the DMD mode of the pressure field at the time-instance corresponding to maximum angular velocity of the airfoil during the downstroke. We see that for the small amplitude oscillation, $A_\theta = 4^\circ$ in figure 6.8(k), there are alternating low and high-pressure structures shed off the suction and pressure sides of the trailing edge, similar to bluff-body shedding. One such trailing-edge vortex is evident at the time-instance plotted in figure 6.8(k). On increasing the amplitude of oscillation to

$A_\theta = 10°$, shown in figure 6.8(l), there is evidence of a larger LEV over the suction-side of the airfoil. Further increasing the amplitude to $A_\theta = 25°$ leads to a larger low-pressure region over the airfoil, which we see in figure 6.8(m). The case of $A_\theta = 29°$ sees a still-larger low-pressure region over the airfoil, which is seen in figure 6.8(n). This is related to the occurrence of the larger shear-layer roll-up discussed previously for this case. At the highest amplitude of oscillation, $A_\theta = 40°$ shown in figure 6.8(o), we see that a large part of the low-pressure region over the airfoil has convected downstream of the airfoil, possibly influencing the pressure-side shear layer in an unfavourable manner at this time-instance. This supports our previous observation that the large-amplitude oscillation causes the shedding of vorticity earlier in the oscillating cycle, thus establishing an unfavourable phase difference and negative energy transfer.

In addition to the differences in the streamwise location of the pressure minimum discussed above, it is also interesting to note that there is a difference in the distance of this structure from the suction surface of the airfoil. We can see qualitatively from figures 6.8(m)-(o) that this pressure minimum is closest to the airfoil surface in the case of $A_\theta = 29°$ and farthest in the case of $A_\theta = 40°$. This can be verified by comparing the surface pressure induced by the DMD mode at $f^* = f_p^* = 0.20$ for these three cases. In figure 6.9 we plot this pressure along the airfoil surface, focusing on the portion of the suction surface

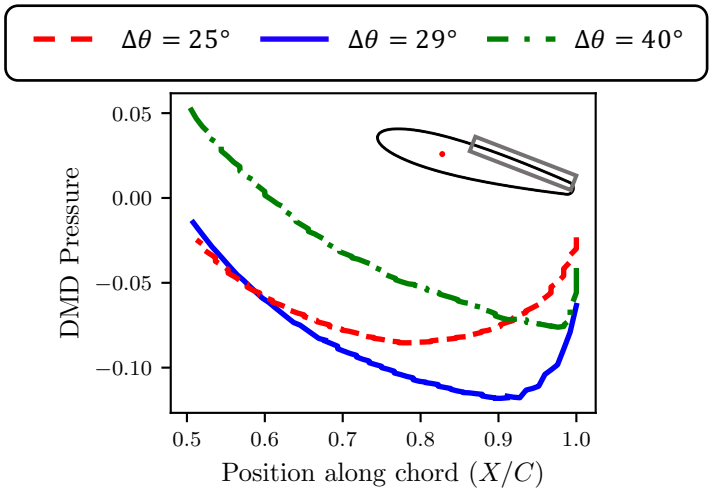

Figure 6.9: Surface pressure from the DMD mode at $f^* = f_p^* = 0.20$, plotted along half the suction surface of the airfoil for three amplitudes of oscillation, $A_\theta = 25°$, $A_\theta = 29°$ and $A_\theta = 40°$. The inset highlights the portion of the airfoil surface along which pressure is plotted. The pressure for the three cases is extracted from the pressure field shown in figures 6.8(m)-(o).

closest to the pressure minimum (region of interest is highlighted in the inset of figure 6.9). We see that the mode at $f^* = f_p^*$ does indeed induce the lowest pressure on the surface in the case of $A_\theta = 29°$. Further, the pressure minimum for $A_\theta = 40°$ occurs farther downstream than in the other two cases, thus supporting our previous observation about the phase of this structure with respect to the motion.

We can also make our argument about the phase and spatial extent of relevant vortex structures with respect to the motion of the airfoil more quantitative by probing individual points in the flow field over time. In figure 6.10, we plot the value of vorticity from the DMD mode at $f^* = f_p^* = 0.20$, i.e., the same DMD modes as in figures 6.8(f)-(j), at three points in the shear layer over time.

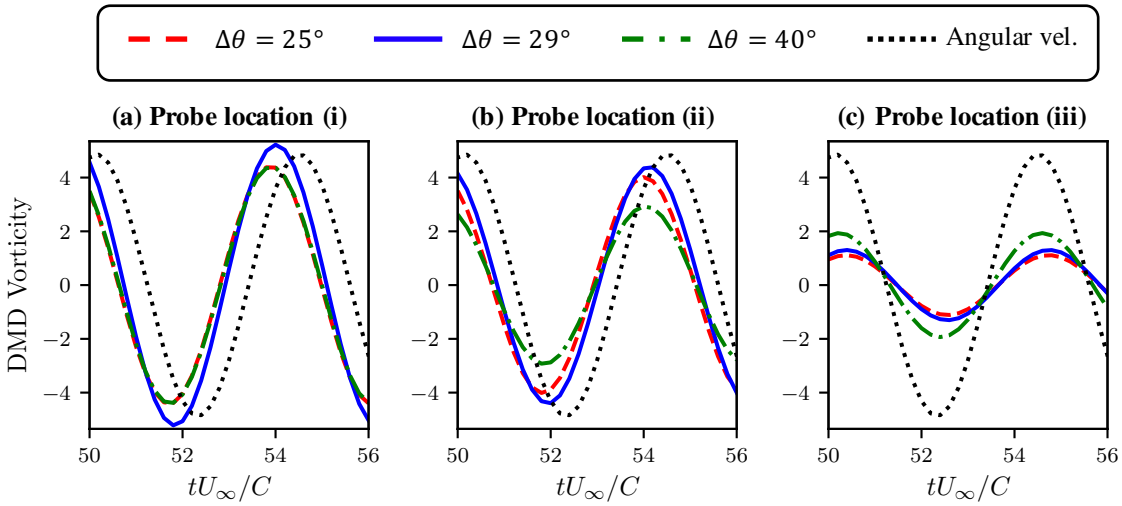

Figure 6.10: Time-series of Z-vorticity from the DMD mode corresponding to $f^* = f_p^* = 0.20$, probed at three locations in the suction-side shear-layer. The probe locations (i),(ii) and (iii) are shown using red circles in figure 6.8(f) and the Z-vorticity is probed from the fields shown in figures 6.8(h)-(j). This is shown for cases with $A_\theta = 25°$, $A_\theta = 29°$ and $A_\theta = 40°$. Also shown qualitatively (amplitude is arbitrary) using a dotted line is the angular velocity at $f_p^* = 0.20$.

Two positions at which we probe these values are located above mid-chord on the airfoil, separated by $0.1C$ in the streamwise direction, while the third point is slightly downstream of the trailing edge. These points are shown using red circles in figure 6.8(f). The time evolution of these quantities is compared with the angular velocity of the airfoil, which is shown qualitatively (focusing on phase with arbitrary amplitude) as a dotted line in the three plots. At probe location (i), corresponding to mid-chord, it is evident that the shear layer in the case of $A_\theta = 29°$ is both stronger (by about 20%) as well as slightly more in-phase with the angular velocity of the airfoil. Moving downstream to probe location (ii), the shear layer in the case of $A_\theta = 29°$ is still roughly 10% stronger

than that of $A_\theta = 25°$, and about 25% stronger than that of $A_\theta = 40°$. However when we move downstream of the airfoil to location (iii), the shear layer in the case of $A_\theta = 40°$ is much larger than the other two cases, although it must be noted that the magnitude is significantly smaller at this downstream position. These measurements hence confirm the qualitative observations discussed previously, i.e., the strength (and to a lesser degree the phase) of the dominant vortex structure in the case of $A_\theta = 29°$ goes through a maximum more in phase with the maximum angular velocity of the pitching airfoil as compared to the other two cases discussed. Further, in the case of $A_\theta = 40°$ the dominant vortex structures are farther downstream as the airfoil goes through its maximum angular velocity. This is due to the fact that the large oscillation amplitude forces the generation and shedding of these structures earlier in the oscillation cycle.

We see from the above discussion that the DMD modes computed by this method over the pitching airfoil are able to provide valuable insight into the interaction between the vortex structures and airfoil motion. At the phase of maximum angular velocity of the airfoil, the qualitative difference in the phase of the separated shear layer in the three cases is able to highlight subtle differences that are not otherwise apparent when analyzing the full flow-field. Further, the decomposition of the pressure field also highlights important differences in the regions of minimum pressure and the resultant induced pressure

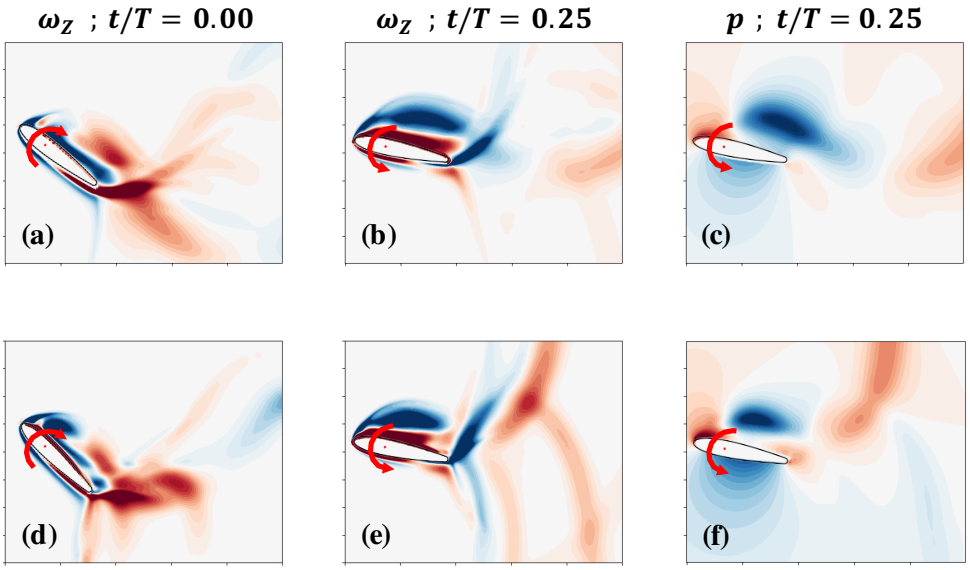

Figure 6.11: Comparison of DMD modes at the pitch frequency ($f^* = f_p^*$) for airfoils oscillating with amplitude $A_\theta = 29°$ and two different frequencies, $f_p^* = 0.20$ and $f_p^* = 0.30$. (a) Z-Vorticity contours of the DMD mode at the maximum pitch-up position for $f^* = f_p^* = 0.20$; (b) Z-Vorticity contours of the DMD mode at the mean pitch-down position for $f^* = f_p^* = 0.20$; (c) Pressure contours of the DMD mode at the mean pitch-down position for $f^* = f_p^* = 0.20$; (d)-(f) Same quantities as in (a)-(c) but for $f^* = f_p^* = 0.30$. Colour-bars for all Z-vorticity and pressure contours here are the same as in figure 6.8.

on the airfoil surface. The maximum size and strength of the vortex structure and pressure minimum in the case of $A_\theta = 29°$ is in line with the fact that this case shows the maximum energy transfer. Further, the downstream position of the vortex convecting over the shear layer, as well as the relative position of the pressure minimum over the suction surface also suggest reasons for the the negative energy transfer in the case of $A_\theta = 40°$.

We now analyze the effect of changing the frequency of oscillation while

keeping the amplitude constant. Specifically, we discuss the DMD modes of the flow around airfoils oscillating with amplitude $A_\theta = 29°$, and frequencies $f_p^* = 0.20$ and $f_p^* = 0.30$. In figure 6.11 we show vorticity contours as well as pressure fields of the DMD mode corresponding to the oscillation frequency for each case. The top panel shows the case with $f^* = f_p^* = 0.20$ and the bottom panel shows the case with $f^* = f_p^* = 0.30$. Figures 6.11(a) and 6.11(d) show the vorticity field at the time-instance corresponding to the peak pitch-up position. Comparing the two cases at this time instance, we see the generation of multiple vortices over a cycle in the case of $f^* = 0.30$, which is particularly evident near the trailing edge and in the wake. Further, we also see evidence of this at the mean pitch down position, shown in figures 6.11(b) and 6.11(e), where the vortices convected into the wake show a fragmented structure. The pressure fields at the mean pitch-down position, shown in figures 6.11(c) and 6.11(f) also show a similar fragmented structure. In particular, we see that the low-pressure region over the suction side of the airfoil is much smaller in the case of $f^* = 0.30$, and this is accompanied by a large high-pressure structure. The presence of these smaller-scale structures in the case of $f^* = 0.30$ indicates that the timescale associated with the dominant flow-structures, the vortex shedding and shear-layer roll-up, is different from that of the oscillation. Comparing this to the fact that we observe increasingly smaller-scale structures at higher frequencies in figure 6.6, the smaller-scale structures in the case of

$f^* = 0.30$ suggest that the dynamics of the flow occur at a lower fundamental frequency than the oscillation frequency of the airfoil. This discrepancy between timescales leads to negative energy transfer in this case.

6.5 Conclusions

We have demonstrated a novel application of Dynamic Mode Decomposition (DMD) to fluid-structure interaction problems involving a rigid body of non-zero thickness performing large-amplitude motions. This formulation focuses on computing the DMD modes of the flow around the moving body in the lab-frame, where the motion of the body is taken into account. We have compared the results from this method and the standard DMD formulation for the flow around a periodically rotating circular cylinder, and showed under what conditions the results match. Specifically, we showed that the modes at frequencies not equal to the oscillation frequency are unmodified. For modes at the oscillation frequency, the method takes into consideration non-inertial effects in the velocity field, and retains some spatial effects of the moving reference frame.

This method is applied to the analysis of the flow around an airfoil performing periodic pitching oscillations. We showed that this method is able to reconstruct the flow-field using a small number of modes (as is the case with the standard DMD), which is useful for the development of low-order models

for these flow. Further, we were able to use the computed modes of the flow at the oscillation frequency to gain insight into the timing and phase of flow structures that interact with the airfoil during an oscillation cycle. We showed that by analyzing the mode corresponding to the oscillation frequency, at the time-instance when the angular velocity of the airfoil goes through a peak, we can gain significant insight into the phase relationship between the fluid and structure. We also showed the ability of this method to capture the difference in timescales between the oscillation frequency and flow structures, by analyzing the decomposition of the flow around airfoils pitching with the same amplitude but different frequencies.

The formulation and applications of this novel DMD methodology discussed here have been published in reference [151].

Chapter 7

The force and moment partitioning method

The characterization of the forces and moments induced on surfaces by fluid flows has been a subject of interest since the earliest studies of fluid mechanics. This is particularly true within the domains of aerodynamics and fluid-structure interactions, where these flow-induced loads play a central role in much of the physics of these problems. Consequently, insight into the mechanisms that underlie the generation of fluid dynamic loads on surfaces is crucial in our ability to analyze, model and predict the behaviour of a large variety of problems.

In this discussion, we are particularly interested in the pressure-induced loads on a surface within a flow. The force and moment induced by the pressure

in a flow-field, denoted by p, on an immersed body whose surface is represented by B are given by,

$$\vec{F}_p = \int_B p\,\hat{n}\,dS \quad \text{and} \quad \vec{M}_p = \int_B p\left[\left(\vec{X} - \vec{X}_c\right) \times \hat{n}\right] dS, \tag{7.1}$$

respectively, where $\vec{X}$ and $\hat{n}$ are the position vector and unit normal vector at any point on the surface B and $\vec{X}_c$ is the point about which the moment is calculated. These forces and moments are usually computed in a simulation by directly evaluating these integrals on the surface of the immersed body. However, due to the elliptic nature of pressure in incompressible fluids, the pressure at any point in space is simultaneously influenced by the entire flow-field surrounding it. The induced pressure on the surface B therefore incorporates the effect of various physically distinct mechanisms – such as multiple vortices in its vicinity, shear/boundary layers, as well as added-mass and viscous diffusion effects. It is not immediately obvious how the individual contributions of each of these mechanisms can be disentangled within the total pressure-induced force and moment. The method presented here therefore aims to demonstrate one such partitioning of the total force and moment into contributions from distinct physical mechanisms.

This method is based on the work of Quartappelle and Napolitano [93], who showed that the pressure-induced forces and moments on an immersed body

can be written in terms of velocity-field gradients by projecting the Navier-Stokes equations onto the gradient of an appropriately constructed auxiliary potential field. The physical relevance of the terms in this projection-based approach was later recognized by Chang [94] and Zhang et al. [95]. The current partitioning is based on these prior formulations, but the specific form derived and used here is different due to our emphasis on vortex-induced pressure.

The force and moment partitioning is presented in dimensionless form, where the force/moment coefficients, as well as velocity-field quantities, are non-dimensionalized using the velocity scale U_∞, and length scale L. Hence the force coefficient on the immersed body in the i-direction is given by $C_{F_i} = F_i/(\frac{1}{2}\rho U_\infty^2 L)$, where F_i is the dimensional form of this total force. Similarly, the moment coefficient in the k-direction is given by $C_{M_k} = M_k/(\frac{1}{2}\rho U_\infty^2 L^2)$, where M_k is the dimensional form of the total moment.

The method presented here partitions these force and moment coefficients into the following components:

$$C_{F_i} = C_{F_i}^{\kappa} + C_{F_i}^{\omega} + C_{F_i}^{\sigma} + C_{F_i}^{\Phi} + C_{F_i}^{\Sigma} \tag{7.2}$$

$$C_{M_k} = C_{M_k}^{\kappa} + C_{M_k}^{\omega} + C_{M_k}^{\sigma} + C_{M_k}^{\Phi} + C_{M_k}^{\Sigma} \tag{7.3}$$

Here the superscripts represent different physically identifiable components of the force/moment on the immersed body. The contribution associated with the

kinematics of the body (i.e. acceleration-associated effects) are represented by the superscript κ, the vorticity-induced components by ω, the effect of viscous shear and diffusion is denoted by σ, effects due to the irrotational component of the flow are represented by Φ, and the contribution from the flow and vorticity on the outer boundaries of the spatial domain is given by Σ.

7.1 The force partitioning method: Theory and derivation

We begin with defining the setup of the force partitioning problem. We would like to partition the flow-induced force in the i-direction on an immersed body. The surface of the immersed body is denoted as B, and it is immersed in a fluid domain where the volume contained by the fluid, external to the body, is denoted as V_f. This fluid domain is bounded externally by the surface Σ, and internally by B. The unit normal vector $\hat{n}$, defining the orientation at every point along the bounding surfaces B and Σ, points out from the fluid volume (into the surfaces B and Σ). The position vector of every point along these surfaces is denoted by $\vec{X}$. A schematic of this setup is shown in figure 7.1.

We start the derivation with the Navier-Stokes momentum equation, writ-

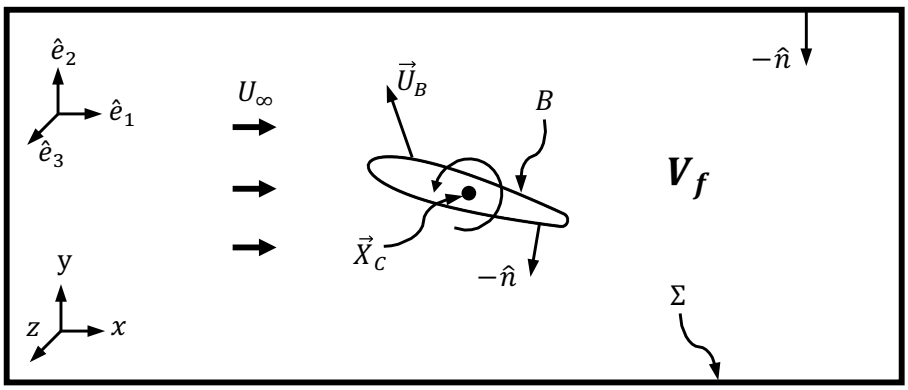

Figure 7.1: Schematic of the problem setup for the force and moment partitioning method, along with relevant symbols.

ten in the following form,

$$\frac{\partial \vec{u}}{\partial t} + \vec{u} \cdot \nabla \vec{u} = -\nabla p + \frac{1}{Re} \nabla^2 \vec{u} \tag{7.4}$$

An auxiliary potential, ϕ_i, is constructed at every time-instant, which is a function of the instantaneous position and shape of the immersed body as well as the outer domain boundary. This potential is defined as:

$$\nabla^2 \phi_i = 0, \quad \text{with} \quad \hat{n} \cdot \nabla \phi_i = \begin{cases} n_i \ , \ \text{on } B \\ \\ 0 \ \ , \ \text{on } \Sigma \end{cases} \tag{7.5}$$

The Navier-Stokes equation (7.4) is now projected on to the gradient of this auxiliary potential, and the result is integrated over the volume of the fluid

domain, V_f:

$$\int_{V_f} \frac{\partial \vec{u}}{\partial t} \cdot \nabla \phi_i \, dV + \int_{V_f} \left(\vec{u} \cdot \nabla \vec{u} \right) \cdot \nabla \phi_i \, dV$$
$$= - \int_{V_f} \nabla p \cdot \nabla \phi_i \, dV + \frac{1}{Re} \int_{V_f} \left(\nabla^2 \vec{u} \, \right) \cdot \nabla \phi_i \, dV. \tag{7.6}$$

We now simplify each term of the above equation separately, starting with the pressure term (first term) on the right-hand side as follows:

$$\int_{V_f} \nabla p \cdot \nabla \phi_i \, dV = \int_{V_f} \nabla \cdot (p \nabla \phi_i) \, dV. \tag{7.7}$$

Using the divergence theorem,

$$\int_{V_f} \nabla \cdot (p \nabla \phi_i) \, dV = \int_{B+\Sigma} p \, \vec{n} \cdot \nabla \phi_i \, dS = \int_B p \, n_i \, dS \tag{7.8}$$

where the last step follows from the boundary condition on the field ϕ_i. Equation (7.8) is evidently the force in the i-direction induced on the body due to the surface pressure distribution exerted by the surrounding fluid.

The viscous term, which is the second term on the right-hand side of equa-

tion (7.6), is treated as follows:

$$\int_{V_f} \left(\nabla^2 \vec{u}\,\right) \cdot \nabla \phi_i \, dV = -\int_{V_f} (\nabla \times \vec{\omega}) \cdot \nabla \phi_i \, dV$$
$$= -\int_{B+\Sigma} \hat{n} \cdot (\vec{\omega} \times \nabla \phi_i) \, dS = \int_{B+\Sigma} (\vec{\omega} \times \hat{n}) \cdot \nabla \phi_i \, dS. \tag{7.9}$$

Finally, we simplify the unsteady term (which is the first term in equation 7.6). On account of the incompressibility constraint, $\nabla \cdot \vec{u} = 0$, and the divergence theorem, we have,

$$\int_{V_f} \frac{\partial \vec{u}}{\partial t} \cdot \nabla \phi_i \, dV = \int_{V_f} \nabla \cdot \left(\frac{\partial \vec{u}}{\partial t} \phi_i \right) dV = \int_{B+\Sigma} \vec{n} \cdot \left(\frac{\partial \vec{u}}{\partial t} \phi_i \right) dS. \tag{7.10}$$

From the definition of the Lagrangian derivative, $d\vec{u}/dt = \partial \vec{u}/\partial t + \vec{u} \cdot \nabla \vec{u}$,

$$\int_{B+\Sigma} \vec{n} \cdot \left(\frac{\partial \vec{u}}{\partial t} \phi_i \right) dS = \int_{B+\Sigma} \vec{n} \cdot \left[\left(\frac{d\vec{u}}{dt} - \vec{u} \cdot \nabla \vec{u} \right) \phi_i \right] dS$$
$$= \int_{B+\Sigma} \vec{n} \cdot \left(\frac{d\vec{u}}{dt} \phi_i \right) dS - \int_{V_f} \nabla \cdot \left[\left(\vec{u} \cdot \nabla \vec{u} \right) \phi_i \right] dV. \tag{7.11}$$

We now plug equations (7.8), (7.9) and (7.11) into equation (7.6), and rearrange terms as follows,

$$\int_B p \, n_i \, dS = -\int_{B+\Sigma} \vec{n} \cdot \left(\frac{d\vec{u}}{dt} \phi_i \right) dS + \int_{V_f} \nabla \cdot \left[\left(\vec{u} \cdot \nabla \vec{u} \right) \phi_i \right] dV$$
$$- \int_{V_f} \left(\vec{u} \cdot \nabla \vec{u} \right) \cdot \nabla \phi_i \, dV + \int_{B+\Sigma} \frac{1}{Re} (\vec{\omega} \times \vec{n}) \cdot \nabla \phi_i \, dS. \tag{7.12}$$

This can be simplified and written in the following form,

$$\int_B p\, n_i dS = -\int_{B+\Sigma} \vec{n} \cdot \left(\frac{d\vec{u}}{dt}\phi_i\right) dS + \int_{V_f} \left[\nabla \cdot \left(\vec{u} \cdot \nabla \vec{u}\right)\right] \phi_i dV + \int_{B+\Sigma} \frac{1}{Re}(\vec{\omega} \times \vec{n}) \cdot \nabla \phi_i dS \tag{7.13}$$

where the three terms on the right-hand side correspond to the pressure loading due to unsteady effects, fluid velocity gradients in the flow around the immersed body, and viscous effects on the surfaces respectively.

We can derive further physical insight into the flow gradient-related effects, i.e. the second term on the right-hand side of equation (7.13), by relating this term to local flow kinematics described by the velocity-gradient tensor, $\nabla \vec{u}$. In particular, it can be shown that the second-invariant of $\nabla \vec{u}$, which is referred to as Q, can be directly related to this term in the following manner:

$$Q = \frac{1}{2}\left[\mathrm{Tr}\left(\nabla \vec{u}\right)^2 - \mathrm{Tr}\left(\nabla \vec{u}^2\right)\right] = -\frac{1}{2}\nabla \cdot \left(\vec{u} \cdot \nabla \vec{u}\right). \tag{7.14}$$

In the above expression, $\mathrm{Tr}(\cdot)$ is the trace of a tensor. Furthermore, Q also corresponds to the difference between local rotation versus strain in the flow-field. This is clear when it is expressed in the following form,

$$Q = \frac{1}{2}\left(||\mathbf{\Omega}||^2 - ||\mathbf{S}||^2\right) \tag{7.15}$$

where $||\cdot||$ is the Frobenius norm of a tensor. The symbols $\mathbf{\Omega}$ and $\mathbf{S}$ are the anti-symmetric and symmetric parts of $\nabla\vec{u}$ respectively, and are given by $\mathbf{\Omega} = \frac{1}{2}\left[\nabla\vec{u} - (\nabla\vec{u})^T\right]$ and $\mathbf{S} = \frac{1}{2}\left[\nabla\vec{u} + (\nabla\vec{u})^T\right]$.

This result can be used in equation (7.13), to rewrite the partitioning of pressure-induced forces as follows:

$$\int_B p\, n_i\, dS = -\int_{B+\Sigma} \hat{n}\cdot\left(\frac{d\vec{u}}{dt}\phi_i\right)dS - \int_{V_f} 2Q\ \phi_i dV + \int_{B+\Sigma}\frac{1}{Re}(\vec{\omega}\times\hat{n})\cdot\nabla\phi_i dS. \tag{7.16}$$

It is now clear from the above equation that the second term on the right-hand side directly relates local flow deformation to the generation of forces on the immersed body. In particular, the sign of Q allows us to separate rotation-induced loading from strain-induced loading.

Additional insight into the physical relevance of the terms in equation (7.16) can be gained by separating the contributions of rotational (vortical) from irrotational flow components in the force/moment production. This is done using the Helmholtz decomposition [152] as follows:

$$\vec{u} = \vec{u}_\Phi + \vec{u}_v = \nabla\Phi + \nabla\times\mathbf{A} \tag{7.17}$$

where Φ and A are scalar and vector potentials respectively. The velocity components $\vec{u}_\Phi$ and $\vec{u}_v$ in the above decomposition are the irrotational and rota-

tional (vortical) components of the velocity field respectively. Note that fields Φ and $\mathbf{A}$ of the Helmholtz decomposition could in principle be non-unique. However, the non-uniqueness associated with an additive harmonic function is eliminated by the application of wall-normal velocity boundary conditions in the calculation of Φ. Furthermore, the fact that the force decomposition depends on the gradient of Φ and curl of $\mathbf{A}$ eliminates any dependence on additive constants in Φ and $\mathbf{A}$.

Using this decomposition, we can write $Q = Q_\Phi + Q_v$. Here $Q_\Phi = -\nabla \cdot \big(\vec{u}_\Phi \cdot \nabla \vec{u}_\Phi\big)/2$ is purely irrotational, and $Q_v = -\big[\nabla \cdot \big(\vec{u}_v \cdot \nabla \vec{u}_v\big) + \nabla \cdot \big(\vec{u}_v \cdot \nabla \vec{u}_\Phi\big) + \nabla \cdot \big(\vec{u}_\Phi \cdot \nabla \vec{u}_v\big)\big]/2$ is non-zero only in the presence of non-zero rotational flow, i.e. where $\vec{u}_v \neq 0$ (which implies $\vec{\omega} \neq 0$). The second term in the right-hand side of equation (7.16) can then be decomposed into contributions from vortical and irrotational effects in the following manner:

$$
\begin{aligned}
-\int_{V_f} 2Q\ \phi_i\, dV &= -\int_{V_f} 2Q_v\ \phi_i\, dV - \int_{V_f} 2Q_\Phi\ \phi_i\, dV \\
&= -\int_{V_f} 2Q_v\ \phi_i\, dV + \int_{V_f} \nabla \cdot \Big(\vec{u}_\Phi \cdot \nabla \vec{u}_\Phi\Big)\ \phi_i\, dV \\
&= -\int_{V_f} 2Q_v\ \phi_i\, dV + \int_{V_f} \nabla \cdot \Big[\nabla\Big(\frac{1}{2}\vec{u}_\Phi \cdot \vec{u}_\Phi\Big)\Big]\ \phi_i\, dV. \qquad (7.18)
\end{aligned}
$$

In the above equation, each term on the right-hand side (7.18) has a clear physical significance. The purely irrotational term (last term in the right-hand side of 7.18) quantifies the force generated exclusively by irrotational or potential

flow mechanisms in the flow-field. The first term on the right-hand side of equation (7.18), due to its dependence on Q_v, is non-zero only in the presence of non-zero vorticity (where $\vec{u}_v \neq 0$). This term therefore corresponds to the component of force generated by vorticity-induced effects in the flow-field. More specifically, its dependence on Q_v suggests that this is the pressure-force generated by vorticity-induced strain and rotation in the flow-field.

It can be shown, by following along the lines of ref. [153], that the irrotational term in equation (7.18) is small in most cases and goes to zero in sufficiently large domains. Therefore for clarity, we refer to this purely irrotational contribution as $\int_{V_f} \nabla \cdot \left[\nabla\left(\frac{1}{2}\vec{u}_\Phi \cdot \vec{u}_\Phi\right)\right] \, \phi_i \, dV = \epsilon^\Phi_{M_k}$ (noting that $\epsilon^\Phi_{M_k} \approx 0$ in most situations), and rewrite the vorticity-induced force in the following manner:

$$-\int_{V_f} 2Q_v \, \phi_i \, dV = -\int_{V_f} 2Q \, \phi_i \, dV - \epsilon^\Phi_{M_k}. \tag{7.19}$$

Lastly, we note that equation (7.16) represents the partitioning of the forces induced solely by the pressure distribution on the immersed body. However, the total force also includes shear contributions. The shear force coefficient in the i-direction can be written as $C^\nu_{F_i} = -(1/Re)\int_B (\vec{\omega} \times \hat{n}) \cdot \hat{e}_i \, dS$, where $\hat{e}_i$ is the Cartesian basis vector in the i-direction.

Using equations (7.18), (7.19) and the above expression for the force induced by viscous shear on the surface in equation (7.16), we arrive at the following

partitioning of the total force on the body:

$$C_{F_i} = -\int_B \hat{n} \cdot \left(\frac{d\vec{U}_B}{dt}\phi_i\right) dS \tag{7.20}$$

$$- \int_{V_f} 2Q\ \phi_i dV - \epsilon^{\Phi}_{F_i} \tag{7.21}$$

$$+ \int_B \frac{1}{Re}\Big\{(\vec{\omega} \times \hat{n}) \cdot \nabla\phi_i - (\vec{\omega} \times \hat{n}) \cdot \hat{e}_i\Big\} dS \tag{7.22}$$

$$+ \int_{V_f} \nabla \cdot \Big[\nabla\Big(\frac{1}{2}\vec{u}_\Phi \cdot \vec{u}_\Phi\Big)\Big]\ \phi_i dV \tag{7.23}$$

$$+ \int_\Sigma \left[-\hat{n} \cdot \left(\frac{d\vec{u}}{dt}\phi_i\right) + \frac{1}{Re}(\vec{\omega} \times \hat{n}) \cdot \nabla\phi_i \right] dS. \tag{7.24}$$

The expressions in (7.20), (7.21), (7.22), (7.23) and (7.24) correspond to the force partitioning components $C^{\kappa}_{F_i}$, $C^{\omega}_{F_i}$, $C^{\sigma}_{F_i}$, $C^{\Phi}_{F_i}$ and $C^{\Sigma}_{F_i}$ respectively shown in equation (7.2). Note that in (7.23) of the above equation, $\epsilon^{\Phi}_{F_i} \approx 0$ in most cases.

We can hence write the final form for the force partitioning as follows:

$$C_{F_i} = C^{\kappa}_{F_i} + C^{\omega}_{F_i} + C^{\sigma}_{F_i} + C^{\Phi}_{F_i} + C^{\Sigma}_{F_i}\ , \text{where} \tag{7.25}$$

$$C^{\kappa}_{F_i} = -\int_B \hat{n} \cdot \left(\frac{d\vec{U}_B}{dt}\phi_i\right) dS \tag{7.26}$$

$$C^{\omega}_{F_i} = -\int_{V_f} 2Q\ \phi_i dV - \epsilon^{\Phi}_{F_i} \approx -\int_{V_f} 2Q\ \phi_i\, dV \tag{7.27}$$

$$C^{\sigma}_{F_i} = \int_B \frac{1}{Re}\,(\vec{\omega} \times \hat{n}) \cdot \left(\nabla\phi_i - \hat{e}_i\right) dS \tag{7.28}$$

$$C^{\Phi}_{F_i} = \int_{V_f} \nabla \cdot \Big[\nabla\Big(\frac{1}{2}\vec{u}_\Phi \cdot \vec{u}_\Phi\Big)\Big]\ \phi_i dV \tag{7.29}$$

$$C^{\Sigma}_{F_i} = \int_\Sigma \left[-\hat{n} \cdot \left(\frac{d\vec{u}}{dt}\phi_i\right) + \frac{1}{Re}(\vec{\omega} \times \hat{n}) \cdot \nabla\phi_i \right] dS \tag{7.30}$$

7.2 The moment partitioning method

The partitioning of moments in the k-direction follows along the same lines as the above derivation. The key difference is the definition of the auxiliary potential, ψ_i, which takes the following form:

$$\vec{\nabla}^2\psi_k = 0, \;\; \text{with} \;\; \hat{n}\cdot\vec{\nabla}\psi_k = \begin{cases} \left[(\vec{X}-\vec{X}_c)\times\hat{n}\right]\cdot\hat{e}_k \;, \text{ on } B \\ \\ 0 \;\; , \text{ on } \Sigma \end{cases} \tag{7.31}$$

Further, the viscous shear-induced moment takes a different form from that shown in equation (7.28). The moment induced in the k-direction by surface shear is given by $C^{\nu}_{M_k} = -(1/Re)\int_B[(\vec{X}-\vec{X}_c)\times(\vec{\omega}\times\hat{n})]\cdot\hat{e}_k\,dS$, where $\hat{e}_k$ is the Cartesian basis vector in the k-direction. The partitioning of moments on the body can hence be written as,

$$C_{M_k} = -\int_B \hat{n}\cdot\left(\frac{d\vec{U}_B}{dt}\psi_k\right)dS \tag{7.32}$$

$$-\int_{V_f} 2Q\;\psi_k dV - \epsilon^{\Phi}_{M_k} \tag{7.33}$$

$$+\int_B \frac{1}{Re}\left\{(\vec{\omega}\times\hat{n})\cdot\nabla\psi_k - (\vec{\omega}\times\hat{n})\cdot\left[\hat{e}_k\times(\vec{X}-\vec{X}_c)\right]\right\}dS \tag{7.34}$$

$$+\int_{V_f}\nabla\cdot\left[\nabla\left(\frac{1}{2}\vec{u}_\Phi\cdot\vec{u}_\Phi\right)\right]\psi_k\,dV \tag{7.35}$$

$$+\int_\Sigma\left[-\hat{n}\cdot\left(\frac{d\vec{u}}{dt}\psi_k\right)+\frac{1}{Re}(\vec{\omega}\times\hat{n})\cdot\nabla\psi_k\right]dS. \tag{7.36}$$

The expressions in (7.32), (7.33), (7.34), (7.35) and (7.36) correspond to the moment partitioning components $C^{\kappa}_{M_k}$, $C^{\omega}_{M_k}$, $C^{\sigma}_{M_k}$, $C^{\Phi}_{M_k}$ and $C^{\Sigma}_{M_k}$ respectively shown in equation (7.3). As in the force partitioning, the term $\epsilon^{\Phi}_{M_k} \approx 0$ (7.35 of the above equation) in most situations.

The final form for the moment partitioning is therefore as follows:

$$C_{M_k} = C^{\kappa}_{M_k} + C^{\omega}_{M_k} + C^{\sigma}_{M_k} + C^{\Phi}_{M_k} + C^{\Sigma}_{M_k} \text{ , where} \tag{7.37}$$

$$C^{\kappa}_{M_k} = -\int_B \hat{n} \cdot \left(\frac{d\vec{U}_B}{dt}\psi_k\right) dS \tag{7.38}$$

$$C^{\omega}_{M_k} = -\int_{V_f} 2Q\ \psi_k dV - \epsilon^{\Phi}_{M_k} \approx -\int_{V_f} 2Q\ \psi_k\, dV \tag{7.39}$$

$$C^{\sigma}_{M_k} = \int_B \frac{1}{Re}(\vec{\omega} \times \hat{n}) \cdot \left\{\nabla\psi_k - \left[\hat{e}_k \times (\vec{X} - \vec{X}_c)\right]\right\} dS \tag{7.40}$$

$$C^{\Phi}_{M_k} = \int_{V_f} \nabla \cdot \left[\nabla\left(\frac{1}{2}\vec{u}_\Phi \cdot \vec{u}_\Phi\right)\right]\ \psi_k\, dV \tag{7.41}$$

$$C^{\Sigma}_{M_k} = \int_\Sigma \left[-\hat{n} \cdot \left(\frac{d\vec{u}}{dt}\psi_k\right) + \frac{1}{Re}(\vec{\omega} \times \hat{n}) \cdot \nabla\psi_k \right] dS \tag{7.42}$$

7.3 Physical significance of each term

We see that the terms in equations (7.26) and (7.38) depend only on the geometry and velocity of the immersed surface B. Due to this, these terms represent the kinematic components of the total loading. Further, it can be shown using the Helmholtz decomposition that this term encapsulates the loading generated by the classical inviscid (potential flow) added-mass as well as a

novel centripetal added-mass mechanism.

The effect of viscosity on forces and moments on the surface are given by the components (7.28) and (7.40). These viscous loads in fact include two distinct mechanisms – the first term in (7.28) and (7.40) is the pressure-induced force and moment respectively due to viscous momentum diffusion; and the second term in (7.28) and (7.40) represents the effect of shear on the surface of the body.

Irrotational or potential flow effects, purely due to the irrotational component of the velocity field ($\vec{u}_\Phi$) are isolated in the terms (7.29) and (7.41). As mentioned earlier, these components can be shown to be small in most cases [153]. The last term, shown in equations (7.30) and (7.42) represents the effect of the velocity field and flow acceleration on the outer boundary of the domain. It can be shown that this term also goes to zero for sufficiently large domains [153].

Of primary interest in the research discussed here is the vorticity-induced component of force and moment, which is shown in equations (7.27) and (7.39). The vorticity-induced force and moment quantify the loading generated by vorticity-induced deformations in the flow-field. It is interesting to point out that the dependence of the vorticity-induced force and moment on Q suggests a mechanism for the production of this force/moment component based on the local flow kinematics. Depending on the sign of Q, equations (7.27) and (7.39) indicate that $C^{\omega}_{F_i}$ and $C^{\omega}_{M_k}$ are dictated by vorticity-induced strain ($Q < 0$) and

rotation ($Q > 0$) in the flow. The quantity Q has long been used as a criterion for the detection of vortices in a flow-field as regions where local rotation dominates over strain ($Q > 0$). Its appearance in the vortex-induced force/moment is interesting because it shows that Q is not just a metric describing local flow kinematics, but that it has a direct bearing on force production. This connection between Q and pressure-induced force can be further reinforced by noting that the non-dimensional pressure Poisson equation for incompressible flow can be expressed as $\vec{\nabla}^2 p = -\vec{\nabla} \cdot \left(\vec{u} \cdot \vec{\nabla} \vec{u} \right) = 2Q$. Thus, Q is in fact the source term in the pressure Poisson equation, and it is therefore not surprising that it also appears in the partitioned forces and moments. The relevance of this relationship between Q and pressure is explored in chapter 10.

In addition to estimating the total aerodynamic loading due to the distinct physical mechanisms discussed above, the volume-integral form of the terms in (7.27) and (7.39) indicates that the contribution of any *individual* vortex to the aerodynamic loading on an immersed body can be determined by constructing the integrals in (7.27) and (7.39) over the precise volume occupied by the vortex of interest. However, the ability to construct integration volumes that isolate the effect of individual flow structures in highly dynamic vortex-dominated flows is itself a challenge, and chapter 9 describes our approach to this task. We note that, in principle, the partitioned aerodynamic loads can be computed independent of the method used to generate these flow-fields, thereby allowing

this method to be used with data from any simulation and potentially, even from an experiment. In this context, the force/moment partitioning method presented here may be viewed as a data-driven method for the analysis of any flow-field with an immersed body.

7.4 An example: Force and moment on a pitching airfoil

We now present an example of the force and moment partitioning outlined above, for a sample case of a two-dimensional airfoil pitching about mid-chord, at $Re = U_\infty C/\nu = 1000$ (where C and U_∞ are chord-length and free-stream velocity). The airfoil is forced to pitch sinusoidally with dimensionless frequency, $f^* = fC/U_\infty = 0.25$, and amplitude $A_\theta = 25^\circ$. Figure 7.2(a) shows a comparison of the total force coefficient in the vertical direction, i.e. the coefficient of lift C_L (where $i = 2$ and $C_{F_2} = C_L$), compared with the sum of the kinematic, vorticity-induced, and viscous components ($C_L^\kappa + C_L^\omega + C_L^\sigma$). Similarly, figure 7.2(b) shows a comparison of the total pitching moment coefficient, C_M (where $k = 3$), with the sum of the terms ($C_M^\kappa + C_M^\omega + C_M^\sigma$). We see that the kinematic, vorticity-induced, and viscous components account for the bulk of the total force and moment production. In fact, it can be shown that irrotational and outer-boundary effects go to zero for sufficiently large domains (see ref. [153]). We also see from this

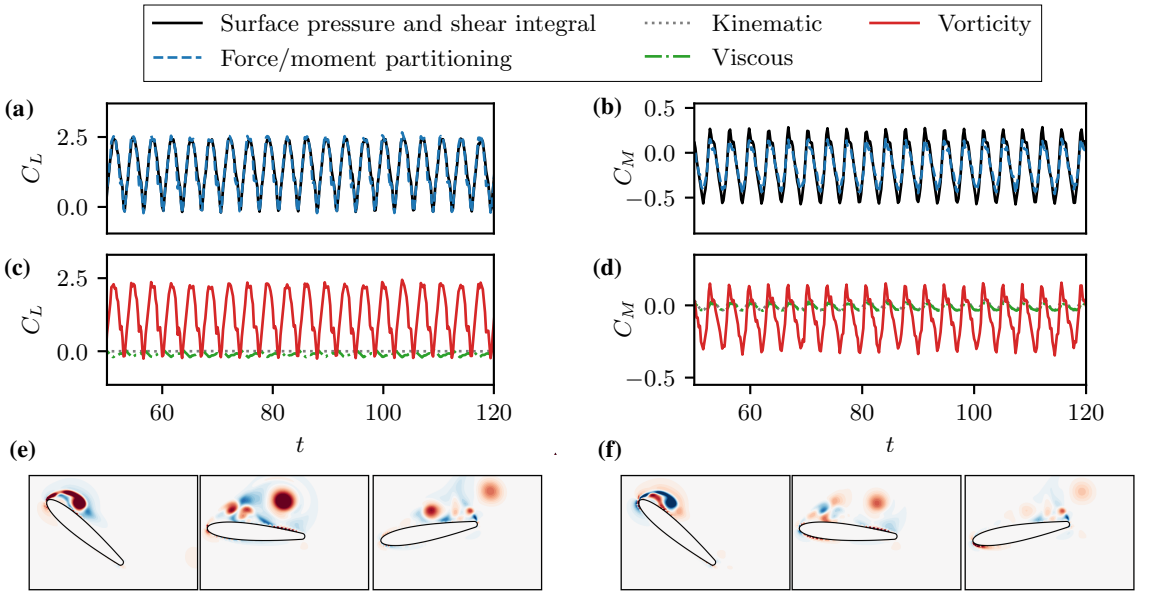

Figure 7.2: Force and moment partitioning for a sample case of a sinusoidally pitching airfoil with dimensionless frequency $f^* = 0.25$ and amplitude $A_\theta = 25°$. (a) Total lift coefficient (C_L) calculated using the conventional surface integral of pressure (equation 7.1) and viscous shear, compared with sum of force partitioning terms, $C_L \approx C_L^\kappa + C_L^\omega + C_L^\sigma$; (b) Comparison of total moment coefficient (C_M) calculated using surface integral compared, with sum of moment partitioning terms, $C_M \approx C_M^\kappa + C_M^\omega + C_M^\sigma$; (c) Comparison of $C_{F_i}^\kappa$, $C_{F_i}^\omega$ and $C_{F_i}^\sigma$; (d) Comparison of $C_{M_k}^\kappa$, $C_{M_k}^\omega$ and $C_{M_k}^\sigma$; (e) Snapshots of vorticity-induced force distribution at three phases during a pitch-down cycle; (f) Snapshots of vorticity-induced moment distribution at three phases during a pitch-down cycle.

comparison that, as expected in these vortex-dominated flows, the vorticity-induced component contributes a much larger lift and moment than the other two components. Lastly, figures 7.2(e) and 7.2(f) show snapshots of the spatial distribution of the vorticity-induced force and moment respectively, i.e. the integrands in equations (7.27) and (7.39), at three time-instances during the pitch-down motion of the airfoil. In both cases we see the strong influence of the leading-edge vortex (LEV). In the context of the lift-force, the LEV induces a strong positive lift, whereas the moment due to the LEV changes sign as it crosses the pitch axis located at mid-chord.

Chapter 8

Flow-induced vibration of cylinders: Insights from force and energy partitioning

In this chapter, we present an application of the force partitioning and energy-based methods discussed in chapters 7 and 4 to the analysis of flow-induced vibration of cylinders. The flow-induced heave oscillations of cylinders is a fundamental problem in the domain of fluid-structure interactions and has been extensively studied in the past [129, 136, 154].

The oscillation response of an elastically-mounted cylinder when immersed in a freestream flow has been shown to depend on many parameters such as Reynolds number and reduced velocity (U^*, defined in section 2.2.2) [52–54].

It also consists of several distinct subcritical as well as supercritical response branches along with associated bifurcations between these branches [54–56]. In past analyses, it as been shown that these response branches correspond to different patterns of vortex shedding in the wake and variations in the lift force experienced by the cylinder [64]. However, these have been largely qualitative analyses, i.e., the effect of changes in vortex shedding has not been directly and quantitatively tied to the forces experienced by the cylinder.

Such a quantitative analysis is a task that is well-suited to the force partitioning method due to its ability to quantify the forcing induced by distinct mechanisms as well as different spatial regions and features of the flow. Furthermore, by using this in conjunction with energy extraction, it is possible to directly relate these different force production mechanisms to the work done to oscillate the cylinder. The focus of this chapter is hence three-fold: (1) we demonstrate the use of a force partitioning method to dissect the contributions of different flow phenomena in driving flow-induced vibrations; (2) an energy-based analysis is performed to rigorously quantify the effect of different force-producing mechanisms on oscillating cylinders, and also to identify bifurcations in the flow-induced oscillation response of a system using energy maps; (3) an application of these tools in the context of shape-effects in flow-induced vibrations is presented to highlight the interaction of these mechanisms in producing bifurcations.

This study is performed using the two-dimensional aeroelastic model discussed in section 2.2.2, wherein a finite-mass cylinder which is mounted on a linear spring is immersed in a freestream flow. The cylinder is allowed to perform heave oscillations transverse to the direction of the freestream flow. Furthermore, the cylinder has (in general) a non-circular shape has horizontal and vertical dimensions L and D respectively, resulting in aspect-ratio $AR = L/D$. For all cases discussed here, the cylinders are initialized at their equilibrium positions, with zero heave velocity. A uniform freestream flow, U_∞, is specified at the upstream boundary. In the case of flow-induced oscillation, transverse lift force on the cylinder initiates heave oscillations, which are allowed to grow until a stationary state is achieved. We refer to this maximum stationary state oscillation amplitude as A_y^*. For forced oscillations, the cylinder is oscillated sinusoidally with prescribed amplitude (A_y^*) and frequency (f^*) until a stationary state is achieved.

8.1 Force and energy partitioning

The force partitioning method used in this work is closely related to that discussed in chapter 7, but is a slight variation due to the fact that it is derived from the Lamb-Gromeka form of the Navier-Stokes equations. For details on this partitioning, the reader is referred to the work of Zhang [95, 153] and

Menon & Mittal [79].

Below we present this partitioning for the transverse force coefficient on the cylinder, i.e. the lift coefficient given by $C_L = F_L/(\frac{1}{2}\rho U_\infty^2 D)$, where F_L is the dimensional lift force. Furthermore, we focus only on the effects of the kinematic force (C_L^κ), the vorticity-induced force (C_L^ω), and the viscous force (C_L^σ) since these are the dominant terms (as we will show below and was also the case in the example shown in section 7.4). This partitioning takes the following form,

$$C_L = C_L^\kappa + C_L^\omega + C_L^\sigma + C_L^\Phi + C_L^\Sigma \approx C_L^\kappa + C_L^\omega + C_L^\sigma \text{ , where} \tag{8.1}$$

$$C_L^\kappa = -\int_B \vec{n} \cdot \frac{d\vec{U}_B}{dt}\phi_2 dS - \int_B \frac{1}{2}|\vec{U}_B|^2 n_i dS \tag{8.2}$$

$$C_L^\omega = \int_{V_f} \left\{ \Big[\nabla \cdot (\vec{\omega} \times \vec{u})\Big]\phi_2 + \nabla \cdot \Big[\nabla\Big(\frac{1}{2}\vec{u}_v \cdot \vec{u}_v + \vec{u}_\Phi \cdot \vec{u}_v\Big)\phi_2\Big] \right\} dV \tag{8.3}$$

$$C_L^\sigma = \frac{1}{Re}\int_B (\vec{\omega} \times \vec{n}) \cdot \Big(\nabla\phi_2 - \hat{e}_i\Big) dS \tag{8.4}$$

In the above equations, ϕ_2 is defined as in equation (7.5) with $i = 2$, and $\vec{\omega} = \nabla \times \vec{u}$ is the vorticity. All other quantities are as defined in section 7.1.

The energy partitioning is based on the fact that the flow-induced oscillations are driven by the energy extracted by the elastic system from the fluid flow. Over one oscillation cycle, the total non-dimensional energy extracted by

the heaving cylinder from the fluid, which we refer to as E^*, can be written as

$$E^* = \int_t^{t+T^*} C_L \dot{y}^* dt \tag{8.5}$$

where $T^* = 1/f^*$ is the dimensionless period of the cycle, and $\dot{y}^*$ is the dimensionless vertical velocity of the cylinder. By partitioning the force on the cylinder as in equation (8.1), we can also partition the work done by (or energy extracted from) each of these force components in driving flow-induced oscillations. Therefore the total energy gained by the cylinder in each oscillation cycle can correspondingly be partitioned into contributions from each component in the force partitioning using equations (8.1) and (8.5). This is given by:

$$E^* \approx E^*_\kappa + E^*_\omega + E^*_\sigma \tag{8.6}$$

We now show a sample force partitioning for a forced-oscillation case with $AR = 1.15$ and $A^*_y = 0.05$. In figure 8.1(a) we plot a comparison of the sum of contributions from these terms $(C^\omega_L + C^\kappa_L + C^\sigma_L)$ with the total lift force on the cylinder. We see that these components account for most of the force on the oscillating cylinder. This is expected for domains that are sufficiently large [153]. This also verifies the adequacy of the integration domain used here. In figure 8.1(b) we show time-series plots of the vorticity-induced force, kinematic force, and viscous force for this case. We see that C^κ_L shows a sinusoidal behaviour,

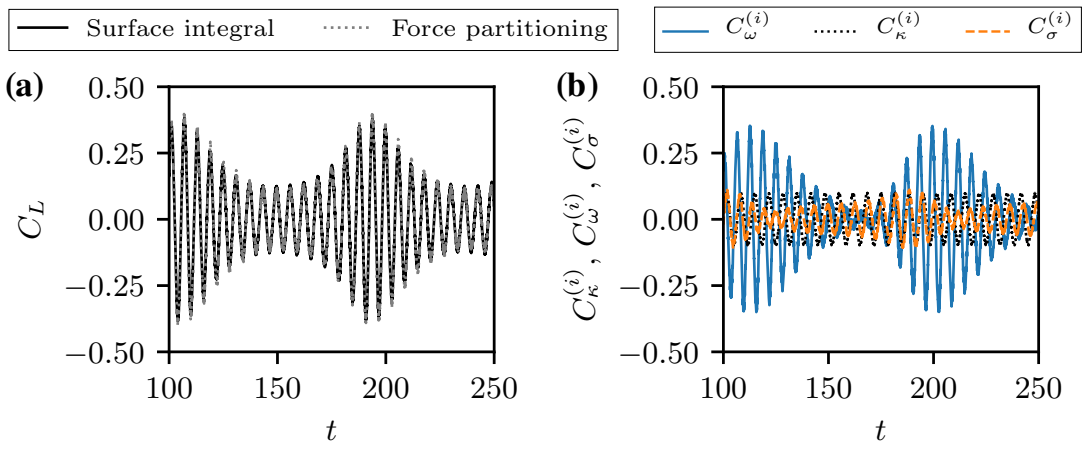

Figure 8.1: Partitioning of the lift force on a cylinder with aspect-ratio $AR = 1.15$, oscillation amplitude $A_y^* = 0.05$, and oscillation frequency $f^* = 0.15$. (a) Total lift-force compared with sum of force contributions from vorticity-induced (C_L^ω), kinematic (C_L^κ), and viscous force (C_L^σ) components; (b) Time-series plots of vorticity-induced, kinematic, and viscous force contributions to lift.

which is dictated by the sinusoidal oscillation of the cylinder due to the fact that it is related to added-mass effects in the absence of rotation [153]. Another observation from figure 8.1(b) is that the vorticity-induced force accounts for the bulk of the force on the cylinder during periods of high lift force. The amplitude of viscous force oscillations too shows variations, however the maximum amplitude is much smaller than that of C_L^ω.

8.2 Effect of cylinder aspect-ratio on the amplitude response

We begin our discussion of the results by describing how changes in the the amplitude response and energy extracted by the cylinder from the flow are affected by the aspect-ratio of the oscillating cylinder. This discussion serves to highlight non-linearities in the amplitude response, dictated by the fact that changes in shape lead to changes in the relative contributions of the underlying mechanisms that drive the oscillation. The behaviour discussed here will set the context for the subsequent application of the aforementioned partitioning methods in analyzing complex oscillation responses, and uncovering the origin of the bifurcations in the amplitude response.

8.2.1 Flow-induced oscillation response

We begin with a qualitative description of the flow-fields for some select flow-induced oscillation cases. Figure 8.2 shows instantaneous vorticity contours of the flow for four different flow-induced oscillation cases at $Re = 100$, with aspect ratios $AR = 1.0$ and $AR = 1.15$, and reduced velocity varying from $U^* = 5.0$ to $U^* = 7.5$. The snapshots are shown after each system has achieved stationary state oscillations. The top panel in figure 8.2 shows snapshots of the

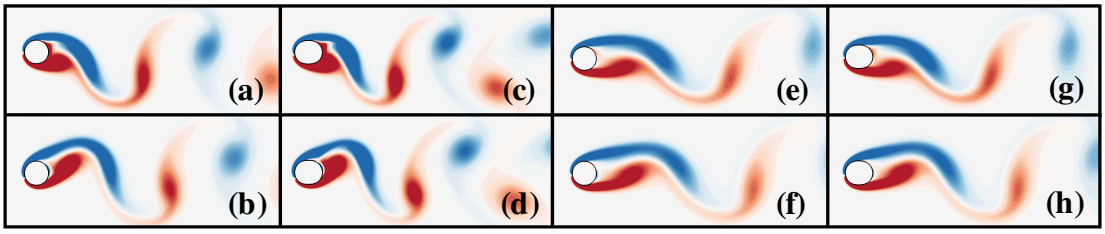

Figure 8.2: Snapshots of the flow around transversely oscillating cylinders with different aspect ratios (AR) and reduced velocity (U^*), at $Re = 100$. The flow is visualized using contours of Z-vorticity. The top panel shows snapshots close to the upper maximum of the oscillation cycle for each case, and the bottom panel show snapshots close to the mean position as the cylinder is moving downwards. Cases shown in (a)-(d) show large amplitude oscillations (of similar magnitude, $A_y^* \approx 0.49$) and (e)-(h) show relatively smaller oscillation amplitudes ($A_y^* \approx 0.28$); (a)-(b) $AR = 1.0$, $U^* = 6.0$; (c)-(d) $AR = 1.15$, $U^* = 5.0$; (e)-(f) $AR = 1.0$, $U^* = 7.5$; (c)-(d) $AR = 1.15$, $U^* = 7.0$.

flow at the time instance when the cylinder is at the position of maximum displacement, and the bottom panel shows snapshots when the cylinder is close to the mean position during the downward motion (position of maximum velocity). Further, figures 8.2(a)-(b) and 8.2(c)-(d) show two cases exhibiting large amplitude oscillations, with $A_y^* \approx 0.49$, while the two cases in figures 8.2(e)-(f) and 8.2(g)-(h) exhibit smaller amplitudes, with $A_y^* \approx 0.28$.

It is immediately apparent that the cases with larger amplitude oscillations, in figures 8.2(a)-(d), have wake vortices that are more closely spaced than the smaller amplitude cases in figures 8.2(e)-(h). This can be qualitatively assessed by simply counting the number of vortices within the frame of the flow visualizations shown. The reason for this is presumably because larger oscillation amplitudes lead to stronger shear layers, and thus earlier roll-up. Further,

even between the two cases with large amplitude, the case with $AR = 1.0$ and $U^* = 6.0$, in figures 8.2(a)-(b), shows a less tight (and possibly less staggered) vortex pattern in the wake as compared to the case with $AR = 1.15$ and $U^* = 5.0$, which is shown in figures 8.2(c)-(d). At the smaller amplitude of oscillation, the difference in wake shedding pattern between the two cases shown in figures 8.2(e)-(f) and 8.2(g)-(h) is less evident. However, we still see that the case with $AR = 1.0$ and $U^* = 7.5$, in figures 8.2(e)-(f), shows a slightly larger spatial wavelength in the wake (in the streamwise direction) than the case with $AR = 1.15$ and $U^* = 7.0$, in figures 8.2(g)-(h). Hence we see that, although the two large amplitude cases have similar oscillation amplitudes, as do the two smaller amplitude cases, a modest change in shape results in a qualitatively different flow. However, these plots and corresponding data do not immediately reveal the role that changes in vortex shedding patterns have on the flow-induced oscillation.

We now discuss the stationary-state amplitude response of flow-induced oscillations for a range of U^* and AR. In figure 8.3(a) we plot the maximum heave amplitude (A_y^*) at $Re = 100$ as a function of U^* for cylinders of different aspect-ratios. We see that the amplitude curves for all the aspect-ratios studied here show the familiar peak that is associated with the initial and lower branch of the cylinder response [129]. Further, the smaller aspect ratios show larger oscillation amplitudes through the entire range of U^* investigated here.

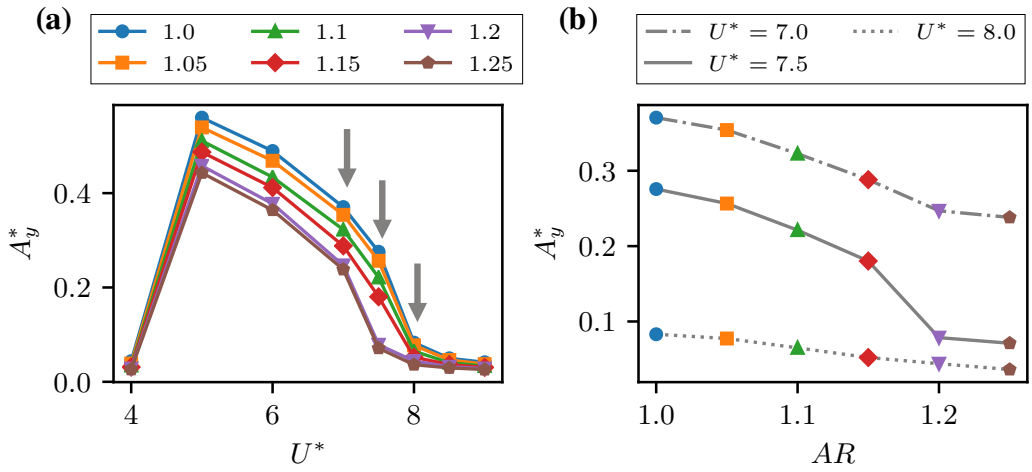

Figure 8.3: Heave amplitude response of flow-induced oscillations at $Re = 100$; (a) Maximum heave amplitude (A_y^*) versus reduced velocity (U^*), plotted for cylinders of various aspect ratios (AR); (b) Maximum heave amplitude as a function aspect ratio at three relevant values of U^*, i.e. $U^* = 7.0, 7.5, 8.0$. Symbols for different aspect ratios correspond to those in (a).

An interesting observation from figure 8.3 is that the U^*-extent of the synchronization regime depends on the aspect-ratio. This is particularly evident at the higher-U^* limit of the synchronization regime ($U^* \approx 7.5$), where we see that higher AR cylinders have a smaller synchronization region.

To more clearly underscore the effect of this AR-dependence on the amplitude response, figure 8.3(b) shows the heave amplitude response as a function of cylinder aspect-ratio for three select values of U^*. These values are indicated by arrows in figure 8.3(a), i.e. $U^* = 7.0$, 7.5 and $U^* = 8.0$. At $U^* = 7.0$, we see that the cylinders all show large amplitude oscillations, and the response is within the lower branch for all values of AR. At $U^* = 8.0$, which lies beyond the lower branch (the so-called desynchronization regime) for all values of AR, we

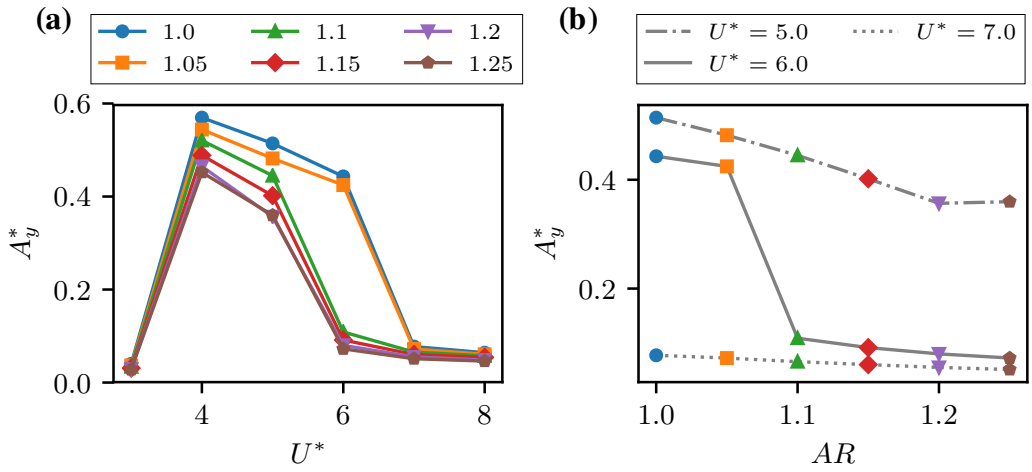

Figure 8.4: Heave amplitude response of flow-induced oscillations at $Re = 250$; (a) Maximum heave amplitude versus reduced velocity for different aspect-ratios; (b) Maximum heave amplitude as a function aspect ratio at $U^* = 5.0, 6.0, 7.0$.

see that A_y^* is small and decreases approximately linearly with increasing AR. In-between these values of U^*, i.e. at $U^* = 7.5$, the smaller aspect-ratio cylinders seem to be on the lower branch whereas the cylinders with $AR \geq 1.2$ show small amplitude oscillations with amplitudes close to those seen at $U^* = 8.0$, which is in the desynchronization regime. There is evidently a sharp transition between the large- and small-amplitude response (between the behaviour seen at $U^* = 7.0$ and $U^* = 8.0$) when the aspect-ratio is increased beyond $AR \geq 1.2$ at $U^* \approx 7.5$. In particular, there is a $2.3\times$ drop in amplitude for 4% increase in AR at $U^* = 7.5$, compared with an approximately $1.2\times$ drop in amplitude for $U^* = 7.0$ and $U^* = 8.0$.

It is interesting to note that this transition becomes more abrupt with increasing Reynolds number (although at different U^* and AR values), which we

show for $Re = 250$. In figure 8.4(a) we show the maximum heave amplitude, A_y^* as a function of U^*, plotted for cylinders of different aspect-ratios using colors and symbols as in figure 8.3. We see that the size of this lock-in regime extends to $U^* = 7.0$ for the cases with $AR = 1.0$ and $AR = 1.05$, while the lock-in regime ends at $U^* = 6.0$ for higher aspect-ratios. This causes a dramatic drop in oscillation amplitude as a function of AR at a fixed reduced velocity of $U^* = 6.0$. This is shown in figure 8.4(b) where we compare the heave amplitude for cases with $U^* = 5.0$, $U^* = 6.0$, and $U^* = 7.0$, as a function of AR. We see that there is an approximately four-fold drop in oscillation amplitude at $U^* = 6.0$, when increasing the aspect-ratio a small amount from $AR = 1.05$ to $AR = 1.1$.

8.2.2 Energy transfer

In order to utilize the force and energy partitioning tools outlined previously to analyze the reasons behind this transition in amplitude, it is essential to first identify the bifurcation causing this behaviour, and the parameters it depends on. As mentioned earlier in chapter 4, energy maps allow us to identify all possible response branches of a flow-induced oscillator, along with their associated bifurcations, by using sinusoidal forced oscillations at matching operating conditions. In the present work, we are interested in bifurcations in the amplitude response as a function of not just the amplitude and frequency of oscillation (as has been done in previous works), but also the cylinder aspect-ratio.

The addition of shape as a parameter in energy transfer would require the generation of three-dimensional energy maps in order to achieve matching conditions in frequency, amplitude, and shape, and this is computationally expensive. To circumvent this issue, we choose to probe the three-dimensional energy landscape of the system at the oscillation frequency expected for each cylinder, which is its observed flow-induced oscillation frequency. While this frequency is mostly determined by the structural parameters, added-mass effects (which are different for cylinders of different shapes) can generate small variations in this frequency as per $f^* = (1/2\pi)\sqrt{k/\left(m + m_a\right)}$, where m_a denotes added-mass. Hence for given structural parameters, the observed flow-induced oscillation frequency varies as a function of shape. In the current analysis we focus on the behaviour corresponding to $U^* = 7.5$, as it is this value of U^* at which we observe the abrupt drop in flow-induced oscillation amplitude discussed in the previous section (§ 8.2.1). For this case, f^* is determined via the corresponding flow-induced oscillation for each cylinder, at $U^* = 7.5$, and is found to range from $0.13 \lessapprox f^* \lessapprox 0.155$. As mentioned above, this variation is due to added-mass effects associated with varying aspect-ratio, and also the fact that the smaller-AR cylinders are within the synchronization regime at $U^* = 7.5$, whereas the larger-AR cylinders are not (as seen in figure 8.3).

In order to map out the amplitude response branches as a function of shape at $U^* = 7.5$, we perform forced oscillation simulations where each cylinder with

a given aspect-ratio is forced to oscillate sinusoidally with a frequency corresponding to its dominant stationary state flow-induced oscillation frequency that is observed at $U^* = 7.5$. Further, we prescribe oscillation amplitudes in the range $0 < A_y^* \leq 0.5$ for each cylinder, and perform approximately 100 such simulations for the set of cylinders. The simulations are allowed to reach a stationary state, and the energy transfer, E^* given by equation (8.5), is then computed for each case and analyzed as a function of oscillation amplitude and cylinder aspect-ratio.

In figure 8.5(a), we show a contour plot of the energy extracted by the oscillating cylinder (undergoing forced oscillations) as a function of heave amplitude A_y^*, and cylinder aspect-ratio AR. The dashed lines show the contours of zero energy transfer, or the equilibrium curves. These equilibrium curves represent the stationary-states of sinusoidal flow-induced oscillators with aspect-ratios $1.0 \leq AR \leq 1.25$ and frequencies corresponding to $U^* = 7.5$. These energy map predictions of the flow-induced oscillation response branches are verified by superimposing the observed stationary state oscillation amplitudes of the flow-induced oscillation cases at $U^* = 7.5$ on the energy map, using the same symbols as in figure 8.3. We see that the stationary state amplitudes do in fact all lie along or near the equilibrium curves in figure 8.5(a).

It must however be noted that the flow-induced oscillations at $U^* = 7.5$ do not necessarily exhibit pure sinusoidal behaviour, especially at small oscilla-

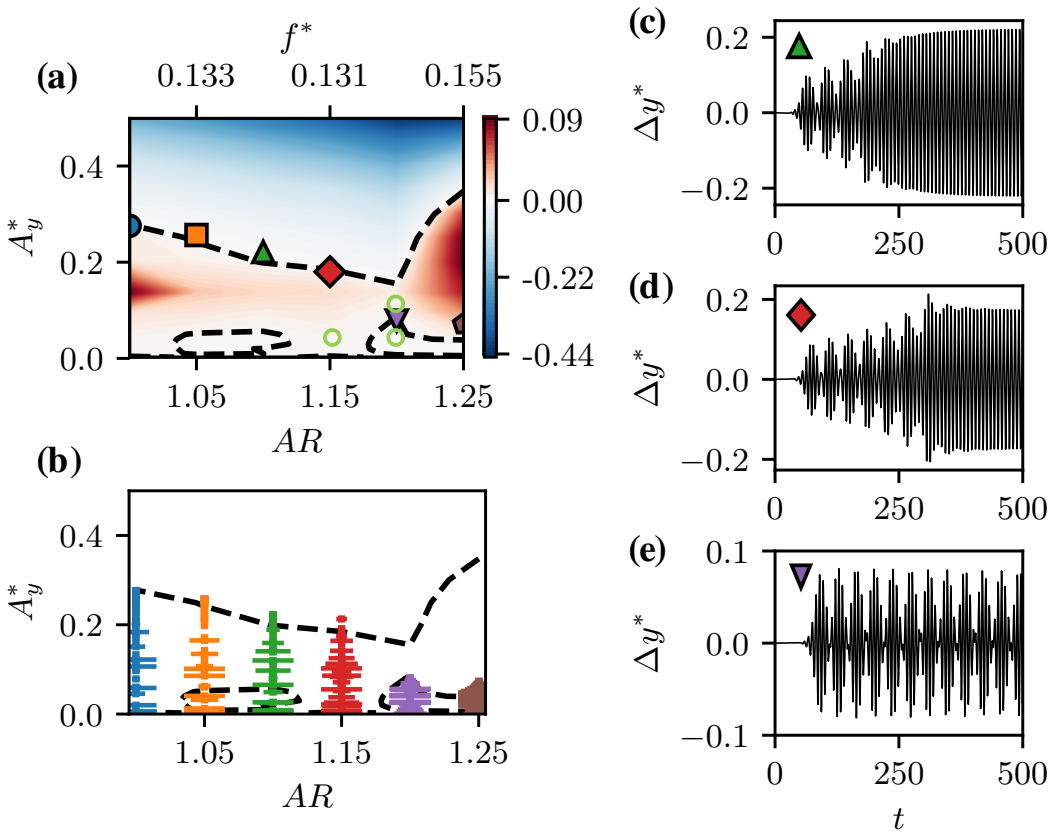

Figure 8.5: (a) Contours of energy transfer between the cylinder and flow, as a function of oscillation amplitude (A_y^*) and aspect ratio (AR). This energy transfer is computed using forced oscillations. The dashed lines show the zero energy transfer contours. Stationary state amplitudes of flow-induced oscillation for cylinders of different aspect ratios, at $U^* = 7.5$, are plotted using symbols as in figure 8.3. Light-green circles show A_y^* and AR of the forced-oscillation cases analyzed in section 8.3; (b) Trajectory of oscillation amplitude during each cycle for the flow-induced oscillation cases at $U^* = 7.5$. The horizontal lines indicate the magnitude of peak-to-peak amplitude difference between successive cycles, indicating non-sinusoidal behaviour; (c)-(e) Flow-induced oscillation response for cases with $U^* = 7.5$, and aspect ratios $AR = 1.1$, $AR = 1.15$ and $AR = 1.2$ respectively.

tion amplitudes, where natural vortex shedding continues to play an important role. Three examples of this non-sinusoidal behaviour are shown in figures 8.5(c)-8.5(e), for cases with $AR = 1.1$, $AR = 1.15$ and $AR = 1.2$ respectively. The presence of a beat phenomenon is clearly observed in these cases, where the oscillation is modulated by the vortex shedding frequency. The degree of non-sinusoidal behaviour during the progression of the cylinder oscillation is shown in figure 8.5(b). This figure shows the trajectory of amplitude growth, from $A_y^* = 0$ to the stationary state amplitude, for each flow-induced oscillation case at $U^* = 7.5$. Along this amplitude trajectory, the size of the horizontal lines (similar to error bars) indicate the magnitude of the amplitude difference between successive cycles, and are therefore a direct measure of departure from sinusoidal behavior. The highly non-sinusoidal behaviour at small amplitudes is clear from the larger horizontal bars at small amplitudes for all cases. The length of these bars progressively gets shorter at larger amplitudes, for $AR \leq 1.15$, indicating the emergence of sinusoidal behaviour as the oscillation amplitude increases. Hence, although the equilibrium curves are indicative of the expected flow-induced oscillation behaviour, we do not expect them to exactly match all the exhibited behavior. Indeed, the correspondence between the equilibrium curves of the energy map and the stationary state amplitude is not exact, especially for cases with small amplitudes.

An interesting observation from the energy map is the presence of multi-

ple equilibria for a given shape - one at large amplitude that stretches across all aspect-ratios, which we will refer to as the high-amplitude equilibrium curve; and another set of curves at small amplitudes. However, amongst the equilibrium curves at small amplitudes, we find that the one at aspect-ratios $1.05 \lessapprox AR \lessapprox 1.10$ is a significantly weaker, and less stable equilibrium than that at $AR \gtrapprox 1.20$. As shown in chapter 4 and by Menon & Mittal [77], the stability of an equilibrium curve on the energy map is given by the sign of dE^*/dA_y^*. The conditions for a stable equilibrium are $E^* = 0$ and $dE^*/dA_y^* < 0$. Comparing the energy extraction and gradients enclosed by the two equilibrium curves at small amplitudes, we find that (not shown here for brevity) the region at aspect-ratios $AR \gtrapprox 1.20$ has roughly $2\times$ the energy loss, and energy gradients that are roughly an order of magnitude more negative, than that at $1.05 \lessapprox AR \lessapprox 1.10$.

This large difference in stability is especially important due to the presence of beating oscillations at small amplitudes, as shown in figure 8.5(b). The fact that beating oscillations can be written as sum of sine waves with different frequencies suggests that the presence of beats in the flow-induced oscillation can be considered as a "frequency perturbation" from the single-frequency sinusoidal oscillation at which the energy extraction is computed for each aspect-ratio. This is because for a given aspect-ratio, the energy extraction is computed by performing forced oscillations at a frequency that corresponds

to the dominant stationary-state flow-induced oscillation frequency observed at $U^* = 7.5$. However, in the frequency spectrum of flow-induced oscillators that exhibit beats, this dominant frequency is accompanied by a second (smaller) frequency peak. The energy map shown in figure 8.5(a) neglects the possible energy extracted by the oscillator at this secondary frequency. We find that this second frequency corresponds to approximately $f^* \approx 0.15$ for all the flow-induced oscillation cases at $U^* = 7.5$. Hence, in order to examine the effect of this "frequency perturbation" on the energy map shown in figure 8.5(a), we compute a second energy map at this fixed frequency of $f^* = 0.15$. We use the same procedure as that described above, except that in this case the oscillation frequency is held constant at $f^* = 0.15$ for all values of AR. Figure 8.6 shows the structure of this energy map, where the $E^* = 0$ contour line is shown using a dashed line as before. We immediately notice that the equilibrium curve that is present at $1.05 \lessapprox AR \lessapprox 1.10$ in figure 8.5(a) is not present at $f^* = 0.15$ in figure 8.6. However, the equilibrium curve at $AR \gtrapprox 1.20$ persists in both cases. This hence provides additional evidence that the equilibrium curve at $1.05 \lessapprox AR \lessapprox 1.10$, seen in figure 8.5(a), is a weaker and less stable equilibrium than that at $AR \gtrapprox 1.20$. Due to these reasons, as we will show below, the latter plays a larger role in the dynamics, and will be referred to as the low-amplitude equilibrium curve.

The topology of the energy map, and the presence of multiple equilibria for

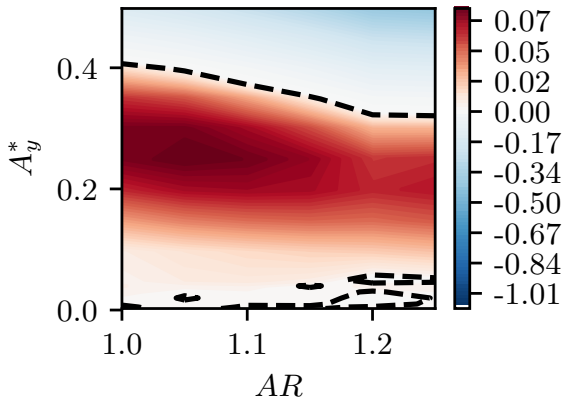

Figure 8.6: Contours of energy transfer between the cylinder and flow, as a function of oscillation amplitude (A_y^*) and cylinder aspect ratio (AR) at $f^* = 0.15$ and $Re = 100$. This energy transfer is computed using forced oscillations. The dashed line shows the zero energy transfer contour.

some aspect-ratios, suggests an explanation for the observed bifurcation in the amplitude response at $U^* = 7.5$. For values of AR that have multiple equilibrium curves at different oscillation amplitudes, we expect a system with an initial condition of zero amplitude (as is the case in this study) to reach its stationary state at the lowest-amplitude equilibrium corresponding to its value of AR. This is due to the fact that the amplitude of oscillation in these cases grows from $A_y^* = 0$ (starting at the bottom of the energy map) at constant AR, until the growth is stopped on the first encounter with a stable equilibrium. Hence for the energy map in figure 8.5(a), the first stationary state encountered by cylinders with $AR \gtrapprox 1.15$ is the low-amplitude equilibrium curve. On the other hand, due to the fact that the low-amplitude equilibrium curve at aspect-ratios $1.05 \lessapprox AR \lessapprox 1.10$ is a weak equilibrium, as explained above, and the oscillations at these amplitudes are non-sinusoidal, the low-amplitude equilibrium

curve at $1.05 \lessapprox AR \lessapprox 1.10$ does not stop the amplitude growth of cylinders with these aspect-ratios. As a result, cylinders with $AR \lessapprox 1.15$ are able to grow to larger amplitudes and settle on the high-amplitude equilibrium curve. Therefore there is a bifurcation from the large-amplitude branch to the small amplitude branch, which occurs at $AR \gtrapprox 1.15$. Hence we see that the mapping out of all possible response branches of the system allows a better understanding of the bifurcation observed in the flow-induced oscillation response.

We see from the above discussion that the abrupt drop in oscillation amplitude seen in the case of $U^* = 7.5$ is due to a bifurcation associated with the emergence of a low-amplitude response branch for $AR \gtrapprox 1.15$. Moreover, we have found that this low-amplitude branch occurs even without the minor variations in f^* for each aspect-ratio. Consequently, the bifurcation appears to be caused purely by the change in cylinder shape. This suggests that there is a change in the forcing mechanism(s) on the cylinder as we increase the cylinder aspect-ratio for low-amplitude oscillations. It must be pointed out that the ability to identify the nature of the bifurcation, and isolate the parameters related to its occurrence is a particular merit of the energy map approach in this context. In what follows, we attempt to dissect the physical origin of this bifurcation, and explain the interaction of forcing mechanisms that give rise to its emergence.

8.3 The initiation and sustenance of flow-induced vibrations

We focus now on the main theme of this work - which is to demonstrate the use of the force partitioning method, in conjunction with an energy-based analysis, to analyze the fluid-dynamic mechanisms that drive flow-induced vibration of cylinders. The aim will be to highlight the relative contributions of different physical mechanisms in the initiation and sustenance of oscillations, as well as to highlight the use of these tools in analyzing bifurcations such as those described in section 8.2. In past studies, such bifurcations have been related to changes in vortex-shedding patterns, however the direct influence of these effects on the forces on the cylinder has been mostly analyzed qualitatively. In this work, by quantifying the energy extracted by the oscillating cylinder from different physical mechanisms, we establish a rigorous way to connect distinct flow mechanisms with the emergence of oscillations. In order to uncover the origin of the bifurcation seen in section 8.2, we analyze the flow physics and forcing mechanisms for some select forced-oscillation cases around the low-amplitude equilibrium curve discussed earlier. Through this, we show that we are able to develop insights that can then be tied back to the fundamental mechanisms driving flow-induced oscillations.

In this discussion, we analyze three forced-oscillation cases close to the bi-

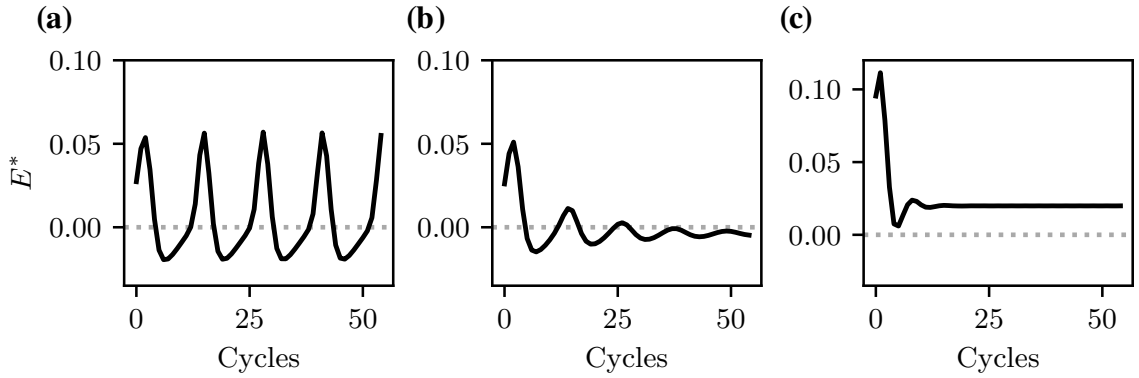

Figure 8.7: Energy extraction (E^*) during each oscillation cycle for cylinders of different aspect ratios and oscillation amplitudes at $Re = 100$ and $f^* = 0.15$; (a) $AR = 1.15$, $A_y^* = 0.05$; (b) $AR = 1.20$, $A_y^* = 0.05$; (c) $AR = 1.20$, $A_y^* = 0.10$.

furcation of interest, keeping the frequency constant at $f^* = 0.15$ for simplicity. This frequency is very close to that of the flow-induced oscillation cases that are involved in the bifurcation. The aspect-ratios and oscillation amplitudes of the cases analyzed here are shown (using light-green circles) on the energy map in figure 8.5(a). The effect of AR is studied by comparing two cases with $AR = 1.15$ and $AR = 1.2$ and constant amplitude of $A_y^* = 0.05$, and the effect of A_y^* is studied by comparing $A_y^* = 0.05$ with $A_y^* = 0.10$ for cases with $AR = 1.2$.

Time-series plots of energy extraction during each oscillation cycle for these cases are shown in figures 8.7(a)-(c). We see that the energy extraction in the case with $AR = 1.15$ and $A_y^* = 0.05$, shown in figure 8.7(a), exhibits a well-defined oscillation in time. This indicates that the oscillation frequency of C_L is not equal to the heave oscillation frequency ($f^* = 0.15$), i.e. the vortex shedding is not locked-in. The mean energy extraction is positive in this case, with $E^* =$

7.12×10^{-3}. The energy transfer in the case with $AR = 1.2$ and $A_y^* = 0.05$, plotted in figure 8.7(b), shows initial oscillations but eventually settles down to a constant value. This final stationary state, with $E^* = -2.92 \times 10^{-3}$, is within the island of $E^* < 0$ corresponding to the low-amplitude branch of the equilibrium curve. Finally, the larger-amplitude case with $AR = 1.2$ and $A_y^* = 0.10$, shown in figure 8.7(c), also shows a constant value of E^* at stationary state, which is positive and much larger than the other two cases, at $E^* = 2.46 \times 10^{-2}$. Further, the locked-in stationary state is achieved much faster in the case of $A_y^* = 0.10$ than in the case of $A_y^* = 0.05$ due to the fact that larger oscillation amplitudes drive the forcing frequency to a locked-in state.

8.3.1 Vorticity and viscous forces in sustained vibration

We now analyze the partitioning of the energy extraction for the cases discussed above, using the force partitioning method described in section 8.1. As discussed in section 8.1, this method allows us to partition the total force on the oscillating cylinder into physically relevant components, shown in equation (8.1). A key point in the analysis presented here is that each of these force components does work on the cylinder, contributing to the total energy extracted by the oscillating cylinder. We can therefore use this force partitioning to compute

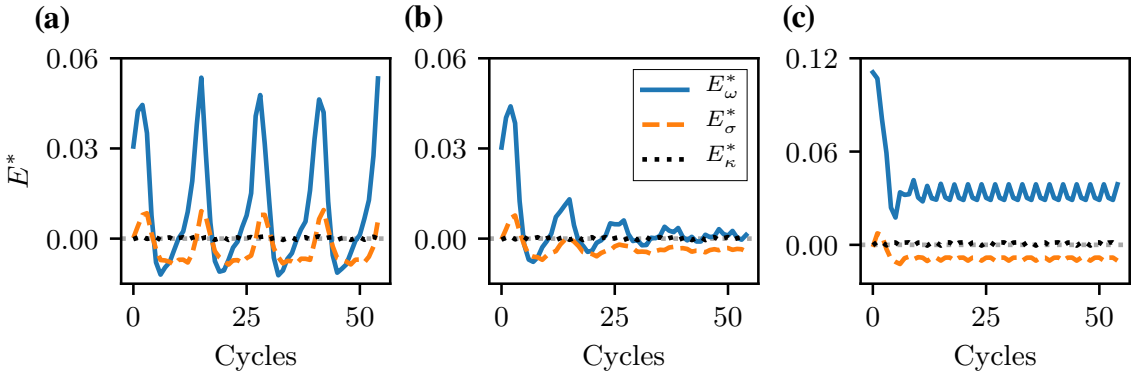

Figure 8.8: Partitioning of the energy extraction per oscillation cycle into contributions from vorticity-induced force (blue, solid line), viscous force (orange, dashed line), and kinematic force (black, dotted line). This is shown for cylinders of different aspect ratios, oscillating with different amplitudes; (a) $AR = 1.15$, $A^*_y = 0.05$; (b) $AR = 1.20$, $A^*_y = 0.05$; (c) $AR = 1.20$, $A^*_y = 0.10$.

the energy delivered to the oscillating cylinder by each of these forcing mechanisms as in (8.6). This allows us to quantify the effect of these force-producing mechanisms in driving the oscillations. In our discussion here, we will focus only on the force/energy contributions from the kinematic force (C^κ_L), vorticity-induced force (C^ω_L), and viscosity-related (C^σ_L) components in the partitioning. This is because, as was verified in section 8.1 (figure 8.1), these components account for nearly all the force on the cylinder.

In figures 8.8(a)-(c) we show the energy extracted by the oscillating cylinder from added-mass effects (E^*_κ), viscous contributions (E^*_σ), and vorticity-related contributions (E^*_ω) for the three cases mentioned above. In all three cases we see that the bulk of the energy extraction is driven by the vorticity-induced force. Another observation that is common to the three cases is that the kine-

A_y^*	AR	E^*	E_ω^*	E_σ^*	E_S^*	E_W^*
0.05	1.15	7.12×10^{-3}	9.98×10^{-3}	-3.02×10^{-3}	1.55×10^{-2}	-1.78×10^{-3}
0.05	1.20	-2.92×10^{-3}	7.50×10^{-4}	-3.73×10^{-3}	1.05×10^{-2}	-5.67×10^{-3}
0.10	1.20	2.46×10^{-2}	3.27×10^{-2}	-8.87×10^{-3}	6.37×10^{-2}	-1.25×10^{-2}

Table 8.1: Summary of mean energy extraction (total energy and components of the energy partitioning) for three forced-oscillation cases with different aspect-ratios and oscillation amplitudes.

matic force contributes nearly zero net energy transfer. This is expected for periodic, non-rotating oscillations of the cylinder. It is easy to show that the second term on the right-hand side of equation (8.2) is zero in the absence of rotation, and the first term corresponds to the traditional added-mass force in ideal fluids [153]. Hence by plugging this first term, which is a sinusoidal term in-phase with the displacement of the cylinder, into the equation for energy transfer (equation 8.5), we see that this integral is zero due to the periodicity of the system. Therefore, the total energy transfer is primarily determined by the contributions from the vorticity-induced force and viscous effects.

In the case with $AR = 1.15$ and $A_y^* = 0.05$, shown in figure 8.8(a), the mean energy extracted by C_L^ω is $E_\omega^* = 9.98 \times 10^{-3}$ and that from C_L^σ is $E_\sigma^* = -3.02 \times 10^{-3}$. As was seen in the case of the total energy, the individual contributions to the total energy also show oscillations in time due to the fact that the forcing is not locked-in. The case with $AR = 1.2$ and $A_y^* = 0.05$ is shown in figure 8.8(b) and we see that energy extraction from the vorticity is very small in this case, with $E_\omega^* = 7.50 \times 10^{-4}$. The negative energy transfer from viscous

effects, $E^*_\sigma = -3.73 \times 10^{-3}$, pushes the total energy extraction below zero. In the high-amplitude case with $AR = 1.2$ and $A^*_y = 0.10$, shown in figure 8.8(c), we see that the energy extracted from the vorticity-induced force has a mean positive value of $E^*_\omega = 3.27 \times 10^{-2}$, and this is much larger than in the other two cases. This case too shows energy loss due to the viscosity-related effects, $E^*_\sigma = -8.87 \times 10^{-3}$, however the large value of E^*_ω compared to the previous case ensures that the total energy extraction is positive in this case. A summary of these mean energy extraction values is shown in table 8.1.

We see from this data that, as expected, the viscous effects result in energy loss in all cases discussed. The sign of the total energy extracted therefore depends on the relative magnitudes of the energy extracted from the vorticity-induced force and the energy lost to viscous dissipation. For the total energy extraction to be positive, E^*_ω needs to be large enough to overcome the losses to viscosity. This confirms that the primary driving force for energy extraction is the vorticity in the fluid. Further, we see that the magnitude of E^*_ω depends strongly on oscillation amplitude as well as the aspect-ratio. In the case of $AR = 1.15$ and $A^*_y = 0.05$, this positive energy extraction from vorticity is responsible for the overall positive energy extraction. However, there is a significant drop in E^*_ω on increasing the aspect-ratio slightly to $AR = 1.2$ at the same amplitude of oscillation. This drop in the energy extracted from the vorticity-induced forces hence allows the dissipative nature of viscous effects

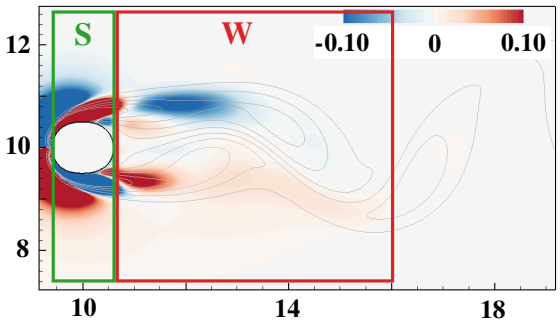

Figure 8.9: Schematic of the integration volumes used to calculate the vorticity-induced force contributions of the shear-layer (denoted by S) and wake (denoted by W). These integration volumes are overlaid on an instantaneous snapshot of contours of C_L^ω for a case with $AR = 1.15$ and $A_y^* = 0.05$.

to push the total energy extraction below zero. On increasing the oscillation amplitude to $A_y^* = 0.10$, a large increase in E_ω^* is observed for a cylinder with the same aspect ratio, $AR = 1.2$. In fact, E_ω^* increases by a little more than an order of magnitude on doubling the amplitude of oscillation from $A_y^* = 0.05$ to $A_y^* = 0.10$ while keeping the aspect-ratio constant at $AR = 1.2$. The energy loss to viscous effects however does not show this disproportionate increase, and E_ω^* hence pushes the total energy extraction to a positive value.

8.3.2 Contributions of the shear-layer and wake to sustained vibration

A useful question to ask at this juncture is – what physical mechanisms and flow phenomena contribute to this complicated dependence of E_ω^* on the cylin-

der aspect-ratio and oscillation amplitude? As pointed out before, the volume-integral form of the vorticity-induced force in equation (8.3) allows us to isolate the contribution of vorticity in different spatial regions in the flow, to the total force on the cylinder. This allows us to decompose E^*_ω into contributions from the work done by the vorticity-induced force from these different spatial regions, on the oscillating cylinder. Here, we specifically focus on the effects of the layer of vorticity over the surface of the cylinder (we refer to this as the "shear layer") and the vortex wake behind the cylinder. We quantify these effects by choosing domains of integration that isolate the vorticity on the surface of the cylinder from that in the wake of the cylinder. In figure 8.9 we show a schematic of these integration volumes, overlaid on a snapshot of contours of C^ω_L for a case with $AR = 1.15$. The rectangular regions denoted by S and W are the integration volumes used in this work for the contributions from the shear layer and wake, respectively. We should note that the integration volumes used here are simply meant to isolate these two mechanisms with the least ambiguity, owing to the lack of strict definitions of the "shear-layer" or "wake" regions. Hence, since we are interested in isolating the layer of vorticity over the surface of the cylinder, the streamwise extent of the "shear-layer" region is defined to span the horizontal length of each cylinder's surface. The region downstream of this is termed the "wake". The force contributions from these volumes (which we denote as C_S and C_W respectively) can be computed

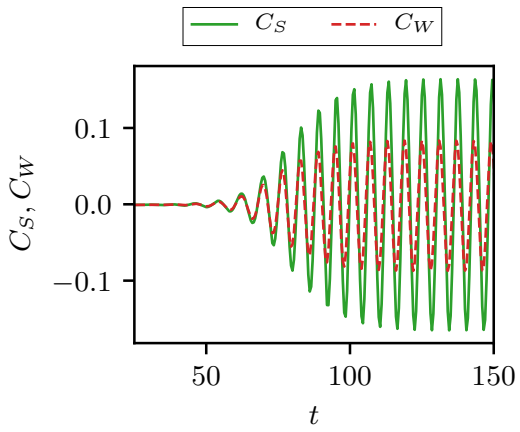

Figure 8.10: Partitioning of vorticity-induced lift force into contributions from the shear layer (C_S; green, solid line) and wake (C_W; red, dashed line) for stationary cylinders with $AR = 1.15$.

using equation (8.3), and as before, we compute the energy extracted by the cylinder from the flow in these volumes by using equation (8.5).

A sample partitioning of the vorticity-induced force contributions to lift from the wake and shear-layer is shown for a *stationary* $AR = 1.15$ cylinder in figure 8.10. It is interesting to note that the amplitude of force due to the shear-layer is significantly higher than that due to the wake in this case. In fact, this is seen to be true for all the aspect-ratios (including $AR = 1.0$) studied in this work. Phenomenologically, this is due to the fact that the wake vortices have lower vorticity magnitudes than the vorticity layer on the surface and they are also farther away from the transverse surfaces of the cylinder than the vorticity layer on the body. This observation will be relevant to our subsequent discussion about the mechanisms driving the onset and growth of flow-induced vibrations.

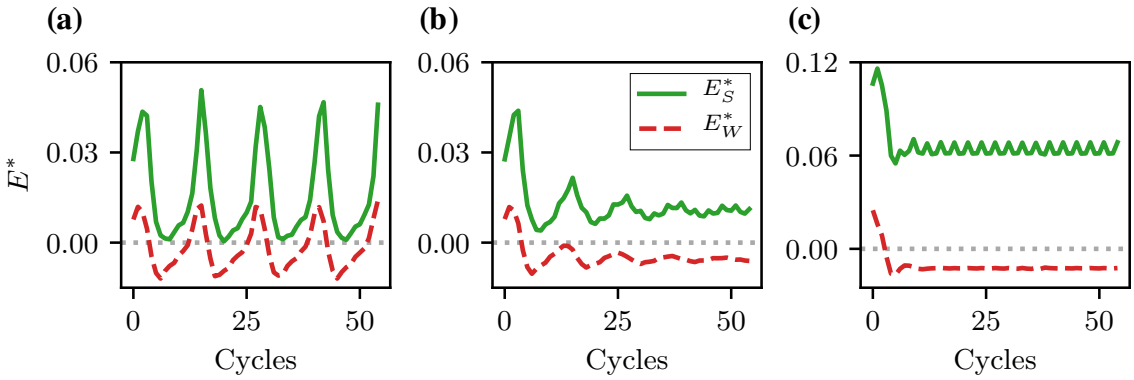

Figure 8.11: Contributions of energy extraction from vorticity-induced force in the shear layer (green, solid line) and wake (red, dashed line), for cylinders of different aspect ratios and oscillating with different amplitudes; (a) $AR = 1.15$, $A^*_y = 0.05$; (b) $AR = 1.20$, $A^*_y = 0.05$; (c) $AR = 1.20$, $A^*_y = 0.10$.

We can now use the above method to examine the mechanisms that cause the complex dependence of E^*_ω on the aspect-ratio and oscillation amplitude, shown in figure 8.8. We compare the energy extracted from the vorticity in the shear layer and wake in figure 8.11, for the stationary states of the three cases discussed above. The energy extraction from the shear layer is denoted by E^*_S and that from the wake is denoted by E^*_W. For the case with $AR = 1.15$ and $A^*_y = 0.05$, we see that both E^*_S and E^*_W exhibit low-frequency oscillations due to the non locked-in state of the system, as was seen before. The mean energy transfer from the shear layer and wake in this case are $E^*_S = 1.55 \times 10^{-2}$, and $E^*_W = -1.78 \times 10^{-3}$. Hence, we see that the shear layer contributes energy to the oscillation, while the wake vortices extract energy from the oscillation.

For the case with $AR = 1.2$ and $A^*_y = 0.05$ too, we find that the shear layer contributes positive energy at the stationary state, with $E^*_S = 1.05 \times 10^{-2}$, and

the wake vortices extract energy, with $E^*_W = -5.67 \times 10^{-3}$. Note that the shear layer energy extraction in this case ($AR = 1.2$) is slightly lower than that in the case with $AR = 1.15$, however the energy loss in the wake is approximately $3\times$ higher. The case with $AR = 1.2$ and larger amplitude of $A^*_y = 0.10$ also shows energy loss due to the wake, along with significantly higher energy extraction in the shear layer. For this case $E^*_S = 6.37 \times 10^{-2}$, which represents a roughly $6\times$ increase from the case with the same aspect-ratio and smaller amplitude of oscillation. The energy lost to the wake is $E^*_W = -1.25 \times 10^{-2}$, which is about $2\times$ of the value computed in the case with smaller oscillation amplitude. A summary of these average energy extraction values is provided in table 8.1.

An important observation from this spatial partitioning of the energy extraction due to the vorticity-induced force is that for all the cases discussed here, the wake vortices actually extract energy *from* the oscillating cylinder during sustained oscillations. It is therefore the positive work done by the shear-layer that is the driving force for sustained oscillations. This is somewhat contrary to conventional notions in the field of flow-induced vibrations, where significant interest has been directed at the vortex shedding patterns in the wake and their relation to the flow-induced vibration response.

This spatial partitioning also allows us to identify the reason behind the change in the sign of E^* for a small increase in the cylinder aspect-ratio (only about a 4% increase) - and the corresponding bifurcation in the amplitude re-

sponse discussed in section 8.2.1 This change in E^* is caused by the fact that the energy extracted from the shear layer reduces slightly on increasing AR, while the energy lost to the wake increases dramatically. The small reduction in E_S^* is associated with slightly weaker shear layers over the longer-AR cylinder, which is expected. The approximately $3\times$ increase in energy loss due to the wake can be related to a change in the phase difference between the wake and the oscillation as AR is increased. Furthermore, this partitioning also suggests why the region of $E^* < 0$ is restricted to low oscillation amplitudes. We see that doubling the oscillation amplitude at this $AR = 1.20$ also approximately doubles E_W^*. However, the energy transfer due to the shear layer increases dramatically, owing to stronger shear layers as a result of larger oscillation amplitude. In summary, this analysis suggests that the low-amplitude stable branch of the equilibrium curve is caused by the rapid detuning of the wake as the aspect-ratio of the cylinder is increased at small amplitude. Further, the low-amplitude nature of this branch is related to the fact that the energy extracted from the shear layer varies non-linearly with oscillation amplitude, and offsets the dissipative effect of the wake at sufficiently large amplitudes.

8.3.3 Role of the shear-layer and wake in the initiation of oscillations

The above observation that the wake takes energy away from the oscillation and the shear layer does positive work to sustain stationary-state oscillations brings up the question regarding the *onset* of flow-induced oscillations. The onset cannot be explained by the same mechanism driving sustained oscillations, i.e. energy extraction driven exclusively by the shear layer. This is because the symmetry-breaking in the wake is known to be responsible for the oscillations in the shear layers, and the resultant oscillating lift-force [128, 155]. Hence we expect that the wake plays a role in facilitating the onset of oscillations on account of this symmetry-breaking. Moreover, since we are using forced oscillations as a proxy for the stationary state of flow-induced oscillations, it is essential to verify that the above findings are not an artefact of forced oscillation and are indeed relevant in sustaining flow-induced oscillations. To explore the mechanisms that govern the dynamics at their onset and also confirm that the previous observations are not specific to forced oscillations, we now analyze the energy partitioning into the wake and shear-layer contributions for two representative flow-induced oscillation cases.

In figure 8.12 we plot the energy extracted from the wake (E_W^*) and shear layer (E_S^*) by two flow-induced oscillating cylinders with different aspect-ratios.

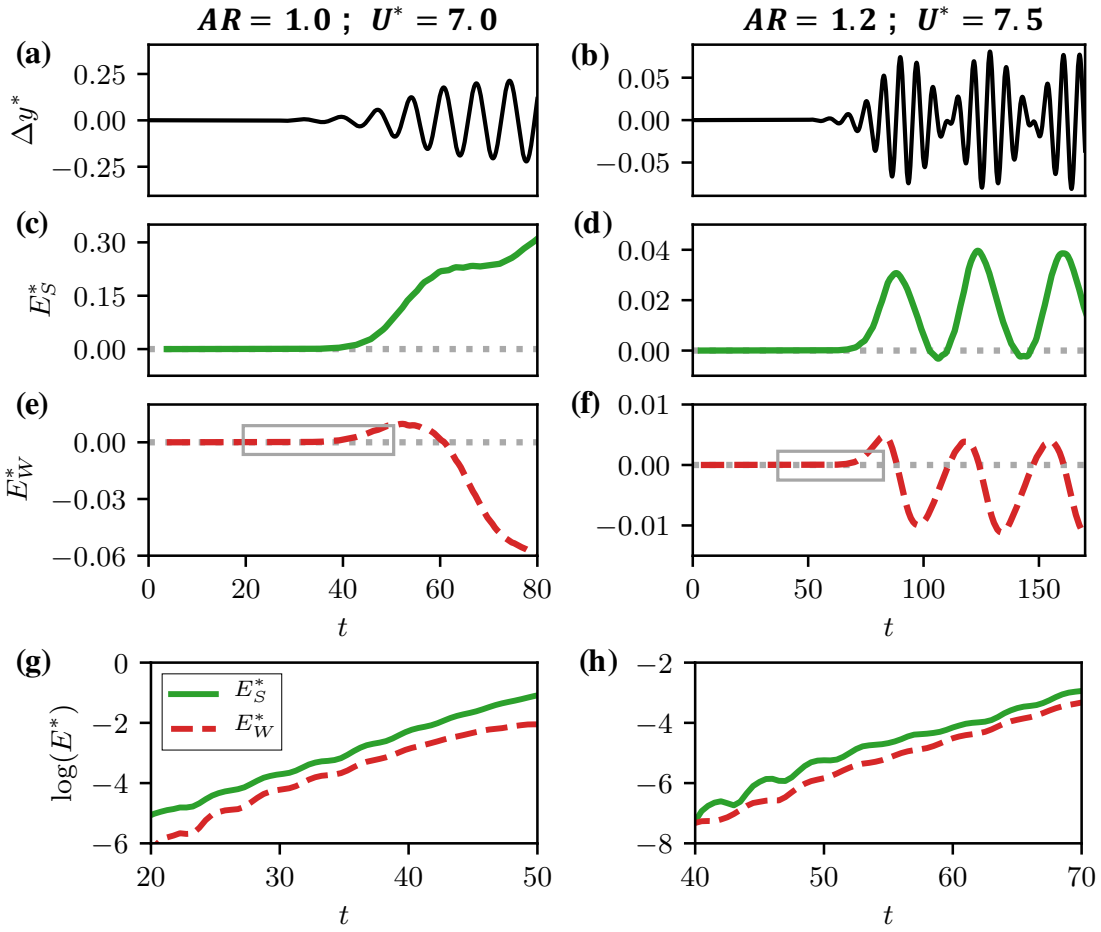

Figure 8.12: Analysis of energy extraction from the shear-layer and wake for two flow-induced oscillation cases very close to the onset of oscillations. Left panel shows a case with $AR = 1.0$, $U^* = 7.0$ and right panel shows a case with $AR = 1.20$, $U^* = 7.5$; (a-b) Amplitude of heave oscillations (Δy^*); (c-d) Energy extraction from C_L^ω in the shear-layer (E_S^*); (e-f) Energy extraction from C_L^ω in the wake (E_W^*); (g-h) Zoom-in of energy contributions from E_S^* and E_W^*, plotted on a semi-log scale for the time-period indicated by the grey boxes in figures (e) and (f).

The U^* values for these cases ($U^* = 7.0$ and $U^* = 7.5$) correspond to those around the bifurcation analyzed in 8.3(b). We are particularly interested in the energy balance very close to the onset, and initial growth, of the oscillation. The left-panel of figure 8.12 shows this early-time heave amplitude and energy partitioning for a case with $AR = 1.0$ and $U^* = 7.0$, which shows locked-in oscillations. The time-series plot of heave amplitude in figure 8.12(a) shows that the onset of oscillation occurs at $t \approx 40$. We see that the energy extraction from both the shear-layer and wake, shown in figures 8.12(c) and 8.12(e), are initially zero before the onset of oscillation. However at the onset, the cylinder initially extracts positive energy from both the shear-layer and the wake. As the oscillations grow, the cylinder continues to extract energy from the shear layer at an increasing rate but the wake now becomes an energy-sink for the oscillations. These observations provide confirmation for our earlier forced-oscillation findings from figure 8.11, relating to the competing effects of the shear-layer and wake at finite oscillation amplitudes. Further it also shows that the vortex shedding in the wake does in fact, play a positive role at the onset of oscillation, which is a manifestation of symmetry-breaking.

In the right-panel of figure 8.12 we provide further evidence to support these observations. In this case, with $U^* = 7.5$ and $AR = 1.20$, the oscillations are not in a locked-in state. This leads to a "beating" phenomenon in the oscillation as shown in the time-series of heave amplitude in figure 8.12(b).

The beats are evident in the energy extraction as well, seen as oscillations in both E_S^* and E_W^*, in figures 8.12(d) and 8.12(f) respectively. The beating phenomenon is particularly interesting for this discussion as it represents multiple "onsets" of oscillation. We see that each time the oscillation amplitude decreases close to zero, there is a brief period of (positive) extraction of energy from the wake. Subsequent increase in oscillation amplitude leads to a "detuning" of the wake, resulting in the wake becoming an energy sink. Further, each instance of amplitude growth is also accompanied by positive energy extraction from the shear layer. However in this case, the absence of frequency lock-in causes a drift in the phase difference between the oscillation and vortex shedding. This unfavourable phase difference in the wake is able to feedback into the shear layer at these small oscillation amplitudes (E_S^* and E_W^* have comparable magnitudes), resulting in an increased detuning of the shear layers, thereby reducing the energy extraction from the shear layers. The periodicity of these mechanisms causes this process to repeat and hence leads to beats in the oscillation amplitude. This is an interesting demonstration of the competing influence of the wake and shear-layer in producing variations in the oscillation amplitude.

From the above cases we note that while at large amplitudes the shear-layer is the driving force for the oscillations, at smaller amplitude, the wake vortices continue to play an important role. Close to the onset of oscillations in

particular, both these mechanisms do positive work on the cylinder. To provide a clearer picture of the relative importance of these two mechanism at the onset of flow-induced oscillations, we examine the contributions of wake vortices and shear layers very early in the initial amplitude growth for the two cases discussed above. In this analysis, we focus on the time-period indicated by the grey boxes in figures 8.12(e) and 8.12(f). The energy contributions from the shear-layer and wake, plotted on a semi-log scale for the two flow-induced oscillation cases discussed above, are shown in figures 8.12(g) and 8.12(h). For both cases, $U^* = 7.0$ and $AR = 1.0$ in figure 8.12(g) as well as $U^* = 7.5$ and $AR = 1.2$ in figure 8.12(h), we see that the shear-layer is the larger contributor of positive energy even at this very early time. This is in line with our earlier observation for a static cylinder (see figure 8.10), where we saw that the shear-layer generates a larger contribution to the lift force than the wake vorticity. Using this static condition as a proxy for the pre-onset state of the oscillator, figures 8.10 and 8.12(g-h) are indicative of the same phenomenon - that it is the pressure variation generated directly by the shear-layers that is the dominant driving mechanism even very close to the onset of oscillation. However we should reiterate that, as mentioned above, the symmetry of the problem requires vortex shedding in the wake to initiate oscillations in the shear-layer forcing. Hence although the shear-layer is the *dominant* mechanism very close to the onset of oscillations, it cannot act independently to initiate the oscillations.

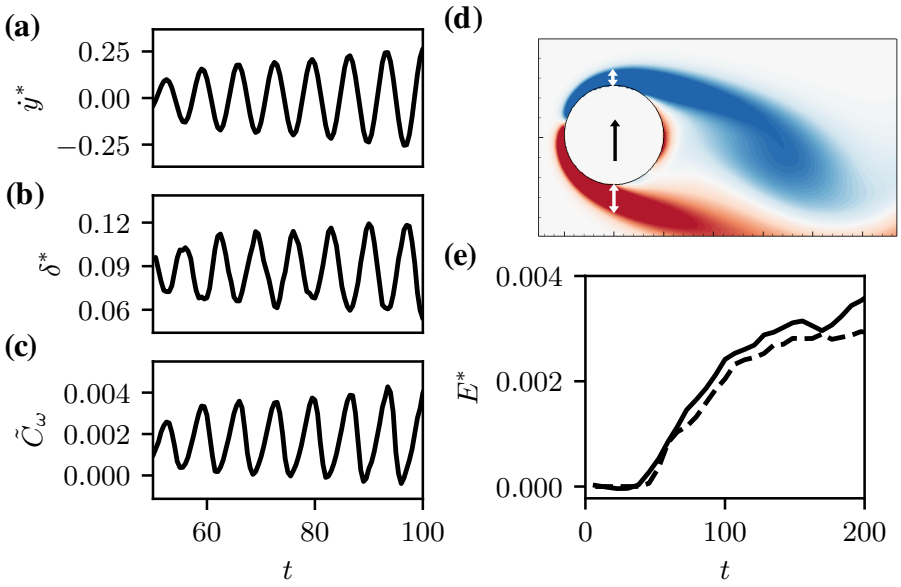

Figure 8.13: Comparison of heave velocity, boundary-layer thickness, and shear-layer forcing for a case of flow-induced oscillations with $AR = 1.0$ and $U^* = 7.0$ (a) Time-series of heave velocity ($\dot{y}^*$); (b) Boundary-layer displacement thickness (δ^*) on the top surface of the cylinder, along the transverse axis; (c) Force contribution from the dominant terms of C_L^ω in the shear-layer on the top surface of the cylinder ($\tilde{C}_\omega$; equation 8.8); (d) Instantaneous snapshot of vorticity contours around the cylinder as it moves upward, with white arrows showing qualitative measure of boundary-layer thickness on the two transverse surfaces; (e) Comparison of total energy extracted from C_L^ω (solid line) with that extracted from $\tilde{C}_\omega$ (dashed line) in a small region inside the top-surface boundary-layer.

8.3.4 Underlying mechanism for the shear-layer contribution to oscillations

As a final piece in this analysis, we seek to provide a physical basis for the net-positive energy contribution of the shear-layer for all the cases simulated here. We hypothesize that the pressure force induced by the shear layers is directly related to changes in the thickness of the shear layers on the transverse

surfaces of the cylinder, which in turn, is driven by the transverse oscillations of the cylinder. Such a relationship would explain two key findings in the above analysis - that the shear-layer forcing is at a favourable phase with respect to the heave velocity of the cylinder, and also that its influence strongly depends on the oscillation amplitude. In order to assess this hypothesis, we compare the boundary layer thickness on the top surface of the oscillating cylinder to the transverse velocity, and also relate the changes in the boundary-layer thickness to the fluctuations in C_L^ω associated with the shear-layer. This comparison is performed for the case of flow-induced oscillations with $AR = 1.0$ and $U^* = 7.0$, which was discussed above.

In figure 8.13(a) we show the time-series of heave-velocity for this case, during a time-period when the amplitude of oscillation is growing. To compare the heave-velocity with the boundary-layer thickness, we compute the displacement thickness on the top-surface of the cylinder along the transverse axis. The displacement thickness is calculated as

$$\delta^* = \int_{y_{min}}^{y_{max}} \Big(1 - \frac{u}{U_{max}}\Big) dy \tag{8.7}$$

where U_{max} is the maximum horizontal velocity in the shear-layer, y_{min} is the $y-$coordinate of the top surface of the cylinder, y_{max} is the $y-$coordinate at which U_{max} occurs. The computed displacement thickness is plotted against

time in figure 8.13(b), and we see that the displacement thickness follows an inverse relationship to the heave-velocity. This confirms that the boundary layer on the transverse surface of the cylinder compresses(expands) with the upward(downward) motion of the cylinder. As further qualitative evidence of this effect, figure 8.13(d) shows an instantaneous snapshot of vorticity contours around the cylinder as it moves upward, and the white arrows show that the boundary layer on the upper surface is thinner than that on the lower surface.

In order to relate this boundary-layer thickness to the vorticity-induced force contained in the shear-layer, we note that the mathematical form for C_L^ω given in equation (8.3) can be expanded into numerous terms involving the gradients of the horizontal and vertical velocity components in the flow. We estimate the importance of each of these terms in driving the oscillations by probing the flow in a small region within the shear-layer and computing the energy extracted by the cylinder from each term. The integration volume used for this exercise is taken as one grid cell, located along the axis of the heave motion at $0.1D$ above the surface of the cylinder (moving with the cylinder). We find that two terms in particular, shown below, correspond to the bulk of the

energy extraction in this region:

$$C_L^\omega \approx \tilde{C}_\omega = \int_{V_f} \left[\left(u_v \frac{\partial u_v}{\partial y} + u_v \frac{\partial u_\Phi}{\partial y} + u_\Phi \frac{\partial u_v}{\partial y} \right) \frac{\partial \phi}{\partial y} \right] dV + \int_{V_f} \left[\frac{\partial}{\partial y} \left(v_v \frac{\partial v_v}{\partial y} + v_v \frac{\partial v_\Phi}{\partial y} + v_\Phi \frac{\partial v_v}{\partial y} \right) \phi \right] dV. \tag{8.8}$$

Here u_v and u_Φ are the rotational and curl-free components of the horizontal velocity, and v_v and v_Φ are the corresponding components of the vertical velocity. The fact that the approximation $\tilde{C}_\omega$ in equation (8.8) dominates the energy extraction is confirmed in figure 8.13(e) by comparing the total energy extraction from C_L^ω in this small region (solid line) with the energy accounted for by $\tilde{C}_\omega$ (dashed line). It is noteworthy that these terms are primarily composed of vertical derivatives of the velocity components. This suggests that the vorticity-induced force in the shear-layer is indeed driven by the fluctuations in the boundary-layer thickness. This can be verified by comparing fluctuations in $\tilde{C}_\omega$, which is plotted in figure 8.13(c) with δ^*. We see that minima in δ^* correspond to maxima in $\tilde{C}_\omega$ as expected. The fact that δ^* is in-turn inversely related to the transverse velocity ($\dot{y}^*$) then explains why the shear-layer has a net-positive influence on the oscillation for all the cases discussed here. This supports our hypothesis regarding the underlying reason for the dominant influence of the shear-layer in sustaining flow-induced vibrations.

8.3.5 Phenomenology of flow-induced vibration

In summary, the above analysis of energy extraction in flow-induced as well as forced oscillations suggests the following phenomenology for the initiation and sustenance of the flow-induced vibration of cylinders:

1. Symmetry breaking in the wake results in vortex shedding, which also induces periodic oscillation in the attached boundary/shear layers.

2. The oscillation in the boundary/shear layer as well as the periodically shed wake vortices induce oscillations in the lift force on the cylinder. Both these effects play a role in initiating the cylinder oscillations. However, the direct contribution of the boundary/shear layer to the oscillating lift and amplitude growth is larger than the contribution of the wake vortices.

3. For oscillations at small amplitudes, the shear-layer is affected both by the oscillation of the cylinder as well as the wake vortex shedding, and the frequency of these two might be different. In this case, the pressure force induced by the shear layer might detune from the cylinder oscillation periodically, resulting in a beating phenomenon in the cylinder motion.

4. Once the oscillations grow beyond a certain amplitude, the lift contribution of the wake vortices goes out of phase with the cylinder oscillation, and wake vortices begin to act as sinks of energy. In contrast, the shear

layer is driven primarily by the cylinder motion and the contribution to energy extraction from the flow increases with oscillation amplitude. It is this mechanism that sustains stationary state oscillations against the constant drain of energy by the vortex shedding in the wake. Further, this increase in shear-layer forcing with amplitude is governed by thickening and thinning of the boundary-layers on the transverse surfaces of the cylinder, which is a consequence of the heaving motion.

8.4 Conclusions

In this work, we use a force partitioning method in conjunction with an energy-based analysis to dissect the contributions of different fluid forcing mechanisms on the flow-induced vibration of cylinders. The work done on the oscillating cylinder by each of these forcing mechanisms, or the energy extracted by the cylinder, provides rigorous quantification of their effect on the oscillation. Further, the force partitioning method also allows us to isolate the contributions of different spatial regions of the flow towards the total vorticity-induced force. The specific mechanisms analyzed in this work are the effect of the shear-layer and the vortex-wake in initiating and sustaining oscillations. These methods therefore allow us to quantify the contributions of specific flow mechanisms/features in driving the flow-induced vibration of cylinders.

We show quantitatively that the driving factor behind the flow-induced oscillations is the vorticity-induced force. For the cases analyzed here, viscous effects are always seen to dissipate energy from the oscillation. Thus, the work done by the vorticity-induced component of the total force needs to overcome these viscous effects in order to generate sustained oscillations. By further decomposing the energy extracted from vorticity into the specific contributions of the shear layer and the wake, we show that while the oscillations are briefly energized at their onset by the vortex shedding in the wake, the growth as well as sustenance of these oscillations is driven directly not by the wake vortices but by the shear layer on the transverse surfaces of the cylinder. In fact, beyond the onset phase, wake vortices actually act as sinks of energy during sustained oscillation. We highlight these findings in the context of the effect of aspect-ratio on flow-induced oscillations of a cylinder and explain the rapid drop in oscillation amplitude with a minor increase in aspect ratio.

Indeed, the conventional use of the term "vortex-induced vibration" to describe the overall phenomenon has an inherent implication that the oscillations of elastically mounted bluff bodies are induced by the wake *vortices* but our analysis shows that this is not the case. Therefore, "vorticity-induced vibration" is a more apt descriptor for the following reasons – firstly, vorticity-induced lift forces dominate over all other possible contributions; and secondly, it is the *vorticity* in the shear layers and not the *vortices* in the wake that

sustain the oscillations. The findings discussed in this chapter have been published in reference [79].

Chapter 9

A physics-based and data-driven framework for the analysis of vortex-dominated flows

As evidenced in the preceding chapters, the dynamics of fluid-structure interactions in vortex-dominated flows is very hard to predict for several reasons. Chief amongst these is the presence of multiple distinct mechanisms for the production of aerodynamic loads on immersed surfaces and the dominant dynamical influence of several vortices. Each of these vortices, as well as other flow features such as shear layers, induces unsteady and non-linear loads on immersed surfaces within the fluid as a result of flow separation, vortex shedding and the interaction of vortices amongst each other as well as with

immersed surfaces within the flow. Vortex-induced loads in such flows therefore give rise to a variety of complex phenomena in problems involving fluid-structure interaction and unsteady aerodynamics.

A prototypical problem that manifests much of the complexity associated with such flows – vortex dominated behavior and complex vortex interactions – is the flow around a pitching airfoil. To illustrate this, figure 9.1(a) shows a data set consisting of 165 two-dimensional Navier-Stokes simulations of flow past a sinusoidally pitching airfoil. This ensemble of cases represents a parameter sweep through the pitching frequency, f^*, and amplitude, A_θ (both defined in the caption of figure 9.1). The complex vortex dynamics inherent in such a problem is highlighted by the snapshots of the vorticity field shown for some select cases in figures 9.1(b)-(e). These snapshots show that this problem is characterized by a variety of vortex patterns that are quite sensitive to changes in oscillation kinematics. The snapshots in figures 9.1(b)-(d), corresponding to the same oscillation amplitude and relatively small differences in oscillation frequency, all show the growth of a strong leading-edge vortex (LEV), along with several other distinct, interacting vortices. However, we see that the phase of the LEV-growth is slightly different in each case, although the snapshots are at the same phase in the oscillation.

As illustrated in chapters 4 and 8, one way to assess the overall aeroelastic interaction of the flow with the airfoil is to evaluate the energy that could po-

tentially be extracted by the airfoil from the surrounding flow as a function of oscillation kinematics. This was defined in equation (4.8). The energy extraction, which is primarily dictated by the phase difference between the dominant aerodynamic loading mechanisms and the oscillation kinematics [77, 151], was shown to determine the flow-induced oscillation response as well as energy-harvesting potential of the airfoil [29, 77]. Figure 9.1(a) shows contours this energy extraction, or the "energy map" of chapter 4, as a function of oscillation frequency and amplitude. As evidenced by these energy contours, the slight variation in oscillation kinematics for the cases shown in figures 9.1(b)-(d), which results in subtle changes in the phase of the LEV as well as different vortex interactions, has consequences for the sign of energy extraction and therefore the dynamics of flow-induced motion. Additionally, all these cases exhibit very different vortex interactions close to the leading and trailing-edges, and this can influence the force production, propulsion, and fluid-structure interaction [100, 156, 157] associated with such configurations.

Therefore in order to analyze the forcing mechanisms and resultant dynamical behaviour of such problems we need to be able to rigorously quantify the aerodynamic loading induced by each of these interacting mechanisms and flow features. While the force and moment partitioning methods (FMPM) discussed in chapters 7 and 8 can determine the loading associated with any vorticity-containing region of the flow, vortex-dominated flows typically contain multiple

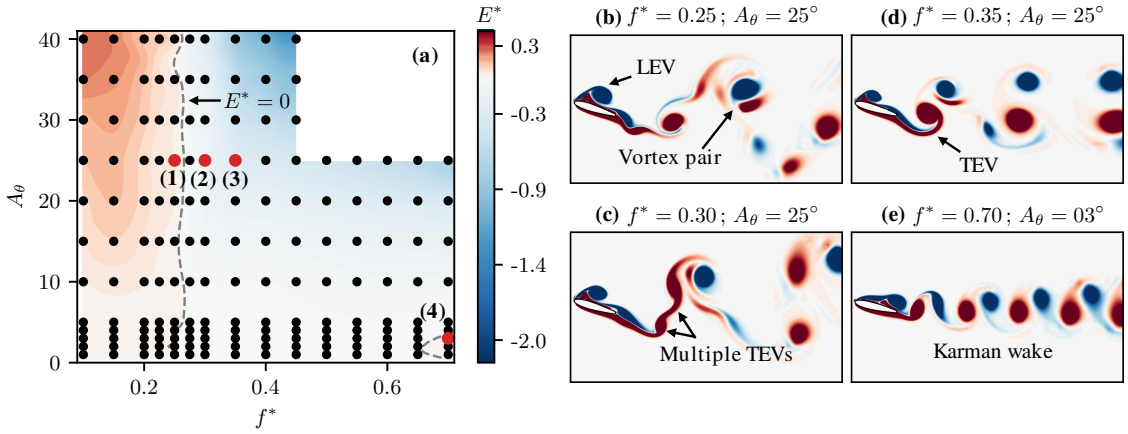

Figure 9.1: Data set showing 165 two-dimensional Navier-Stokes simulations of an airfoil pitching sinusoidally about its mid-chord. The oscillation amplitude is A_θ and dimensionless frequency is $f^* = fC/U_\infty$ (where C and U_∞ are chord-length and free-stream velocity). Frequency and amplitude for each case in the data set is shown as circles in (a). Coloured contours in (a) show mean energy extracted by the oscillating airfoil over a cycle, E^*. The contour corresponding to $E^* = 0$ is shown as dashed curve in (a). Figures (b)-(c) show snapshots of the vorticity field for select cases in this data set, with f^* and A_θ for each case specified.

vortices which interact, deform as well as change their volume and location as they are advected with the flow. Thus, to effectively apply FMPM to such flows, appropriate methods are required to isolate, track, as well as determine the time-varying volumes occupied by each vortex in an automated manner. This is an important but non-trivial exercise, and a number of previous studies have developed tools for some aspects of this task, and demonstrated their utility in the analysis of vortex dominated flows [122, 158–160].

In this chapter, we describe a data-driven framework for automated tracking of vortices in relatively complex flows that is specifically suited to the application of FMPM. This procedure takes in time-resolved flow-field data and (1) isolates and tracks multiple individual vortex structures; (2) identifies and groups vortical structures that occur repeatedly (or periodically) in the given flow-field data; and (3) extracts the time-history of kinematic quantities as well as force/moment production due to any selected vortex on the immersed body.

9.1 Automated tracking of vortices and estimation of aerodynamic loads

The input to this framework is time-resolved data of the fluid velocity field, as well as information on the position and velocity of all material points on the surfaces of the immersed body and external domain boundaries. Here we

assume that the velocity field is defined within the fluid domain V_f, and is represented in discrete form, i.e. on a spatial grid using the set of grid points $\{\zeta\}$ and discrete temporal snapshots at N_t time-instances. In this discussion, we will denote individual time-snapshots as t_j where the temporal index is $j \in \{1, 2, \cdots, N_t\}$. We will outline the steps involved in this framework using a sample case of a two-dimensional, sinusoidally pitching airfoil, with dimensionless oscillation frequency $f^* = fC/U_\infty = 0.55$ and amplitude $A_\theta = 25°$. A schematic of the steps involved in this methodology is shown in figure 9.2, where we show snapshots of results from each stage in the procedure for this sample case.

9.1.1 Vortex detection

The first step in isolating and quantifying the influence of individual vortex structures is the task of detecting coherent vortex structures in the given flow-field. This problem of vortex detection has attracted significant research interest, and numerous definitions of coherent vortex structures have been proposed in literature, based on Eulerian [161–163] and Lagrangian [164, 165] criteria. In the context of this work, the aim of this vortex detection step is simply to identify the spatial volume corresponding to vortical regions in the flow-field, and this step can be implemented with many of the available vortex detection methods. In principle, the only requirement on the choice of the vortex

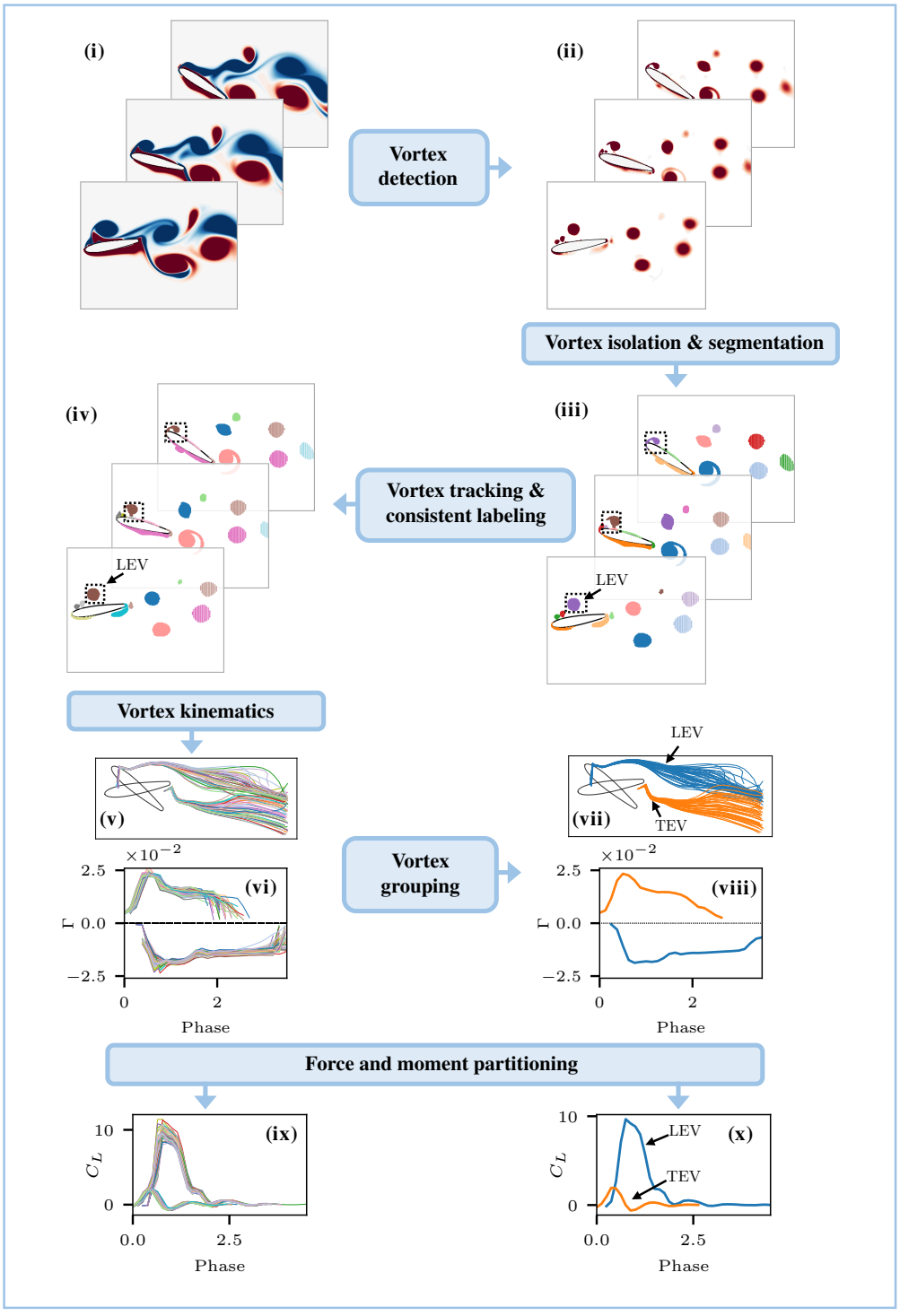

Figure 9.2: Schematic of the steps involved in the framework for the automated tracking of vortices and estimation of aerodynamic loads. The steps are illustrated using a sample case of a sinusoidally pitching airfoil with dimensionless frequency $f^* = 0.55$ and amplitude $A_\theta = 25°$.

detection method is that it generate an Eulerian scalar field representing the *interior* of the region occupied by vortical structures. This requirement stems from the fact that estimating the loading induced by vortex structures, using the vorticity-induced force and moment shown in equations (7.27) and (7.39), requires the identification of the spatial volume corresponding to these structures. In fact, the majority of existing vortex detection criteria do satisfy this requirement, and can therefore be used as a starting point in this framework.

In the implementation presented here, we utilize the Q-criterion [161] for detecting vortical regions in a given flow-field, primarily due to the formulation of the FMPM where Q makes an explicit appearance. This results in the Q scalar field, which was defined in equation (7.15) and is reiterated below for completeness:

$$Q = \frac{1}{2}\big(||\mathbf{\Omega}||^2 - ||\mathbf{S}||^2\big). \tag{9.1}$$

Here $\mathbf{\Omega}$ and $\mathbf{S}$ are the anti-symmetric and symmetric parts of the velocity-gradient tensor ($\nabla\vec{u}$) respectively (see equation 7.15). This Q field is a metric that compares the strength of rotation with strain in a local region of the flow, with 'vortices' corresponding to regions where $Q > 0$ i.e. where rotation dominates over strain. In figure 9.2, we show a sample vortex detection step for a 2D pitching airfoil. Figure 9.2(i) shows the vorticity field at three time snap-

shots during the pitch-down motion for this case. These flow-fields represent the input data for this procedure, and figure 9.2(ii) shows the $Q > 0$ field, which represents the vortices in the flow-field.

9.1.2 Vortex isolation and segmentation

Having identified vortical regions in the flow-field, the next step in this framework involves isolating the spatial volume corresponding to vortices, and then segmenting out the region occupied by each vortex. As shown in figure 9.2(ii), the vortex detection step results in a scalar field representing the distribution of the chosen quantity (such as Q in this case) at every time-snapshot. Using this scalar field, we perform a two-step method to isolate and segment the volume occupied by individual vortex structures. The first sub-step, i.e. the vortex isolation sub-step, simply involves applying an appropriate threshold to extract volumes within the domain that are occupied by vortices at time-snapshot t_j. In the context of the Q-criterion, we apply a threshold $Q > Q_{threshold}$, where $Q_{threshold}$ is small compared with the maximum value of Q in the field, in order to approximate the more physically relevant $Q > 0$ threshold for vortex detection. In general, the chosen threshold depends on factors such as errors/uncertainties in the underlying data, and on the vortex detection method used. In this work we use the threshold $Q_{threshold} = 5$. We show in figure 9.3 that the aerodynamic loading due to flow structures isolated using

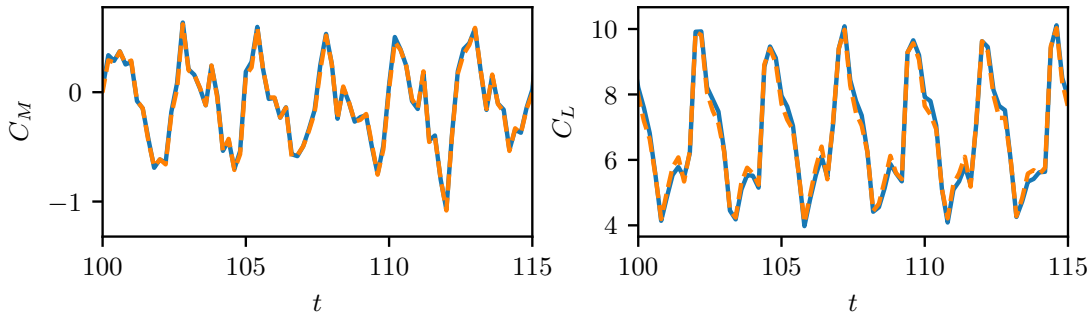

Figure 9.3: Comparison of total C_M and C_L induced by all vortex structures detected using the $Q > 0$ threshold (---) with those detected using the $Q > 5.0$ threshold (—).

$Q_{threshold} = 5$ is very similar to that using $Q_{threshold} = 0$. In terms of the flow-field data represented on the set of grid points $\{\zeta\}$, this thresholding results in a subset of grid points, $\{\zeta^{\Omega}\} = \{\zeta : Q(\zeta) > Q_{threshold}\}$, which consists of several disconnected (i.e. isolated) vortical regions. Each of these regions is a "dense" set of grid points where grid points within a particular $Q > Q_{threshold}$ region are closer to each other than they are to points within another such region.

Next, we segment these vortical regions into distinct volumes occupied by each individual vortex. This is performed using the well-known DBSCAN (density-based spatial clustering of applications with noise) clustering algorithm [166] on the set of grid points $\{\zeta^{\Omega}\}$. We note that while the use of clustering in the detection of coherent structures has been proposed in prior studies [123–126], the aim here is not to *detect* vortex structures using this approach. Rather, the use of clustering here simply aims to segment multiple distinct vortical regions in a flow and can be used in conjunction with other

methods of vortex detection.

DBSCAN is a density-based clustering technique that detects clusters as groups of points that have at least a certain number of neighbouring points, n_d, within a specified distance, ϵ. The required parameters, ϵ and n_d, are the maximum distance between two data-points for them to be considered in the same cluster, and the minimum number of data-points in the neighbourhood of another point to create a cluster, respectively. We find that ϵ can be conveniently chosen based on the maximum grid-spacing in the region of interest. Correspondingly, n_d depends on the number of grid-points that surrounds any given point within ϵ distance. The result of the DBSCAN clustering at any time-snapshot t_j is a segmentation of the domain into N_j non-intersecting clusters, where each cluster corresponds to a distinct subset of the $\{\zeta^\Omega\}$ grid points. The p^{th} cluster at time-snapshot t_j is denoted by $V_p^j \subset \{\zeta^\Omega\}$, such that $V_p^j \cap V_q^j = \emptyset$, for $p \neq q$. Here the subscripts, $(p, q) \in \{1, \cdots, N_j\}$, are arbitrary numeric "labels" assigned to each cluster, and the superscripts specify the index for time-snapshot t_j. The grid points within each set V_p^j therefore define the spatial extent of the p^{th} vortical structure at any given time instant t_j. We denote the set of all such volumes at time-snapshot t_j as $V_\Omega^j = \{V_1^j, V_2^j, \cdots, V_{N_j}^j\}$.

A sample result of this procedure is shown in figure 9.2(iii), where at each time-snapshot we see several clusters corresponding to distinct vortex structures. Each cluster is assigned a numeric label from 1 to N_j at every time-

snapshot (where N_j itself can vary from one time-snapshot to the next). In figure 9.2(iii), this label is graphically represented by the color of the vortex structure. This DBSCAN-based approach has several advantages in the context of clustering spatial regions in a flow-field. One is that the DBSCAN algorithm, unlike some other clustering techniques, does not require prior information on the number of clusters present in the flow domain. Secondly, this method is able to detect clusters of arbitrary shapes, which is particularly important in highly dynamic vortex-dominated flows. Lastly, a density-based technique that detects clusters based on the proximity of "vortical" grid points (ζ^{Ω}) to each other naturally lends itself to flow-field data. If the flow is sufficiently well-resolved to capture distinct vortical structures, it also necessarily has enough grid points between these vortical structures in order to distinguish them. This ensures that by isolating regions of $Q > Q_{threshold}$, the vortex structures of interest will present themselves as disconnected "dense" spatial regions in the domain. These can be efficiently segmented using a density-based clustering technique.

9.1.3 Vortex tracking and consistent labeling

Application of the above clustering algorithm independently at every time-snapshot often results in cluster labels (which, for time-step t_j range from 1 to N_j) that have no temporal continuity with the other time snapshots. This is

shown in figure 9.2(iii), where the result of clustering is shown at three consecutive time-snapshots and numeric cluster labels are represented by different colors. We see, for instance, that the leading-edge vortex, which is highlighted using a dashed box at each time-snapshot in figure 9.2(iii), is labelled (colored) differently between subsequent time-snapshots. It is easy to see that this mis-labelling also occurs for the other vortex structures that were isolated in the previous time-step. Consistent labeling of the vortex structures over all the time-snapshots is essential in order to generate continuous time-histories of any attributes associated with these vortex structures. These attributes may include the geometry of vortices (location, size, shape etc.) or kinematic/dynamical behaviour such as net circulation and crucially, the aerodynamic loads associated with the vortex, which are obtained from the FMPM.

To achieve temporally consistent labeling of the segmented vortices, we employ a vortex tracking procedure based on a simple model of vortex convection. We start by computing the centroids of all clusters identified at time t_j. This set of centroids is denoted by $\{\vec{X}_1^j, \vec{X}_2^j, \cdots, \vec{X}_{N_j}^j\}$. The centroids are obtained as an integrated average of the coordinates within each corresponding volume $V_p^j \in V_\Omega^j$. The numerical integration can done using various schemes and here we employ the simplest, midpoint (area-weighted) integration scheme. Similarly, we define the convection velocity of each cluster as an area-weighted average of the flow velocity within each set of grid points V_p^j. These are denoted

by $\{\vec{U}_1^j, \vec{U}_2^j, \cdots, \vec{U}_{N_j}^j\}$. Then at any time t_j, we first compute the predicted position of all structures detected at the previous time-snapshot using a Forward Euler scheme. For the p^{th} cluster in the previous time-snapshot, this predicted position is given by $\vec{X}_p' = \vec{X}_p^{j-1} + \vec{U}_p^{j-1}\Delta t$, where $p \in \{1, ..., N_{j-1}\}$ denotes the cluster labels at time t_{j-1} and Δt is the time-step between these consecutive snapshots. Hence at every time-snapshot t_j, we have the actual centroidal positions of each vortex structure detected directly from the flow-field at that time-snapshot, i.e. $\{\vec{X}_1^j, \cdots, \vec{X}_{N_j}^j\}$, as well as predicted positions of all vortex structures computed from the previous time-snapshot, i.e. $\{\vec{X}_1', \cdots, \vec{X}_{N_{j-1}}'\}$.

Subsequently, a distance matrix of size $(N_j \times N_{j-1})$ is computed between the actual vortex centroids at t_j and the centroids of the vortex structures predicted from the previous time-snapshot. This matrix is denoted as D, and its p^{th}-row and q^{th}-column entry is given by $D_{p,q} = |\vec{X}_p^j - \vec{X}_q'|$. Here $|\cdot|$ is the L-2 norm. In order to improve the robustness of the distance comparison, we also include the sign of the average vorticity in each cluster as an extra dimension in this difference. These pairwise distances are then sorted in ascending order of magnitude, the rationale being that small entries in D likely correspond to the same physical vortex structure between successive snapshots. Each pair of labels, (p, q) in this sorted list is tested against certain conditions, such as either the label in the present or previous time step has not been already assigned to another cluster, or that $D_{p,q}$ is not greater than a specified distance. For pairs

of labels that satisfy these conditions the label at the current time-snapshot (p) is changed to match that at the previous time-snapshot (q). This is repeated until either all cluster labels in the current time-snapshot have been matched with a corresponding cluster from the previous time-snapshot, or there are no more pairs that satisfy the specified criteria. The remaining cluster labels at the current time-snapshot are then considered as being vortices that have appeared at the current time-step, and are given new labels that are distinct from all previously used labels. The labels from the previous snapshot (t_{j-1}) that do not find a match with any vortices at t_j correspond to structures that have either exited the domain of interest or dissipated below the prescribed threshold. The labels corresponding to these structures are retired. The final result is that the label for each identified vortex is carried from one time to the next in a continuous and consistent manner. Furthermore, the time-varying volume occupied by a vortex with label p is now fully described at any time i by the set of grid points within each V_p^j.

In figure 9.2(iv) the result of this vortex tracking process is shown. We see that the leading-edge vortex, highlighted using the dashed box at each time-snapshot, as well as other vortices which were arbitrarily labelled at each time-snapshot in figure 9.2(iii) are now labeled in a way that results in the consistent tracking of these vortex structures. We note that the above procedure for feature tracking falls under the category of "attribute correspondence" in

the flow visualization domain (where the attribute in this case is the position), and a similar method has been shown to work well even in 3D flows [167, 168].

9.1.4 Vortex kinematics, ranking and grouping

Once each segmented vortex has a unique and consistent label over time, we can compute temporal histories of various kinematic attributes for these vortices including, but not limited to,

- Centroid location, including location of inception and location of exit.
- Vortex area (2D) or volume (3D).
- Shape (as defined by the vortex boundary).
- Vortex strength.

Additionally, vortices can now also be ranked based on any of these kinematic attributes. Here we choose to rank the vortices in terms of their circulation (representing vortex strength). For a vortex structure with label p, we compute its time-dependent circulation (in 2D) as $\Gamma_p(t_j) = \sum_{V_p^j} \omega_z \Delta x \Delta y$, where the summation is over the grid cells in the set V_p^j at each time-snapshot (t_j), ω_z is the time-varying vorticity at the center of each grid cell, and Δx and Δy are the linear dimensions of the grid cell. Due to the periodic nature of the pitching airfoil problem being analyzed here, we perform this ranking over each cycle of the airfoil's oscillation. This is done by integrating the magnitude of circulation for

each vortex detected in a particular cycle over all time-snapshots within that cycle. We then sort the vortices in every cycle by this total magnitude of circulation, and retain only the top few vortices for analysis. It must be noted that this rank-reduction of the set of isolated vortices can be performed in several different ways, and is only intended to simplify subsequent analysis.

In figures 9.2(v) and 9.2(vi) we show sample results of the kinematic analysis described above. Figure 9.2(v) shows vortex trajectories, represented as the loci of the centroid of each structure, for the two "top-ranked" vortices identified in each oscillation cycle using the circulation-based ranking described above. Figure 9.2(vi) shows time-series plots of circulation for these two "top" vortices, plotted against the phase of the airfoil's oscillation. It is clear that the trajectories of the two strongest vortices, although they seem chaotic, all correspond to vortices shedding off either the leading or trailing edge of the airfoil. In fact, the leading-edge vortex (LEV) and trailing-edge vortex (TEV) are observed to be the strongest vortices, in terms of circulation, for the majority of cases analyzed in the current data set. This is evident from the flow snapshots in figures 9.2(i)-(iv) for the specific case being analyzed in this section.

In addition to the analyses suggested above, the available kinematic information can also be used to group the set of the detected vortex structures based on similarities in any chosen attribute. For instance, the centroid location of each vortex as a function of time allows us to group vortices based on location

of inception. In particular, in the rank-reduced set of vortices obtained above, vortices emerging from the leading-edge could be assigned to one group and those emanating from the trailing-edge could be assigned to a different group. We perform this grouping of vortex structures by using a clustering-based approach. We again use the DBSCAN algorithm described above for this task, primarily because it does not require knowledge of the number of classes beforehand. Figures 9.2(vii) and 9.2(viii) show the result of such a vortex grouping, applied to the two top-ranked vortices identified using circulation. The identified groups are shown using different colors for each group, and figure 9.2(vii) shows the categorized spatial trajectories. Here the grouping is based on the location of the vortex centroid at its inception, its location on exiting the domain of interest, and the mean and standard deviation of its circulation. We see that this method works well even when the kinematics are not perfectly repeatable over each cycle. Further, ensemble-averages can computed over a given group, and figure 9.2(viii) shows the ensemble-averaged circulation as a function of oscillation phase for two groups of vortices, the LEVs and the TEVs.

9.1.5 Force and moment evaluation

Having accomplished the isolation and tracking of the various vortex structures, we can now perform the final step in this analysis framework, which is to quantify the aerodynamic loading due to these flow structures on the immersed

body. As shown in equations (7.27) and (7.39), the induced force and moment on an immersed body due to vortical regions of the flow can be quantified by integrating kinematic flow-field quantities over specifically constructed integral volumes. Thus, for a vortex structure with label p, which occupies the volume specified by V_p^j at time t_j, the time-varying induced loads can be estimated by the following expression:

$$C_{F_i}^{\omega_p}(t_j) \approx -2 \int_{V_p^j} Q\ \phi_i\ dV \quad ; \quad C_{M_k}^{\omega_p}(t_j) \approx -2 \int_{V_p^j} Q\ \psi_k\ dV \tag{9.2}$$

Here the integrands can be readily calculated at every time-snapshot given the instantaneous flow-field and geometry of the immersed surface B. Therefore, using the procedure described above to isolate and track the volumes corresponding to each vortex structure in the flow makes it straightforward to compute the force and moment induced by each of these structures as they evolve with the flow

In figures 9.2(ix) and 9.2(x) we show a result of this force computation for the sample case discussed here, where the coefficient of lift (C_L) due to the two "top-ranked" vortices, i.e. the LEV and TEV, are plotted against the phase of the oscillation. The multiple curves in figure 9.2(ix) correspond to LEVs and TEVs shed during several oscillation cycles of the pitching airfoil. This procedure therefore allows us to quantify the force and moment production due to

each of these vortices. Further, the vortex grouping procedure described above also allows the computation of statistics of the aerodynamic loads over multiple occurrences of a single type of vortex. This is demonstrated in figure 9.2(x), where the ensemble-averaged C_L, computed over all occurrences of LEVs and TEVs separately, is shown as a function of the phase of oscillation. Thus, using the framework described in this section, we can analyze high-dimensional, time-resolved flow-fields and extract a wide range of quantities associated with the kinematics as well as dynamical influence of individual vortex structures.

9.2 Application to pitching airfoils

We now present an application of the methods described in the previous section to the analysis of the two-dimensional flow past an airfoil which is undergoing prescribed sinusoidal pitch oscillations over a range of amplitudes and frequencies of oscillation. As we will show, this canonical problem exhibits numerous distinct vortex-dynamic regimes, which have been shown to be more complex [61] than those behind the more well-studied problem of an oscillating cylinder. Further the flow is characterized by several dominant interacting vortex structures, and even relatively small changes in the kinematics lead to substantially different vortex-dynamic behaviour. In this section, we will first employ a data-driven method to reduce this large ensemble of flow-fields to a

small number of distinct regimes, and subsequently utilize the methods discussed in prior sections to analyze these vortex-dominated flow-fields at the level of individual vortices.

The data-set analyzed here consists of 165 distinct cases of a two-dimensional NACA0015 airfoil, which undergoes prescribed sinusoidal pitching oscillations at Reynolds number, defined based on free-stream velocity U_∞, and chord-length C, as $Re = U_\infty C/\nu = 1000$. The sinusoidal pitching amplitude is given by $\theta = \theta_0 + A_\theta \sin(2\pi f^* t)$. Here θ is the instantaneous angle-of-attack, θ_0 is the mean angle-of-attack, and A_θ is the pitching amplitude (reported in degrees). Further, f^* is the dimensionless pitching frequency, given by $f^* = fC/U_\infty$, with corresponding oscillation period $T^* = 1/f^*$, and t is the dimensionless time (also non-dimensionalized by U_∞ and C). The airfoil is forced to pitch about mid-chord with mean angle-of-attack $\theta_0 = 15^\circ$. We analyze oscillation amplitudes and frequencies in the range $0.5 \leq A_\theta \leq 40$ and $0.10 \leq f^* \leq 0.70$ respectively. The time-resolved flow-field data used for this analysis consists of 500 temporal snapshots for each case, recorded after the flow has reached a stationary state. This corresponds to between 10 and 70 oscillation cycles, depending on f^* for the particular case.

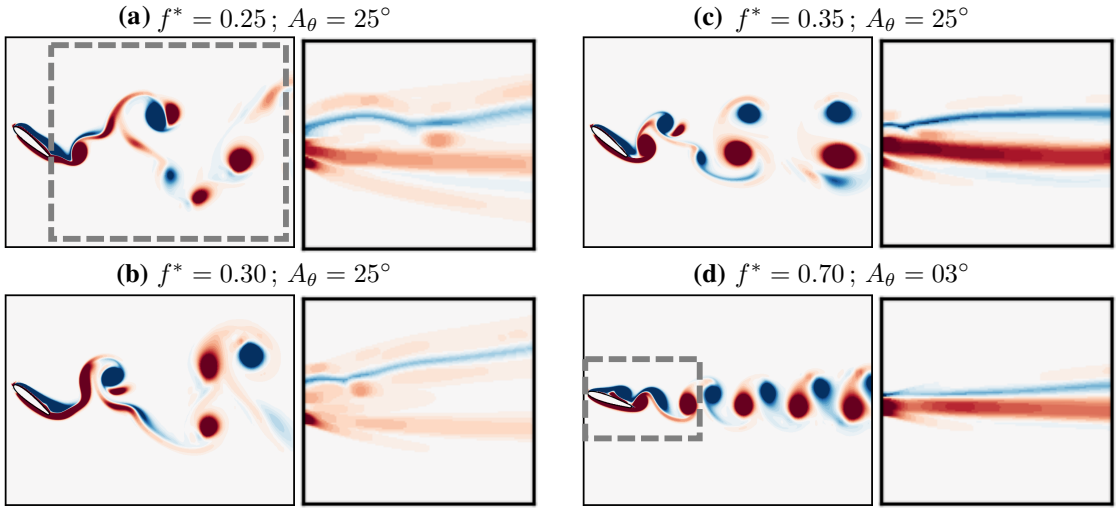

Figure 9.4: Instantaneous snapshots of the vorticity field (left panel for each case) for four representative cases of pitching airfoils, and corresponding time-averaged vorticity fields in the wake ($\bar{\omega}$; right panel for each case). The instantaneous snapshots are shown at the phase of maximum angle of attack, in order to highlight leading and trailing edge vortex interactions and trajectories. (a) $f^* = 0.25$, $A_\theta = 25^\circ$; (b) $f^* = 0.30$, $A_\theta = 25^\circ$; (c) $f^* = 0.35$, $A_\theta = 25^\circ$; (d) $f^* = 0.70$, $A_\theta = 03^\circ$. The dashed box in (a) shows the region used for calculating $\bar{\omega}$, and that in (d) shows the domain used for the analysis in section 9.2.2.

9.2.1 Rank-reduction based on vortex shedding regimes

Due to the large size of the present data-set, we begin by performing a "rank-reduction" of this data to facilitate the analysis. The aim here is to reduce the set of 165 time-resolved flow-fields to a smaller set of distinct regimes (i.e. a "rank-reduced set") that captures the important features present in the data set. We then perform the subsequent vortex analysis on this rank-reduced set of cases. In the present application, distinct vortex-dynamic regimes are

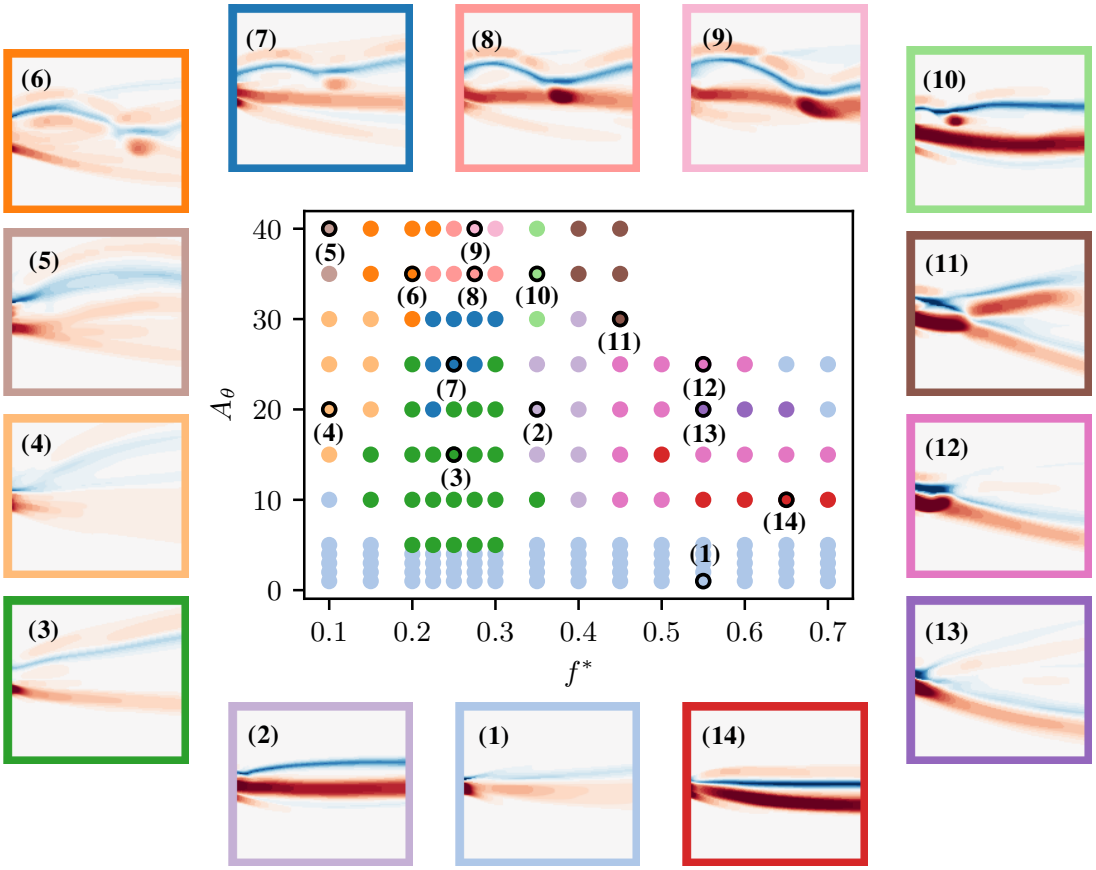

Figure 9.5: Final clustering result for distinct vortex-dynamic regimes in the data-set of pitching airfoil simulations. The plot in the center shows all the simulations in the data-set in f^*-A_θ space, with markers of different colors corresponding to different clusters of vortex-dynamic regimes. Time-averaged vorticity fields corresponding to the simulation closest to the centroid of each cluster (indicated using numeric labels for each cluster) are shown around the central f^*-A_θ plot.

identified based on vortex patterns in the wake of the pitching airfoil. Further, we take a data-driven approach to perform this rank-reduction, by identifying groups (or clusters) within this ensemble of flow-fields that have similar vortex-wake patterns.

Given this large ensemble of time-resolved flow-fields representing each member of the ensemble, the first step involves extracting appropriate information from each case in order to identify similarities in their vortex patterns. While there are several ways to extract important patterns from time-resolved flow-fields, such as modal decomposition techniques [106], we use a "zeroth-order mode" of the flow-field – the time-averaged vorticity field. In figure 9.4, we show instantaneous snapshots of vorticity (left panel for each case) for four representative cases from this data-set, along with their corresponding time-averaged wake-vorticity fields (right panel for each case). The wake region used for this calculation of mean vorticity is shown using a dashed rectangular box in figure 9.4(a), and is of size $4.5C \times 4C$. It is interesting to note that, although the cases in figures 9.4(a)-(c) have similar kinematics, they show substantial differences in their vortex dynamics, and consequently in their mean vorticity patterns. Using this extracted "feature vector" of the flow-field for each case, we subsequently use a sequence of data-driven tools to discover similarities within the data-set, and eventually arrive at a small number of cases representing distinct vortex dynamic regimes. Further details of the method,

which involves dimensionality reduction using principle component analysis, followed by clustering based on Gaussian mixture modeling, and a statistical evaluation of the robustness of the results, are provided in appendix B.

The rank-reduction process employed here results in 14 clusters representing distinct vortex-wake patterns. Figure 9.5 shows the demarcation of all cases in the data-set into these 14 clusters. The plot at the center of figure 9.5 shows the frequency and amplitude of all the cases in the data-set using circles, and these circles are colored based on the cluster membership for each case. The case closest to the centroid of each of these 14 clusters is highlighted using a numeric cluster label in this frequency-amplitude plot. Further, we also show the mean vorticity field ($\bar{\omega}$) corresponding to the "centroidal" case for each cluster. These $\bar{\omega}$ plots are labelled using the same cluster labels as well as framed using the cluster color corresponding to each cluster in the frequency-amplitude plot. We see that this procedure results in the identification of several distinct vortex-dynamic regimes. For the remainder of this paper, We use these representative centroidal cases to analyze the vortex dynamics in this data-set.

9.2.2 Analysis of vortex kinematics

We now demonstrate the utility of the analysis framework described in section 9.1, applied to the distinct vortex-dynamic regimes identified in the previ-

ous sub-section. For each representative case in figure 9.5, the time-resolved flow-field data is analyzed using the framework outlined in section 9.1 and in the discussion above. While the wake-identification process in the previous sub-section takes a "global" view of the flow-field, the aim of the methods demonstrated here is to dissect these regimes in terms of individual vortex structures – their kinematics, dynamics and the forces/moments they induce on the pitching airfoil.

We will largely focus on the leading-edge vortex (LEV) and the trailing-edge vortex (TEV) in this discussion due the dominant role they play in the fluid dynamics of pitching airfoils. In addition, the LEV and TEV are seen to be amongst the "strongest" vortices (in terms of circulation) for all cases analyzed here. However, we note that the methods demonstrated can be applied to the simultaneous analysis of many other flow structures as well, and we present an example of such an analysis later in this section. Since a particular focus of this method is to evaluate the influence of specific vortex structures in terms of forces and moments induced on a body, we will center this analysis on the flow in the vicinity of the airfoil. The spatial domain of interest is hence constructed such that its horizontal extent begins upstream of the airfoil at the leading edge (when the airfoil is at $\theta = 0^{\circ}$) and extends $1.5C$ downstream of the trailing edge. The vertical size of the domain of interest is $2C$. A schematic of this analysis domain is shown in figure 9.4(d).

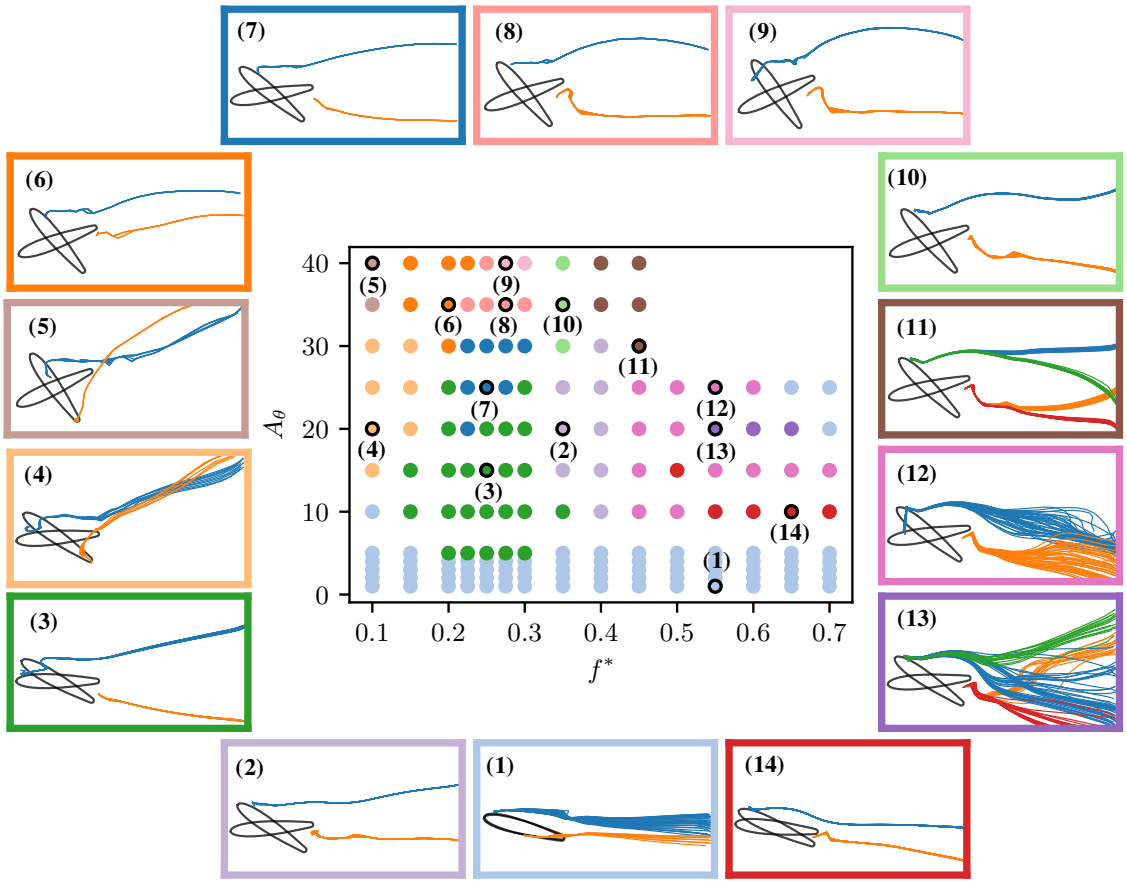

Figure 9.6: Leading-edge vortex (—) and trailing-edge vortex (—) trajectories corresponding to each vortex-wake regime identified in section 9.2.1. Figure in the center shows all the simulations in the data-set in f^*-A_θ space, with markers of different colors corresponding to different regimes. The vortex trajectories shown correspond to the simulation closest to the centroid of each cluster. Also shown on each trajectory plot is the maximum and minimum angle-of-attack of the oscillating airfoil for each case.

In figure 9.6 we show the trajectories of all the LEVs (in blue) and TEVs (in orange) for each of the 14 representative ("centroidal") cases identified using the rank-reduction procedure described above. These trajectories consists of an average of 40 oscillation cycles after the flow reaches a stationary state. As in figure 9.5, all simulations in the data-set are represented in the frequency-amplitude plot using circles corresponding to their frequencies and amplitudes of oscillation, colored by their cluster membership. The plots showing LEV and TEV trajectories for each of the 14 representative ("centroidal") cases are given numeric labels corresponding to each cluster's "centroidal" case indicated in the frequency-amplitude plot. Further, these LEV and TEV trajectories are overlaid on snapshots of the airfoil surface at its extreme angles-of-attack for each case.

We see from figure 9.6 that the distinct wake regimes identified previously also correspond to several distinct LEV and TEV trajectories in the vicinity of the airfoil. These vortex trajectories plots reveal several interesting features of the vortex dynamics in this problem. First, for all but two cases the LEV is shed at the maximum pitch-up phase and the TEV is shed at maximum pitch-down phase. The two cases labels (4) and (5) for which this does not happen are both the lowest frequency cases in the current data set ($f^* = 0.10$). These two cases also show trajectories that are quite distinct; whereas in most other cases (excluding cases $11 - 13$) the LEV and TEVs travel along trajectories that

do not cross, these two cases show trajectories that cross in the near wake and are indicative of vortex entrainment. As we will show, these observations are significant in terms of the forces induced by the TEV as the oscillation frequency is varied.

A second interesting behavior that is noted is that for case (11), where we see a bifurcation in the trajectories of the LEVs and TEVs. Examination of the vortex shedding behavior for this case shows that this is associated with the appearance of period-doubling bifurcation, wherein shed vortices alternate between these two trajectories from cycle to cycle. Furthermore, examination of cases $(10)-(13)$ also reveals what appears to be a period-doubling route to chaos in this flow. For case (10), the trajectories are highly repeatable from cycle-to-cycle. A slight increase in frequency coupled with a decrease in amplitude results in the period-doubling behavior seen for case (11). Further increase in frequency and decrease in amplitude, in case (12), shows the appearance of cycle-to-cycle variability in the vortex trajectories which can be viewed as emerging chaotic behavior. Case (13) shows further increase in non-periodicity of the flow with the vortex trajectories of both the LEVs and TEV showing large cycle-to-cycle variations, which is indicative of well-developed chaos.

This bifurcation in trajectories is highlighted in figure 9.7, where the scatter plot on the left shows the Y-coordinate of each LEV (blue circles; top panel) and TEV (orange circles; top panel) as it exits the analysis domain. These exit

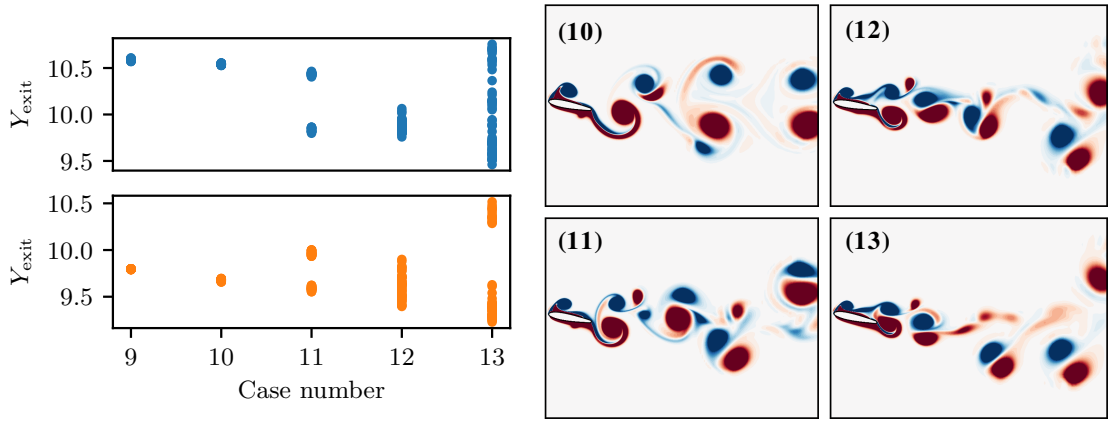

Figure 9.7: Scatter plot on the left shows the Y-coordinate of each LEV (top panel; •) and TEV (bottom panel; •) as it exits the analysis domain, for cases (9)-(13) in figure 9.6. The scatter plot is generated from vortices in ≈ 40 oscillation cycles in each case. Right panel shows an instantaneous snapshot of vorticity for the cases numbered (10)-(13) in figure 9.6.

locations are plotted against the case numbers used in the above discussion. We see that cases (9) and (10) each show one repeatable exit location each for the LEV and TEV, whereas the period-doubling in case (11) shows up as two repeatable exit locations. This exit location gets less repeatable for cases (12) and (13), with case (13) in particular showing a large spread in exit locations. This resembles a typical return map for such period-doubling bifurcations, and a period-doubling route to chaos has indeed been observed in previous work on unsteady airfoils [148]. However, the occurrence of such a bifurcation is not obvious from simple flow-field visualizations, particularly in very large data-sets such as this. This is highlighted in the right panel of figure 9.7, where we show instantaneous vorticity snapshots for the cases (10)-(13). While these snapshots show some differences in the flow, they are not indicative of clear

trends in the kinematics such as that discussed above. Therefore the ability to identify such behaviour in very large ensembles of flow data is a demonstration of the utility of the current data-driven analysis approach.

In addition to vortex trajectories, the method allows us to extract a variety of other quantities associated with the kinematics and geometry of the vortices, including, for instance, their circulation. As an example, figure 9.8(a) shows a plot of phase-averaged circulation versus oscillation phase (t/T^*) for LEVs (—; blue) and TEVs (—; orange) in all 14 cases representing distinct vortex dynamics identified above. The circulation is computed as $\Gamma = \int_{A_\Omega} \omega_z dA$, where A_Ω is the area occupied by a particular vortex and ω_z is the out-of-plane vorticity. We overlay this circulation time-series for all 14 cases to highlight the wide variety of observed behaviour. Further, this data can also be parsed to analyze trends in circulation versus airfoil kinematics. Figures 9.8(b) and 9.8(c) show the peak value of circulation (defined as maximum value for TEV and minimum value for LEV) plotted against f^* and A_θ respectively. We see that clear trends emerge from this data, showing that the magnitude of peak LEV circulation is inversely proportional to f^* and directly proportional to A_θ. The TEV shows an interesting non-monotonic trend against f^* and is weakly monotonic with A_θ. While in the current paper we do not focus further on this data, we point out that this easily extracted time-resolved circulation data could be useful for understanding vortex dynamics as well as for the development and

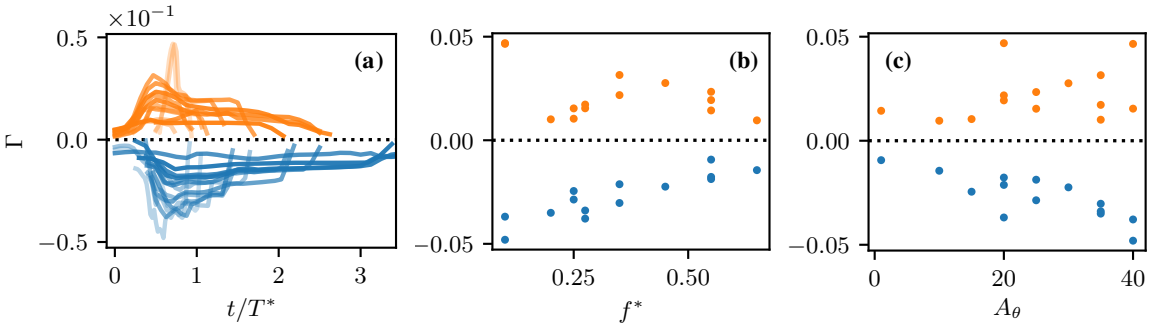

Figure 9.8: (a) Phase-averaged circulation, Γ, for LEVs (—; $\Gamma < 0$) and TEVs (—; $\Gamma > 0$), plotted against oscillation phase (t/T^*) for all 14 cases representing distinct vortex dynamics; (b) Scatter plot of peak Γ versus oscillation frequency (f^*) for LEVs (●) and TEVs (●); (c) Scatter plot of peak Γ versus oscillation amplitude (A_θ) for LEVs (●) and TEVs (●). Peak value is defined as most negative value for LEV and most positive value for TEV. Note: Transparency in (a) is arbitrary and is purely for visualization.

validation of simplified vortex models [22, 89].

As a final demonstration of this framework for kinematic analyses, we present an example of its application to many simultaneously evolving and interacting vortex structures, in addition to the LEV and TEV. As mentioned earlier, the discussion thus far focused exclusively on the LEV and TEV due to the fact that they are the dominant vortices in the majority of cases. However for oscillations at very low frequencies, we see the generation and shedding of several other vortices that are comparable to, or only slightly weaker than the LEV and TEV in terms of circulation. Hence we choose the case with $f^* = 0.10$ and $A_\theta = 40°$ for this demonstration. Figures 9.9(a)-(c) show three instantaneous snapshots of the vortices in the flow-field, visualized as regions of $Q > 0$. Several vortices of varying strength and size have been indicated using numeric

labels in these snapshots. We see that this case features a complex flow-field with vortices shed off the upper and lower surfaces of the leading edge, labeled (1) and (6) respectively. Further, there are also secondary LEVs shed off both these surfaces, labeled (4) and (5) respectively, as well as multiple types of trailing-edge vortices, labelled (2) and (3) respectively. Figure 9.9(d) shows the extracted vortex trajectories and and we see that the method is able to accurately detect, track, as well as group all these different vortices. This is also an example of a case where identifying groups of vortices based purely on location of inception would not be sufficient, and using other attributes that are available with the current method (such as mean and standard deviation of circulation in this case) becomes necessary. Although not shown here for brevity, the accurate isolation, tracking, and grouping of these vortices now allows us to extract and analyze a variety of kinematic and dynamic quantities relevant to these vortices, in much the same way as in the analysis of LEVs and TEVs presented in the rest of this paper.

9.2.3 Vortex-induced forces and moments

We now demonstrate the utility of this framework in dissecting the dynamical influence of individual flow-structures on the immersed surface. As in the previous section, the focus here will be on the influence of the LEV and TEV. We begin with an overview of the force and moment generated by the LEV

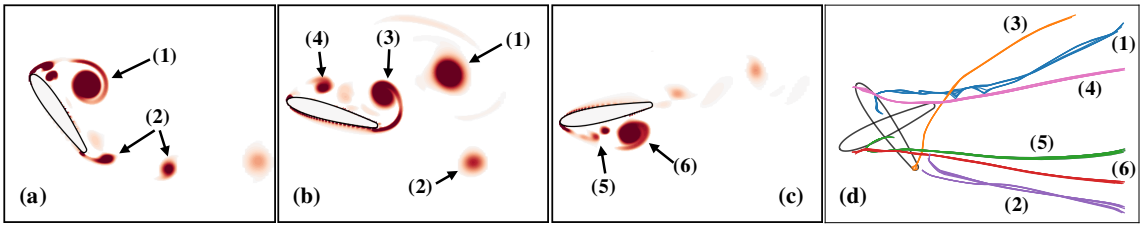

Figure 9.9: An example showing the use of current framework to isolate, track, and group several (> 2) vortices simultaneously. For this case, $f^* = 0.10$ and $A_\theta = 40°$. (a)–(c) Instantaneous snapshots of the flow visualized using regions of $Q > 0$. Snapshots are shown at three phases in a single oscillation cycle. Arrows and numeric labels highlight six types of vortices that are analyzed. (d) Spatial trajectories of the six types of vortices highlighted in the flow snapshots. Colors show different vortex types and numeric labels correspond to those in (a)–(c).

and TEV in all 14 centroidal cases. This is shown in figure 9.10, where the phase-averaged C_L and C_M, overlaid on each other for all 14 cases, are plotted against the phase of oscillation, t/T^*. Figures 9.10(a) and 9.10(b) show the LEV-induced coefficients of lift (C_L^{LEV}) and moment (C_M^{LEV}) respectively, and we see that there is a wide range in the peak value of lift and moment induced by the LEV as the airfoil's oscillation kinematics are varied. Further, we see clear variations in the phase of the peak lift and moment, which is an important consideration and will be discussed in more detail in this section. Figures 9.10(c) and 9.10(d) show the TEV-induced lift (C_L^{TEV}) and moment (C_M^{TEV}) for these cases. We again see large variability in the peak loading induced by the TEV. It is particularly interesting to point out the large peak in TEV-induced lift and moment seen in two particular cases, which are indicated using an arrow in figure 9.10(c). These cases correspond to low-frequency oscillations which,

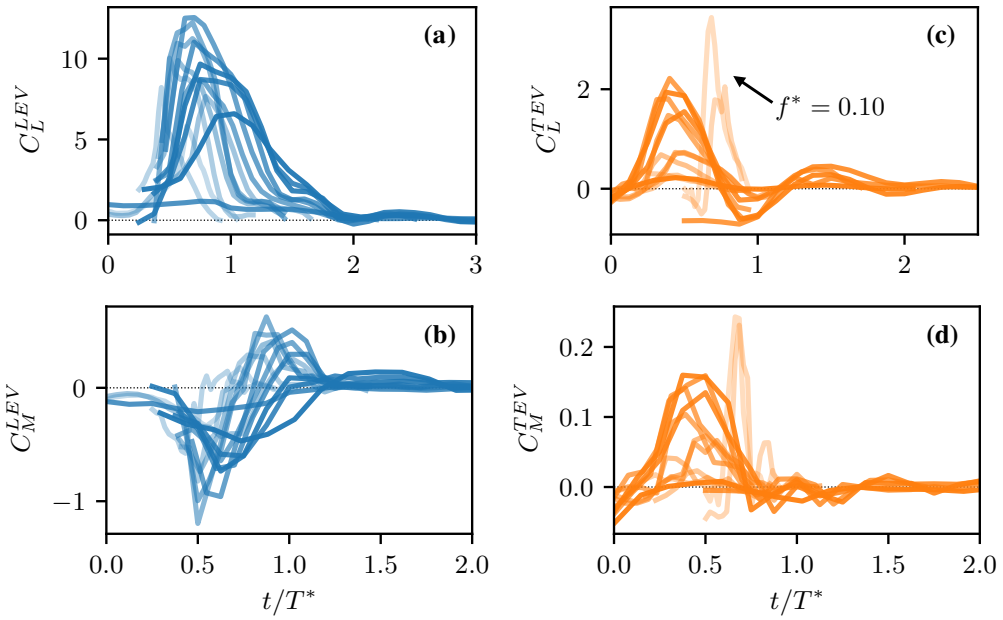

Figure 9.10: Phase-averaged C_L (top panel) and C_M (bottom panel) induced by LEVs (—) and TEVs (—), overlaid for all 14 cases representing distinct vortex dynamic regimes. X-axis shows the phase of oscillation (t/T^*); (a) C_L due to LEVs; (b) C_M due to LEVs; (c) C_LM due to TEVs; (d) C_M due to TEVs. Note: Transparency is arbitrary and is purely for visualization.

as seen in the previous section, behave differently from all other cases even in terms of the vortex kinematics. The remainder of this section will focus on demonstrating the efficacy of this framework in analyzing some aspects of the behaviour highlighted here – particularly the relative importance of the LEV and TEV as the airfoil kinematics are varied, and the phase of their induced loading with respect to the airfoil's motion.

We now focus our discussion on some select cases in the data-set, and delve further into the details of the aerodynamic loading induced by the LEV and TEV. In figure 9.11, we compare the vortex-induced force and moment in three

cases representing distinct vortex-dynamic regimes, with labels (5), (2) and (13). These cases correspond to airfoils oscillating with the same amplitude and at different frequencies. The frequencies of oscillation are $f^* = 0.10$, $f^* = 0.35$, and $f^* = 0.55$ in figures 9.11(a), 9.11(b) and 9.11(c) respectively. The amplitude of oscillation is $A_\theta = 20^\circ$ for all three cases. The top panel for each case shows the phase-averaged coefficient of lift (C_L) induced by the LEV (—; blue solid line), TEV (—; orange solid line), and the total C_L induced by all vortex structures (- - -; grey dashed line). Similarly, the middle panel shows the coefficient of moment (C_M) induced by the LEV, TEV, and all vortex structures. In the bottom panel, the force and moment time-series are compared with the phase of the angular velocity of the airfoil. The oscillation phase is represented as t/T^* on the X-axis.

It is immediately apparent on comparing the time-series plots of the C_L and C_M induced by the LEV (—; blue solid line) with the total induced by all vortex structures (- - -; grey dashed line), that the LEV accounts for the bulk of the vortex-induced force as well as moment production. In fact, this is true of nearly all the cases analyzed in this work. Moreover, these cases show that the LEV dictates a larger proportion of the force and moment production as the oscillation frequency is increased. We also see that the aerodynamic loading due to the TEV (—; orange solid line) is comparable to that of the LEV only in the lowest-frequency case at $f^* = 0.10$, and is negligible at higher

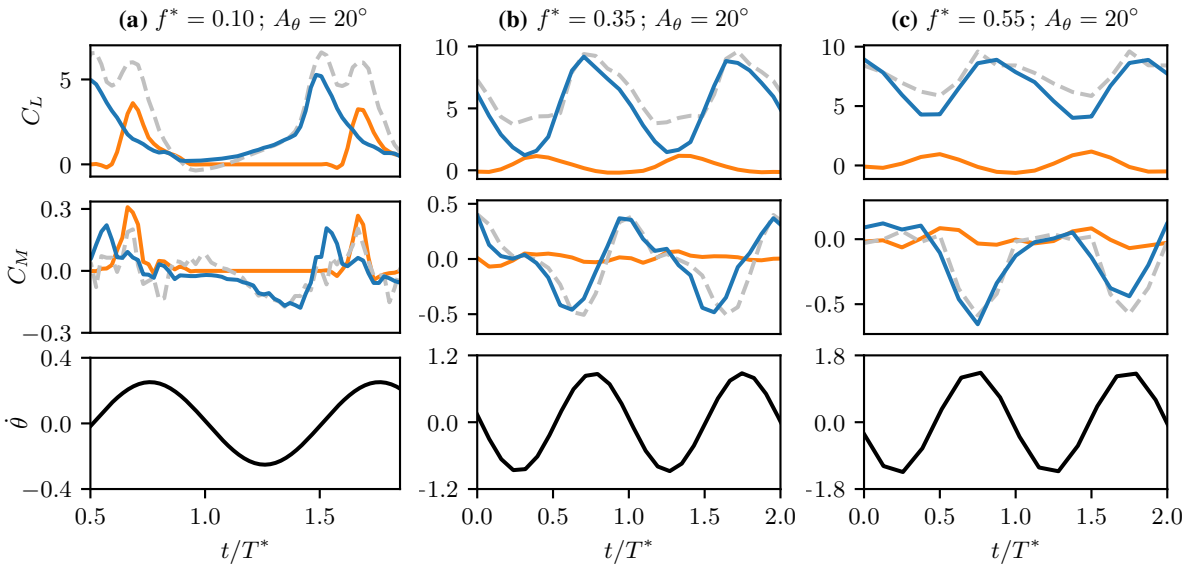

Figure 9.11: Top panel shows C_L induced by the LEV (—) and TEV (—), compared with total C_L induced by all vortical regions (- - -). Middle panel shows C_M induced by the LEV (—) and TEV (—), compared with total C_M induced by all vortical regions (- - -). Bottom panel shows angular velocity ($\dot{\theta}$). All quantities are plotted against phase of oscillation (t/T^*) for three cases representing different vortex dynamic regimes. (a) $f^* = 0.10$, $A_\theta = 20°$; (b) $f^* = 0.35$, $A_\theta = 20°$; (c) $f^* = 0.55$, $A_\theta = 20°$.

frequencies. This is related to the delayed separation of the TEV that was observed at low frequencies using the vortex trajectories in figure 9.6. This delayed separation therefore allows the TEV to benefit from the feeding shear-layer on the pressure side of the airfoil for a longer duration.

Another important aspect of the forces and moments induced by these vortex structures is their phase with respect to the oscillation of the airfoil. The phase difference between the force/moment production and the kinematics can be shown to be a primary determinant of the energy extracted by an elastic structure from the surrounding flow [77, 151]. This energy extraction is in turn responsible for the initiation and sustenance of flow-induced oscillations, and is an important quantity in the study of aeroelastic response branches and their stability [27, 29, 75, 77–79]. For a pitching airfoil, it can be shown that the energy extracted by the airfoil from the flow depends on the phase difference between C_M and $\dot{\theta}$, and is maximum when they are in-phase [77]. In the present case, we see from figures 9.11(a)-(c) that $\dot{\theta}$ and the LEV-induced C_M get progressively more out-of-phase as the oscillation frequency is increased. In addition, there is also a variation in the phase of C_L with respect to the kinematics of the airfoil. This is relevant in multi-degree-of-freedom applications such as energy harvesting. In particular, for systems based on energy extraction from heave oscillations that are instigated by pitching-related non-linearities [169], the phase of the LEV-induced C_L with respect to the oscillation is an impor-

tant aspect in their performance. This method can therefore inform design considerations in these applications to either enhance or diminish the energy extraction from various flow-structures, as necessary.

As a final demonstration of the current method, we use flow-field data in conjunction with the computed forces and moments in order to explain the phase-behaviour observed above. In particular, we analyze the physics behind the observation that the LEV-induced moment is more out-of-phase with angular velocity as the oscillation frequency is increased. For this analysis we focus on two cases which have oscillation frequencies $f^* = 0.20$ and $f^* = 0.35$, with equal amplitudes of $A_\theta = 35^\circ$. These cases are chosen because they correspond to positive and negative energy extraction (E^*) respectively, or favourable and unfavourable phase difference between C_M and $\dot{\theta}$. In addition, these cases lie very close to the boundary between positive and negative energy extraction by the pitching airfoil (see $E^* = 0$ contour in figure 9.1), and therefore represent a situation where an increase in oscillation frequency (at constant amplitude) causes C_M to go from in-phase to out-of-phase with respect to $\dot{\theta}$. The cases with $f^* = 0.20$ and $f^* = 0.35$ are labelled (6) and (10) in the preceding discussion, and their analysis is presented in figures 9.12(a) and 9.12(b) respectively.

In figure, 9.12 the top panel shows the moment induced by the LEV for each case, denoted as C_M^{LEV}. This is compared with $\dot{\theta}$ in the middle panel. We note that moment and angular velocity are positive in the anti-clockwise

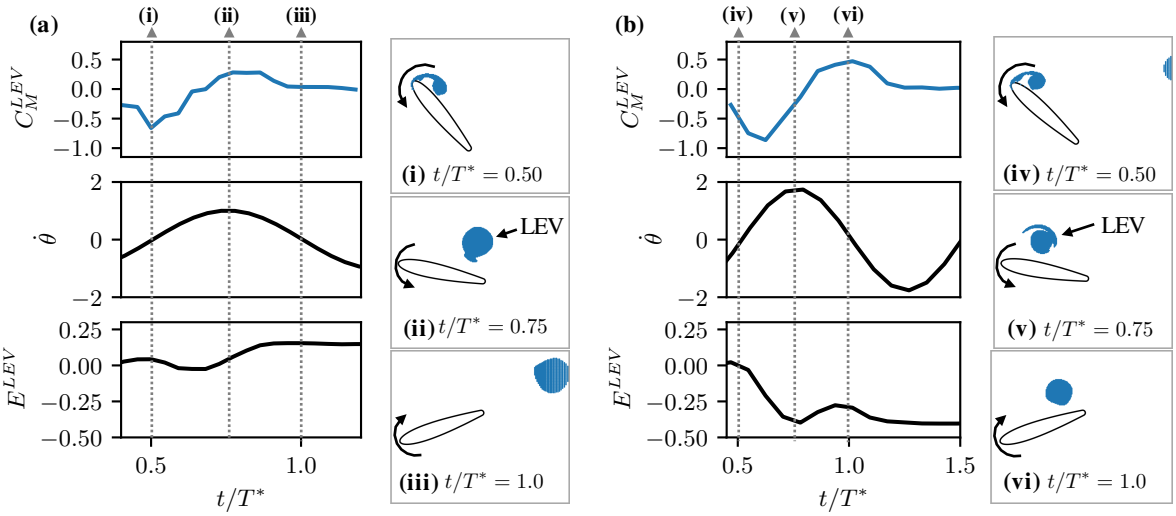

Figure 9.12: Comparison of the phase difference between LEV-induced moment and angular velocity for two cases: (a, i–iii) $f^* = 0.20$, $A_\theta = 35°$; and (b, iv–vi) $f^* = 0.35$, $A_\theta = 35°$. For each case, time-series plots show phase-averaged LEV-induced coefficient of moment (top panel; C_M^{LEV}), angular velocity (middle panel; $\dot{\theta}$), and energy extraction from LEV-induced moment (bottom panel; E^{LEV}). Snapshots for each case show the LEV's position at three phases of oscillation, $t/T^* = 0.5$, $t/T^* = 0.75$ and $t/T^* = 1.0$ (indicated by vertical dashed lines). Note: Angular velocity and moment are positive in the anti-clockwise (pitch-down) direction.

direction. The bottom panel shows the LEV-induced energy extraction for each case, computed, as a function of time. This is the energy extracted exclusively from the LEV-induced moment, C_M^{LEV}, and is given by,

$$E^{LEV}(t) = \int_0^t C_M^{LEV}\ \dot{\theta}\ dt. \tag{9.3}$$

We first point out that the energy extracted from the LEV is indeed positive for the lower frequency case in figure 9.12(a) and negative for the higher frequency case in figure 9.12(b). This is related to the phase difference between C_M^{LEV} and $\dot{\theta}$. It is easy to see that the maxima of C_M^{LEV} and $\dot{\theta}$ align well for $f^* = 0.20$ in figure 9.12(a), whereas these maxima are shifted by approximately 90° from each other for $f^* = 0.35$ in figure 9.12(b). In order to relate these time-series plots with the dynamics of the flow, figures 9.12(i)-(iii) and 9.12(iv)-(vi) show instantaneous snapshots of the LEV and airfoil at three phases of oscillation. Here $t/T^* = 0.5$ represents the beginning of the pitch-down motion from the maximum angle-of-attack, $t/T^* = 0.75$ occurs at the mean angle-of-attack during the pitch-down motion, and $t/T^* = 1.0$ is the end of the pitch-down motion. These phases are indicated by the vertical dashed lines in figures 9.12(a) and 9.12(b).

In both cases, we see from figures 9.12(i) and 9.12(iv) that the LEV is attached to the airfoil at the start of the pitch-down stroke. It induces a strong

pitch-up (negative) moment on the airfoil in both cases, as seen in the C_M^{LEV} plots at $t/T^* = 0.5$. In the low-frequency case however, $t/T^* = 0.5$ is immediately followed by a reduction in the pitch-up (negative) moment. This indicates that the LEV separates very soon after the airfoil begins pitching-down (at $t/T^* = 0.5$) in the $f^* = 0.20$ case. This is in contrast to the higher-frequency case, where figure 9.12(b) shows that the negative peak in C_M^{LEV} occurs later in the cycle (at $t/T^* \approx 0.625$). Although not shown here, flow snapshots indicate that the earlier separation of the LEV in the low-frequency case occurs because the slower pitching motion allows the LEV to begin developing earlier in the previous pitch-up stroke. This early roll-up and slower pitching velocity, compared to higher-frequency motion, allows more time for the LEV's growth and saturation, hence promoting earlier shedding.

This phase-difference in the LEV's growth and shedding has significant consequences as the airfoil reaches its maximum pitch-down angular velocity at $t/T^* = 0.75$. For the low-frequency case, figure 9.12(ii) shows a snapshot at $t/T^* = 0.75$ when the LEV is positioned downstream of the hinge location (mid-chord). The LEV-induced suction therefore generates a peak in pitch-down (positive) moment, which coincides with the peak in angular velocity. This is seen at $t/T^* = 0.75$ in figure 9.12(a). This favourable timing between the LEV and airfoil kinematics in the low-frequency case results in C_M^{LEV} being in-phase with $\dot{\theta}$, and the airfoil extracting positive energy from the LEV.

In the high-frequency case, on the other hand, snapshot 9.12(v) shows that the LEV is yet to convect past the hinge location at $t/T^* = 0.75$. This is due to the airfoil's faster motion as well as the delayed separation of the LEV. As a consequence, figure 9.12(b) shows that C_M^{LEV} is small and slightly negative at $t/T^* = 0.75$, when $\dot{\theta}$ is at its peak. The maximum C_M^{LEV} in this case is attained later in the cycle, at $t/T^* = 1.0$, when the LEV is located above the downstream half of the airfoil as shown in figure 9.12(vi). However, $t/T^* = 1.0$ corresponds to the start of the pitch-up stroke. Due to the fact that the maximum pitch-down moment is induced by the LEV at the start of the airfoil's pitch-up motion, the phase between C_M^{LEV} and $\dot{\theta}$ is unfavourable and hence leads to negative energy extraction from the LEV.

This analysis highlights the competing influence of the pitching timescale and important flow timescales (such as those for vortex shedding and convection) in determining the phase of the forcing with respect to the kinematics. This also demonstrates that in addition to accurately tracking and quantifying the kinematic and dynamic effects of particular vortex structures, this framework also allows us to precisely correlate these estimated quantities with observed flow phenomena.

9.3 Conclusions

We have presented a data-driven and physics-based computational framework for the analysis of vortex-dominated flows. This is a flexible and automated method to accurately evaluate kinematic quantities and the aerodynamic loading of individual vortex structures in complex vortex-dominated flows. This method uses a force and moment partitioning formulation which breaks down the aerodynamic loading on an immersed body into physically insightful components. This formulation is combined with a suite of physics-informed and data-driven methods to simultaneously detect, isolate, segment, track, and categorize several distinct vortices in complex flow-fields. The end result is a framework that takes in time-resolved flow fields and provides quantitative details of the kinematic evolution as well as the aerodynamic loading due to each vortex structure in the problem.

We present an application of these methods to a large data-set of 165 two-dimensional pitching airfoil simulations at a wide range of kinematic operating conditions. The analysis reveals several interesting aspects of the vortex kinematics, such as period-doubling in vortex trajectories and the dependence of circulation on the airfoil kinematics. These are generally non-trivial to extract from such large ensembles of flow-field data. Further, the utility of this method in analyzing the dynamical influence of key vortex structures is also

demonstrated. In particular, we quantify the force and moment induced by leading and trailing-edge vortices for various cases, and highlight how their relative importance varies with the kinematics of the airfoil's oscillation. We also analyze the phase between the forces/moments generated and the motion of the airfoil, and connect this to their relevance in flow-induced oscillation and energy harvesting.

It is important to highlight that while the present analysis focuses exclusively on vortex structures (detected as regions of $Q > 0$), the framework is equally applicable to the analysis of other flow structures that are defined by some metric/variable. Furthermore, several aspects in the current implementation of the vortex analysis as well as vortex pattern-based rank-reduction methods can be modified due to the versatile nature of the framework. For instance, while vortices are identified using the Q-criterion in this implementation, a variety of other tools aimed at detecting coherent structures can be used instead [164, 165]. The DBSCAN-based method for isolating and segmenting these vortices can also be replaced by spectral and graph clustering techniques [122, 125, 126]. Additionally, the grouping of these vortices can be performed based on vortex shape, size, as well as dynamical influence, in place of the trajectory and circulation-based grouping used here.

This method is also described in reference [170].

Chapter 10

Significance of the strain-dominated region around a vortex on induced aerodynamic loads

Unsteady aerodynamics is one area where a number of studies have focused on determining the aerodynamic loads induced by vortices in a flow [15, 80, 84, 91, 171–174]. This task is made difficult not only by the fact that most flows consist of multiple interacting vortices and shear layers, but also that there continues to be significant ambiguity regarding the very definition of a vortex [164] and its relationship to the induced pressure field.

A method for vortex identification that is commonly used is the so-called "Q-criterion" [161, 163]. The quantity Q, as highlighted in equation (7.15), is the second invariant of the velocity gradient tensor and can be defined as $Q = \frac{1}{2}\left(||\mathbf{\Omega}||^2 - ||\mathbf{S}||^2\right)$. Here $\mathbf{S}$ and $\mathbf{\Omega}$ are the strain-rate and rotation tensors given by $\mathbf{S} = \frac{1}{2}\left[\nabla\vec{u} + (\nabla\vec{u})^T\right]$ and $\mathbf{\Omega} = \frac{1}{2}\left[\nabla\vec{u} - (\nabla\vec{u})^T\right]$ respectively. A vortex, according to the Q-criterion, is then defined as a connected region where $Q > 0$. This corresponds to regions where the Frobenius norm of the rotation tensor is greater than that of the strain-rate tensor.

As discussed in section 7.3, it is interesting that while the quantity Q has mostly been associated with the flow kinematics, Jeong & Hussain [163] noted that the pressure Poisson equation for incompressible flow, derived by taking the divergence of the Navier-Stokes equation, can be expressed as:

$$\nabla^2 p = -\rho\nabla\cdot(\vec{u}\cdot\nabla\vec{u}) \equiv \rho\nabla\vec{u} : (\nabla\vec{u})^T \equiv 2\rho Q. \tag{10.1}$$

Equation (10.1) shows that Q appears in the source term of the pressure Poisson equation and is thus not merely a kinematic quantity, but one with direct implications for the *dynamics* of the flow as well. Furthermore, while regions of positive Q, which are used to identify vortices, may draw much of our attention, equation (10.1) shows that regions with negative Q, i.e. strain-dominated regions, are no less significant with regard to their effect on pressure.

A question that immediately arises from equation (10.1) is: do vortices have regions of negative Q associated with them and, if so, how significant are these regions? To answer this, we first note that the following Neumann boundary condition completes the prescription of the above boundary-value problem: $\hat{n} \cdot \nabla p = \hat{n} \cdot \left[-\rho \frac{d\vec{u}}{dt} + \mu \nabla^2 \vec{u} \right]$. We now consider a vortex in an infinite quiescent flow for which the boundary condition at the far-field would be homogeneous. The divergence theorem applied to the pressure Poisson equation would therefore require that $\int_{V_f} Q \, dV \equiv 0$, where V_f is the volume of the flow domain. This implies that, for such a vortex, the volume integral of the negative Q region is equal to the volume integral of positive Q in the vortex core. Furthermore, immediately outside the region of positive Q, the velocity gradients have to be non-zero and therefore, this region immediately surrounding the vortex core should have $Q < 0$. Thus, for any vortex in a viscous flow, the positive-Q core is necessarily associated with a negative-Q "corona" of equivalent significance. This can easily be confirmed for exact vortex solutions of the Navier-Stokes equations such as the Rankine vortex [175], the Lamb–Oseen vortex [176], and others. While the presence of boundaries and other flow complexities might eliminate the strict equipartitioning of Q for a vortex, we nevertheless expect that every vortex will have a significant corona of negative Q around it. This observation, combined with equation (10.1), suggests that the strain dominated region around a vortex could have a significant contribution to the net aerody-

namic load induced by a vortex. However, although the overall effect of these strain-dominated regions on aerodynamic loading has implicitly been included in past studies, our physical intuition regarding aerodynamic loading has generally been tied to the growth, motion and overall evolution of the rotational core of vortices. The role of the strain-induced region on force production has, thus far, not garnered significant attention.

In this chapter, we examine the aerodynamic loads induced by vortices on an immersed surface, and in particular, we focus on the distinct roles played by regions of positive as well as negative Q associated with vortices. For this analysis, we choose to focus on the problem of a sinusoidally pitching airfoil that exhibits dynamic stall, and generates leading-edge (LEV) and trailing-edge vortices (TEVs). Using this analysis, we examine the phenomenon of dynamic stall and show that our understanding of vortex-induced loads is incomplete without also discussing the role played by the corona of negative Q around a vortex.

10.1 Problem description

The dynamic stall problem discussed here is simulated using the flow solver and computational setup described in sections 2.1 and 2.2.1. This two-dimensional model consists of a sinusoidally pitching NACA0015 airfoil with chord-length

C and a rounded trailing edge, immersed in a uniform free-stream flow with velocity U_∞. The pitch oscillation is prescribed as: $\theta = \theta_0 + A_\theta \sin(2\pi f^* t)$ where θ is the instantaneous pitch angle, θ_0 is the mean pitch angle and A_θ is the pitch amplitude. The dimensionless pitching frequency is given by $f^* = FC/U_\infty$ where F is the pitch frequency. The Reynolds number of the flow is $Re = U_\infty C/\nu = 1000$.

The analysis presented here employs the force partitioning method and data-driven analysis framework discussed in chapters 7 and 9 to precisely quantify the force contributions of various vortices and vortical regions in the flow. We are particularly interested in analyzing the lift force, which is expressed in terms of the lift coefficient C_L. We show in section 10.2 that this lift force is dominated by the vortex-induced component, which is given by equation (7.27), and has the following form:

$$C_{F_i}^{\omega} \approx -\int_{V_f} 2\,Q\;\phi_2\,dV \tag{10.2}$$

where ϕ_2 is given by equation (7.5) with $i = 2$.

We perform this vortex isolation, tracking and force evaluation within a sub-domain of size $2.5C \times 2C$ around the airfoil within which the computed vortex-induced lift is approximately equal to that integrated over the entire flow domain. Furthermore, we partition the vortex-induced lift into compo-

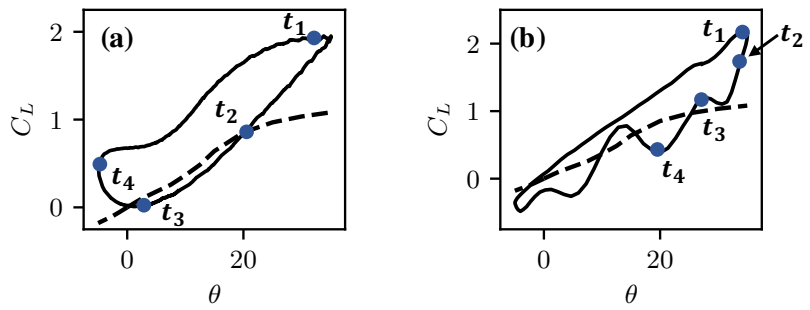

Figure 10.1: Coefficient of lift (C_L) versus pitch-angle (θ) plots for the two cases: (a) $f^* = 0.35$, $A_\theta = 20°$; (b) $f^* = 0.10$, $A_\theta = 20°$. Labels t_1–t_4 correspond to time-instances examined in subsequent discussion and figures. The dashed line indicates the lift coefficient for corresponding static airfoil [177].

nents associated with positive-Q regions and negative-Q regions; these are referred to as "rotation-induced" and "strain-induced" lift, respectively, and the corresponding lift coefficients denoted by C_L^Ω and C_L^S, respectively.

10.2 Analysis of dynamic stall

The analysis is based on two cases of a pitching airfoil with different dimensionless pitching frequencies: $f^* = 0.35$ and 0.10. The other parameters which are kept the same for these cases are $Re = 1000$, $\theta_0 = 15°$ and $A_\theta = 20°$. Figure 10.1 shows the lift versus pitch angle for the two cases. While both cases exhibit the classic features of dynamic stall (instantaneous lift that significantly exceeds the corresponding static lift followed by a rapid drop in lift), the differences between the two due to the pitching frequency provide an effective substrate to examine vortex-induced forces in a comprehensive manner.

10.2.1 Case 1: $f^* = 0.35$

We first discuss the case with $f^* = 0.35$, and specifically examine the time-instances marked t_1–t_4 in figure 10.1. Figure 10.2(a) shows a snapshot of vorticity at time t_1, and we see four key features: a large primary LEV (pLEV) from the previous cycle which is in the near-wake of the foil, a large TEV which is near the trailing edge, a secondary LEV (sLEV) which is located near mid-chord and a shear layer on the suction side which is the initial stage in the formation of the next pLEV.

Figures 10.2(b)-(e) show the Q fields at time instances $t_1 - t_4$, overlaid with contours of ϕ_2. These Q fields clearly identify the key vortices that are generated during the pitching cycle as regions of positive Q and for time t_1, figure 10.2(b) can be correlated with the vorticity plot in figure 10.2(a). Also noticeable in the plots of Q are the large regions of $Q < 0$ that surround the vortices, which corroborates our earlier discussion about the existence of such regions around vortices. These regions of negative Q tend to be more spread out than the vortex cores. There is also a region of negative Q near the leading edge of the airfoil that is sustained throughout the pitching cycle.

The distribution of ϕ_2 has some distinctive features that have important implications for the vortex-induced lift. First, it has opposite sign over the two surfaces of the airfoil. Thus, a vortex adjacent to one surface of the airfoil would generate a force in the opposite direction to that induced by the same

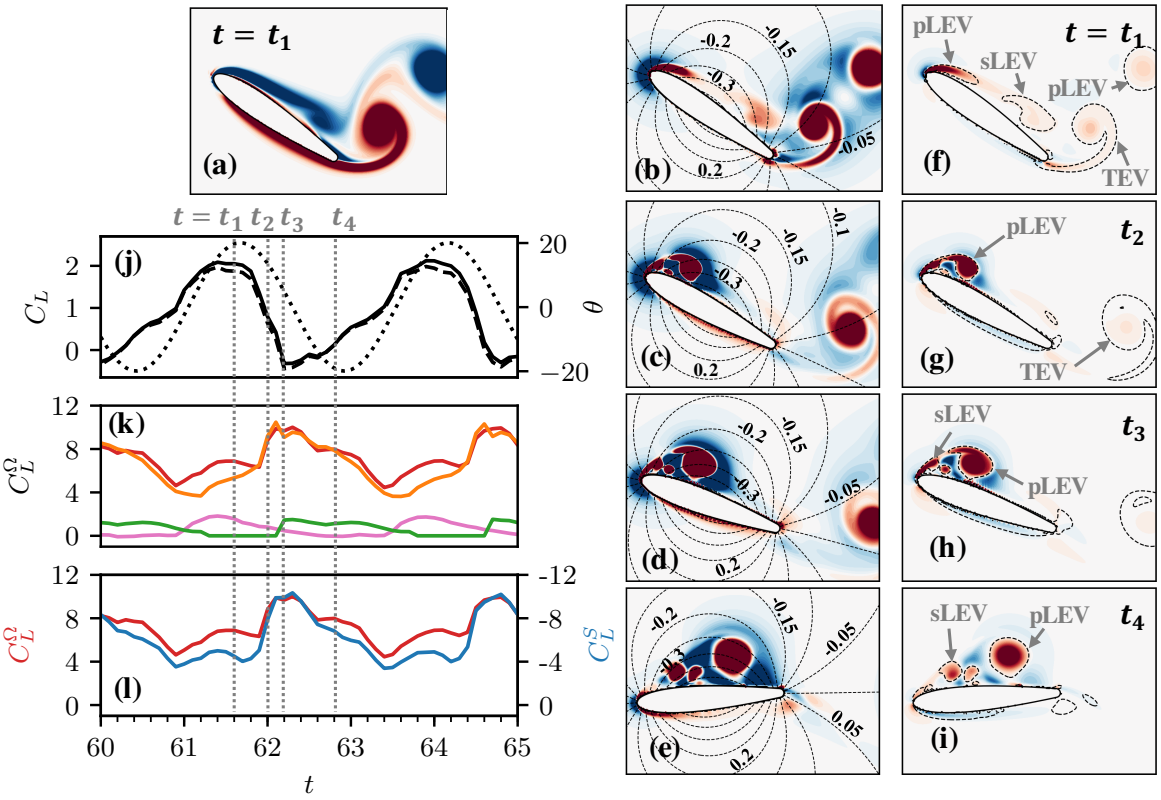

Figure 10.2: Flow snapshots and lift contributions for the case with $f^* = 0.35$. (a) Contours of spanwise vorticity at time t_1. (b)-(e) Filled contours of Q, with levels $[-40, 40]$, overlaid with line contours of ϕ_2. (f)-(i) Distribution of vortex-induced lift ($-2Q\phi_2$) with contour levels $[-65, 65]$. Dashed lines and labels show integration volumes corresponding to each vortex which are used to compute the vortex-induced lift associated with these regions as per equation (10.2). Snapshots (b)-(e) and (f)-(i) are at time-instances $t_1 - t_4$ from top to bottom. (j) Total lift coefficient (C_L; —) compared with vortex-induced lift ($C^{\omega}_{F_i}$; ---). Pitch angle is shown for reference (θ; ·····). (k) Rotation-induced lift (C^{Ω}_L; —) and contributions from the primary LEV (—), TEV (—) and secondary LEV (—). (l) Rotation-induced lift due to regions of $Q > 0$ (C^{Ω}_L; —) and strain-induced lift due to regions of $Q < 0$ (C^{S}_L; —). Time instances $t_1 - t_4$ are indicated using dashed grey lines.

vortex adjacent to the other surface. Second, the magnitude of ϕ_2 is highest near mid-chord and decays towards the leading and trailing edges. Therefore, a vortex located near mid-chord would generate a larger lift force than the same vortex located near the leading or trailing-edges. Finally, ϕ_2 decays with distance from the airfoil and hence, as expected, the influence of a vortex on the lift would diminish with distance from the airfoil.

Figures 10.2(f)-(i) show corresponding contour plots of the integrand of the vortex-induced lift, $-2Q\phi_2$. This represents the vortex-induced lift per unit volume of fluid and these plots can be interpreted based on the distribution of Q and ϕ_2 shown in figures 10.2(b)-(e). We see that the most lift-inducing flow structures are those with large Q magnitudes and/or those near mid-chord due to the large magnitude of ϕ_2.

The dynamical influence of the various flow structures observed in the flow snapshots discussed above are quantified in figures 10.2(j)-(l). Figure 10.2(j) shows the time-variation of the total lift coefficient, shown as a solid black line, and the vortex-induced lift coefficient (dashed black line) over two pitching cycles. First, it is noted that the vortex-induced lift is nearly identical to the total lift and this highlights the predominance of this component of the lift force. As for the case shown in section 7.4, the added mass and viscous contributions have orders of magnitude $O(10^{-2})$ and $O(10^{-1})$ respectively. Second, the lift curve shows a rapid drop between t_1 and t_3, which represents the typi-

cal signature of dynamic stall. The generally accepted notion is that dynamic stall occurs when an attached leading-edge vortex, which generates high lift, undergoes a "shedding" event [57, 80, 172]. We can evaluate this notion rigorously by computing the distinct lift contributions of each vortex highlighted above. This is done using an automated framework that segments and tracks the volumes of the $Q > 0$ regions occupied by each of the vortices. These spatial volumes are shown as $Q = 0$ contours using the dashed lines in figures 10.2(f)-(i). The resulting "rotation-induced lift" for the various vortices is presented in figure 10.2(k). We see that the pLEV is indeed the dominant generator of lift on the airfoil, with the sLEV and the TEV generating much smaller contributions (peak lift due to sLEV and TEV is about 15% of the pLEV). However, very surprisingly, we note that from time t_1 to t_3 while the total lift on the airfoil falls, the lift induced by the pLEV actually increases and reaches a peak at t_3. This increase in pLEV-induced lift is consistent with its growth while staying attached in a region of relatively large ϕ_2, as seen in figures 10.2(c)-(d) as well as 10.2(g)-(h). When the pLEV is released and starts to move away from the surface of the foil, as seen in figures 10.2(e) and 10.2(i) at t_4, the lift induced by it reduces, as expected. However, the total lift actually increases during this time, from t_3 to t_4. Thus, the total lift on the airfoil is nearly perfectly out of phase with the lift induced by the pLEV. This observation runs contrary to our phenomenological understanding of the role of LEVs in lift enhancement

and dynamic stall. In fact, this phase-lag between the growth of the pLEV and the lift maximum has been previously reported by Xia & Mohseni [173] and Gharali & Johnson [15].

The cause of this seemingly anomalous behavior becomes clear when we examine the components of the vortex-induced lift associated the negative Q regions (what we call "strain-induced lift") as shown in figure 10.2(l). This plot shows that even though the positive lift induced by the growing LEV does indeed increase between phases t_2 and t_3, this increase is counteracted by an increase in the negative lift induced by regions of $Q < 0$ that surround the LEV. These regions of negative Q occur in areas where the ϕ_2 has a high magnitude, as seen in figures 10.2(c)-(e), and that helps accentuate their effect on the total lift. Thus, the rapid drop in lift occurs not due to the "shedding" of the LEV but due to the growth of the strain-dominated negative Q regions that develop around the growing LEV. Similarly, the rise in total lift between t_3 and t_4, which occurs despite the reduction in pLEV-induced lift, is driven by the slightly more rapid reduction in the negative strain-induced lift. Some studies have in fact, reported a phase lag between the onset of dynamic stall and attainment of peak LEV circulation [15, 173]. For the current case, we show that such a phase lag, which runs counter to our intuition regarding dynamic stall, can be explained by the significant influence of strain-induced loading. Thus, this case challenges our conventional understanding of phenomenolog-

ical connection between LEV evolution and dynamic stall, and points to the significant role that the strain dominated regions can play in determining the aerodynamic loads on the surface.

10.2.2 Case 2: $f^* = 0.10$

We now contrast this behaviour with that at low-frequency oscillations of $f^* = 0.10$. The hysteresis plot in figure 10.1(b) shows that the pitch-angle reversal in this case corresponds to a sharper initial drop in lift, indicating that the vortices in this low frequency oscillation interact differently with the timescale of oscillation. The snapshots of Q, shown for this case in figures 10.3(b)-(e), highlight the main vortex structures in the flow. We see that it is dominated by the same three vortices as in the previous case - the primary and secondary LEVs and the TEV. However, on comparing figures 10.3(b) and 10.2(d), which correspond to time instances soon after the pLEV-separation in the present and previous case respectively, we see that the pLEV in the current low-frequency case is larger in size and farther away from the surface of the airfoil. This is a result of the slower pitching motion, which allows more time for the growth and downstream motion of the pLEV.

This increased distance of the pLEV from the surface has important consequences for the lift induced by the pLEV as well as its surrounding region of strain. Figures 10.3(f)-(i) show snapshots of $(-2Q\phi_2)$ for this case, and we

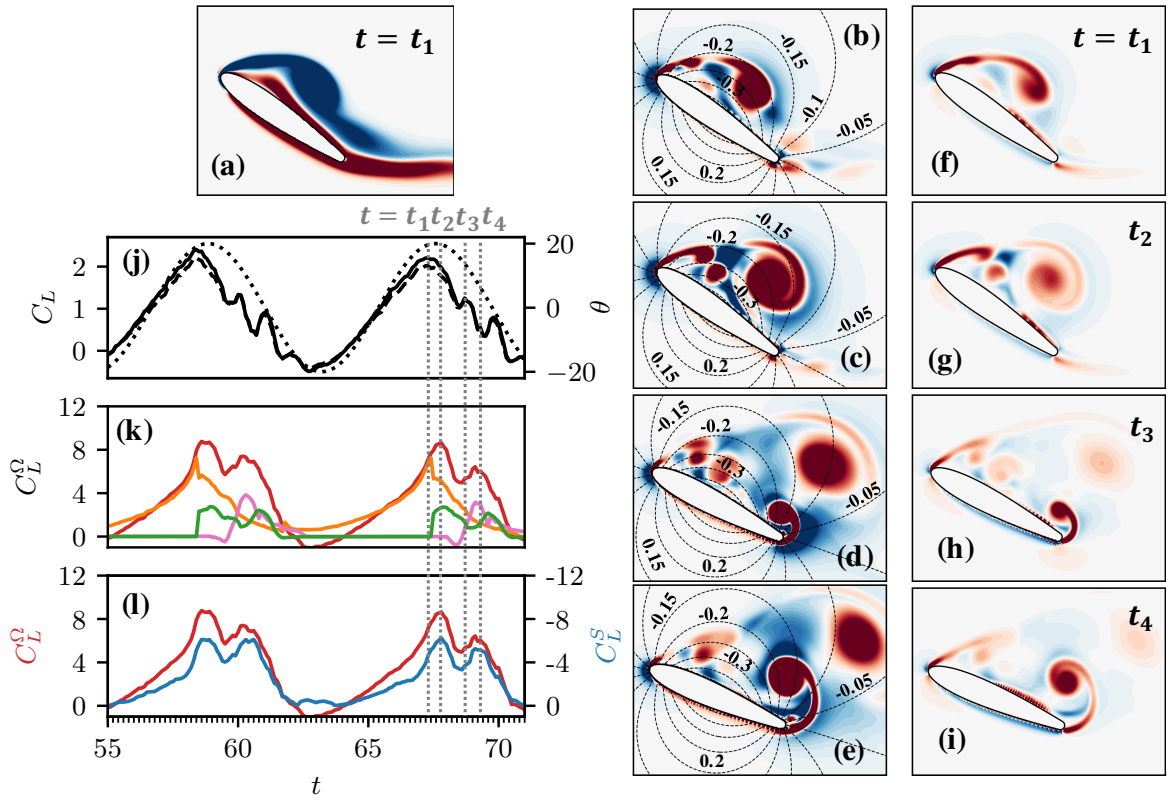

Figure 10.3: Flow snapshots and lift contributions for the case with $f^* = 0.10$. (a) Contours of spanwise vorticity at time t_1. (b)-(e) Filled contours of Q, with levels $[-40, 40]$, overlaid with line contours of ϕ_2. (f)-(i) Distribution of vortex-induced lift ($-2Q\phi_2$) with contour levels $[-65, 65]$. Snapshots (b)-(e) and (f)-(i) are at time-instances $t_1 - t_4$ from top to bottom. (j) Total lift coefficient (C_L; —) compared with vortex-induced lift ($C^{\omega}_{F_i}$; ---). Pitch angle is shown for reference (θ; ·····). (k) Rotation-induced lift (C^{Ω}_L; —) and contributions from the primary LEV (—), TEV (—) and secondary LEV (—). (l) Rotation-induced lift due to regions of $Q > 0$ (C^{Ω}_L; —) and strain-induced lift due to regions of $Q < 0$ (C^{S}_L; —). Time instances $t_1 - t_4$ are indicated using dashed grey lines.

see from figures 10.3(g) and 10.3(h) that the induced-force density of the pLEV as well as the straining regions around it are significantly smaller than in the $f^* = 0.35$ case discussed earlier (note the difference in $(-2Q\phi_2)$ contour levels between the two cases). In particular, a comparison of the lift distribution in figures 10.3(g)-(i) with that of figures 10.2(g)-(i) shows a stark contrast in the distance of the pLEV from the wall soon after pLEV-separation, as well as the resultant confinement of the strain associated with the pLEV near the wall.

The implications of these observations are evident in figures 10.3(j)-(l). Figure 10.3(j) again shows that the vortex-induced lift dominates the overall lift production. The contributions of total rotation-induced lift (i.e. $Q > 0$ regions) as well as those of the individual vortices are quantified in figure 10.3(k). First, we note that the peak in the total rotation-induced lift aligns (at time t_2) well with that for the total lift. This is in contrast to the previous case where the two were quite out-of-phase. Second, the contribution of the pLEV peaks at time t_1, which is in-phase with C_L but slightly ahead of the the peak rotation-induced lift. The sLEV appears around this time and augments the rotation-induced lift, resulting in the peak C_L^Ω at t_2. There is also a second peak in the total rotation-induced lift at t_4 which, as evident from figure 10.3(k), is generated by the trailing-edge vortex.

Finally, figure 10.3(l) shows the contribution of the rotation and strain-induced lifts to the total vortex-induced lift. We note that the strain-induced

lift has a time-profile that is similar to the rotation-induced lift but remains consistently lower in magnitude for most of the pitching cycle. This is consistent with the observation that regions of large-strain around the vortices are generated relatively further away from the airfoil in this case as compared with the previous case. Furthermore, this also explains the fact that C_L is in-phase with the rotation-induced lift in this case, unlike the behaviour seen for $f^* = 0.35$.

Thus, this lower frequency case presents a more conventional phenomenology of dynamic stall where the total lift correlates, as expected, with the growth and movement of the rotational cores of the vortices. The strain-induced lift force, despite being comparable in magnitude to the rotation-induced lift and of significantly greater magnitude than the total lift, does not play as significant a role for this case, as it does for the first one.

10.3 Conclusions

We have shown that while studies of vortices and their effects on aerodynamic loads have mostly focused on the rotational cores of vortices, vortex cores are in fact surrounded by dynamically significant regions where strain dominates over rotation. In particular, these strain-dominated regions exert a considerable, and sometimes even dominant, influence on the induced aerody-

namic loads. By using simulations of flow past a pitching airfoil and employing a powerful force partitioning method to separate the force contributions of various regions of the flow, we have shown that the lift induced by the strain dominated regions around vortices is of a magnitude comparable to that induced by the rotational cores of the vortices. For one of the two cases presented here, we also show that dynamic stall, i.e. the rapid drop in lift for an unsteady airfoil, is less connected with the conventional notion of leading-edge vortex shedding and more with the formation and evolution of the strain dominated "corona" of the leading edge-vortices.

We close by pointing out that previous investigations [89, 91, 92, 173] of vortex-induced aerodynamic loads do implicitly include the effect of strain-dominated regions of a vortex in estimating induced loads. However, the accompanying interpretations of the mechanisms and phenomenology has been based primarily on the rotational vortex cores and has largely ignored the strain-dominated regions associated with vortices. The current study showcases the significant and sometimes dominant influence of the strain-dominated regions around a vortex, and highlights the utility of explicitly accounting for these effects when examining the mechanisms that govern aerodynamic loading in vortex-dominated flows.

The results discussed in this chapter have been published in reference [178].

Chapter 11

Vortex-induced lift on three-dimensional wings: Spanwise and cross-span vortices

In previous chapters we demonstrated the utility of the force partitioning method in uncovering fundamental insights into the mechanisms driving force generation and flow-induced oscillations in some canonical two-dimensional problems. In particular, we showed that the analysis of these flows at the level of individual vortex structures and their associated strain goes a long way in extending our understanding of their dynamics. In this chapter, present preliminary first steps in extending such investigations to three-dimensional flows.

This chapter reports on the vortex-induced lift production mechanisms in low Reynolds number flows over low aspect-ratio wings. The specific focus is on the roles that vortex structures containing spanwise oriented and non-spanwise oriented vorticity play in lift production. This interest in spanwise vorticity-containing structures is motivated by the fact that several previous studies have highlighted the dominant role of the leading-edge vortex in lift production, and its importance in applications such as biological flight [9, 81, 84]. However, as mentioned in previous chapters, these studies have mostly qualitatively correlated the occurrence and evolution of specific vortex structures to the lift on wings. Moreover, we showed in chapter 10 that the strain region associated with vortices also has important dynamical significance, but these regions are generally not given as much attention. Therefore we aim to use the force partitioning method of chapter 7 to quantify the role of these vortices and their strain in lift production on three-dimensional wings, and also estimate their influence within different regions of the flow-field around the wing and in the wake.

11.1 Problem description

In this chapter, we analyze the three-dimensional incompressible flow over flat-plate wings with rectangular and triangular (delta) planforms. The rect-

angular wing studied has a $2:1$ span-to-chord aspect-ratio. The cross section of the wing is a flat plate with a thickness of 15% of the chord. The delta wing analyzed has the same cross-section and aspect-ratio as the rectangular wing when the chord-length is measured at its maximum location (which is mid-span). Therefore this $2:1$ aspect-ratio delta wing has a sweep angle of 45°. Figures 11.1(a) and 11.1(b) show schematics of the rectangular and delta wings.

We denote the chord-length of the wings as C, and they are placed in a uniform incoming freestream flow which has velocity U_{∞}. The chord-based Reynolds number of the flow is $Re = U_{\infty}C/\nu = 1000$. The flow over both wings is simulated in a large computational domain that has dimensions $18C \times 20C \times 20C$ in the streamwise, spanwise and "wall-normal" direction. The domain is discretized using a Cartesian grid with $192 \times 256 \times 128$ grid points. The grid around the wing is isotropic with a resolution of approximately 72 points across the chord (or 144 points across the span), and the grid is expanded away from the wing. A schematic of this domain and the Cartesian grid is shown in figure 11.1(c). A Dirichlet velocity boundary condition is specified at the upstream (inlet) boundary of the domain, and homogeneous Neumann boundary conditions are specified at all other boundaries.

We use the force partitioning formulation of chapter 7 to quantify the vortex-induced lift force induced by different regions of the flow-field. We report our

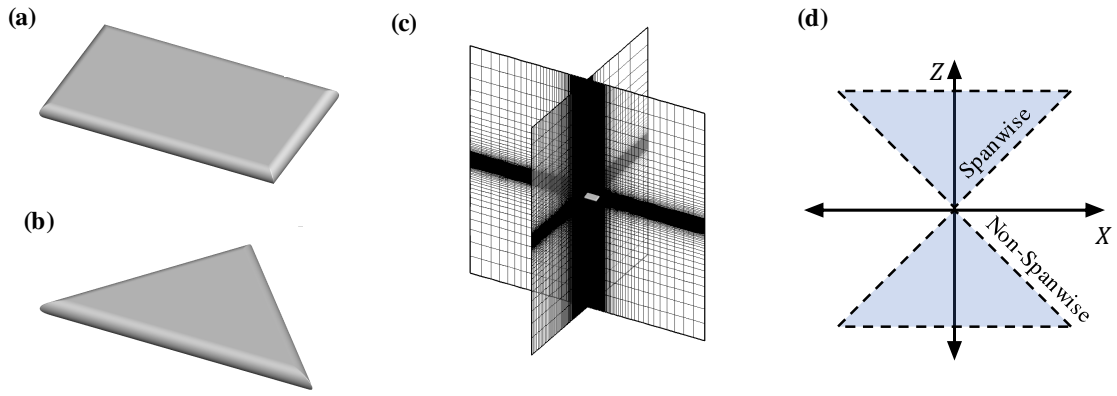

Figure 11.1: (a) and (b) show the geometry of the rectangular and delta wings respectively. (c) Computational domain and the Cartesian computational grid.

results in terms of the lift coefficient, $C_L = F_L/(\frac{1}{2}\rho U_\infty^2 A)$, where F_L is the dimensional form of the lift and A is the area of the wing. We express the lift coefficient associated with the vortex-induced force as C_L^ω, and for a particular volume of the flow, V_f, this force is given by,

$$C_L^\omega \approx -\int_{V_f} 2\,Q\;\phi_2\,dV \tag{11.1}$$

where ϕ_2 is given by equation (7.5) with $i = 2$.

A specific focus in this work is isolating the distinct roles that spanwise and non-spanwise oriented vortices play in lift production over three-dimensional wings. While there are many methods to identify the volumes in the flow-field occupied by vortices aligned in particular directions, we use a simple method based on the direction of the vorticity unit vector at every point in the flow-field. In our coordinate system, X and Z are the streamwise and spanwise directions

respectively, and the three components of the vorticity vector, $\vec{\omega}$, are denoted as ω_x, ω_y and ω_z. The component of the vorticity unit vector in the spanwise direction is therefore given by,

$$\eta_z = \frac{\omega_z}{\sqrt{\omega_x^2 + \omega_y^2 + \omega_z^2}}. \tag{11.2}$$

The magnitude of η_z in equation (11.2) represents the cosine of the angle between the spanwise direction (Z-axis) and the local vorticity vector at any point in the flow-field. Here we identify "spanwise oriented" vorticity very simply as regions where this angle is less than 45°, which implies $|\eta_z| > \cos(\pi/4)$. Geometrically, this condition is satisfied at any point in space if the local vorticity vector lies within either of two symmetric cones whose axes are aligned with the positive and negative Z-axes (spanwise direction), with each cone having a half-angle of 45° and its apex at the point of interest. Therefore vorticity vectors that lie within this cone are oriented more in the spanwise direction than in any other direction. Conversely, the remaining vorticity vectors are designated as non-spanwise oriented. A projection of this demarcating cone in the X-Z plane is shown in the schematic in figure 11.1(d).

We perform this analysis of spanwise and non-spanwise vorticity within a subdomain of the full computational grid. The subdomain has dimensions $6C \times 3C \times 3C$ in the X, Y and Z directions. It is positioned symmetrically with

the wing in the Y and Z directions, and includes 4.5 chord-lengths in the wake of the wing in the streamwise direction. We have verified that this subdomain captures the bulk of the force induced on the wing by the surrounding flow. We express the lift coefficient associated with the vortex-induced force corresponding to the spanwise and non-spanwise vorticity components as $C_L^{\omega z}$ and $C_L^{\omega xy}$.

11.2 Rectangular wing

We begin our analysis with a discussion of the vortex-induced lift on the rectangular wing described in section 11.1 above. Figures 11.2(a)-(b) show instantaneous snapshots of the flow, visualized using iso-surfaces of Q (at levels [-2.0,2.0]). The vortical and straining structures shown are colored by the integrand of the vortex-induced force, $-2Q\phi_2$, which indicates their local contributions to lift production. We see that this flow consists of a variety of vortex structures, both in the vicinity of the wing as well as in the wake. In particular, we highlight the generation and shedding of a leading-edge vortex (LEV) over the suction surfaces of the wing as well as prominent tip-vortices. We see that as the LEV sheds into the near-wake, its structure gets slightly deformed from its initial span-wise orientation. Farther downstream, the effect of vortex tilting and stretching transform it into a horseshoe-type structure. We will show

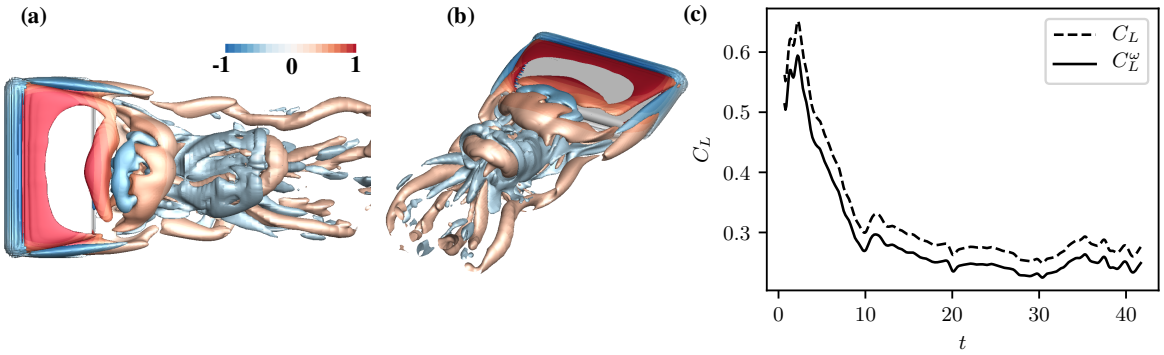

Figure 11.2: Vortex-induced lift on the rectangular wing. (a)-(b) Isometric and top-view, respectively, of iso-surfaces of Q at levels [-2.0, 2.0], coloured by $-2Q\phi_2$. (c) Comparison of total lift coefficient (C_L) with vortex-induced lift (C_L^ω).

in the subsequent discussion that these effects have important consequences on lift production. Figure 11.2(c) compares the total lift coefficient on the wing (C_L) to the vortex-induced contribution (C_L^ω). It is clear that the vortex-induced effects account for the bulk of the lift production on the wing, as is expected.

11.2.1 Contributions of spanwise and non-spanwise vorticity

We now begin to analyze the roles that different vortex structures (and their associated strain-field) play in the production of lift on the wing. As mentioned in section 11.1, of particular focus in this work is the separate contributions of spanwise and non-spanwise oriented vorticity in the flow. These contributions are isolated in a very simple manner using the angle of the vorticity unit vector, defined as in equation (11.2), computed at every point in the domain.

In figures 11.3(a) and 11.3(b), we visualize the flow features that result from this segmentation by plotting Q iso-surfaces ($Q = 2.0$) colored by $-2Q\phi_2$ as in figure 11.2, and masking the regions that correspond to $|\eta_z| \leq \cos(\pi/4)$ and $|\eta_z| > \cos(\pi/4)$ respectively.

Figure 11.3(a) shows that the spanwise-oriented vorticity, $|\eta_z| > \cos(\pi/4)$, mainly isolates the LEV and shear-layer over the surface of the wing, along with the shedding of the LEV in the near-wake. Farther downstream, there are smaller regions of spanwise vorticity that result from vortex interactions, breakdown, etc. On the other hand, the regions of $|\eta_z| \leq \cos(\pi/4)$ shown in figure 11.3 correspond to largely streamwise oriented structures, which consist of the tip vortices (although figure 11.3(a) shows a minor spanwise contribution near the tips, this has a small effect) and a dense region of vortex structures in the mid-span portion of the far-wake. These far-wake streamwise structures are a result of vortex-tilting due to the freestream, and include the "legs" of the horseshoe vortex that originate from the LEV. Overall, this simple segmentation of vortical and strain structures based on the orientation of the vorticity unit vector does a fairly good job of isolating important aspects of the flow physics – the shear-layer and LEV, the shedding, deformation and tilting of the LEV, as well as the tip vortices.

We can now use equation (11.1), along with the segmentation described above, to quantify the contributions of the spanwise and non-spanwise vorticity-

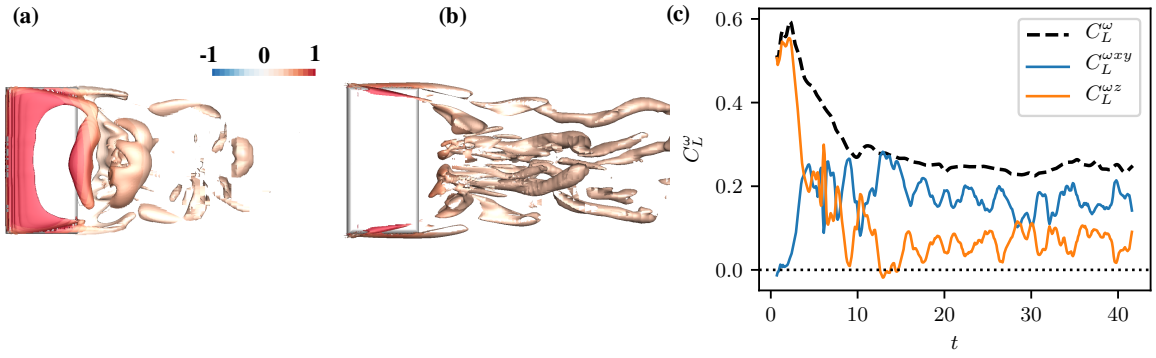

Figure 11.3: Spanwise and non-spanwise vorticity for the rectangular wing. (a)-(b) Top-view of Q iso-surfaces (level [2.0]) colored by $-2Q\phi_2$. Spanwise vorticity structures are shown in (a), by masking $|\eta_z| \leq \cos(\pi/4)$ regions; non-spanwise vorticity structures are shown in (b), by masking $|\eta_z| > \cos(\pi/4)$ regions. (c) Comparison of total vortex-induced lift coefficient (C_L^ω) with contributions from spanwise ($C_L^{\omega z}$) and non-spanwise ($C_L^{\omega xy}$) vorticity.

containing regions to the total vortex-induced lift. Figure 11.3(c) shows this comparison, from which several interesting observations can be made. We see that early in the simulation, as the flow develops over the wing, the total vortex-induced lift (C_L^ω) goes through a large-magnitude transient phase that is primarily driven by the spanwise oriented vorticity. This corresponds to the develpment of the spanwise shear-layer over the wing, and this transient has been shown to be an important factor in the initiating flow-induced oscillations of wings [77].

Soon after this transient, we observe a large drop in the spanwise lift contribution, along with a growth in the non-spanwise contribution. In fact, the spanwise vorticity eventually has a lower contribution to the total lift than the non-spanwise vorticity. This is a surprising and counter-intuitive result in light

of previous work and, therefore, our conventional understanding that the lift is dominated by the spanwise oriented LEV. Another interesting aspect of this comparison is that the growth and subsequent fluctuations of the lift induced by non-spanwise vorticity mirrors the corresponding fluctuations in spanwise vorticity. This hints at the role of vortex tilting in the creation of non-spanwise vorticity from spanwise vorticity, which is initially the dominant component according to figure 11.3(c). In the rest of this paper, we further dissect these lift components into spatial regions as well as vortical and strain contributions to uncover additional insights and explain the counter-intuitive dominance of non-spanwise vorticity in lift production.

11.2.2 Spanwise and non-spanwise vorticity in the wake

In order to better understand the relative contributions of non-spanwise and spanwise vorticity to the total vortex-induced lift, we now analyze their local contributions within different spatial regions over the wing as well as in the wake of the wing. Our interest in analyzing contributions in the wing's wake is motivated by the observation in section 11.2.1 and figure 11.3 that the growth of non-spanwise vorticity-induced lift is driven by the shedding, tilting, and stretching of spanwise vorticity in the wake. This is evident from

the emergence of significant non-spanwise vorticity in the wake of the wing, as seen in the flow visualization in figure 11.3(b), as well as the mirroring between the lift induced by non-spanwise and spanwise vorticity following the initial dominance of the spanwise component in figure 11.3(c). Therefore in this section, we analyze this behavior by quantifying the local lift induced by these structures at their inception over the wing and also at increasing downstream distances from the wing as they evolve with the flow in the wake.

The lift induced by structures corresponding to spanwise and non-spanwise vorticity within these local regions is estimated by dividing the analysis domain into cuboids that enclose the different regions of interest. The streamwise extent of each of these cuboids is shown in the schematic in figure 11.4(a), where the vertical dashed lines are planes normal to the streamwise direction. These streamwise-normal planes serve as a simple way to demarcate regions of the flow at increasing downstream distances from the wing. In this analysis, each analysis region has a length of one chord-length in the streamwise direction, and they span the size of the analysis domain in the other two directions. The region of interest over the wing is placed so that it is centered at mid-chord, i.e. its upstream and downstream ends are close to the leading and trailing edges respectively. The lift induced by spanwise and non-spanwise vorticity within each of these regions is then quantified by performing the volume integral in equation (11.1) within each of these regions separately.

In figure 11.4 we plot time-averages of the total vortex-induced lift coefficient (C_L^{ω}), as well as spanwise ($C_L^{\omega z}$) and non-spanwise ($C_L^{\omega xy}$) vorticity contributions, within each of these regions as a function of downstream distance from the wing. We first point out that the largest portion of lift is indeed induced within the region over the wing (downstream distance equals 0), and this lift production is dominated by spanwise oriented vorticity. As shown earlier in figure 11.3(a), the spanwise oriented vorticity over the wing largely corresponds to the LEV and leading-edge shear-layer, which we expect to have a significant contribution to lift. We also see that the non-spanwise vorticity in this region, which figure 11.3(b) shows mainly consists of the tip vortices, has a negative effect on lift. This is expected, and is in line our intuition based on classical (inviscid) aerodynamics and the effect of tip vortices on finite wings. Therefore on the whole, the lift production mechanisms in the region over the wing align with expectations from theory and prior work.

As we move into the wake, we see that the total vortex-induced lift displays an unexpected non-monotonic trend with downstream distance. It first begins to reduce in magnitude within the near-wake compared to the region over the wing. Farther downstream at about two chord-lengths from mid-chord (or 1.5 chord-lengths from the trailing-edge) the vortex-induced lift in fact has a negative value with magnitude approximately 25% of the peak value over the wing. This is rather surprising as we expect the effect of vortices far away from the

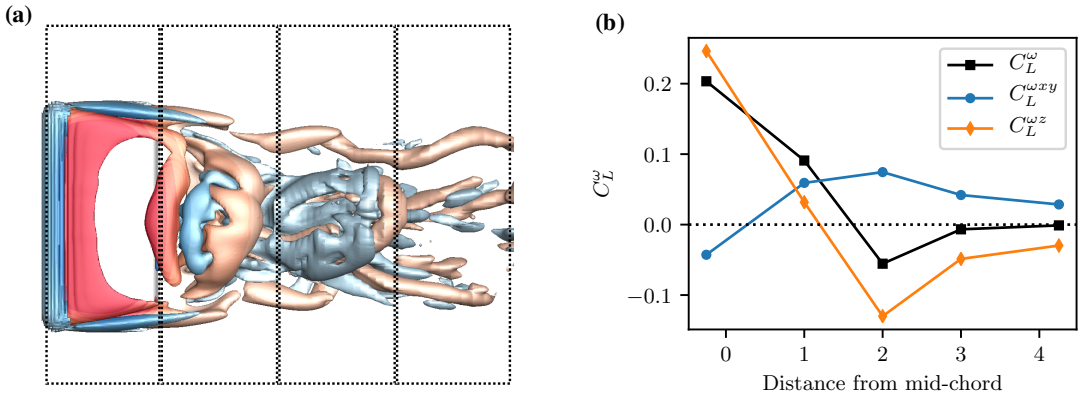

Figure 11.4: (a) Schematic of distinct cuboidal integration volumes at different downstream distances from the wing. (b) Time-averaged vortex-induced lift coefficient on the rectangular wing as a function of downstream distance from the mid-chord due to all vortex structures (C_L^{ω}), spanwise vorticity containing structures ($C_L^{\omega z}$) and non-spanwise vorticity containing structures ($C_L^{\omega xy}$).

wing to have a monotonically diminishing effect. It is clear that this negative lift in the wake is driven by a precipitous drop in the lift induced by spanwise oriented vorticity, which also turns negative within this region. In fact, the magnitude of the negative lift induced by spanwise vorticity approximately two chord-lengths downstream is roughly 50% of its peak value over the wing, which is quite significant. Simultaneously, we see a growth in the lift induced by non-spanwise vorticity, although its magnitude is not large enough to offset the negative lift induced by spanwise structures. All three curves peak at approximately two chord-lengths downstream, and subsequently approach zero as we move farther downstream due to their increasing distance from the wing.

This non-monotonic trend in vortex-induced lift as we move farther down-

stream, and particularly the fact that spanwise vorticity in the wake induces negative lift on the wing while non-spanwise wake-vorticity induces positive lift, is an intriguing result that justifies further analysis. It has been shown in previous work that although much of the focus in the literature concerning aerodynamics has been on the role that vortices play in force production, vortices are generally associated with regions of strain that in fact have a significant dynamical effect. In the context of this study, we hypothesize that the drop in lift due to spanwise structures and the subsequent negative lift might be a result of the development and growth of vortex-induced strain associated with these vortices after they shed into the wake of the wing. The strain-dominated regions, which correspond to $Q < 0$, would induce negative lift according to equation (11.1). Furthermore, it can be shown using simple vortex models that vortex cores, i.e. regions of $Q > 0$, are generally associated with higher vorticity magnitudes whereas the region of strain around a vortex is a larger diffused region with lower magnitudes of vorticity. As a result, these different regions would be affected to different degrees by vortex stretching and tilting due to the non-linear nature of these mechanisms, and can therefore have different effects on the lift production in the wake.

To investigate the effect of rotation and strain further, we decompose the vortex-induced lift associated with spanwise and non-spanwise vorticity into their corresponding vortical and strain regions. This is done by first identi-

fying spanwise and non-spanwise oriented structures using the vorticity unit vector as before, and then further decomposing these into regions of $Q > 0$, corresponding to vortex cores, and $Q < 0$, corresponding to strain-dominated flow. These four separate components of the flow-field are then used to estimate their contributions to lift within each of the integration regions described earlier using equation (11.1).

In figure 11.5(a) we show the time-averaged vortex-induced lift due to the rotational and strain regions associated with spanwise oriented vorticity. Similarly, figure 11.5(b) shows the corresponding contributions due to non-spanwise oriented vorticity. We first note that within the region around the wing (distance from mid-chord equals zero), the postitive lift due to rotational regions of spanwise vorticity, shown in red in figure 11.5(a), are the dominant lift producing mechanism. As discussed before, this corresponds to the effect of the LEV and the leading edge shear layer. The non-spanwise vorticity in the vicinity of the wing, i.e. primarily the tip vortices, produces negative total lift, as highlighted earlier. By decomposing the effect of non-spanwise rotation and strain, we see that the core of the tip vortices in fact produces positive lift, but the total effect of the tips is negative due to the strain regions. It is interesting to point out that this is in fact consistent with inviscid theory where the induced velocity due to tip vortices is implicated in lift reduction. In this case, the regions of strain around the tip vortex core correspond to the induced velocity.

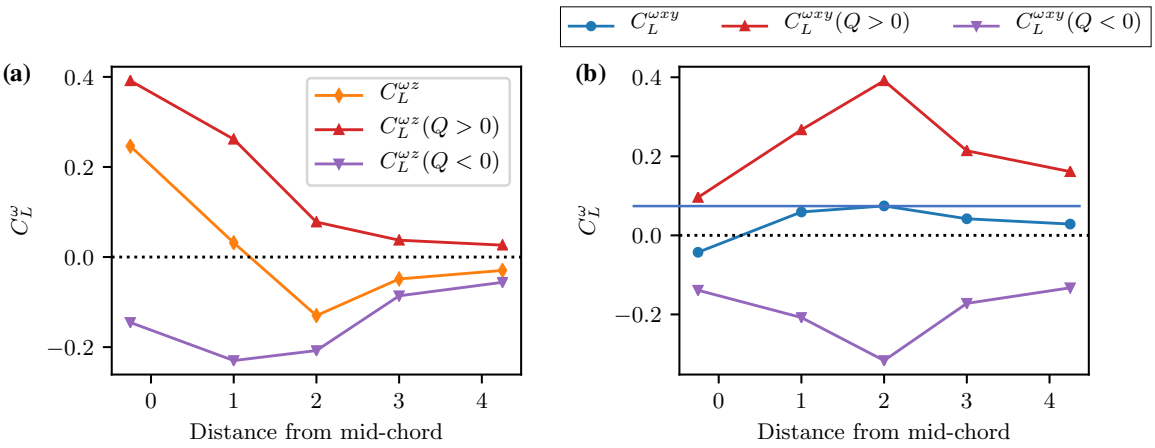

Figure 11.5: Time-averaged vortex-induced lift coefficient on the rectangular wing as a function of downstream distance from the mid-chord due to vortex cores ($Q > 0$) and strain regions ($Q < 0$) corresponding to: (a) Spanwise vorticity containing structures ($C_L^{\omega z}$); (b) Non-spanwise vorticity containing structures ($C_L^{\omega xy}$).

As we move downstream, there is a large drop in the magnitude of positive lift induced by spanwise vortex cores, accompanied by a smaller drop in the magnitude of negative lift due to spanwise strain regions. The net effect of this difference between the strain and rotational regions is the production of negative lift in the wake due to spanwise vorticity. Simultaneously, figure 11.5(b) shows that there is a large increase in the magnitude of positive lift induced by non-spanwise vortex cores in the wake, along with a smaller increase in the magnitude of negative lift due to non-spanwise straining regions.

The different rates of increase/decrease in the lift induced by vortex cores and their associated straining regions highlights some important flow physics that occurs in the wake. For one, as pointed out earlier, vortex cores are more susceptible to the effects of vortex tilting and stretching than their associated

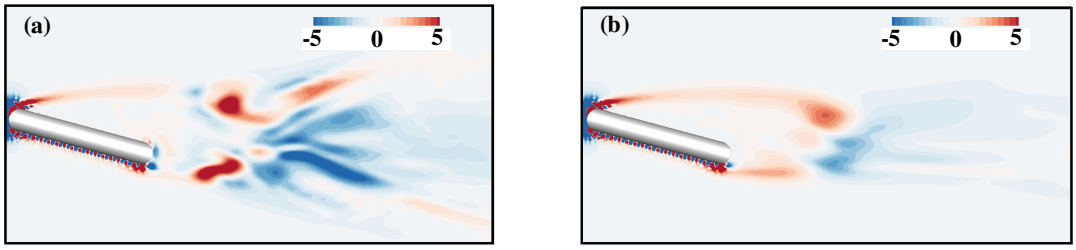

Figure 11.6: Contours showing the time-averaged Q field around the rectangular wing. (a) Slice at mid-span. (b) Slice between mid-span and wing-tip.

strain regions. Therefore, we expect the spanwise vortex cores to experience more vortex tilting than the associated straining regions. This therefore contributes to the larger drop in the lift magnitude induced by spanwise rotational cores as compared with their associated strain regions. Furthermore, the growth of vortex-induced strain after the shedding of the LEV and other spanwise oriented vortices in the wake is another factor that augments strain-induced lift due to spanwise vorticity in the wake. To illustrate this latter effect, figure 11.6 shows snapshots of the time-averaged Q field in the wake of the rectangular wing. Figure 11.6(a) shows the field at the mid-span location and figure 11.6(b) shows the field at a location between mid-span and the wing-tip. At both locations, the time-averaged distribution of Q shows the emergence of strong region of strain ($Q < 0$ in blue) in the wake of the wing. This region would therefore enhance the negative lift induced in the wake, as per equation (11.1).

In the case of the non-spanwise vorticity, the preferential tilting of the rotational regions of spanwise vorticity to create rotational non-spanwise vorticity,

as well as the preferential stretching of the streamwise rotational cores explains the larger increase in magnitude of rotation-induced lift as opposed to strain-induced lift in the case of non-spanwise vortices. Therefore by dissecting the lift producing mechanisms into contributions due to the orientation of vorticity, the vortical or straining nature of this vorticity, as well as different spatial regions, we have been able to shed interesting insight into the lift generating mechanisms on the wing.

11.3 Delta wing

We now contrast the flow physics of vortex-induced lift production on the rectangular wing discussed in the previous section with the corresponding influence of vortices and vortex shedding over a delta wing. The suppressed LEV-shedding in the case of delta wings, compared to rectangular wings, has been well documented in past work [84], and we expect this to have a substantial effect on the wake dynamics highlighted in the previous section. This therefore presents an interesting case to contrast with the rectangular wing analyzed above, especially with regards to the role of vortex shedding in the wake, along with the associated tilting, stretching and vortex-induced strain mechanisms, in lift production.

We begin by examining the overall vortex dynamics present in this case, and

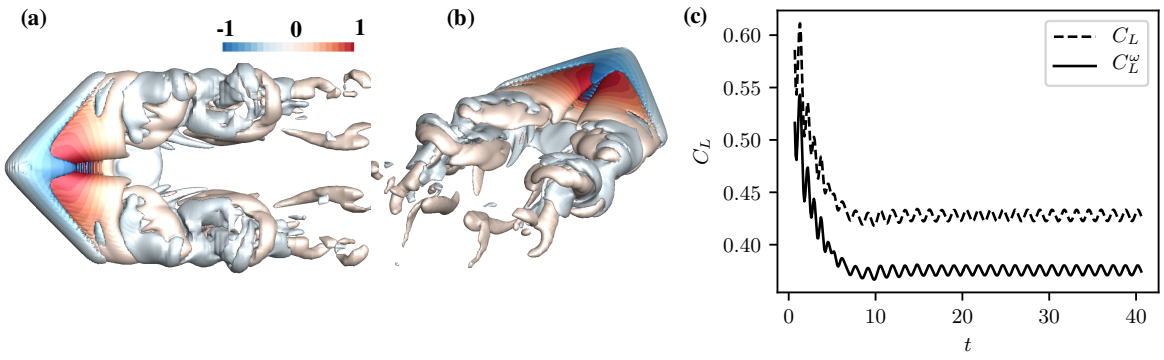

Figure 11.7: Vortex-induced lift on the delta wing. (a)-(b) Isometric and top-view, respectively, of iso-surfaces of Q at levels [-2.0,2.0], coloured by $-2Q\phi_2$. (c) Comparison of total lift coefficient (C_L) with vortex-induced lift (C_L^ω).

comparing it to the rectangular wing. Figures 11.7(a) and 11.7(b) show instantaneous visualizations of the Q iso-surfaces at levels [-2.0,2.0], colored by their contributions to vortex-induced lift ($-2Q\phi_2$). It is immediately apparent that there is significantly less vortex shedding in the mid-span region of the wake in this case, as compared to the rectangular wing. It should be pointed out that the vortex shedding in the mid-span region of the rectangular wing was mainly due to the LEV, and this LEV shedding is largely absent in the case of the delta wing. However, the delta wing does exhibit substantial shedding closer to the tips of the wing. In figure 11.7(c) we compare the total lift coefficient to the vortex-induced component, and we see that the vortex-induced lift is the dominant contributor in this case too. It is noteworthy that the delta wing produces a much higher lift coefficient than the rectangular wing.

We now evaluate the lift production due to non-spanwise and spanwise vorticity in the flow by using the direction of the vorticity unit vector at every

point in the field to make this demarcation, as was done before. In this case, the sweep of the delta wing's leading edge (45°) brings in a new direction to consider, in addition to the generic streamwise and spanwise directions. This introduces ambiguity in the separation of spanwise and non-spanwise oriented vorticity over the surface of the wing, and we therefore focus on the separate effects of these components of vorticity exclusively in the wake of the wing. In figures 11.8(a) and 11.8(b) we visualize these spanwise and non-spanwise structures, respectively, as Q iso-surfaces colored by the integrand of vortex-induced force. We see that while the case of the rectangular wing showed substantial spanwise vortex shedding in the wake, these structures are considerably reduced in the wake of the delta wing. This is also true of the non-spanwise structures in the wake. Moreover, we also see that the vortex structures in the wake of the delta wing extend to a smaller distance downstream, especially in the case of spanwise vorticity. These observations suggest that there might be different lift producing dynamics at play in the wake of the delta wing, as compared to the rectangular wing.

We quantify the dynamical influence of the vorticity over the wing, as well as non-spanwise and spanwise contributions in its wake, using the same procedure as was discussed in the context of the rectangular wing above. Figure 11.8(c) shows these trends in vortex-induced lift as we move downstream from the wing. An immediate difference that we see between the delta wing and the

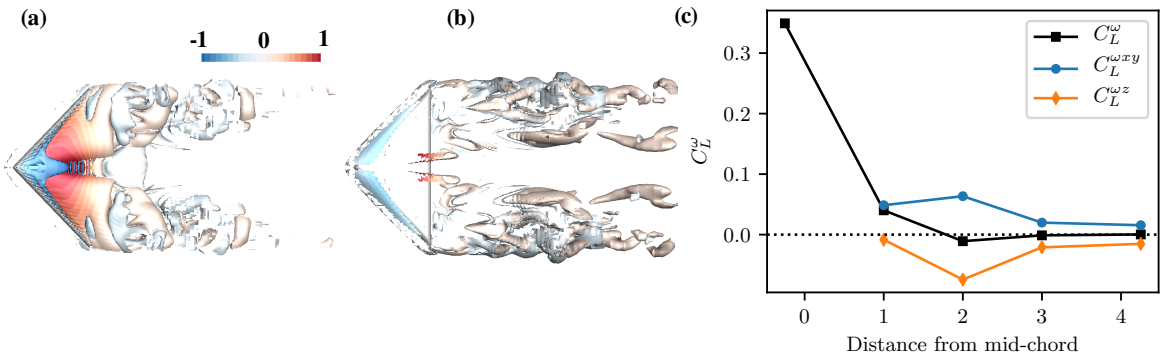

Figure 11.8: For the delta wing: (a) Q iso-surfaces (levels [-2.0,2.0]) colored by $-2Q\phi_2$ for spanwise vorticity structures (by masking $|\eta_z| \leq \cos(\pi/4)$). (b) Corresponding non-spanwise vorticity structures (by masking $|\eta_z| > \cos(\pi/4)$ regions). (c) Time-averaged vortex-induced lift coefficient as a function of downstream distance from the mid-chord due to all vortex structures (C_L^ω), spanwise vorticity containing structures ($C_L^{\omega z}$) and non-spanwise vorticity containing structures ($C_L^{\omega xy}$).

rectangular wing is the fact that the total vortex-induced lift in this case does not exhibit the strongly non-monotonic trend that was observed in the case of the rectangular wing. The vortex-induced lift produced on the delta wing is largely dominated by the influence of vortex structures over the surface of the wing (at zero downstream distance). As we move downstream from the wing, the vortex-induced lift drops sharply in magnitude, but we do not see the production of significant negative lift as was seen for the rectangular wing. The peak in the negative lift in this case, which occurs at two chord-lengths downstream, is negligible relative to the peak lift on the wing. In contrast, the wake of the rectangular wing saw a negative lift magnitude of approximately 25% relative to its peak positive lift over the wing. We also note that while the spanwise and non-spanwise vorticity in the wake had induced-lift of mag-

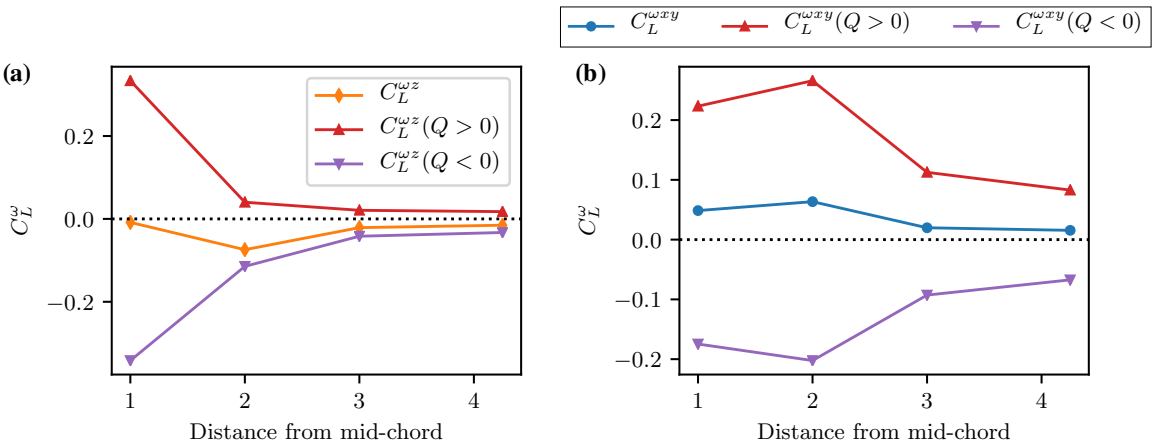

Figure 11.9: Time-averaged vortex-induced lift coefficient on the delta wing as a function of downstream distance from the mid-chord due to vortex cores ($Q > 0$) and strain regions ($Q < 0$) corresponding to: (a) Spanwise vorticity containing structures ($C_L^{\omega z}$); (b) Non-spanwise vorticity containing structures ($C_L^{\omega xy}$).

nitudes of approximately 50% of the peak lift over the rectangular wing, they have significantly smaller relative effects in the wake of the delta wing. These observations point to the weakened influence of vortex shedding in this case.

We now further decompose the spanwise and non-spanwise vortex-induced lift contributions in the wake into their respective rotational and straining components, as was done earlier in this paper for the rectangular wing. This decomposition is plotted for the spanwise and non-spanwise vorticity in figures 11.9(a) and 11.9(b) respectively. We first note that the rotational and strain regions associated with the non-spanwise vorticity shown in figure 11.9(b) behave similarly to what was observed in the case of the rectangular wing – the positive lift due to non-spanwise vorticity in the wake is due to the larger growth of positive lift associated with vortex cores than the growth of negative lift in-

duced by the non-spanwise straining regions. Although the magnitude of these contributions to the lift coefficient is similar to that seen over the rectangular wing, they have a smaller relative effect when scaled by the peak value of lift generated in the region over the wing.

On examining the spanwise vorticity contributions shown in figure 11.9(a), we notice substantial differences between the delta wing and rectangular wing. In the case of the delta wing too the magnitude of lift induced by spanwise rotational vortex cores and strain decrease by slightly different amounts as we move downstream in the wake, i.e. the magnitude of negative lift due to spanwise strain reduces slightly less than the positive lift due to spanwise vortex cores. However, this difference is small for the delta wing as compared to that observed for the rectangular wing. It therefore results in less negative lift due to spanwise vorticity in the wake of the delta wing when measured relative to the peak value over the wing (which is much larger for the delta wing), as well as in terms of the magnitude of the negative lift coefficient itself. This is a fairly significant improvement in lift production for the delta wing and can be explained by the weakened shedding of spanwise vorticity in its wake. The absence of the strong LEV being shed into the wake leads to the generation of weaker straining regions associated with the wake vortices, and also presumably less preferential tilting of spanwise vortex cores. These effects therefore result in a smaller discrepancy between the negative lift due to the

spanwise oriented strain and the positive lift due to spanwise oriented vortex cores. Therefore we have been able to highlight some interesting consequences of the suppressed vortex shedding over a delta wing, and how this phenomenon relates to the lift induced by wake vortices.

11.4 Conclusions

In this study, we have demonstrated some first steps in the analysis of force production due to distinct vortex structures in three-dimensional flows. We performed a partitioning of the lift on low aspect-ratio wings induced by vortex structures containing spanwise and non-spanwise oriented vorticity. The force partitioning method allows us to isolate the force contributions due to these distinct vorticity components, as well as to analyze their individual influence within different spatial regions of the flow-field. We showed that the lift production on a $2:1$ aspect-ratio rectangular wing is dominated by the overall contribution of non-spanwise vorticity. This is somewhat counter-intuitive as we expected the spanwise vorticity within the LEV to dominate lift production. To understand this better, we further decomposed these lift-producing components into their contributions within different spatial regions over the wing and at increasing distances downstream of the wing. Surprisingly, we found that the spanwise component of vorticity induces a negative lift on the wing at

about two chord-lengths downstream in the wake. however, the non-spanwise vorticity induces positive lift in this region. We explained this behaviour by separating and quantifying the influence of vortex cores and their associated strain in the wake for the spanwise and non-spanwise vorticity. We showed that while the lift production due to spanwise vortex cores rapidly drops in the wake, the associated negative lift due to the strain regions does not drop as rapidly due to the growth of vortex-induced strain and the preferential tilting of vortex cores. This discrepancy between the spanwise oriented vortex cores and their associated strain regions therefore results in a net negative lift in the wake of the rectangular wing. On comparing this with the corresponding behavior in the case of the delta wing, we showed that the influence of the wake is significantly diminished due to the suppressed vortex shedding. The suppressed shedding therefore eliminated the negative lift in the wake and results in a significant increase in lift coefficient on the wing.

Chapter 12

Summary and future outlook

In this dissertation, we have developed several insights and novel techniques for the analysis of flow-induced oscillations and vortex-dominated flows. The majority of work reported on here is based on computational simulations of flows interacting with moving boundaries that have been performed using a sharp-interface immersed boundary solver. For simulations of flow-induced oscillations, this flow solver is coupled with simple two-dimensional aeroelastic models consisting of linear spring-mass-damper oscillators that are immersed in incompressible fluid flows and allowed to perform pitching and heaving oscillations. These oscillations are driven by the non-linear loads induced on the oscillator by the fluid flow. Details of this computational setup and flow solver are given in chapter 2.

12.1 Aeroelastic oscillations and energy maps

In chapter 3 we reported on the aeroelastic oscillation response of a two-dimensional pitching airfoil at Reynolds number $Re = 1000$. We showed that this system is capable of very large amplitude oscillations which depend on a range of parameters. In particular, the location of the elastic axis was shown to be a significant factor that is responsible for non-intuitive oscillation behaviour. We also proposed a scaling for the critical reduced velocity at which the onset of large amplitude oscillations occurs. We showed that this onset is determined by a competition between the timescale associated with the oscillator's elasticity and the natural timescale of the fluid forcing.

In chapter 4, we proposed the idea of energy maps as a tool to analyze, predict, and control flow-induced oscillation responses. This tool is based on the fact that the growth/decay of flow-induced oscillations is determined by the energy extracted from the fluid flow by the oscillator. Furthermore, this energy extraction by a body undergoing flow-induced oscillations at a given kinematic state can in fact be determined by performing prescribed oscillations of the same body at precisely matching kinematics. This correspondence between flow-induced and prescribed oscillations allows us to map out the energy extraction landscape of a flow-induced oscillator by performing prescribed

oscillations (which are simpler to study) at a range of operating conditions of interest. This results in an energy map which identifies all possible equilibrium states, the stability of these equilibria, as well as possible bifurcations between these states for the flow-induced oscillator.

We showed in section 4.3 that the energy map can be used to analyze and predict non-intuitive amplitude responses observed in flow-induced oscillations. In addition, the energy map was shown to have a complex topology, which is determined by the presence of multiple distinct oscillation response branches. In chapter 5 we took this idea further to study the response of aeroelastically pitching wings to gust perturbations. We showed that knowledge of the response branches of the oscillator from the energy map allowed us to predict small as well as large amplitude aeroelastic oscillations that result from the wing-gust interactions. The energy map also allowed the prediction of subcritical oscillations which occur below the critical flutter speed. Lastly, we used the topology of the energy maps to make informed control decisions by altering structural properties of the wing to push the oscillator into regions of negative energy extraction. These control decisions were shown to have a significant impact on reducing flutter oscillations.

In order to analyze the structure of the energy map, we proposed a novel extension to the Dynamic Mode Decomposition technique in chapter 6. While this method is usually limited to flows over stationary bodies, the proposed formu-

lation extends its applicability to flows in the vicinity of (and interacting with) moving boundaries. This allowed us to probe frequency and phase relationships between the motion of pitching airfoils and the dominant flow features around them, which provided insights that are not evident from traditional analyses of the full flow-fields.

12.2 Partitioning of forces, moments and vortex-induced loads

A second significant focus of this dissertation is the development and application of the force and moment partitioning methods presented in chapter 7. These methods allow us to rigorously partition flow-induced loads on immersed bodies into contributions from vortex-induced, kinematic, viscous, and inviscid mechanisms. Of particular focus in this work is the vortex-induced component of force and moment. As discussed in section 7.3, this component makes a direct connection between the local kinematics of the flow and its dynamical influence via the Q field. It quantifies the forces/moments induced on immersed bodies due to vortices and vortex-induced strain, and can be applied to estimate the dynamical influence of individual vortices (or vorticity-containing regions) in a flow. In order to deploy this method to the analysis of vortex-dominated flows containing many interacting vortices, we developed a

physics-based and data-driven framework to isolate, track and categorize each vortex in these flows as they interact and evolve with the flow. This framework, described in chapter 9, represents a flexible and automated method that takes in two-dimensional time-resolved flow-field data and yields the kinematics as well as dynamical influence of each vortex that exists in the flow throughout its spatio-temporal evolution.

The force/moment partitioning method and vortex tracking framework have been used to provide insights into fundamental problems in flow-induced oscillations and unsteady aerodynamics. In chapter 8, force partitioning was combined with energy extraction to yield an energy partitioning method which estimates the direct effect of different force producing mechanisms on flow-induced vibrations via their work done on the vibrations. We used this to analyze the mechanisms driving flow-induced vibration of cylinders. We were able to quantify the effect of different forcing mechanisms as well as influence of shear-layer and wake vorticity in flow-induced vibrations. We showed that sustained oscillations are in fact driven by the shear layer and inhibited by the wake. This is contrary to the conventional notion that the vortex shedding in the wake is the primary driver of cylinder vibrations.

The force partitioning method was then applied to the analysis of lift production in two canonical problems in aerodynamics in chapters 10 and 11. We studied the dynamic stall of pitching wings in chapter 10, where we partitioned

the effect of different vortices as well as the strain-dominated flow induced by these vortices on lift production. We showed that although most of the focus of past studies in unsteady aerodynamics has been on the role of vortices in force production, vortex-induced strain can in fact have a significant, and even dominant, effect on the production of forces in some situations. Finally, in chapter 11 we demonstrated some preliminary work in extending such analyses to three-dimensional flows. In particular, we quantified the distinct roles that vortex structures containing spanwise and non-spanwise vorticity play in the lift production of rectangular and delta wings. We showed that while the spanwise vorticity produces significant lift over the wing, it has a negative contribution in the wake. We analyzed the different behaviour exhibited by the vortex cores and strain regions associated with spanwise and non-spanwise vorticity in different regions over the wing and in the wake, and related this to mechanisms such as vortex stretching and tilting. These findings therefore highlighted interesting physics in the force production mechanisms in three-dimensional flows.

12.3 Future work

With the development of the tools and analyses summarized above, the research presented in this dissertation has made tangible advances in our under-

standing of flow-induced oscillations and aerodynamic force production. Nevertheless, there are several limitations in this study and much work remains to be done to expand and generalize the insights and methods developed here.

For one, the physics of flow-induced oscillations highlighted here are based primarily on two-dimensional low-Reynolds number flows. Further investigation is required to fully analyze how the dynamics would be affected by the introduction of new time-scales and strong intrinsic three-dimensional effects associated with higher Reynolds numbers. This therefore raises several open questions relating to the dynamics of flow-induced oscillations as well as the mechanisms for force-production mechanisms in such flows. It must be noted that many of the methods demonstrated in this work, including the force/moment partition, are also applicable to the analysis of three-dimensional flows. Therefore, as illustrated by the preliminary results presented in chapter 11, this is an important direction of ongoing and future work.

The current study also does not address the flow-induced oscillation of bodies with multiple intrinsic modes/frequencies of flutter. In the case of wings, we have focused only on the dynamics of pitch oscillations to highlight and account for aerodynamic non-linearities such as those associated with dynamic stall; and in the case of vibrating cylinders, transverse oscillations are generally observed to occur with larger amplitudes than in-line oscillations [54,56,136,137]. Nonetheless, multi-modal oscillations are a natural extension of the current

work. We believe that the current approach of generating energy maps can, in principle, be extended to such systems, with additional modes of oscillation corresponding to added dimensions on the energy map. For instance, in the purely pitching system described in this work, the energy map is a function of pitch amplitude and frequency. On inclusion of heave oscillations, the energy landscape would be a function of the pitch amplitude and frequency as well as the heave amplitude and frequency. In these high-dimensional energy landscapes, the equilibria can still be identified as hypersurfaces of $E^* = 0$. Therefore, while the energy map based analysis, prediction and control described in this work is feasible in systems with multiple modes of oscillation, it is likely more complicated.

Furthermore, we have shown that energy maps can have highly complex topologies that may be difficult and expensive to fully resolve. In this work we have not investigated the physics behind the complex energy landscape, and this is a very promising direction for future work. It is also useful at this point to consider the practical feasibility of the gust control strategies demonstrated in chapter 5, which rely on the complex energy map topology. These strategies rely on "tailoring" structural properties of the system such as natural frequency and elastic axis. Such on-the-fly structural modifications have been shown to be possible with the use of smart materials for various aerospace applications [179], flutter suppression [180, 181], as well as control-

ling the stiffness distribution in wings [182–184]. This hence underscores the practical relevance of the findings discussed, which we expect will complement aero-structural efforts in the control of flow-induced vibration.

There are also several interesting challenges that remain in the context of our investigations into the force-production mechanisms that govern flow-induced oscillations and vortex-dominated flows. In chapter 9 we demonstrated an automated framework that enables the estimation of vortex-induced loads due to individual vortices in complex vortex-dominated flows. Although this framework was shown to be very useful, it is currently limited to the analysis of two-dimensional flow-fields. However, many relevant problems in areas such as biological propulsion and physiological flows are inherently three-dimensional. In our analysis of a canonical three-dimensional flow in chapter 11, we highlighted interesting physics that would greatly benefit from higher fidelity methods to partition different volumes in the flow. Therefore the extension of the vortex isolation and tracking framework to three-dimensional problems would be a significant step forward in our analysis of these problems. The development of such a framework and its use in the analysis of force production in problems involving biological and physiological flows are current and upcoming extensions of this work.

Another important direction of ongoing and future efforts is the use of the force/moment partitioning analysis framework in dissecting fluid dynamic loads

in flow-fields generated from laboratory experiments. The primary challenge in this context is accurately computing the force/moment partitioning terms from laboratory flow-fields. This difficulty stems from uncertainties and errors in the velocity field measurements, especially those that would induce divergence errors. Although the development of similar methods [97, 185–187] has made the formulation more amenable to under-resolved flow-field data, we expect that these issues will reduce the accuracy of the computed force/moment partitioning. This is a challenge that remains to be addressed.

Lastly, we are currently also considering extensions of the force/moment partitioning methods presented here to derive additional insight into other problems relating to the pressure induced on surfaces within fluids. For instance, the partitioning of pressure-induced loads can be combined with acoustics theory to determine the sources of noise that result from pressure fluctuations on immersed surfaces. Another example is the extension of this method to the partitioning of local pressure (or pressure gradients) on immersed surfaces. These extensions of the force/moment partitioning method are both subjects of ongoing study.

Appendix A

Aerodynamic loads on canonical airfoils at low Reynolds numbers

The aerodynamic characteristics of airfoils at low Reynolds number (Re) have been known to be markedly different from those at the high Reynolds numbers encountered in conventional air-vehicles. With recent interest in unmanned and micro-aerial vehicles, as well as bio-inspired flight, this low-Reynolds number behaviour has been garnering academic as well as practical interest. In spite of this, there is little readily available data in the literature concerning low-Reynolds number aerodynamics which are on par with high-Re datasets such as in refs. [142, 188]. The availability of such data is important for practical design considerations as well as validation of computational models.

APPENDIX A. AERODYNAMIC LOADS AT LOW REYNOLDS NUMBERS

A compilation of early measurements at relatively low Reynolds numbers ($Re \approx 5 \times 10^4 - 5 \times 10^5$) can be found in the work of Carmichael [189] and Selig *et al.* [190–192]. There have been few studies of very low-Re airfoil flows since, especially at $Re \approx 10^3$. This is in part due to the difficulty in achieving such flows in experiments, as well as the repeatability of experiments in this sensitive regime [193]. While computational studies of flow over stationary airfoils at low-Re have also been carried out, many of these have been performed at a single angle-of-attack [140, 194]. To explore a larger portion of the parameter space, Kunz and Kroo [195] as well as Mateescu and Abdo [196] studied low-Re airfoil aerodynamics over a large range of angles-of-attack, Reynolds numbers and airfoil shape. However, they employed *steady models* that ignore unsteady effects such as vortex shedding. More recently, Kurtulus [138] as well as Liu *et al.* [139] studied the flow over a NACA 0012 airfoil over a range of angles-of-attack at $Re = 1000$ using time-resolved simulations. Although both of these studies provide time-resolved aerodynamic quantities at low-Re, they have been performed for a single airfoil shape and Re.

Here we describe results from two-dimensional simulations of low-Re flow ($500 \leq Re = U_\infty C/\nu \leq 2000$) over three different NACA airfoils, obtained using highly-resolved, unsteady incompressible Navier-Stokes simulations. The is to provide a comprehensive database of the variation in key aerodynamics quantities (force coefficients, center-of-pressure and Strouhal numbers) with

Reynolds number, angle-of-attack and airfoil shape. This data should provide an improved understanding of airfoil aerodynamics at these very low Reynolds numbers and also serve as a database for validation of computational models.

The airfoils used here are from the NACA family: NACA 0012, NACA 0015 and NACA 4415. The airfoil (chord length C) is immersed in a domain of size $18C \times 20C$, and a non-uniform Cartesian grid with 480×448 points is employed. Grid convergence and verification of the solver for this setup are discussed in section 2.3. All reported quantities are scaled using the fluid density (ρ), freestream velocity (U_∞), and chord length (C) as characteristic scales.

As will become apparent in the next section, these low-Reynolds number flows over airfoils may be unsteady and also not strictly periodic. Well converged statistics therefore necessitate very long integration times ($c/U_\infty \sim 150 - 250$), which translates to $3 - 5 \times 10^5$ time-steps in our simulations. Thus, even these two-dimensional simulations require significant computational resources. Each simulation has been performed on 210 processors and required approximately 48 hours to turn around. Result from a total of 72 simulations are reported here.

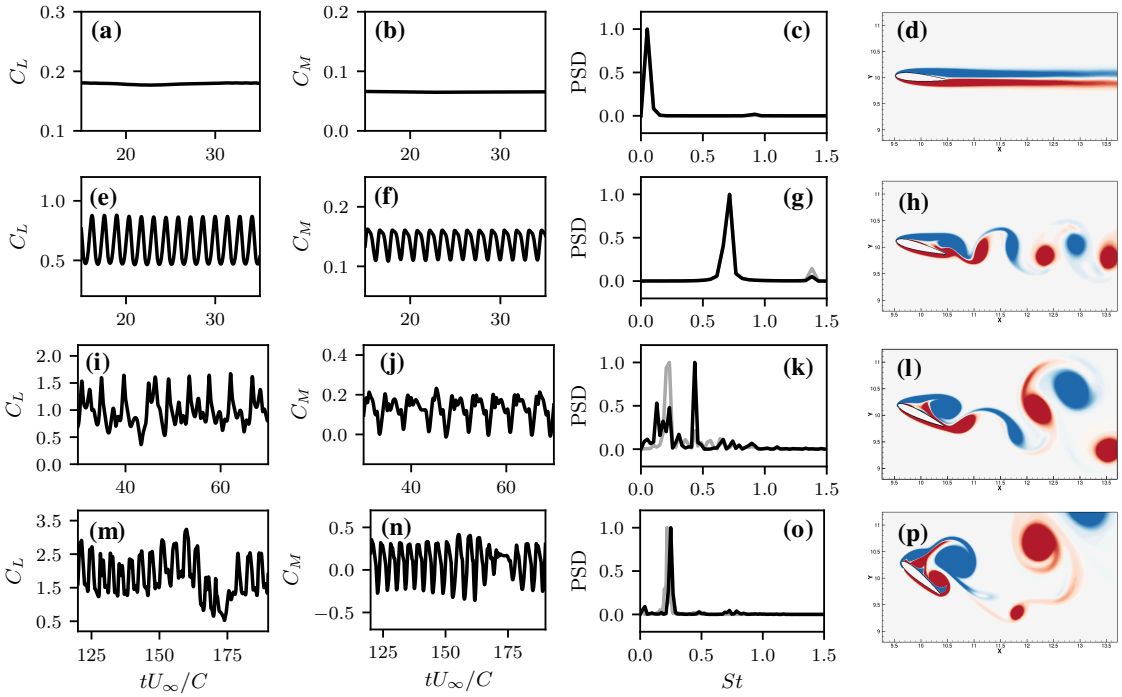

Figure A.1: C_L (leftmost pane) and C_M (middle-left pane) time-series plots, frequency spectra of C_L and C_M (middle-right pane), and snapshots of vorticity fields (rightmost pane) for different regimes of unsteady behaviour at $Re = 1000$. Frequency spectra are shown in terms of St, with the black and grey lines showing the spectra of C_L and C_M respectively, each scaled by the magnitude of the peak for clarity. (a)-(d) $\alpha = 5°$; (e)-(h) $\alpha = 15°$; (i)-(l) $\alpha = 25°$; (m)-(p) $\alpha = 40°$.

A.1 Flow regimes

We begin with a qualitative discussion of the flow behaviour observed at different angles-of-attack for the NACA 0015 airfoil at $Re = 1000$. We see that the wake behind the airfoil transitions from a steady wake, to a Karman vortex street, and finally to a leading-edge vortex (LEV) dominated flow as the angle-of-attack is increased well past the static stall angle. The steady, pre-vortex shedding regime is shown in figures A.1(a)-(d), for $\alpha = 5^\circ$. Figures A.1(e)-(h) correspond to $\alpha = 15^\circ$ where periodic oscillations in C_L and C_M result from the Karman vortex shedding. Figures A.1(i)-(l) show the behaviour at $\alpha = 25^\circ$, where the C_L and C_M time-series show low as well as high-frequency components due to a 1P-1S (one vortex pair and single vortex) shedding mode. The high-frequency mode corresponds to Karman vortex-shedding, and the formation and shedding of the LEV causes the low-frequency oscillations. In figure A.1(m)-(p) we see the characteristics of the $\alpha = 40^\circ$ case which are dominated by the low-frequency shedding of a large LEV and a small TEV. The time-variations of the coefficients for this case also exhibits stochastic variations interspersed with quasi-periodic behavior. The complex behavior of the flow at these low Reynolds numbers is due to the simultaneous presence of a number of length scales of comparable magnitude such as the chord length, the airfoil thickness, the frontal projected height of the airfoil and the thicknesses of the

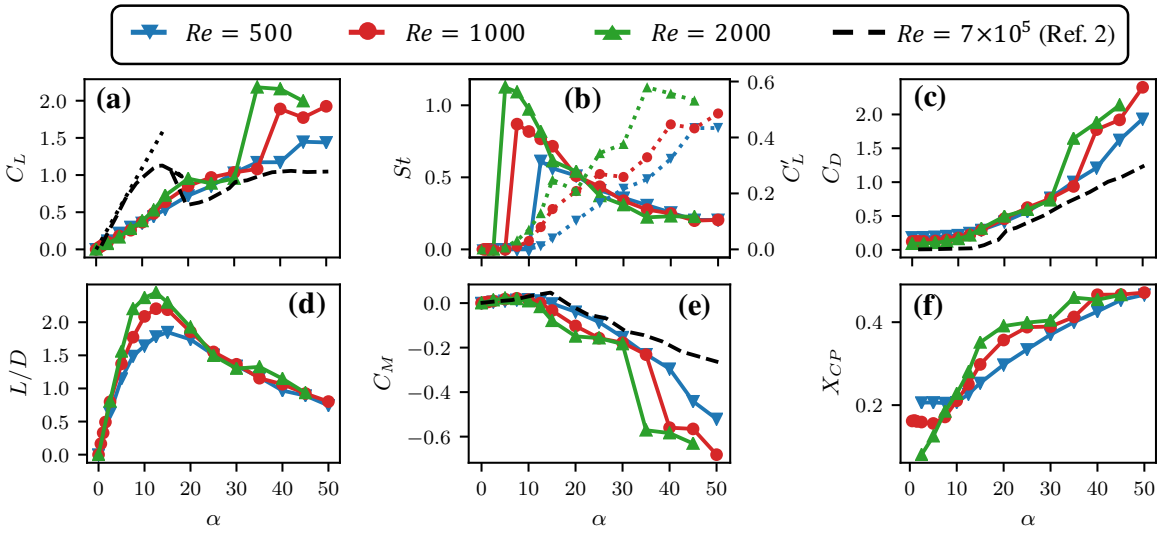

Figure A.2: Aerodynamic quantities for the NACA 0015 airfoil for $Re = 500, 1000, 2000$. Dashed line shows experimental measurements at Re=7×10^5 from Ref. [188]. (a) Coefficient of mean lift, C_L. Dotted line indicates $C_L = 2\pi\alpha$.; (b) Strouhal number (St; solid lines) and standard deviation (C'_L; dotted lines) of C_L oscillations; (c) Coefficient of mean drag, C_D; (d) Lift-to-drag ratio.; (e) Coefficient of mean moment about quarter-chord, C_M; (f) Mean location of center-of-pressure, X_{CP}.

boundary layer on the suction and pressure surfaces of the airfoil. Further, the non-periodic nature of the flow for the high angle-of-attack cases necessitates extremely long integration times to accumulate reliable statistics.

A.2 Effect of Reynolds Number

Figure A.2 shows a comparison of computed force coefficients for the NACA 0015 airfoil at $Re = 500, 1000$ and 2000, as a function of angle-of attack, α. These are also compared with the high-Re experimental measurements of C_L, C_D and C_M from Sheldahl and Klimas at $Re = 7 \times 10^5$ [188]. Figure A.2(a) shows the

trend for mean C_L. At low α, the mean C_L is similar for the three values of Re, and the lift-slope is about half of the theoretical value of 2π as well as the slope at high Reynolds number (7×10^5). The mean C_L increases monotonically for $Re = 500$ and 1000, whereas there is a mild stall at $20^\circ \leq \alpha \leq 25^\circ$ for $Re = 2000$. However none of the cases shows any indication of the deep stall apparent for the high Reynolds number case. Also contrary to the high-Re behaviour, all three cases exhibit a significant increase in mean C_L for approximately $\alpha \geq 35^\circ$. This increase is caused by the formation and shedding of a leading-edge vortex and the magnitude of this jump in mean C_L is found to increase with Reynolds number.

Figure A.2(b) highlights the unsteady nature of C_L, with the standard deviation of C_L plotted using dotted lines and the Strouhal number (St) of lift oscillations plotted using solid lines. At low angles, St is zero due to the flow being steady, as seen in figures A.1(a)-(c). This is followed by a jump in St as α is increased, which corresponds to the onset of unsteady vortex shedding, followed by a monotonic decrease in St. We see that the onset of unsteadiness ranges from $\alpha \approx 12.5^\circ$ for Re=500 to $\alpha \approx 5^\circ$ for Re=2000. It is noted that figure A.2(b) shows the most dominant frequency, however at high angles-of-attack ($\alpha > 25^\circ$) the lift oscillations exhibit multiple frequencies, as seen in figure A.1. The intensity of C_L fluctuations are captured by the standard deviation, C_L'. The $Re = 500$ and 1000 cases show a mostly monotonic increase in the

intensity of lift fluctuations with α, but the $Re = 2000$ case shows a complex non-monotonic behavior.

The behaviour of C_D, shown in figure A.2(c), is unremarkable except for jump in the value beyond $\alpha \approx 20^\circ$ for the two higher Reynolds number cases. It must also be noted that as expected, the drag in these cases is larger than that at high-Re. Figure A.2(d) shows the lift-to-drag ratio for these cases. The peak in C_L/C_D occurs between $\alpha \approx 15^\circ$ for $Re = 500$, and $\alpha \approx 10^\circ$ for $Re = 2000$. Also, we see that the peak lift-to-drag ratio at these low Reynolds numbers is significantly lower than those at much higher Reynolds number used in conventional aerospace applications, which can be in the range $C_L/C_D \approx 20 - 50$ at high Reynolds numbers [188].

Figure A.2(e) shows C_M and we see that at small α the moment is close to zero and shows very small variation with α. This is one feature that these low-Reynolds numbers flows appear to share with their higher Reynolds number counterparts. The magnitude of C_M increases with Re at high α, and is negative for $\alpha > 10^\circ$. This is related to a shift in the center-of-pressure, which we plot in figure A.2(f). We see that X_{CP} stays constant for small angles at lower Re, with this value being farther downstream for lower Re. On increasing α we see that X_{CP} moves downstream, reaching close to mid-chord at $\alpha = 50^\circ$.

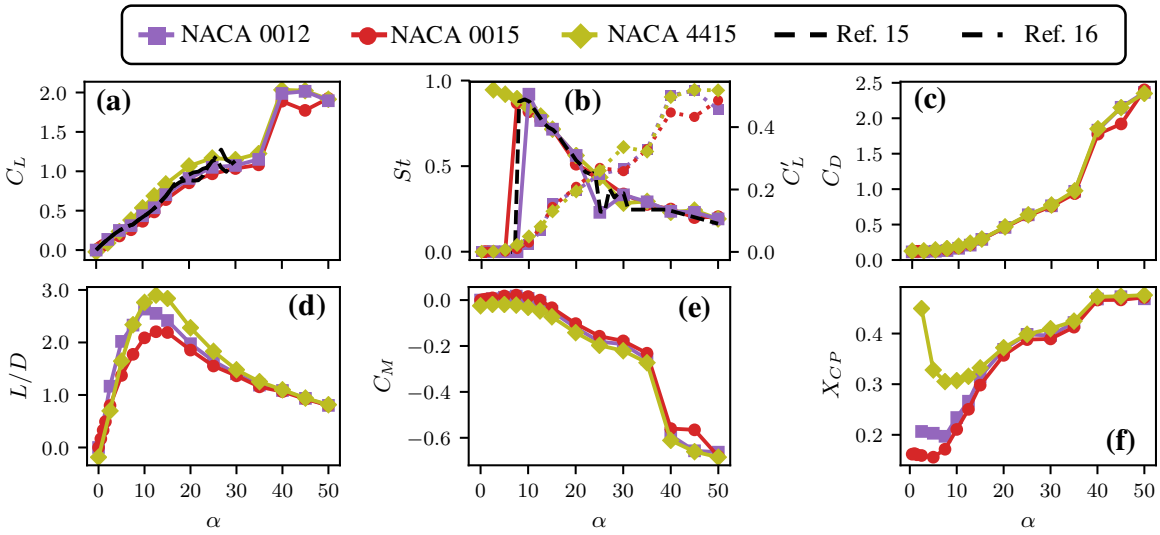

Figure A.3: Force coefficients as a function of angle-of-attack (α) for three airfoil shapes at Re=1000. The dashed line shows measurements from Kurtulus [138] and Liu *et al.* [139]. (a) Coefficient of mean lift, C_L. Dotted line indicates $C_L = 2\pi\alpha$.; (b) Strouhal number (St; solid lines) and standard deviation (C'_L; dotted lines) of C_L oscillations; (c) Coefficient of mean drag, C_D; (d) Lift-to-drag ratio.; (e) Coefficient of mean moment about quarter-chord, C_M; (f) Mean location of center-of-pressure, X_{CP}.

A.3 Effect of Airfoil Shape

We now briefly describe the effect of shape on the aerodynamic characteristics by comparing the simulation data for NACA 0012, NACA 0015, and NACA 4415 airfoils at $Re = 1000$. Figure A.3(a) shows that the NACA 4415 produces a small but measurable negative lift at $\alpha = 0°$ and this unusual effect is contrary to what is observed at conventional Reynolds numbers (see Ref. [142]). In fact, such peculiar behaviour at low-Re has been previously reported at small angles-of-attack [193]. The lift for the NACA 4415 also increases more rapidly with angle-of-attack compared to the other airfoils, leading to a larger mean lift

at the intermediate angles-of-attack. The other significant difference amongst the three airfoils is in the lift-to-drag ratio and the center-of-pressure. The NACA 4415 airfoil generates the largest value of C_L/C_D which is about 32% higher than the NACA 0015 airfoil. The center-of pressure of the NACA 4415 airfoil is also quite disparate from the other two airfoils for $\alpha < 15^\circ$. Also shown in figure A.3(a) and (b) are comparisons of the mean and Strouhal number of C_L fluctuations computed in this work for a NACA 0012 airfoil at $Re = 1000$ (purple line) with the results of Kurtulus [138] (dashed line) and Liu *et al.* [139] (dash-dotted line). We note that the comparison for both these quantities is quite good.

The aerodynamic characteristics discussed in this appendix are published in reference [177].

Appendix B

Data-driven identification of distinct vortex-wake patterns

In this chapter, we discuss the implementation of the data-driven procedure that was briefly described in section 9.2.1 for the identification of distinct vortex dynamic regimes in the wake of pitching airfoils from the large ensemble of flow-field data from 165 simulations. An outline of the main steps involved in this process is shown in figure B.1. We also show the size of the data set involved in each of these steps along the left-side of figure B.1.

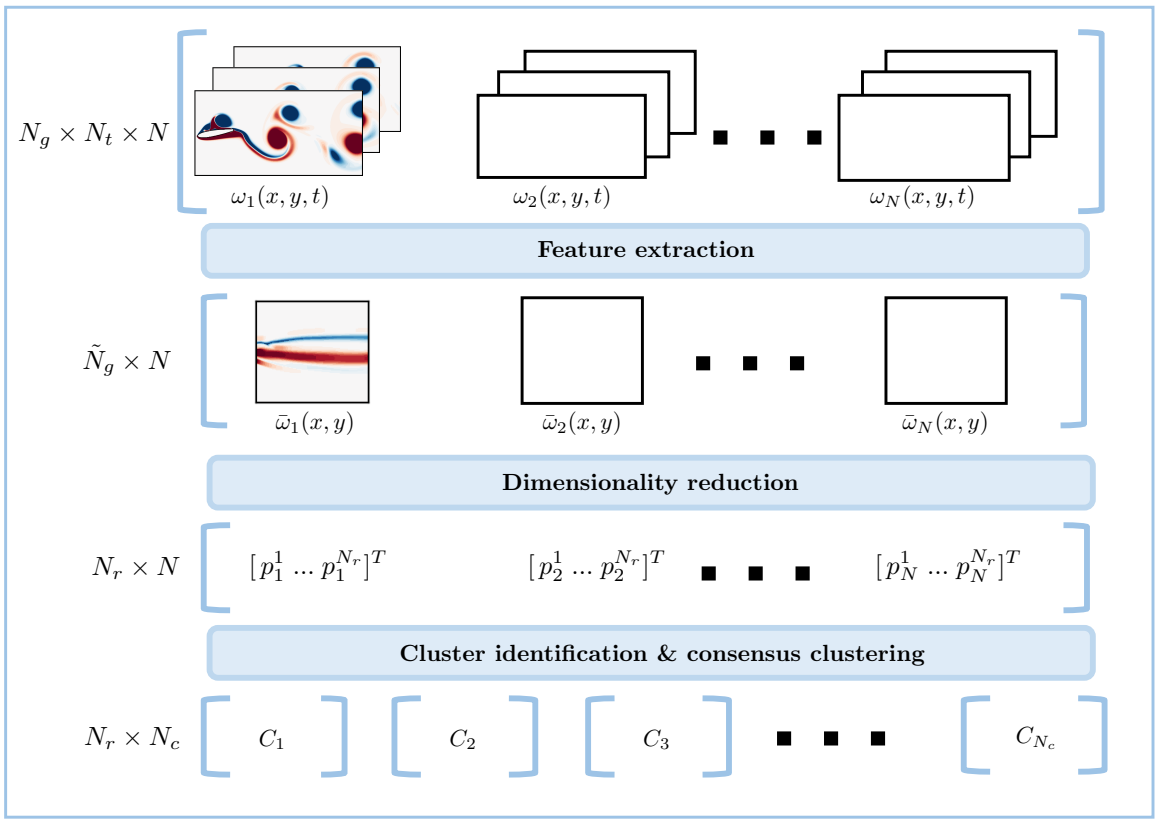

Figure B.1: Schematic of steps involved in the clustering-based framework for the identifying distinct vortex-dynamic regimes. The size of the data at each step is indicated along the left. Snapshots of the vorticity field and the time-averaged vorticity field in the wake for a sample case are shown in ω_1 and $\bar{\omega}_1$.

B.1 Feature extraction

The input data to this procedure consists of a large ensemble of time-resolved flow-fields representing each member of the ensemble. The first step involves distilling the relevant information required from the full flow-field of each member, in order to measure similarity between ensemble members. This is important because the dimensionality of the input data in its raw form, depending on the grid-size and number of time-snapshots, can be intractable in most problems. For example, the 165 cases in the present application, each with grid size of 1.23×10^5 and sampled with 500 time-snapshots, result in a very high-dimensional data-set approaching 10^{10} floating-point entries. Further, the task of discovering similarities in time-resolved data is considerably more complicated than in static data. For these reasons, the first step in this process involves extracting features from this high-dimensional data, by focusing on relevant spatial regions of the flow-field, and condensing the time-evolution of the flow-field into a static representation. In terms of computational complexity, for an ensemble consisting of N members, each of which is initially represented by N_g grid points and N_t temporal samples, this "feature extraction" step reduces the size of the dataset from $N_g \times N_t \times N$ to $\tilde{N}_g \times 1 \times N$ floating-point entries, where $\tilde{N}_g \leq N_g$ is the spatial dimension of the extracted feature. For an ensemble member (i), we refer to this extracted "feature vector"

as γ_i.

The static features extracted in this process are meant to serve as representations of the dynamics of each flow-field. Hence, modal decomposition techniques [106], such as Principal Orthogonal Decomposition, are often good feature vector candidates [130]. In this work, we use a "zeroth-order" mode of the flow-field, the time-averaged vorticity field ($\bar{\omega}$). The extracted feature vector is computed over a region smaller than the total grid-size, and is of size $\tilde{N}_g = 49392$ grid points. This feature extraction step results in a reduction of the size of the data from $N_g \times N_t \times N \approx 10^{10}$ floating-point entries to $\tilde{N}_g \times 1 \times N \approx 8 \times 10^6$ entries.

B.2 Dimensionality reduction

Upon identifying a representative feature of the vortex-dynamics in the flow, the next step involves further reducing the dimensionality of this extracted data based on spatial information. This dimensionality reduction can be achieved using a large variety of methods [121], and in this work, we utilize Principle Component Analysis (PCA) for this task. We assemble the ensemble of N feature vectors, each of which is given by $\gamma_i \in \mathbb{R}^{\tilde{N}_g}$, into a large matrix of size $\tilde{N}_g \times N$ and compute the principle components of this matrix. The projection of each feature vector on the first N_r principal components is

then computed, where N_r is chosen so as to retain $\approx 90\%$ of the variance. This step hence reduces the dimension of each feature vector, which we denote in this PCA-space by $\tilde{\gamma}_i$, to N_r. The resulting size of the data-set, which is $N_r \times N$ floating-point entries, is typically many orders of magnitude smaller than the original size. In the present case, we use $N_r = 25$, and this step reduces the feature space from $\approx 8 \times 10^6$ to $\approx 4 \times 10^3$ floating-point entries.

B.3 Clustering

The compact data-set that results from the above steps can now be efficiently grouped into clusters that share similar features. In this work, we use Gaussian mixture modelling (GMM) to perform this clustering task. GMM is a method for Bayesian mixture modelling, which fits multivariate Gaussian mixtures over given data. In the context of clustering, each component Gaussian distribution in the mixture model denotes a cluster of data that shares similar features [197–199]. Hence for a normal distribution $N_k(\tilde{\gamma} \mid \tilde{\mu}_k, \tilde{\mathbf{\Sigma}}_k)$, defined over the N_r-dimensional PCA-space of feature vectors $\tilde{\gamma}$, and parameterized by its N_r-dimensional mean and $N_r \times N_r$ dimensional covariance matrix, the mixture model probability density is given by

$$p(\tilde{\gamma} \mid \mathbf{\Theta}) = \sum_{k=1}^{N_c} \pi_k N_k(\gamma \mid \tilde{\mu}_k, \tilde{\mathbf{\Sigma}}_k) \tag{B.1}$$

This is a sum of N_c mixture components, each weighted by a mixture weight π_k. The mixture weights (π_k), and the mean and covariance of each component ($\tilde{\mu}_k, \tilde{\Sigma}_k$) are the parameters of the model, denoted by Θ. To estimate these parameters, we use the expectation-maximization algorithm [200] for maximum-likelihood estimation, implemented in the open-source *scikit-learn* package [201].

Some key advantages of using GMM are its inherent simplicity, formal statistical basis, and its flexibility to fit non-isotropic clusters. GMM requires specifying the number of clusters in the data beforehand, which is represented in equation B.1 by N_c. We estimate this using the Bayesian information criterion [202], which is a model selection criterion that penalizes high model complexity, and is well suited to mixture modeling based methods [203]. The Bayesian information criterion (BIC) takes the form:

$$BIC = N_\Theta \ln(N) - 2\ln(\tilde{L}) \tag{B.2}$$

where N_Θ is the number of parameters in the model, and is proportional to N_c. The function $\tilde{L}$ is the log-likelihood, which is analogous to the optimization function maximized in fitting equation B.1 to the data given by γ_i. Hence low values of BIC represent a good balance between model complexity (proportional to N_c) and the fit of the model.

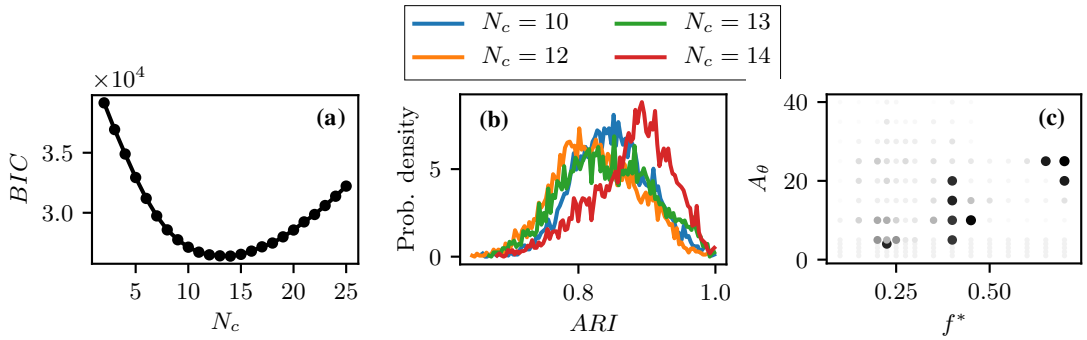

Figure B.2: (a) Bayesian information criterion (BIC) versus number of clusters (N_c). The minimum BIC at $N_c = 14$ indicates the best-fit for N_c; (b) Probability density of pair-wise ARI for 100 independent clustering results with $N_c = 10$, $N_c = 12$, $N_c = 13$, and $N_c = 14$; (c) Variability in clustering assignment for each case in the dataset, evaluated. The darker markers represent higher variability.

The number of clusters is determined in the present case by iterating through values in the range $2 \leq N_c \leq 25$, and performing 3000 independent instances of clustering at each N_c. We then pick the clustering result that represents the best BIC (from the 3000 independent results) at each value of N_c, and this BIC is plotted against N_c in figure B.2(a). The optimal N_c, given by the minimum of the BIC-curve, is hence determined to be $N_c = 14$ in the data-set analyzed here.

B.4 Consensus clustering

Lastly, the distinct vortex regimes identified are tested for robustness using multiple independent runs of the GMM algorithm, with random initial seeds, on the given data. In this work, we generate a set of 100 independent clustering

results, each of which is selected as the best result (based on BIC) from 3000 initializations. We compare independent clustering results pair-wise using the the adjusted Rand index [204]. This metric assigns a score of 0 in the event of random clustering, and 1 in the event of an exact match between two clustering results. We first use this to verify the suitability of the chosen N_c value, with the aim to obtain the smallest possible set of representative cases from this large data-set of flow-fields. Hence we compare the chosen value of $N_c = 14$ to clustering results obtained by using smaller N_c values, $N_c = 10$, $N_c = 12$ and $N_c = 13$. We generate a set of 100 independent clustering results at each value of N_c and then compute the ARI between all 99×100 pairs of results in each set. This is plotted as a probability distribution in figure B.2(b) for each N_c. We see that $ARI \gtrapprox 0.7$ for all pairs, which is a quantitative indication that the data-set consists of highly repeatable clusters, hence suggesting the existence of true clusters (as opposed to random clustering, which would not be repeatable). Further, while the mean ARI for the cases with $N_c = 10$, $N_c = 12$, and $N_c = 13$ are similar to each other, $N_c = 14$ has a higher mean ARI as well as a bias towards higher ARI values. This suggests that the chosen value of $N_c = 14$ is indeed a better fit to the data than the lower values. This process also allows a quantitative way to determine a "consensus clustering" [205, 206], i.e. the clustering that is most similar to all others generated in this set of independent results. This is chosen based on the mean ARI for

each independent clustering, i.e. the mean of its ARI computed against the 99 other independent results. The clustering result with the lowest mean ARI, representing the closest match to all other members of the set, is chosen as the final clustering result [205, 206].

The repeatability of clustering that is discussed above is assessed over the entire clustering result. We now propose an additional metric for evaluating the repeatability of cluster assignments for each case in the data-set. We construct "distance matrices", M_{ij}, for each pair (C_i, C_j) of independent clustering results, with size $N \times N$ (N is the number of cases in the data-set). The (p, q) entry of M_{ij} is given by the following: $M_{ij}(p, q) = 0$ if the p^{th} and q^{th} data-points in the ensemble are clustered either in the same cluster or different clusters in both C_i and C_j, and $M_{ij}(p, q) = 1$ if the p^{th} and q^{th} points are clustered separately in C_i but together in C_j or vice-versa. This is similar to [207] and [208]. M_{ij} is then averaged for all pairs (C_i, C_j), and subsequently averaged for each data-point N. The result is a vector of size N which measures the variability in cluster assignment for each of the N members in the ensemble, thus indicating which ensemble members are most likely to be erroneously assigned to the wrong cluster. In figure B.2(c), each ensemble member is plotted in frequency-amplitude space, with the visibility of each marker representing the measured variability. As expected, we see that members closer to cluster boundaries are most likely to be mis-classified.

Bibliography

[1] R. D. Blevins, *Flow-induced vibration*. Van Nostrand Reinhold Company, 1990.

[2] W. Shyy, Y. Lian, J. Tang, D. Viieru, and H. Liu, *Aerodynamics of low Reynolds number flyers*. Cambridge University Press, 2007.

[3] J. Young, J. C. Lai, and M. F. Platzer, "A review of progress and challenges in flapping foil power generation," *Progress in Aerospace Sciences*, vol. 67, pp. 2–28, 5 2014.

[4] Q. Xiao and Q. Zhu, "A review on flow energy harvesters based on flapping foils," *Journal of Fluids and Structures*, vol. 46, pp. 174–191, 4 2014.

[5] M. M. Bernitsas, K. Raghavan, Y. Ben-Simon, and E. M. H. Garcia, "VIVACE (Vortex Induced Vibration Aquatic Clean Energy): A New Concept in Generation of Clean and Renewable Energy From Fluid Flow," *Journal of Offshore Mechanics and Arctic Engineering*, vol. 130, no. 4, p. 041101, 11 2008.

[6] T. Theodorsen, "General theory of aerodynamic instability and the mechanism of flutter," National Advisory Committee for Aeronautics, Tech. Rep., 1935.

[7] S. L. Brunton and C. W. Rowley, "Modeling the unsteady aerodynamic forces on small-scale wings," *47th AIAA Aerospace Sciences Meeting*, no. 1127, 2009.

[8] L. E. Ericsson and J. P. Reding, "Fluid mechanics of dynamic stall part I. Unsteady flow concepts," *Journal of Fluids and Structures*, vol. 2, no. 1, pp. 1–33, 1988.

[9] J. D. Eldredge and A. R. Jones, "Leading-edge vortices: Mechanics and modeling," *Annual Review of Fluid Mechanics*, vol. 51, pp. 75–104, 2019.

[10] W. J. McCroskey, "Unsteady Airfoils," *Annual Review of Fluid Mechanics*, vol. 14, no. 1, pp. 285–311, 1982.

[11] M. H. Akbari and S. J. Price, "Simulation of dynamic stall for a NACA 0012 airfoil using a vortex method," *Journal of Fluids and Structures*, vol. 17, no. 6, pp. 855–874, 2003.

[12] T. Lee and P. Gerontakos, "Investigation of flow over an oscillating airfoil," *Journal of Fluid Mechanics*, vol. 512, pp. 313–341, 2004.

[13] M. R. Amiralaei, H. Alighanbari, and S. M. Hashemi, "An investigation into the effects of unsteady parameters on the aerodynamics of a low Reynolds number pitching airfoil," *Journal of Fluids and Structures*, vol. 26, no. 6, pp. 979–993, 2010.

[14] M. A. Ashraf, J. Young, and J. C. Lai, "Reynolds number, thickness and camber effects on flapping airfoil propulsion," *Journal of Fluids and Structures*, vol. 27, no. 2, pp. 145–160, 2011.

[15] K. Gharali and D. A. Johnson, "Dynamic stall simulation of a pitching airfoil under unsteady freestream velocity," *Journal of Fluids and Structures*, vol. 42, pp. 228–244, 2013.

[16] E. H. Dowell, "Nonlinear Oscillations of a Fluttering Plate," *AIAA Journal*, vol. 4, no. 7, pp. 1267–1275, 1966.

[17] E. J. Jumper, R. L. Dimmick, and A. J. S. Allaire, "The effect of pitch location on dynamic stall," *Journal of Fluids Engineering*, vol. 111, no. 3, pp. 256–262, 1989.

[18] P. Holmes and J. Marsden, "Bifurcation to divergence and flutter in flow-induced oscillations: an infinite dimensional analysis," *Automatica*, vol. 14, no. 4, pp. 367–384, 1978.

[19] K. D. Jones and M. F. Platzer, "Time-domain analysis of low-speed airfoil flutter," *AIAA Journal*, vol. 34, no. 5, pp. 1027–1033, 1996.

[20] E. H. Dowell and K. C. Hall, "Modeling of Fluid-Structure Interaction," *Annual Review of Fluid Mechanics*, vol. 33, no. 1, pp. 445–490, 2001.

[21] K. C. Hall, "Eigenanalysis of Unsteady Flows About Airfoils, Cascades, and Wings," *AIAA Journal*, vol. 32, no. 12, pp. 2426–2432, 1994.

[22] K. Ramesh, J. Murua, and A. Gopalarathnam, "Limit-cycle oscillations in unsteady flows dominated by intermittent leading-edge vortex shedding," *Journal of Fluids and Structures*, vol. 55, pp. 84–105, 2015.

[23] D. Poirel, Y. Harris, and A. Benaissa, "Self-sustained aeroelastic oscillations of a NACA0012 airfoil at low-to-moderate Reynolds numbers," *Journal of Fluids and Structures*, vol. 24, no. 5, pp. 700–719, 2008.

[24] D. Poirel, V. Métivier, and G. Dumas, "Computational aeroelastic simulations of self-sustained pitch oscillations of a NACA0012 at transitional Reynolds numbers," *Journal of Fluids and Structures*, vol. 27, no. 8, pp. 1262–1277, 2011.

[25] A. Ducoin and Y. L. Young, "Hydroelastic response and stability of a hydrofoil in viscous flow," *Journal of Fluids and Structures*, vol. 38, pp. 40–57, 2013.

[26] G. Dimitriadis and J. Li, "Bifurcation Behavior of Airfoil Undergoing Stall Flutter Oscillations in Low-Speed Wind Tunnel," *AIAA Journal*, vol. 47, no. 11, pp. 2577–2596, 2009.

[27] T. L. Morse and C. H. Williamson, "Prediction of vortex-induced vibration response by employing controlled motion," *Journal of Fluid Mechanics*, vol. 634, pp. 5–39, 2009.

[28] K. Onoue, A. Song, B. Strom, and K. S. Breuer, "Large amplitude flow-induced oscillations and energy harvesting using a cyber-physical pitching plate," *Journal of Fluids and Structures*, vol. 55, pp. 262–275, 2015.

[29] Y. Zhu, Y. Su, and K. Breuer, "Nonlinear flow-induced instability of an elastically mounted pitching wing," *Journal of Fluid Mechanics*, vol. 899, 2020.

[30] Z. Peng and Q. Zhu, "Energy harvesting through flow-induced oscillations of a foil," *Physics of Fluids*, vol. 21, no. 12, pp. 1–9, 2009.

[31] T. von Karman and W. R. Sears, "Airfoil theory for non-uniform motion," *Journal of the Aeronautical Sciences*, vol. 5, no. 10, 1938.

[32] H. G. Küssner, "Zusammenfassender Bericht über den instationären Auftrieb von Flügeln," *Luftfahrtforschung*, vol. 13, no. 12, pp. 410–424, 1936.

[33] A. Kuethe, “Circulation measurements about the tip of an airfoil during flight through a gust,” *NACA-TN-685*, 1939.

[34] K. Granlund, B. Monnier, M. Ol, and D. Williams, “Airfoil longitudinal gust response in separated vs. attached flows,” *Physics of Fluids*, vol. 26, no. 2, pp. 0–14, 2014.

[35] G. Perrotta and A. R. Jones, “Unsteady forcing on a flat-plate wing in large transverse gusts,” *Experiments in Fluids*, vol. 58, no. 8, 2017.

[36] S. J. Corkery, H. Babinsky, and J. K. Harvey, “On the development and early observations from a towing tank-based transverse wing–gust encounter test rig,” *Experiments in Fluids*, vol. 59, no. 9, pp. 1–16, 2018.

[37] H. Biler, C. Badrya, and A. R. Jones, “Experimental and Computational Investigation of Transverse Gust Encounters,” *AIAA Journal*, vol. 57, no. 11, pp. 4608–4622, 2019.

[38] R. Singh and J. D. Baeder, “Direct calculation of three-dimensional indicial lift response using computational fluid dynamics,” *Journal of Aircraft*, vol. 34, no. 4, pp. 465–471, 1997.

[39] V. Parameswaran and J. D. Baeder, “Indicial Aerodynamics in Compressible Flow - Direct Computational Fluid Dynamic Calculations,” *Journal of Aircraft*, vol. 34, no. 1, pp. 1–3, 1997.

[40] C. Wales, D. Jones, and A. Gaitonde, "Prescribed velocity method for simulation of aerofoil gust responses," *Journal of Aircraft*, vol. 52, no. 1, pp. 64–76, 2015.

[41] S. J. Huntley, D. Jones, and A. Gaitonde, "Aeroelastic gust response of an aircraft using a prescribed velocity method in viscous flows," *23rd AIAA Computational Fluid Dynamics Conference, 2017*, no. June, pp. 1–18, 2017.

[42] C. Badrya, J. D. Baeder, and A. R. Jones, "Application of prescribed velocity methods to a large-amplitude flat-plate gust encounter," *AIAA Journal*, vol. 57, no. 8, pp. 3261–3373, 2019.

[43] G. Yang and S. Obayashi, "Numerical analyses of discrete gust response for a flexible aircraft," *21st AIAA Applied Aerodynamics Conference*, vol. 41, no. 6, 2003.

[44] D. Tang and E. H. Dowell, "Limit cycle oscillations of two-dimensional panels in low subsonic flow," *International Journal of Non-Linear Mechanics*, vol. 37, no. 7, pp. 1199–1209, 2002.

[45] M. Gennaretti and F. Mastroddi, "Study of Reduced-Order Models for Gust-Response Analysis of Flexible Wings," *Journal of Aircraft*, vol. 41, no. 2, pp. 304–313, 2004.

[46] A. Zaide and D. Raveh, "Numerical simulation and reduced-order modeling of airfoil gust response," *AIAA Journal*, vol. 44, no. 8, pp. 1826–1834, 2006.

[47] D. E. Raveh, "CFD-based models of aerodynamic gust response," *Journal of Aircraft*, vol. 44, no. 3, pp. 888–897, 2007.

[48] D. E. Raveh, "Gust-response analysis of free elastic aircraft in the transonic flight regime," *Journal of Aircraft*, vol. 48, no. 4, pp. 1204–1211, 2011.

[49] C. Wales, A. Gaitonde, and D. Jones, "Reduced-order modeling of gust responses," *Journal of Aircraft*, vol. 54, no. 4, pp. 1350–1363, 2017.

[50] R. E. D. Bishop and A. Hassan, "The lift and drag forces on a circular cylinder oscillating in a flowing fluid," *Proceedings of the Royal Society of London. Series A. Mathematical and Physical Sciences*, vol. 277, no. 1368, pp. 51–75, 1 1964.

[51] C. Feng, "The measurement of vortex induced effects in flow past stationary and oscillating circular and D-section cylinders," *Masters thesis, The University of British Columbia, Canada*, 1968.

[52] P. Anagnostopoulos and P. W. Bearman, "Response characteristics of a

vortex-excited cylinder at low reynolds numbers," *Journal of Fluids and Structures*, vol. 6, no. 1, pp. 39–50, 1992.

[53] J. R. Meneghini and P. W. Bearman, "Numerical simulation of high amplitude oscillatory flow about a circular cylinder," *Journal of Fluids and Structures*, vol. 9, no. 4, pp. 435–455, 5 1995.

[54] T. K. Prasanth and S. Mittal, "Vortex-induced vibrations of a circular cylinder at low Reynolds numbers," *Journal of Fluid Mechanics*, vol. 594, no. 2008, pp. 463–491, 2008.

[55] A. Khalak and C. Williamson, "Motions, Forces and Mode Transitions in Vortex-Induced Vibrations At Low Mass-Damping," *Journal of Fluids and Structures*, vol. 13, no. 7-8, pp. 813–851, 1999.

[56] S. P. Singh and S. Mittal, "Vortex-induced oscillations at low reynolds numbers: Hysteresis and vortex-shedding modes," *Journal of Fluids and Structures*, vol. 20, no. 8, pp. 1085–1104, 2005.

[57] L. W. Carr, "Progress in analysis and prediction of dynamic stall," *Journal of Aircraft*, vol. 25, no. 1, pp. 6–17, 1988.

[58] M. M. Koochesfahani, "Vortical patterns in the wake of an oscillating airfoil," *AIAA Journal*, vol. 27, no. 9, pp. 1200–1205, 1989.

[59] E. G. Drucker and G. V. Lauder, "Locomotor forces on a swimming fish:

Three-dimensional vortex wake dynamics quantified using digital particle image velocimetry," *Journal of Experimental Biology*, vol. 202, no. 18, pp. 2393–2412, 1999.

[60] M. S. Triantafyllou, A. H. Techet, and F. S. Hover, "Review of experimental work in biomimetic foils," *IEEE Journal of Oceanic Engineering*, vol. 29, no. 3, pp. 585–594, 2004.

[61] T. Schnipper, A. Andersen, and T. Bohr, "Vortex wakes of a flapping foil," *Journal of Fluid Mechanics*, vol. 633, pp. 411–423, 2009.

[62] M. M. Zdravkovich, "Modification of Vortex Shedding in the Synchronization Range." *American Society of Mechanical Engineers (Paper)*, vol. 104, no. December, pp. 513–517, 1982.

[63] A. Ongoren and D. Rockwell, "Flow structure from an oscillating cylinder Part 2. Mode competition in the near wake," *Journal of Fluid Mechanics*, vol. 191, pp. 225–245, 1988.

[64] C. H. K. Williamson and A. Roshko, "Vortex formation in the wake of an oscillating cylinder," *Journal of Fluids and Structures*, vol. 2, no. 4, pp. 355–381, 1988.

[65] D. Brika and A. Laneville, "Vortex-induced vibrations of a long flexible

circular cylinder," *Journal of Fluid Mechanics*, vol. 250, no. EM5, pp. 481–508, 1993.

[66] H. M. Blackburn and R. D. Henderson, "A study of two-dimensional flow past an oscillating cylinder," *Journal of Fluid Mechanics*, vol. 385, pp. 255–286, 1999.

[67] R. Govardhan and C. H. Williamson, "Modes of vortex formation and frequency response of a freely vibrating cylinder," *Journal of Fluid Mechanics*, vol. 420, pp. 85–130, 2000.

[68] J. Carberry, J. Sheridan, and D. Rockwell, "Controlled oscillations of a cylinder: Forces and wake modes," *Journal of Fluid Mechanics*, vol. 538, pp. 31–69, 2005.

[69] T. J. Mueller and J. D. DeLaurier, "Aerodynamics of Small Vehicles," *Annual Review of Fluid Mechanics*, vol. 35, no. 1, pp. 89–111, 2003.

[70] T. Sarpkaya, "Fluid forces on oscillating cylinders," *Journal of the Waterway, Port, Coastal and Ocean Division*, vol. 104, no. 3, pp. 275–290, 1978.

[71] T. Staubli, "Calculation of the Vibration of an Elastically Mounted Cylinder Using Experimental Data From Forced Oscillation," *Journal of Fluids Engineering*, vol. 105, no. 2, p. 225, 1983.

[72] R. Gopalakrishnan, "Vortex-Induced Forces on Oscillating Bluff Cylinders," Ph.D. dissertation, Massachusetts Institute of Technology, 1993.

[73] F. S. Hover, A. H. Techet, and M. S. Triantafyllou, "Forces on oscillating uniform and tapered cylinders in crossflow," *Journal of Fluid Mechanics*, vol. 363, pp. 97–114, 1998.

[74] T. L. Morse and C. H. K. Williamson, "Employing controlled vibrations to predict fluid forces on a cylinder undergoing vortex-induced vibration," *Journal of Fluids and Structures*, vol. 22, no. 6-7, pp. 877–884, 2006.

[75] S. Kumar, Navrose, and S. Mittal, "Lock-in in forced vibration of a circular cylinder," *Physics of Fluids*, vol. 28, no. 11, 2016.

[76] S. S. Bhat and R. N. Govardhan, "Stall flutter of NACA 0012 airfoil at low Reynolds numbers," *Journal of Fluids and Structures*, vol. 41, pp. 166–174, 2013.

[77] K. Menon and R. Mittal, "Flow physics and dynamics of flow-induced pitch oscillations of an airfoil," *Journal of Fluid Mechanics*, vol. 877, pp. 582–613, 2019.

[78] K. Menon and R. Mittal, "Aeroelastic response of an airfoil to gusts: Prediction and control strategies from computed energy maps," *Journal of Fluids and Structures*, vol. 97, 2020.

[79] K. Menon and R. Mittal, "On the initiation and sustenance of flow-induced vibration of cylinders: insights from force partitioning," *Journal of Fluid Mechanics*, vol. 907, no. A37, 2020.

[80] B. Y. M. H. Dickinson and K. G. Götz, "Unsteady Aerodynamic Performance of Model Wings At Low Reynolds Numbers," *Journal of Experimental Biology*, vol. 174, no. 1, pp. 45–64, 1993.

[81] C. P. Ellington, C. D. Van Berg, A. P. Willmott, and A. L. Thomas, "Leading-edge vortices in insect flight," *Nature*, vol. 384, no. 6610, pp. 626–630, 1996.

[82] C. H. Williamson, "Vortex dynamics in the cylinder wake," *Annual Review of Fluid Mechanics*, vol. 28, pp. 477–539, 1996.

[83] M. S. Triantafyllou, G. S. Triantafyllou, and D. K. P. Yue, "Hydrodynamics of Fishlike Swimming," *Annual Review of Fluid Mechanics*, vol. 32, no. 1, pp. 33–53, 2000.

[84] S. P. Sane, "The aerodynamics of insect flight," *Journal of Experimental Biology*, vol. 206, no. 23, pp. 4191–4208, 2003.

[85] Z. J. Wang, "Dissecting Insect Flight," *Annual Review of Fluid Mechanics*, vol. 37, no. 1, pp. 183–210, 2005.

[86] R. Mittal, "Matters of the heart," *Journal of Fluid Mechanics*, vol. 844, pp. 1–4, 2018.

[87] J. Lighthill, "Fundamentals concerning wave loading on offshore structures," *Journal of Fluid Mechanics*, vol. 173, pp. 667–681, 1986.

[88] T. Sarpkaya, "On the force decompositions of lighthill and Morison," *Journal of Fluids and Structures*, vol. 15, no. 2, pp. 227–233, 2 2001.

[89] C. Wang and J. D. Eldredge, "Low-order phenomenological modeling of leading-edge vortex formation," *Theoretical and Computational Fluid Dynamics*, vol. 27, no. 5, pp. 577–598, 2013.

[90] W. R. Graham, C. W. Pitt Ford, and H. Babinsky, "An impulse-based approach to estimating forces in unsteady flow," *Journal of Fluid Mechanics*, vol. 815, pp. 60–76, 2017.

[91] C. W. Pitt Ford and H. Babinsky, "Lift and the leading-edge vortex," *Journal of Fluid Mechanics*, vol. 720, pp. 280–313, 2013.

[92] K. Onoue and K. S. Breuer, "Vortex formation and shedding from a cyber-physical pitching plate," *Journal of Fluid Mechanics*, vol. 793, pp. 229–247, 4 2016.

[93] L. Quartappelle and M. Napolitano, "Force and moment in incompressible flows," *AIAA Journal*, vol. 21, no. 6, pp. 911–913, 1982.

[94] C. C. Chang, "Potential flow and forces for incompressible viscous flow," *Proceedings of the Royal Society A: Mathematical, Physical and Engineering Sciences*, vol. 437, no. 1901, pp. 517–525, 1992.

[95] C. Zhang, T. L. Hedrick, and R. Mittal, "Centripetal acceleration reaction: An effective and robust mechanism for flapping flight in insects," *PLoS ONE*, vol. 10, no. 8, pp. 1–16, 2015.

[96] B. Protas, A. Styczek, and A. Nowakowski, "An Effective Approach to Computation of Forces in Viscous Incompressible Flows," *Journal of Computational Physics*, vol. 159, no. 2, pp. 231–245, 4 2000.

[97] L. S. Pan and Y. T. Chew, "A general formula for calculating forces on a 2-D arbitrary body in incompressible flow," *Journal of Fluids and Structures*, vol. 16, no. 1, pp. 71–82, 1 2002.

[98] M. S. Howe, "On the force and moment on a body in an incompressible fluid, with application to rigid bodies and bubbles at high and low reynolds numbers," *Quarterly Journal of Mechanics and Applied Mathematics*, vol. 48, no. 3, pp. 401–426, 1995.

[99] J. Magnaudet, "A 'reciprocal' theorem for the prediction of loads on a body moving in an inhomogeneous flow at arbitrary Reynolds number," *Journal of Fluid Mechanics*, vol. 689, pp. 564–604, 2011.

[100] A. Martín-Alcántara, R. Fernandez-Feria, and E. Sanmiguel-Rojas, "Vortex flow structures and interactions for the optimum thrust efficiency of a heaving airfoil at different mean angles of attack," *Physics of Fluids*, vol. 27, no. 7, 2015.

[101] M. Moriche, O. Flores, and M. García-Villalba, "On the aerodynamic forces on heaving and pitching airfoils at low Reynolds number," *J. Fluid Mech*, vol. 828, pp. 395–423, 2018.

[102] J. Z. Wu, X. Y. Lu, and L. X. Zhuang, "Integral force acting on a body due to local flow structures," *Journal of Fluid Mechanics*, vol. 576, pp. 265–286, 2007.

[103] J. N. Kutz, "Deep learning in fluid dynamics," *Journal of Fluid Mechanics*, vol. 814, pp. 1–4, 2017.

[104] K. Duraisamy, G. Iaccarino, and H. Xiao, "Turbulence modeling in the age of data," *Annual Review of Fluid Mechanics*, vol. 51, pp. 357–377, 2019.

[105] S. L. Brunton, B. R. Noack, and P. Koumoutsakos, "Machine Learning for Fluid Mechanics," *Annual Review of Fluid Mechanics*, vol. 52, no. 1, pp. 477–508, 2020.

[106] K. Taira, S. L. Brunton, S. T. M. Dawson, C. W. Rowley, T. Colonius,

B. J. McKeon, O. T. Schmidt, S. Gordeyev, V. Theofilis, and L. S. Ukeiley, "Modal Analysis of Fluid Flows: An Overview," *AIAA Journal*, vol. 55, no. 12, 2017.

[107] C. W. Rowley, I. Mezi, S. Bagheri, P. Schlatter, and D. S. Henningson, "Spectral analysis of nonlinear flows," *Journal of Fluid Mechanics*, vol. 641, pp. 115–127, 2009.

[108] P. J. Schmid, "Dynamic mode decomposition of numerical and experimental data," *Journal of Fluid Mechanics*, vol. 656, pp. 5–28, 2010.

[109] K. K. Chen, J. H. Tu, and C. W. Rowley, "Variants of dynamic mode decomposition: Boundary condition, Koopman, and fourier analyses," *Journal of Nonlinear Science*, vol. 22, no. 6, pp. 887–915, 2012.

[110] P. J. Schmid, "Application of the dynamic mode decomposition to experimental data," *Experiments in Fluids*, vol. 50, no. 4, pp. 1123–1130, 2011.

[111] P. J. Schmid, L. Li, M. P. Juniper, and O. Pust, "Applications of the dynamic mode decomposition," *Theoretical and Computational Fluid Dynamics*, vol. 25, no. 1-4, pp. 249–259, 2011.

[112] S. Bagheri, "Koopman-mode decomposition of the cylinder wake," *Journal of Fluid Mechanics*, vol. 726, pp. 596–623, 2013.

[113] M. S. Hemati, C. W. Rowley, E. A. Deem, and L. N. Cattafesta, "Debiasing the dynamic mode decomposition for applied Koopman spectral analysis of noisy datasets," *Theoretical and Computational Fluid Dynamics*, vol. 31, no. 4, pp. 349–368, 2017.

[114] A. T. Mohan and D. V. Gaitonde, "Analysis of airfoil stall control using dynamic mode decomposition," *Journal of Aircraft*, vol. 54, no. 4, pp. 1508–1520, 2017.

[115] C. Pan, D. Yu, and J. Wang, "Dynamical mode decomposition of Gurney flap wake flow," *Theoretical and Applied Mechanics Letters*, vol. 1, no. 1, p. 012002, 2011.

[116] A. Goza and T. Colonius, "Modal decomposition of fluid–structure interaction with application to flag flapping," *Journal of Fluids and Structures*, vol. 81, pp. 728–737, 8 2018.

[117] A. Cesur, C. Carlsson, A. Feymark, L. Fuchs, and J. Revstedt, "Analysis of the wake dynamics of stiff and flexible cantilever beams using POD and DMD," *Computers and Fluids*, vol. 101, pp. 27–41, 9 2014.

[118] A. T. Mohan, D. V. Gaitonde, and M. R. Visbal, "Model reduction and analysis of deep dynamic stall on a plunging airfoil," *Computers and Fluids*, vol. 129, pp. 1–19, 4 2016.

[119] R. Mittal and G. Iaccarino, "Immersed Boundary Methods," *Annual Review of Fluid Mechanics*, vol. 37, no. 1, pp. 239–261, 2005.

[120] A. K. Jain, M. N. Murty, and P. J. Flynn, "Data Clustering: A Review," *ACM Computing Surveys*, vol. 31, no. 3, 1999.

[121] J. Han, J. Pei, and M. Kamber, *Data mining: concepts and techniques*. Elsevier, 2011.

[122] A. G. Nair and K. Taira, "Network-theoretic approach to sparsified discrete vortex dynamics," *Journal of Fluid Mechanics*, vol. 768, pp. 549–571, 2015.

[123] G. Froyland and K. Padberg-Gehle, "A rough-and-ready cluster-based approach for extracting finite-time coherent sets from sparse and incomplete trajectory data," *Chaos*, vol. 25, no. 8, p. 87406, 2015.

[124] E. Ser-Giacomi, V. Rossi, C. López, and E. Hernández-García, "Flow networks: A characterization of geophysical fluid transport," *Chaos*, vol. 25, no. 3, p. 36404, 2015.

[125] A. Hadjighasem, D. Karrasch, H. Teramoto, and G. Haller, "Spectral-clustering approach to Lagrangian vortex detection," *Physical Review E*, vol. 93, no. 6, 2016.

[126] K. L. Schlueter-Kuck and J. O. Dabiri, "Coherent structure colouring:

Identification of coherent structures from sparse data using graph theory," *Journal of Fluid Mechanics*, vol. 811, pp. 468–486, 2017.

[127] K. Padberg-Gehle and C. Schneide, "Network-based study of Lagrangian transport and mixing," *Nonlinear Processes in Geophysics*, vol. 24, no. 4, pp. 661–671, 2017.

[128] M. M. Zdravkovich, "Review and classification of various aerodynamic and hydrodynamic means for suppressing vortex shedding," *Journal of Wind Engineering and Industrial Aerodynamics*, vol. 7, no. 2, pp. 145–189, 1981.

[129] C. Williamson and R. Govardhan, "Vortex-Induced Vibrations," *Annual Review of Fluid Mechanics*, vol. 36, no. 1, pp. 413–455, 2004.

[130] M. S. Hemati, "Learning wake regimes from snapshot data," *46th AIAA Fluid Dynamics Conference*, pp. 1–14, 2016.

[131] M. Wang and M. S. Hemati, "Detecting exotic wakes with hydrodynamic sensors," *Theoretical and Computational Fluid Dynamics*, vol. 33, no. 3-4, pp. 235–254, 2019.

[132] B. Colvert, M. Alsalman, and E. Kanso, "Classifying vortex wakes using neural networks," *Bioinspiration and Biomimetics*, vol. 13, no. 2, 2018.

[133] R. Mittal, H. Dong, M. Bozkurttas, F. M. Najjar, A. Vargas, and A. von

Loebbecke, "A versatile sharp interface immersed boundary method for incompressible flows with complex boundaries," *Journal of Computational Physics*, vol. 227, no. 10, pp. 4825–4852, 2008.

[134] J. H. Seo and R. Mittal, "A sharp-interface immersed boundary method with improved mass conservation and reduced spurious pressure oscillations," *Journal of Computational Physics*, vol. 230, no. 19, pp. 7347–7363, 8 2011.

[135] R. Ghias, R. Mittal, and H. Dong, "A sharp interface immersed boundary method for compressible viscous flows," *Journal of Computational Physics*, vol. 225, no. 1, pp. 528–553, 7 2007.

[136] P. W. Bearman, "Circular cylinder wakes and vortex-induced vibrations," *Journal of Fluids and Structures*, vol. 27, no. 5-6, pp. 648–658, 7 2011.

[137] Navrose, V. Yogeswaran, S. Sen, and S. Mittal, "Free vibrations of an elliptic cylinder at low Reynolds numbers," *Journal of Fluids and Structures*, vol. 51, pp. 55–67, 2014.

[138] D. F. Kurtulus, "On the Unsteady Behavior of the Flow around NACA 0012 Airfoil with Steady External Conditions at Re=1000," *International Journal of Micro Air Vehicles*, vol. 7, no. 3, pp. 301–326, 2015.

[139] Y. Liu, K. Li, J. Zhang, H. Wang, and L. Liu, "Numerical bifurcation anal-

ysis of static stall of airfoil and dynamic stall under unsteady perturbation," *Communications in Nonlinear Science and Numerical Simulation*, vol. 17, no. 8, pp. 3427–3434, 8 2012.

[140] S. Mittal and T. E. Tezduyar, "Massively parallel finite element computation of incompressible flows involving fluid-body interactions," *Computer Methods in Applied Mechanics and Engineering*, vol. 112, no. 1-4, pp. 253–282, 1994.

[141] H. M. Blackburn and G. E. Karniadakis, "Two- and Three-Dimensional Simulations of Vortex-Induced Vibration of a Circular Cylinder," *3rd Int. Offshore & Polar Engng Conf., Singapore*, no. 1977, pp. 715–720, 1993.

[142] I. H. Abbott and A. E. Von Doenhoff, *Theory of wing sections, including a summary of airfoil data*. Courier Corporation, 1959.

[143] S. H. Strogatz, *Nonlinear Dynamics And Chaos*. CRC Press, 2015.

[144] C. H. K. Williamson and R. Govardhan, "A brief review of recent results in vortex-induced vibrations," *Journal of Wind Engineering and Industrial Aerodynamics*, vol. 96, no. 6-7, pp. 713–735, 2008.

[145] J. S. Leontini, B. E. Stewart, M. C. Thompson, and K. Hourigan, "Predicting vortex-induced vibration from driven oscillation results," *Applied Mathematical Modelling*, vol. 30, no. 10, pp. 1096–1102, 2006.

[146] Military Specification, "Airplane Strength and Rigidity Vibration, Flutter, and Divergence," *MIL-A-8870C*, 1993.

[147] D. Dessi and F. Mastroddi, "A nonlinear analysis of stability and gust response of aeroelastic systems," *Journal of Fluids and Structures*, vol. 24, no. 3, pp. 436–445, 2008.

[148] S. Sarkar and H. Bijl, "Nonlinear aeroelastic behavior of an oscillating airfoil during stall-induced vibration," *Journal of Fluids and Structures*, vol. 24, no. 6, pp. 757–777, 2008.

[149] D. Kim and H. Choi, "Immersed boundary method for flow around an arbitrarily moving body," *Journal of Computational Physics*, vol. 212, no. 2, pp. 662–680, 2006.

[150] J. H. Tu, C. W. Rowley, D. M. Luchtenburg, S. L. Brunton, and J. N. Kutz, "On dynamic mode decomposition: Theory and applications," *Journal of Computational Dynamics*, vol. 1, no. 2, pp. 391–421, 2014.

[151] K. Menon and R. Mittal, "Dynamic mode decomposition based analysis of flow over a sinusoidally pitching airfoil," *Journal of Fluids and Structures*, vol. 94, p. 102886, 2020.

[152] G. K. Batchelor, *An Introduction to Fluid Dynamics*. Cambridge University Press, 1967.

[153] C. Zhang, "Mechanisms for Aerodynamic Force Generation and Flight Stability in Insects," Ph.D. dissertation, Johns Hopkins University, 2015.

[154] T. Sarpkaya, "A critical review of the intrinsic nature of vortex-induced vibrations," *Journal of Fluids and Structures*, vol. 19, no. 4, pp. 389–447, 2004.

[155] G. S. Triantafyllou, M. S. Triantafyllou, and C. Chryssostomidis, "On the formation of vortex streets behind stationary cylinders," *Journal of Fluid Mechanics*, vol. 170, pp. 461–477, 1986.

[156] J. M. Anderson, K. Streitlien, D. S. Barrett, and M. S. Triantafyllou, "Oscillating foils of high propulsive efficiency," *Journal of Fluid Mechanics*, vol. 360, pp. 41–72, 1998.

[157] Q. Zhu, M. J. Wolfgang, D. K. Yue, and M. S. Triantafyllou, "Three-dimensional flow structures and vorticity control in fish-like swimming," *Journal of Fluid Mechanics*, vol. 468, pp. 1–28, 2002.

[158] Y. Huang and M. A. Green, "Detection and tracking of vortex phenomena using Lagrangian coherent structures," *Experiments in Fluids*, vol. 56, no. 7, 2015.

[159] M. P. Rockwood, K. Taira, and M. A. Green, "Detecting vortex formation

and shedding in cylinder wakes using Lagrangian coherent structures," *AIAA Journal*, vol. 55, no. 1, pp. 15–23, 2017.

[160] M. Rockwood, Y. Huang, and M. Green, "Tracking coherent structures in massively-separated and turbulent flows," *Physical Review Fluids*, vol. 3, no. 1, pp. 1–19, 2018.

[161] J. C. R. Hunt, A. A. Wray, and P. Moin, "Eddies, streams, and convergence zones in turbulent flows," Center for Turbulence Research, Tech. Rep., 1988.

[162] M. S. Chong, A. E. Perry, and B. J. Cantwell, "A general classification of three-dimensional flow fields," *Physics of Fluids A*, vol. 2, no. 5, pp. 765–777, 1990.

[163] J. Jeong and F. Hussain, "On the identification of a vortex," *Journal of Fluid Mechanics*, vol. 285, pp. 69–94, 1995.

[164] G. Haller, "Lagrangian Coherent Structures," *Annual Review of Fluid Mechanics*, vol. 47, no. 1, pp. 137–162, 2015.

[165] A. Hadjighasem, M. Farazmand, D. Blazevski, G. Froyland, and G. Haller, "A critical comparison of Lagrangian methods for coherent structure detection," *Chaos*, vol. 27, no. 5, p. 53104, 2017.

[166] M. Ester, H.-P. Kriegel, J. Sander, and X. Xu, "A Density-Based Algorithm for Discovering Clusters in Large Spatial Databases with Noise," in *Proceedings of the 2nd International Conference on Knowledge Discovery and Data Mining*, 1996, pp. 226–231.

[167] F. Reinders, F. H. Post, and H. J. W. Spoelder, "Visualization of time-dependent data with feature tracking and event detection," *The Visual Computer*, vol. 17, pp. 55–71, 2001.

[168] F. H. Post, B. Vrolijk, H. Hauser, R. S. Larameeand, and H. Doleisch, "The State of the Art in Flow Visualisation: Feature Extraction and Tracking," *Computer Graphics Forum*, vol. 22, no. 4, pp. 775–792, 2003.

[169] Q. Zhu, M. Haase, and C. H. Wu, "Modeling the capacity of a novel flow-energy harvester," *Applied Mathematical Modelling*, vol. 33, no. 5, pp. 2207–2217, 2009.

[170] K. Menon and R. Mittal, "Quantitative analysis of the kinematics and induced aerodynamic loading of individual vortices in vortex-dominated flows: A computation and data-driven approach," *arXiv preprint arXiv:2011.04632*, 2020.

[171] W. Shyy and H. Liu, "Flapping wings and aerodynamic lift: The role of leading-edge vortices," *AIAA Journal*, vol. 45, no. 12, pp. 2817–2819, 2007.

[172] K. K. Chen, T. Colonius, and K. Taira, "The leading-edge vortex and quasisteady vortex shedding on an accelerating plate," *Physics of Fluids*, vol. 22, no. 3, pp. 1–11, 2010.

[173] X. Xia and K. Mohseni, "Lift evaluation of a two-dimensional pitching flat plate," *Physics of Fluids*, vol. 25, no. 9, p. 91901, 2013.

[174] K. Mulleners and M. Raffel, "Dynamic stall development," *Experiments in Fluids*, vol. 54, no. 2, 2013.

[175] P. K. Kundu and I. M. Cohen, *Fluid Mechanics*. Elsevier, 2008.

[176] H. Lamb, *Hydrodynamics*. Cambridge University Press, 1993.

[177] K. Menon and R. Mittal, "Aerodynamic characteristics of canonical airfoils at low Reynolds numbers," *AIAA Journal*, vol. 58, no. 2, pp. 977–980, 2020.

[178] K. Menon and R. Mittal, "Significance of the strain-dominated region around a vortex on induced aerodynamic loads," *Journal of Fluid Mechanics*, vol. 918, no. R3, pp. 1–10, 2021.

[179] T. A. Weisshaar, "Morphing aircraft systems: Historical perspectives and future challenges," *Journal of Aircraft*, vol. 50, no. 2, pp. 337–353, 2013.

[180] A. Chattopadhyay, C. E. Seeley, and R. Jha, "Aeroelastic tailoring using

piezoelectric actuation and hybrid optimization," *Smart Materials and Structures*, vol. 8, pp. 83–91, 1999.

[181] V. Giurgiutiu, "Review of smart-materials actuation solutions for aeroelastic and vibration control," *Journal of Intelligent Material Systems and Structures*, vol. 11, no. 7, pp. 525–544, 2000.

[182] T. A. Weisshaar, "Adaptive Wings- Control and Optimization Issues," *Composites*, vol. 2, pp. 457–476, 1992.

[183] L. Librescu, L. Meirovitch, and S. S. Na, "Control of cantilever vibration via structural tailoring and adaptive materials," *AIAA Journal*, vol. 35, no. 8, pp. 1309–1315, 1997.

[184] B. Jenett, S. Calisch, D. Cellucci, N. Cramer, N. Gershenfeld, S. Swei, and K. C. Cheung, "Digital Morphing Wing: Active Wing Shaping Concept Using Composite Lattice-Based Cellular Structures," *Soft Robotics*, vol. 4, no. 1, pp. 33–48, 2017.

[185] J. C. Wu, "Theory for Aerodynamic Force and Moment in Viscous Flows," *AIAA Journal*, vol. 19, no. 4, pp. 432–441, 1981.

[186] F. Noca, D. Shiels, and D. Jeon, "Measuring instantaneous fluid dynamic forces on bodies, using only velocity fields and their derivatives," *Journal of Fluids and Structures*, vol. 11, no. 3, pp. 345–350, 1997.

[187] F. Noca, D. Shiels, and D. Jeon, "A comparison of methods for evaluating time-dependent fluid dynamic forces on bodies, using only velocity fields and their derivatives," *Journal of Fluids and Structures*, vol. 13, no. 5, pp. 551–578, 1999.

[188] R. E. Sheldahl and P. C. Klimas, "Aerodynamic characteristics of seven symmetrical airfoil sections through 180-degree angle of attack for use in aerodynamic analysis of vertical axis wind turbines," Sandia National Laboratories, Albuquerque, NM (United States), Tech. Rep., 1981.

[189] B. H. Carmichael, "Low Reynolds number airfoil survey, volume 1," *NASA Contractor Report 165803*, vol. 165803, 11 1981.

[190] M. Selig, J. Guglielmo, A. Broeren, and P. Giguère, *Summary of Low-Speed Airfoil Data, Vol. 1*. Virginia Beach, VA: SoarTech Publications, 1995.

[191] M. Selig, C. Lyon, P. Giguère, C. Ninham, and J. Guglielmo, *Summary of Low-Speed Airfoil Data, Vol. 2*. Virginia Beach, VA: SoarTech Publications, 1996.

[192] C. Lyon, A. Broeren, P. Giguère, A. Gopalarathnam, and M. Selig, *Summary of Low-Speed Airfoil Data, Vol. 3*. Virginia Beach, VA: SoarTech Publications, 1997.

[193] J. Tank, L. Smith, and G. R. Spedding, "On the possibility (Or lack thereof) of agreement between experiment and computation of flows over wings at moderate Reynolds number," *Interface Focus*, vol. 7, no. 1, 2017.

[194] L. E. Jones, R. D. Sandberg, and N. D. Sandham, "Direct numerical simulations of forced and unforced separation bubbles on an airfoil at incidence," *Journal of Fluid Mechanics*, vol. 602, pp. 175–207, 2008.

[195] P. J. Kunz and I. M. Kroo, "Analysis, Design, and Testing of Airfoils for Use at Ultra- Low Reynolds Numbers," *Fixed Flapping and Rotary Wing Aerodynamics for Micro Aerial Vehicle Applications*, pp. 35–60, 2001.

[196] D. Mateescu and M. Abdo, "Analysis of flows past airfoils at very low Reynolds numbers," *Proceedings of the Institution of Mechanical Engineers, Part G: Journal of Aerospace Engineering*, vol. 224, no. 7, pp. 757–775, 2010.

[197] J. D. Banfield and A. E. Raftery, "Model-Based Gaussian and Non-Gaussian Clustering," *Biometrics*, vol. 49, no. 3, pp. 803–821, 1993.

[198] C. Fraley and A. E. Raftery, "How Many Clusters? Which Clustering Method? Answers Via Model-Based Cluster Analysis," *The Computer Journal*, vol. 41, no. 8, pp. 578–588, 1998.

[199] C. Fraley and A. E. Raftery, "Model-based clustering, discriminant anal-

ysis, and density estimation," *Journal of the American Statistical Association*, vol. 97, no. 458, pp. 611–631, 2002.

[200] A. P. Dempster, N. M. Laird, and D. B. Rubin, "Maximum Likelihood from Incomplete Data Via the EM Algorithm," *Journal of the Royal Statistical Society: Series B (Methodological)*, vol. 39, no. 1, pp. 1–22, 1977.

[201] F. Pedregosa, G. Varoquaux, A. Gramfort, V. Michel, B. Thirion, O. Grisel, M. Blondel, P. Prettenhofer, R. Weiss, V. Dubourg, J. Vanderplas, A. Passos, D. Cournapeau, M. Brucher, M. Perrot, and E. Duchesnay, "Scikit-learn: Machine Learning in Python," *Journal of Machine Learning Research*, vol. 12, pp. 2825–2830, 2011.

[202] G. Schwarz, "Estimating the dimension of a model," *The Annals of Statistics*, vol. 6, no. 2, pp. 461–464, 1978.

[203] G. J. McLachlan and D. Peel, *Finite mixture models*. John Wiley & Sons, 2004.

[204] L. Hubert and P. Arabie, "Comparing partitions," *Journal of Classification*, vol. 2, no. 1, pp. 193–218, 1985.

[205] S. Monti, P. Tamayo, J. Mesirov, and T. Golub, "Consensus clustering: A resampling-based method for class discovery and visualization of gene

expression microarray data," *Machine Learning*, vol. 52, no. 1-2, pp. 91–118, 2003.

[206] N. X. Vinh and J. Epps, "A novel approach for automatic number of clusters detection in microarray data based on consensus clustering," *Proceedings of the 2009 9th IEEE International Conference on Bioinformatics and BioEngineering, BIBE 2009*, no. June 2014, pp. 84–91, 2009.

[207] W. M. Rand, "Objective criteria for the evaluation of clustering methods," *Journal of the American Statistical Association*, vol. 66, no. 336, pp. 846–850, 1971.

[208] A. Gionis, H. Mannila, and P. Tsaparas, "Clustering aggregation," *ACM Transactions on Knowledge Discovery from Data*, vol. 1, no. 1, 2007.